Joint stereo-PIV and NO-LIF

in turbulent premixed hydrogen-air flames

Christelle C. G. Magand

Supervisor: Pr. J. B. Moss

Cranfield University

School of Engineering

Ph.D. Thesis

September 2009

A thesis submitted in partial fulfilment of the requirements of the degree of Doctor of Philosophy

Joint stereo-PIV and NO-LIF in turbulent premixed hydrogen-air flames

Christelle C. G. Magand

A thesis submitted in partial fulfilment of the requirements for the degree of Doctor of Philosophy at Cranfield University, 2009

ABSTRACT

A new technique to simultaneously and instantaneously resolve 3D velocity/2D strain rate fields and scalar/scalar gradient fields was developed and evaluated in this study. This technique combines Planar Laser Induced Fluorescence of the NO radical (NO-PLIF) and Stereoscopic Particle Image Velocimetry (SPIV). It was found that the NO-PLIF technique allowed the determination of various iso-c contours and as such would, in principle, allow the study of the influence of the heat release on various properties, provided a calibration of the NO-PLIF signal as a function of temperature is achieved. It was also shown that the NO-PLIF technique may not be unambiguous at detecting flame extinction. The SPIV technique allowed the determination of the velocities in 3D and of the strain rates in 2D from which the most extensive and the most compressive strain rates but not the intermediate strain rate could be extracted. Information on strain rates and progress variable gradients were of particular interest in this study as they were needed to study the turbulence-scalar interaction which appears explicitly in the transport equation for the scalar dissipation rate which was derived recently.

Using the technique above mentioned, this work also aimed at gathering and analysing data such as flame normal orientation, progress variable gradients, velocity change across the flame front and strain rates along the flame contours in turbulent premixed hydrogen/air flames with added nitrogen. The flame normal orientation was found to be consistent with the regime of the flames studied. A new method was designed and presented to infer from the progress variable gradients the component of

the flame normal in the third dimension. The velocity change across the flame front, inferred from the SPIV data, was found to be extremely small. It is thought that the (low) heat release of the flames studied contributed more to corrugation of the flame front than acceleration of the gases across the flame front. The strain rates were studied along apparently non-wrinkled and clearly wrinkled flame contours. Their variation could not successfully be linked to curvature solely. Their values were mostly below the value expected for extinction strain rates.

Last, this study aimed at investigating the turbulence-scalar interactions in turbulent premixed hydrogen/air flames with added nitrogen via the characteristics of the alignment of the flame normal vectors with the principal strain rates. The results of this study are quite different from earlier experimental results obtained for turbulent premixed ethylene/air flames. The strong preferential alignment of the flame front normal with the most extensive strain rate observed for ethylene/air flames could not be observed for the hydrogen/air flames with added nitrogen studied in the present work. The key outcome of this study was that no preferential alignment could be observed for most of the flames. A slight preferential alignment of the flame front normal with the most compressive strain rate was observed for the flames with very low adiabatic flame temperature. The differences observed were attributed partly to Lewis number effects and partly to the low heat release superimposed on the hydrodynamic fields in the flames studied.

ACKNOWLEDGEMENTS

I would like to thank Nicolas for his love and encouragement; my parents, Michèle and Michel, for always being present and supportive and my colleagues at Cranfield University - Adam, Alessio, Dmitry, Edouard, Eduardo, Fatiha, Maz, Nicholas and Thierry – for their advices and good mood.

I would also like to thank Alan Hutchings, Dave Whittington, Clive Wood, Bryan Scully and Richard Kennewell for their technical support.

I am very grateful to Pr. J. B. Moss & Dr. J. B. Kelman for supervising me during this PhD, for their support, availability and expertise.

CONTENTS

ABSTRACT ..... **i**

ACKNOWLEDGEMENTS ..... **iii**

CONTENTS ..... **iv**

NOTATION ..... **vii**

LIST OF FIGURES ..... **xii**

LIST OF TABLES ..... **xvii**

CHAPTER I - Introduction **1**
1.1 Environmental issues 2
1.2 Computational modeling 4
1.3 Goal of the work 5
1.4 Structure of the thesis 7

CHAPTER II - Optical Diagnostics **9**
2.1 Laser Diagnostics in Combustion: a brief survey 10
2.1.1 Scalar Measurements: species concentration and temperature 11
2.1.1.1 Raman and Rayleigh scattering 12
2.1.1.2 Coherent Anti-Stokes Raman Spectroscopy (CARS) 14
2.1.1.3 Resonantly Enhanced Multiphoton Ionisation (REMPI) 15
2.1.1.4 Degenerate Four-Wave Mixing (DFWM) 16
2.1.1.5 Cavity Ringdown Spectroscopy (CRD) 17
2.1.1.6 Tunable Diode Laser Absorption Spectroscopy (TDLAS) 18
2.1.1.7 Laser Induced Fluorescence (LIF) 19
2.1.2 Velocity Measurements 19
2.1.2.1 Laser Doppler Velocimetry (LDV) 20
2.1.2.2 Particle Image Velocimetry (PIV) 22
2.1.3 Chosen techniques 22
2.1.4 Comparison between radicals for PLIF experiments 23
2.2 Laser Induced Fluorescence of the radical NO 24
2.2.1 Spectroscopy of the NO radical 26
2.2.2 Spectroscopic models for NO-LIF 31
2.2.3 Calculation of the predicted behaviour of the fluorescence signal as a function of temperature 39
2.2.4 Calibration of the dye laser grating 54
2.3 Particle Image Velocimetry (PIV) 59
2.3.1 Principle 59
2.3.2 Seeding 60
2.3.3 Limitations of two-dimensional PIV systems 62
2.3.4 Three-dimensional Particle Image Velocimetry (3D-PIV) 64
2.3.4.1 Lateral displacement system 65
2.3.4.2 Angular displacement system 66
2.4 Simultaneous measurements of velocity fields and scalar fields in reacting flows in the literature 69

CHAPTER III - Structure of turbulent premixed hydrogen-air flames 72
3.1 Turbulent premixed flames 73
3.1.1 Parameters used to characterise premixed flames 73
3.1.2 Parameters used to characterise turbulent flows.....75
3.1.3 Regime diagrams for turbulent premixed combustion.....76
3.1.4 Premixed hydrogen-air flames in the literature 78
3.2 Modeling of Turbulent Premixed Flames 83
3.2.1 Modeling strategies.....83
3.2.2 Motivations behind experimental testing as a complement of combustion modeling 84
3.2.3 Turbulence-chemistry interactions in turbulent premixed flames 84
3.2.4 Modeling of the scalar dissipation rate of the progress variable 86

CHAPTER IV - Experimentation.....91
4.1 Characterisation of the burner 92
4.1.1 The burner 92
4.1.1.1 General description 92
4.1.1.2 The flow measurement system 94
4.1.1.3 The pilot flame.....97
4.1.1.4 The piloted flames.....99
4.1.2 Laminar flame simulations.....100
4.1.2.1 Input data and method used for the laminar flame simulations.....100
4.1.2.2 Results of the simulations.....103
4.1.2.3 Extrapolation for the flames studied 107
4.1.3 Hot wire anemometry experiments.....109
4.1.3.1 Principles 109
4.1.3.2 Experiments 111
4.1.3.3 Results 112
4.1.3.3.1 Calibration curves of the probes 112
4.1.3.3.2 Results 115
4.1.3.4 Interpretation of the results.....116
4.1.3.5 Uncertainties on the measurements 118
4.1.4 Theoretical characterisation of the flames 118
4.2 Experimental set-up for combined NO-PLIF and SPIV measurement.....119
4.2.1 Equipment used for combined NO-PLIF and SPIV measurement.....119
4.2.2 Experimental set-up 121
4.2.3 Timing Configuration 123
4.2.4 Calibration of the data.....127
4.2.4.1 Calibration of the SPIV images 127
4.2.4.2 Calibration of the NO-PLIF images.....130
4.2.5 Position of the images taken.....131

CHAPTER V - Processing and analysis of the NO-PLIF data 132
5.1 Conversion of the NO-PLIF images into progress variable images.....133
5.1.1 The raw NO-PLIF images 133
5.1.2 The NO-PLIF camera background 134
5.1.3 Flat field images 135
5.1.4 Signal-to-noise ratio.....135
5.1.5 Conversion of the raw NO-PLIF into progress variable images 136
5.2 Mapping of the NO-PLIF data onto the SPIV data 138

5.3 Selected progress variable images 139
5.4 Calculation of the 2D vector normal to chosen isoscalar surfaces and analyses of the orientation of the 2D vector normal 145
5.4.1 Flame front selection 145
5.4.2 Calculation of the 2D vectors normal to the flame front 148
5.5 Investigation of the progress variable gradient images 152
5.6 Presentation of a new method to calculate the 3D vectors normal to the isoscalar surfaces 159
5.7 Critical evaluation of the NO-PLIF technique 162

CHAPTER VI - Processing and analysis of the SPIV data 163
6.1 Calculation of the velocity vector fields 164
6.2 Analysis of the velocity vector fields: acceleration across the flame front 167
6.3 Calculation of the strain rate fields 170
6.4 Analyses of the strain rate fields 172
6.4.1 Extinction strain rates: background 172
6.4.2 Selected experimental results 174
6.4.2.1 Analyses of the strain rates along non-wrinkled iso-c contours 174
6.4.2.2 Strain rates along wrinkled iso-c contours 180
6.5 Evaluation of the SPIV technique 186

CHAPTER VII - Flame normal alignment with the principal strain rates 187
7.1 Calculation of the strain rate matrices, their eigenvalues and eigenvectors 188
7.2 Background to the role of strain rate in combustion modeling 189
7.3 Experimental results 191
7.4 Analysis of the results: comparison with the ethylene flames results and explanation of the differences 198
7.4.1. Pdfs of the principal strain rates 198
7.4.2 Flame normal alignment with the principal strain rates 200

CHAPTER VIII - Conclusion 203

LIST OF REFERENCES 209

APPENDIX CHAPTER II 218

APPENDIX CHAPTER V 225

NOTATION

Abbreviations

Symbol	Description
2D	Two-dimensional
3D	Three-dimensional
A/D	Analog to Digital
ASCII	American Standard Code for Information Interchange
CARS	Coherent Anti-Stokes Raman Spectroscopy
CCD	Charge Coupled Device
CFC	ChloroFluoroCarbon
CRD	Cavity Ringdown Spectroscopy
DFWM	Degenerate Four Wave Mixing
DNS	Direct Numerical Simulation
DPTV	Defocused Particle Tracking Velocimetry
FFT	Fast Fourier Transform
FWHM	Full Width at Half Maximum
ICCD	Intensified Charge-Coupled Device
ID	Internal Diameter
IR	InfraRed
LDA	Laser Doppler Anemometry
LDV	Laser Doppler Velocimetry
LES	Large Eddy Simulation
LIF	Laser Induced Fluorescence
LITGS	Laser Induced Thermal Grating Spectroscopy
MPI	Multi-Photon Ionisation
P.C.	Personal Computer
PDA	Phase Doppler Anemometry
Pdf	Probability Density Function
PIV	Particle Image Velocimetry
PLIF	Planar Laser Induced Fluorescence
PS	Polarisation Spectroscopy
RANS	Reynolds Average Navier Stokes
REMPI	Resonantly Enhanced Multi-Photon Ionisation
r.m.s	Root Mean Square
SPIV	Stereoscopic Particle Image Velocimetry
SS	Stainless Steel
TDLAS	Tunable Diode Laser Absorption Spectroscopy
TTL	Transistor-Transistor Logic
UV	UltraViolet

Roman Symbols

Symbol	Description	Unit
a	Average Polarisability	$C.m^2.V^{-1}$
A	Spontaneous emission rate	s^{-1}
A_{21}	Einstein A coefficient for spontaneous emission 2→1	s^{-1}
A_{lk}	Transition probability for multiphoton transition l→k	
b_{12}	Stimulated absorption rate for the transition 1→2	s^{-1}

b_{21}	Stimulated emission rate for the transition 1→2	s^{-1}
B_{12}	Einstein B coefficient for absorption 1→2	s^{-1}
B_{21}	Einstein B coefficient for stimulated emission 2→1	s^{-1}
c_v	Speed of light in vacuum	$m.s^{-1}$
c	Progress variable	
c_{CAL}	Calibration constant	
c_i	Concentration of the species i	$mol.L^{-1}$
C_{NO}	Concentration of NO	ppm
c_w	Specific heat of the wire	$J.K^{-1}$
d	Absorbing length	m
D	Displacement	m
d_f	Distance between the interference fringes	m
Da	Damköhler number	
D_j^k	Molecular diffusive flux of the species k	$m^{-2}.s^{-1}$
d_p	Diameter of the particle image	m
d_s	Diameter of a speckle grain	m
d_t	Diameter of the tracer particle	m
d_w	Diameter of the wire	m
$\vec{E}$	Electric field	$V.m^{-1}$
E_i	Energy of the level i	J
E_{xx}	Spatial gradient of the x-component of the velocity in the x-direction	s^{-1}
E_{xy}	Spatial gradient of the x-component of the velocity in the y-direction	s^{-1}
E_{xz}	Spatial gradient of the x-component of the velocity in the z-direction	s^{-1}
E_{yx}	Spatial gradient of the y-component of the velocity in the x-direction	s^{-1}
E_{yy}	Spatial gradient of the y-component of the velocity in the y-direction	s^{-1}
E_{yz}	Spatial gradient of the y-component of the velocity in the z-direction	s^{-1}
E_{zx}	Spatial gradient of the z-component of the velocity in the x-direction	s^{-1}
E_{zy}	Spatial gradient of the z-component of the velocity in the y-direction	s^{-1}
E_{zz}	Spatial gradient of the z-component of the velocity in the z-direction	s^{-1}
E_1	First eigenvalue of the 2D strain rate matrices	s^{-1}
E_2	Second eigenvalue of the 2D strain rate matrices	s^{-1}
E_{11}	First component of the 2*2 strain rate matrice	s^{-1}
E_{12}	Second component of the 2*2 strain rate matrice	s^{-1}
E_{21}	Third component of the 2*2 strain rate matrice	s^{-1}
E_{22}	Fourth component of the 2*2 strain rate matrice	s^{-1}
f	Frequency	Hz
f_{SL}	Frequency of the scattered light	Hz
$f_B(T)$	Boltzmann function	
f_D	Doppler broadened Gaussian profile of the laser signal	
$f^{\#}$	Aperture of the viewing optics	
$f(\vec{x})$	Function f	
$f(\vec{s})$	Fourier transform of f	
F_i	Body force	N
$g_{\lambda,i}$	Overlap factor between the transition and the laser signal	
h	Planck's constant	$m^2.kg.s^{-1}$
h_t	Total enthalpy	$m^2.s^{-2}$
I	Intensity	W
I_0	Initial intensity	W

I_1	Intensity of the pump beam	W
I_2	Intensity of the Stokes beam	W
I_3	Intensity of the CARS signal	W
I_ν	Intensity of the incident laser excitation signal at the frequency ν for LIF in the two-level model	W
I_υ^0	Intensity of the incident laser excitation signal at the frequency ν for LIF for the five-level model	W
I_ν^{sat}	Saturation spectral intensity of the incident laser excitation signal at the frequency ν for LIF	W
I_i	Intensity of the incident laser signal	W
I_{Laser}	Intensity of the laser signal	W
I_{pump}	Intensity of the pump beam	W
I_{probe}	Intensity of the probe beam	W
$I_{Raman,zz}$	Intensity of the Raman shifted scattered signal	W
$I_{Rayleigh}$	Intensity of the Rayleigh scattered signal	W
I_{sig}^{int}	Intensity of the DFWM signal	W
J	Total angular momentum quantum number	
k	Boltzmann constant	$J.K^{-1}$
Δk	Phase mismatch	
Ka	Karlovitz number	
Ka_δ	Second Karlovitz number	
l	Length of the probe, cavity length, path length	m
L	Integral length scale	m
m	Mass	kg
M	Magnification	
M_n	Nominal magnification	
N	Quantum number corresponding to the angular momentum of nuclear rotation	
N_1	Population of the energy level 1	
N_2	Population of the energy level 2	
N_1^0	Initial population of the energy level 1	
N_{at}	Atomic number density	m^{-3}
N_c	Scalar dissipation rate	s^{-1}
N_{ds}	Total number density of scatterers	m^{-3}
N_{GS}	Density of molecules in the ground state	m^{-3}
N_l	Number of scatterers in the probed volume	
n_{L1}	Number of incident laser photons	
n_{L2}	Number of photons per pulse for the ionisation laser	
N_{NO}	Density of NO	m^{-3}
N_p	Total number of particles in the flow	
Nu	Nusselt number	
n_i	Index of refraction of the species i	
n_1, n_2, n_3	Index of refraction of the medium at $\omega_1, \omega_2, \omega_3$	
n_{fuel}	Molar concentration of the fuel	$mol.L^{-1}$
n_{air}	Molar concentration of the air	$mol.L^{-1}$
n_{O2}	Molar concentration of O_2	$mol.L^{-1}$
n_{N2}	Molar concentration of N_2	$mol.L^{-1}$
P	Pressure	Pa
$\vec{P}$	Polarisation	$C.m^{-2}$

Q	Quenching factor	
R	Reflectivity of the mirrors	
Re	Reynolds number	
R_p	Resistance of the probe	Ω
S	Total spin quantum number	
S_L	Laminar flame speed	$m.s^{-1}$
S_{REMPI}	REMPI signal rate	s^{-1}
T	Temperature	K
T_0	Reference temperature	K
T_1	Longitudinal relaxation time	s
T_2	Transverse relaxation time	s
t	Time	s
T_m	Temperature of the medium	K
T_p	Temperature of the probe	K
u	Local fluid velocity	$m.s^{-1}$
u_i, u_j	Component of the velocity in the x_i-direction, in the x_j-direction	$m.s^{-1}$
u'	Fluctuating component of the velocity	$m.s^{-1}$
U_f	Velocity of the fluid medium	$m.s^{-1}$
v	Velocity	$m.s^{-1}$
V	Mean velocity determined by hot wire anemometry	$m.s^{-1}$
V_{1x}, $V_{1y,}$ V_{2x}, V_{2y}	Component of the eigenvectors of the 2*2 strain rate matrice in the x-direction and in the y-direction	
W	Power necessary to maintain the wire at constant temperature in hot wire anemometry experiments	W
x_i	Mole fraction of the species i	
x_i, x_j	Axes of the orthonormal basis used in the modeling section	
$X_i(t)$	Position vector of the particle i at time t	
Y_k	Mass fraction of the species k	

Greek Symbols

Symbol	Description	Unit
δ	Fraction of the flame thickness corresponding to the inner layer	
$\delta()$	Dirac function	
δ_L	Laminar flame thickness	m
Δ	Indicates variation of the variable to follow	
ΔX_1, ΔX_2, ΔY_1, ΔY_2	Apparent particle displacement in the x-direction for camera 1, camera 2, in the y-direction for camera 1, camera 2 for SPIV	m
Δx, Δy, Δz	True particle displacement in the x, y and z direction	m
ε	Molar absorptivity	$m^2.mol^{-1}$
ε_0	Permittivity of free space	$A^2.s^4.kg^{-1}.m^{-3}$
$\tilde{\varepsilon}_c$	Progress variable variance	
Φ	Equivalence ratio	
γ	Polarisability anisotropy	
κ	Molecular diffusivity	$m^2.s^{-1}$
λ	Wavelength	nm
μ	Mean frequency of the laser	Hz

μ_{12}	Atomic dipole moment	C.m
μ_{fm}	Dynamic viscosity of the fluid medium	Pa.s
ν	Frequency	Hz
ν_i	Wavenumber of the incident beam	cm^{-1}
ν_f	Frequency of the emitted fluorescence	Hz
ν_k	Kinematic viscosity	$m^2.s^{-1}$
ν_{LASER}	Frequency of the laser signal	Hz
ν_0	Mean frequency of the laser signal	Hz
ν_{12}	Frequency of the Raman transition	Hz
θ	Angle	°
θ_x, θ_y	Component of θ in the x-direction, y-direction	
π	Pi	
ρ	Density	$kg.m^{-3}$
ρ_{abs}	Absorber density	m^{-3}
ρ_{air}	Density of the air	$g.L^{-1}$
ρ_{fm}	Density of the fluid medium	$kg.m^{-3}$
σ	Cross-section	m^2
$\sigma_{\Delta X1}$	Uncertainty arising from the interrogation of the PIV photographs	
$\sigma_{\Delta X}$	Uncertainty arising from the interrogation of the PIV photographs	
$\sigma_{\Delta x}$	Total uncertainty on the measurement of the displacement in PIV experiments	
σ_{lk}	Absorption cross-section for the transition l→k	
σ_{kl}	Ionisation cross-section	
σ_{st}	Standard deviation of the distribution	
Σ	Flame surface density	
τ_{ij}	Viscous tensor	$N.m^{-2}$
χ_{CARS}	Susceptibility in CARS experiments	
ω_e	Frequency of the harmonic oscillator	Hz
ω_1	Frequency of the pump laser	Hz
ω_2	Frequency of the downshifted Stokes beam	Hz
ω_3	Frequency of the CARS signal	Hz
Ω	Solid angle	

LIST OF FIGURES

Figure 1.1: Electrolysis of water 4

Figure 2.1: Physical processes involved in a REMPI experiment [19]. 15
Figure 2.2: Principle of a CRD experiment [18].....17
Figure 2.3: Scheme of the experimental arrangement of a typical LDV experiment .20
Figure 2.4: Electronic configuration of NO.....27
Figure 2.5: De-excitation pathways for a species having absorbed photons 32
Figure 2.6: Representation of the two-level model 33
Figure 2.7: Representation of the three-level model 35
Figure 2.8: Representation of the five-level model for NO-LIF.....36
Figure 2.9: Population fraction as a function of temperature for the state 2Π1/2e and for J between 1.5 and 20.5 40
Figure 2.10: Population fraction as a function of temperature for the state $^2\Pi_{1/2f}$ and for J between 1.5 and 20.5 40
Figure 2.11: Population fraction as a function of temperature for the state $^2\Pi_{3/2e}$ and for J between 1.5 and 20.5 41
Figure 2.12: Population fraction as a function of temperature for the state $^2\Pi_{3/2f}$ and for J between 1.5 and 20.5 41
Figure 2.13: Population fraction as a function of temperature for the state $^2\Pi_{1/2}$ and for J between 1.5 and 20.5 43
Figure 2.14: Population fraction as a function of temperature for the state $^2\Pi_{3/2}$ and for J between 1.5 and 20.5 43
Figure 2.15: $R_{11}+{}^RQ_{21}(9.5)$ line shape as a function of temperature and laser profile at 225.980nm.....45
Figure 2.16: Overlap Factor between the transition $R_{11}+{}^RQ_{21}(9.5)$ and the laser tuned at 225.980nm as a function of temperature 46
Figure 2.17: Variation of the total electronic quenching cross-section as a function of temperature 49
Figure 2.18: Variation of the normalised collisional quenching rate as a function of temperature for a premixed laminar hydrogen/air flame with an equivalence ratio of 0.35.....50
Figure 2.19: Expected variation of the fluorescence signal as a function of temperature 52
Figure 2.20: Curve comparing the progress variable calculated using the NO-PLIF signal and the progress variable calculated using the temperature 53
Figure 2.21: First calibration spectra.....54
Figure 2.22: Second calibration spectra 57
Figure 2.23: Third calibration spectra for the dye laser grating 58
Figure 2.24: Sketch of the PIV principle.....60
Figure 2.25: The seeder 62
Figure 2.26: Sketch of the perspective error [58] 63
Figure 2.27: Sketch of the SPIV arrangement in the lateral displacement system 65
Figure 2.28: Sketch of the SPIV arrangement in the angular displacement system ...67
Figure 2.29: Sketch of the Scheimpflug angular displacement system.....68

Figure 3.1: The Borghi regime diagram for turbulent premixed combustion [74] 76
Figure 3.2: The Peters regime diagram for premixed turbulent combustion [75] 77

Figure 4.1: The piloted burner mounted on the x, y, z traverse of a milling machine bed 92
Figure 4.2: The piloted burner 93
Figure 4.3: Sketch of the top part of the burner 93
Figure 4.4: Sketch of the burner 94
Figure 4.5: The control panel 95
Figure 4.6: Block diagram of the flow measurement system and mixing of the gases 96
Figure 4.7: View of the top of the burner 97
Figure 4.8: View of the top of the burner 97
Figure 4.9: Sketch of the perforated plate 98
Figure 4.10: Turbulence grid 99
Figure 4.11: Unstrained laminar flame speed as a function of the equivalence ratio and the dilution 103
Figure 4.12: Laminar Flame Speed as a function of dilution for Φ=1 104
Figure 4.13: Progress variable as a function of distance for undiluted hydrogen-air flames 105
Figure 4.14: Progress Variable as a function of distance for values of dilution of 0.20, 0.18, 0.16, and 0.14 and equivalence ratio of 1 105
Figure 4.15: Flame Thickness as a function of the equivalence ratio 106
Figure 4.16: Flame Thickness as a function of dilution for nitrogen diluted hydrogen/air flames with an equivalence ratio of 1 107
Figure 4.17: Extrapolated values of the unstrained laminar flame speed as a function of the equivalence ratio for a dilution value of 0.105 107
Figure 4.18: Extrapolated values of the flame thickness as a function of the equivalence ratio for a dilution value of 0.105 108
Figure 4.19: Typical measuring chain in a hot wire anemometry experiment 111
Figure 4.20: Geometry of the experiments 112
Figure 4.21: Calibration curve of the first probe 113
Figure 4.22: Calibration curve of the second probe 113
Figure 4.23: Curve linking dU/dV and V for the first probe 114
Figure 4.24: Curve linking dU/dV and V for the second probe 114
Figure 4.25: Radial profile of the fluctuating component of the velocity in air flows in the inner nozzle of the burner 115
Figure 4.26: Axial profile of the fluctuating component of the velocity in air flows on the centre line of the inner nozzle of the burner 115
Figure 4.27: Radial profile of the fluctuating component of the velocity in air flows in the inner nozzle of the burner 116
Figure 4.28: Turbulence intensity as a function of the exit velocity for hydrogen-diluted air mixtures corresponding to flames with a dilution ratio of 0.105 and an equivalence ration between 0.35 and 2 117
Figure 4.29: The Coumarin 445 molecule 119
Figure 4.30: Experimental set-up for combined NO-PLIF and SPIV 121
Figure 4.31: Camera arrangement for combined NO-PLIF and SPIV measurements 122
Figure 4.32: Optical arrangement for combined NO-PLIF and SPIV measurements 123
Figure 4.33: Timing configuration description 124
Figure 4.34: Connections between the different pieces of equipment 125
Figure 4.35: Microsoft PowerPoint generated calibration grid 127

Figure 4.36: Calibration plate and its support used for the experiments.....128
Figure 4.37: Sketch of the calibration device and its orientation.....128
Figure 4.38: Averaged calibration images for the SPIV camera 1 129
Figure 4.39: Averaged calibration images for the SPIV camera 2 129
Figure 4.40: Instantaneous calibration image for the Princeton NO-PLIF camera ..131
Figure 4.41: Position of the images taken with regard to the burner and the flames 131

Figure 5.1: Example of an instantaneous raw NO-PLIF image.....133
Figure 5.2: Example of an averaged background image for the Princeton NO-LIF camera.....134
Figure 5.3: Example of an averaged flat field image 135
Figure 5.4: Example of a progress variable image.....137
Figure 5.5: Position of the flames studied in the Peters regime diagram for premixed turbulent combustion 140
Figure 5.6: Examples of progress variable images for flame A 141
Figure 5.7: Examples of progress variable images for flame B.....141
Figure 5.8: Examples of progress variable images for flame C (a), for flame E (b) and for flame F (c) 142
Figure 5.9: Examples of progress variable images for flame I 142
Figure 5.10: Example of different iso-c lines for flame C.....146
Figure 5.11: Length of the iso-scalar surfaces as a function of c.....147
Figure 5.12: Sketch illustrating the calculation of the 2D vectors normal to the flame front.....149
Figure 5.13: Sketch of the orientation test for the vector normal to the iso-c lines..149
Figure 5.14: Angle between the y-axis and the vectors normal to the flame front ...150
Figure 5.15: Orientation of the 2D flame normal (from top left to bottom right: (a) Flame A, (b) Flame B, (c) Flame C, (d) Flame E, (e) Flame F, (f) Flame I) 151
Figure 5.16: Sketch of the four 8*8 boxes.....153
Figure 5.17: Progress variable image and its corresponding gradient image for flame A.....153
Figure 5.18: Spatial gradient of the progress variable as a function of the progress variable for flame A 154
Figure 5.19: Spatial gradient of the progress variable as a function of the progress variable for hydrogen/air flames with an equivalence ratio between 3 and 0.4 155
Figure 5.20: Spatial gradient of the progress variable as a function of the progress variable for nitrogen-diluted hydrogen/air flames with an equivalence ratio of 1.....155
Figure 5.21: Value of the maximum gradient as a function of the equivalence ratio for hydrogen/air flames (dilution=0.21).....157
Figure 5.22: Position of the maximum gradient as a function of the equivalence ratio for hydrogen/air flames (dilution=0.21) 157
Figure 5.23: Value of the maximum gradient as a function of the dilution for stoichiometric nitrogen-diluted hydrogen/air flames 158
Figure 5.24: Position of the maximum gradient as a function of the dilution for stoichiometric nitrogen-diluted hydrogen/air flames 158
Figure 5.25: Sketch of the angle between the flame and the laser sheet.....160

Figure 6.1: Schematic representation of the calculation of the velocity vector fields 166
Figure 6.2: Vector field across different iso-c lines for flame E 167

Figure 6.3: Sketch of the different zones of vector orientation corresponding to different expressions for the velocity variation.....168
Figure 6.4: Pdf of the velocity variation across the flame front along a normal vector for flame E 170
Figure 6.5: Velocity field minus average unburnt velocity across different iso-c lines for flame E 170
Figure 6.6: Extinction strain rates for hydrogen/air flames as a function of equivalence ratio [109] 173
Figure 6.7: Extinction strain rates for hydrogen/air flames with added nitrogen as a function of dilution [109].....173
Figure 6.8: Strain rates along non-wrinkled iso-c contours in an instantaneous shot of flame A (from top left to bottom right: (a) Exx (b) Exy (c) Eyx (d) Eyy (e) Ezx and (f) Ezy).....175
Figure 6.9: Strain rates along non-wrinkled iso-c contours in an instantaneous shot of flame C (from top left to bottom right: (a) Exx (b) Exy (c) Eyx (d) Eyy (e) Ezx and (f) Ezy).....176
Figure 6.10: Strain rates along non-wrinkled iso-c contours in an instantaneous shot of flame E (from top left to bottom right: (a) Exx (b) Exy (c) Eyx (d) Eyy (e) Ezx and (f) Ezy).....177
Figure 6.11: Gradient of the progress variable along non-wrinkled iso-c contours for flame A (image 84).....178
Figure 6.12: Gradient of the progress variable along non-wrinkled iso-c contours for flame C (image 89).....179
Figure 6.13: Gradient of the progress variable along non-wrinkled iso-c contours for flame E (image 133) 179
Figure 6.14: Strain rates along wrinkled iso-c contours in an instantaneous shot of flame C (from top left to bottom right: (a) Exx (b) Exy (c) Eyx (d) Eyy (e) Ezx and (f) Ezy).....181
Figure 6.15: Strain rates along wrinkled iso-c contours in an instantaneous shot of flame C (from top left to bottom right: (a) Exx (b) Exy (c) Eyx (d) Eyy (e) Ezx and (f) Ezy).....182
Figure 6.16: Strain rates along the iso-c contours of a pocket of unburnt gases in burnt gases for flame C (from top left to bottom right: (a) Exx (b) Exy (c) Eyx (d) Eyy (e) Ezx and (f) Ezy) 183
Figure 6.17: Strain rates along the iso-c contours of a pocket of unburnt gases in burnt gases for flame C (from top left to bottom right: (a) Exx (b) Exy (c) Eyx (d) Eyy (e) Ezx and (f) Ezy) 184
Figure 6.18: Strain rates along the iso-c contours of a pocket of burnt gases in unburnt gases for flame C (from top left to bottom right: (a) Exx (b) Exy (c) Eyx (d) Eyy (e) Ezx and (f) Ezy) 185

Figure 7.1: Pdf of principal strain rates in flame A (c=0.8) 192
Figure 7.2: Pdf of flame normal alignment with the principal strain rates for flame A (c=0.8).....192
Figure 7.3: Pdf of principal strain rates in flame B (c=0.8).....193
Figure 7.4: Pdf of flame normal alignment with the principal strain rates for flame B (c=0.8).....193
Figure 7.5: Pdf of principal strain rates in flame C (c=0.8).....194
Figure 7.6: Pdf of flame normal alignment with the principal strain rates for flame C (c=0.8).....194

Figure 7.7: Pdf of principal strain rates in flame E 195
Figure 7.8: Pdf of flame normal alignment with the principal strain rates for flame E 195
Figure 7.9: Pdf of principal strain rates in flame F (c=0.8) 196
Figure 7.10: Pdf of flame normal alignment with the principal strain rates for flame F (c=0.8) 196
Figure 7.11: Pdf of principal strain rates in flame I (c=0.6).....197
Figure 7.12: Pdf of flame normal alignment with the principal strain rates for flame I (c=0.6) 197
Figure 7.13: Graphs taken from [14]: (a) experimental graph showing the pdfs of the principal strain rates for a premixed ethylene-air flame with Φ=0.55 (Da=1.37 and Ka=7.58) and (b) graphs showing the pdfs of the principal strain rates of a DNS flame (Da=6.8, Ka=0.3).....199
Figure 7.14: Flame normal alignment with the principal strain rates found in [14]: (a) Φ=0.55, Ka=7.58 and Da=1.37, (b) Φ=0.55, Ka=1.00 and Da=13.76 and (c) Φ=0.70, Ka=2.40 and Da=4.01.....201

LIST OF TABLES

Table 2.1: Electronic configurations and electronic energies of the ground state and the first four excited electronic states of the NO molecule 28
Table 2.2: Summary of the different Hund's cases 30
Table 2.3: Notations corresponding to the different transitions observed between the ground electronic state and the first excited state [24] 31
Table 2.4: Expression for the fluorescence signal in different cases of laser-excitation when considering the five-level model.....37
Table 2.5: List of the transitions shown in the LIFSim curve between 225.880 and 226.100 nm 55
Table 2.6: List of the transitions shown in the LIFSim spectrum between 225.890 and 225.990 nm 57
Table 2.7: List of the transitions shown in the LIFSim spectrum between 225.970 and 225.990 nm 58
Table 2.8: Liquid droplet vs solid particles for seeding in fluid flows.....61
Table 2.9: Table of the advantages and drawbacks of the lateral displacement system 65
Table 2.10: Table of the advantages and drawbacks of the angular displacement system 67

Table 4.1: Measuring devices on the control panel of the rig.....95
Table 4.2: Summary of the flames studied 99
Table 4.3: Revised reaction mechanism for hydrogen oxidation [96] 101
Table 4.4: Thermodynamic properties of the species involved in the oxidation of hydrogen [96].....101
Table 4.5: Unstrained laminar flame speed and laminar flame thickness for the flames studied.....108
Table 4.6: Equations between u' and $\bar{U}$ for air and different mixtures.....117
Table 4.7: Summary of the characteristics of the flames studied 119

Table 5.1: Table showing the occurrence of pocket of gas burning in the unburnt gas region and of pockets of unburnt gases in the burnt gas region.....144

Table 6.1: Table showing the expression for the velocity variation as a function of the value of the components of the normal vectors 169

CHAPTER I

Introduction

This chapter describes the context of the present work, states its aims and goals and finally gives a plan for the dissertation.

Being able to control fire has been a major breakthrough for humankind. Studies [1-3] suggest that hominids might already have been able to control fire at least some 800,000 years ago. The heat produced by fire allowed people to survive in colder climates and allowed them to cook food protecting them against diseases. The light scared away dangerous animals. Fire has proved one of humankind's most useful discoveries [4]. As well as allowing them to cook food and produce heat, fire also enabled people to shape landscapes protecting them against unwanted fire and favouring biodiversity. Fire gave people the possibility to work metals and produce tools or weapons. Little by little, fire pervaded every aspect of a human being's life. Nowadays, we use fire almost constantly: most of our electricity is produced by thermal power stations and most of our transport makes use of combustion via engines or gas turbines.

1.1 Environmental issues

Although people have been studying the impact of human activities on the environment since the 1920's, it is only since the 1970's that real concerns have been expressed. We are starting to realise that our activities damage the environment and that the changes we are bringing to our environment might have dreadful consequences on our habitat and health and that theses changes might be irreversible [5]. In particular, biodiversity is threatened by fishing and hunting, intensive agriculture may be held partly responsible for the pollution of soils and groundwater; issues like waste management are a direct consequence of our consumption habits; industries have a huge impact on the quality of our air and on climate.

The climate of the Earth [5] is mainly determined by the radiation it receives from the Sun, the radiation emitted by its atmosphere and the radiation escaping the Earth and its atmosphere. Most of the radiations emitted by the Sun are absorbed and warm the surface of the Earth while the remaining is reflected. The radiations emitted by the surface of the Earth are mostly absorbed by the greenhouse gases of the atmosphere. Without the greenhouse gases, the Earth would have a much lower temperature than what it actually is. The radiations coming from the sun are mainly in the visible and the near infrared while the radiations from the earth are in the infrared.

The main gases of the atmosphere – O_2, N_2, Ar - are not greenhouse gases. They do not significantly absorb or emit infrared radiations. Greenhouse gases are the gases which can absorb infrared radiations. The major greenhouse gases of the atmosphere are water vapour, carbon dioxide and ozone. Other gases such as methane, nitrous oxide and the CFCs can also contribute to the greenhouse effect.
The greenhouse effect occurs naturally. However, human activities, especially since the 19th century, have caused an increase in concentration of greenhouse gases in the atmosphere. As a consequence, the greenhouse effect has been enhanced and is now held responsible for climate change. Climate change could mean global warming, the rise of the sea level, more droughts and floods.
Combustion, in particular of fossil fuels, has dramatically contributed to the increased concentration of greenhouse gases in the atmosphere, in particular of carbon dioxide.
To preserve the environment, more and more stringent regulations are being enforced. In December 1997, the 3rd conference of the parties met in Kyoto, and adopted the so-called Kyoto protocol which aims at reducing greenhouse gas emissions so as to minimise climate change and, in particular, global warming [6].

The energy and the transport sectors are particularly concerned by greenhouse gas emissions. Their intensive use of combustion makes them an important contributor to air pollution.

This is crucial to improve combustion processes so as to make them safer for the environment. In the premixed combustion field, a first step toward the achievement of this goal was to use lean mixtures. In that context, the use of hydrogen as a fuel for combustion systems may also prove beneficial for the environment [5]. Indeed, the combustion of hydrogen in air occurs with very low emissions: very low NO_x emissions and virtually no volatile organic compounds or carbon monoxide or dioxide emissions. Although not naturally present on Earth in significant quantities, hydrogen can be produced by electrolysis of water [5] using renewable energies such as solar or wind energies in which case its production causes virtually no air pollution and no greenhouse gas emissions.

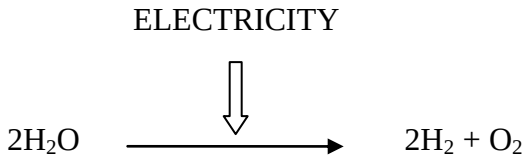

Figure 1.1: Electrolysis of water

The cost of hydrogen production by electrolysis is still high. However, in the present context of unstable oil and natural gas prices and providing development of the technology, hydrogen might be the answer to our concerns regarding the development of new sustainable ways of producing energy. However, premixed hydrogen-air flames have been little studied experimentally. The properties of hydrogen differ widely from the properties of other more common hydrocarbon fuels which may have consequences especially for combustion modeling. Computational modeling has become the method of choice to study combustion. It reduces the cost and time to design, develop and validate more efficient combustors. It also benefits the environment by reducing the number of experiments.

1.2 Computational modeling

The complexity of the interactions between turbulent motions of the gas flows, heat transfer and chemical reactions at a molecular level makes the establishment of a combustion theory a very difficult task.

In recent years, computational modeling has revolutionised the combustion field [7].
The starting point for computational modeling is the set of instantaneous local balance equations which are the Navier-Stokes, species and energy transport equations.
However, these equations usually cannot be solved directly. A Direct Numerical Simulation (DNS) – i.e. a calculation of all the time scales and length scales without any assumptions or models – can only be performed for very simplified cases.
The first step toward a numerical solution of these equations for more complex problems is the Reynolds averaging technique (Reynolds Averaged Navier-Stokes or RANS). Each property (density, concentration, temperature…) of these equations are decomposed into a mean and a deviation from the mean. The newly calculated

equations contain parameters such as Reynolds stresses, species fluxes, temperature fluxes… which need closures. Various models [7] have been proposed and tested through the years: the Eddy-break-up model, the Bray-Moss-Libby model, models based on an estimation of the flame surface area… These numerical models need to be validated by experiments.

An alternative method (Large Eddy Simulation or LES) consists in calculating only the behaviour of the largest eddy which are dependent on the geometry of the flow and implementing models for the smaller eddies which are supposed to be self similar and less sensitive to the model detail. Each property of the original set of equations, instead of being averaged as in RANS, is spatially filtered. So-called subgrid-scale models for the Reynolds stresses, species fluxes, enthalpy fluxes… are then required along with the filtered equations to simulate a problem. Then again, the models need experimental validation.

1.3 Goal of the work

The goal of the present work was to develop a new strategy which would allow the instantaneous and simultaneous measurement of both the velocity field and a scalar field in premixed turbulent flames. Combustion modeling, for example the modeling of the scalar dissipation rate which was under particular scrutiny in this work, requires velocity gradient/strain rate information and scalar gradient information (see chapter III). The diagnostics selected were Stereoscopic Particle Image Velocimetry (SPIV) for the measurement of the three-dimensional (3D) velocity fields and Planar Laser Induced Fluorescence of the NO radical (NO-PLIF) for the measurement of the progress variable field. They allow access to the components of the gradients of both the velocity (strain rates) and the progress variable (progress variable gradients). SPIV has been implemented with various other techniques. However, simultaneous SPIV and NO-PLIF had never been realised before. The NO-PLIF technique implemented here allows the determination of the location of the flame front and the calculation of the two-dimensional flame normal vectors. However, NO-PLIF does not allow the direct calculation of the three-dimensional flame normal vectors. But, a method, making use of the data concerning the progress variable gradient, was designed and is presented here to evaluate the 3D vectors normal to the flame front. The strengths and

weaknesses of the diagnostics employed here were also discussed with a view to improve their eventual implementation in future works.

Hydrogen is an interesting fuel in point of view of the environment. However, it possesses unusual properties and few literature sources are available concerning turbulent premixed hydrogen-air flames. These aspects will be reviewed in more details later in the thesis (chapter III). As a consequence, the flames chosen for this study were lean premixed turbulent nitrogen-diluted hydrogen-air flames. The present work aimed at collecting data and giving an analysis and interpretation of these data with a view to, eventually, relating them to current premixed combustion models. One of the most challenging issues in combustion modeling is the modeling of the reaction rate. As will be explained later in chapter III, the reaction rate can be related to the flame surface density which, in its turn, can be related to the scalar dissipation rate via the dissipation rate of the progress variable variance. Recently, Swaminathan et al. [8] derived a transport equation for the dissipation rate of the progress variable. One of the terms in this equation represents the turbulence-scalar interactions. The study of this term allows the determination of the influence of the turbulence on scalar gradient i.e. whether the action of turbulence dissipates or creates scalar gradient. This interaction has been studied before especially in flows with no chemical reactions present or with only passive chemical reactions (details in chapter VII). Only a few literature sources [9-14] report investigation conducted in flows with nonpassive chemical reactions. Contrary to the classical picture, obtained when studying flows with passive chemical reactions or no chemical reactions at all, it was found that the action of turbulence was mainly to create scalar gradients. The effects of heat release and Damköhler number on the turbulent-scalar interactions were also studied. However, the effects of Lewis number on the turbulence-scalar interactions have not been studied yet. Here, the turbulence-scalar interactions were studied in turbulent premixed hydrogen-air flames i.e. flames with a Lewis number much smaller than the flames used in previous studies. The results obtained for these flames were then compared to experimental results reported in the literature [14] concerning more conventional hydrocarbon flames.

1.4 Structure of the thesis

The present dissertation contains eight chapters which are briefly described here.

Chapter two – Optical Diagnostics

This chapter reviews the most widespread laser diagnostics in combustion and briefly describes their principles. It also states the reasons why SPIV and NO-PLIF were selected in the present work and describes in more details the two selected diagnostics.

Chapter three – Structure of turbulent premixed hydrogen-air flames

This chapter briefly reviews the tools most commonly used to study turbulent premixed flames. A literature survey of turbulent premixed hydrogen/air flames highlights the potential benefits of using hydrogen as a fuel and the differences observed between hydrogen-air flames and more conventional hydrocarbon premixed flames. The source of these differences and their implications for both modeling and application are briefly discussed. This chapter concludes with an explanation of the motivation for diagnostic experimental testing as a necessary complement to combustion modeling and outlines the distinctive features of a model recently developed at the University of Cambridge for turbulent hydrocarbon-air flames, which will be evaluated in later chapters for the N_2-diluted hydrogen flames of the present study.

Chapter four – Experimentation

The first part of this chapter contains a description of the burner used in the present work. The simulations performed on the Chemkin 4.1 software [15] to characterise the flames studied in this work are also reported as well as the experimental campaign performed on the burner using hot wire anemometry. The second part of this chapter describes the experimental set-up for the simultaneous NO-PLIF and SPIV experiments.

Chapter five – Processing and analysis of the NO-PLIF data

This chapter describes the conversion of the NO-PLIF data into progress variable images and the method used to calculate the two-dimensional vectors normal to the chosen isoscalar surfaces. It analyses the influence of the value of c on the isoscalar surfaces and on the orientation of the 2D vectors normal to the isoscalar surfaces. This chapter also gives an analysis of the gradient of the progress variable. Finally, this chapter proposes a new method to calculate, from the progress variable gradients, the three-dimensional vectors normal to the isoscalar surfaces.

Chapter six – Processing and analysis of the SPIV data

This chapter describes the conversion of the SPIV data into velocity fields and strain rate fields. It also presents an analysis of the velocity fields and of the strain rate fields along chosen flame contours.

Chapter seven – Flame normal alignment with the principal strain rates

This chapter describes how the principal strain rates were calculated from the SPIV data and compares them with the alignment of the flame normals inferred from the PLIF measurements. The results are discussed in the light of recent proposals regarding the modeling of turbulent premixed flames.

Chapter eight – Conclusion

This chapter sums up the work done here, the results obtained and their analysis. It also gives recommendations for future work.

CHAPTER II

Optical Diagnostics

This chapter reviews the most widespread laser diagnostics in combustion and briefly describes their principles. It also states the reasons why SPIV and NO-PLIF were selected in the present work and describes in more details the two selected diagnostics.

2.1 Laser Diagnostics in Combustion: a brief survey

Laser diagnostics [16-19] use the interactions between light and matter to gain information on combustion flows. They are usually divided in two main categories depending on whether light is scattered by matter or is absorbed/emitted by matter. The scattering methods are further classified in two classes: the elastic scattering methods (Lorenz-Mie scattering, Rayleigh scattering) in which the energy of the incident photon is not modified and the inelastic scattering methods in which the energy of the incident photon is decreased (Stokes Raman scattering) or increased (Anti-Stokes Raman scattering).

Laser techniques present many advantages over physical probing: they are non-intrusive, they do not usually perturb the system studied, they measure in-situ and their spatial and temporal resolution is usually good [16].

In the next sections, we will briefly review the main laser techniques used to measure concentrations, velocities and temperatures in the combustion field [16-19].

We will also compare them and justify the choice of the two diagnostics used in the present work.

In this work, the goal was to implement laser diagnostics to simultaneously and instantaneously measure the velocity/strain rate fields and the progress variable/progress variable gradient fields in order to be able to analyse the turbulence-scalar interactions in premixed turbulent hydrogen/air flames at atmospheric pressure. While for the measurement of velocity/strain rate fields, the Stereoscopic Particle Image Velocimetry (PIV) technique stood out of the other techniques for obvious reasons which will be described in the next sections, the choice of a technique for the mapping of the flames in terms of progress variable is rather more delicate. Indeed, the mapping of the flame in terms of progress variable can be achieved either by using the temperature (varying from room temperature to ~ 1400K in this work) or by using the concentrations of species present in the flames which [3] can vary from parts per billion (for minor species such as OH, NO or CH) to % levels (for major species such as H_2, N_2 or CO_2). The following sections will briefly survey the main techniques which could be employed and give their detection limits as well as their advantages and drawbacks.

2.1.1 Scalar Measurements: species concentration and temperature

Various techniques have been used to measure species concentrations and/or temperature in flames:

- Spontaneous Raman and Rayleigh scattering which allow temperature measurements as well as concentration measurements of major species [16],
- Laser-Induced Fluorescence (LIF) which allows temperature measurements and concentration measurements of minor species [16-19],
- Resonantly Enhanced Multiphoton Ionisation (REMPI) which allows the detection of minor species [18],
- Degenerate Four-Wave Mixing (DFWM) which allows the detection of minor species [18],
- Cavity Ringdown Spectroscopy (CRD) which allows the detection of minor species [18],
- Coherent Anti-Stokes Raman Scattering (CARS) which allows measurements of both temperature and concentrations [18],
- Tunable Diode Laser Absorption (TDLAS) which allows the detection of minor species [18],
- Laser-Induced Thermal Grating Spectroscopy (LITGS) which allows the detection of minor species [18],
- Polarisation Spectroscopy (PS) which also allows the detection of minor species [18]
- …

A brief survey of Raman and Rayleigh scattering, CARS, REMPI, DFWM, CRD, TDLAS and LIF will be given here. LIF and in particular NO-PLIF will be reviewed in more depth in section 2.2.

2.1.1.1 Raman and Rayleigh scattering

In Raman and Rayleigh scattering [16] experiments, an incident photon is deviated from its straight trajectory by the atoms and molecules of the gas mixture.
In these experiments, the laser need not be tuned at a resonance wavelength of the probe species. Usually, these experiments are performed with an incident beam in the visible or UV range.

The intensity of the scattered light depends on temperature and concentrations.

The intensity of the Rayleigh signal scattered into a solid angle Ω at 90^o from the incident laser beam is [19]:

$$I_{Rayleigh} \propto I_i N_{ds} \Omega \left(\frac{\partial \sigma}{\partial \Omega} \right)_{medium} \tag{2.1}$$

in which I_i is the intensity of the incident laser beam, N_{ds} is the total number density of scatterers, $\left(\frac{\partial \sigma}{\partial \Omega} \right)_{medium}$ is the differential Rayleigh cross-section for excitation in a mixture of different species *i* [19].

$$\left(\frac{\partial \sigma}{\partial \Omega} \right)_{medium} = \sum_i x_i \left(\frac{\partial \sigma}{\partial \Omega} \right)_i \tag{2. 2}$$

in which x_i is the mole fraction of the species *i*.

$$\left(\frac{\partial \sigma}{\partial \Omega} \right)_i = \frac{4\pi^2 (n_i - 1)^2 \nu_i^4}{N^2 c_\nu{}^4} \text{ [19]} \tag{2.3}$$

in which n_i is the index of refraction of the species i and ν_i is the wavenumber of the incident laser beam.

Equation (2.2) shows the dependence of the Rayleigh signal on concentrations hence allowing the measurement of species concentrations if the total number density of scatterers is known.

From equation (2.1), one can see that the Rayleigh signal is proportional to the total number density of scatterers. As a consequence, at constant pressure, the Rayleigh signal is inversely proportional to the temperature.
However, the composition of the gas mixture must be known to allow the derivation of the temperature. It needs to be measured by some other means at the same time or, at least, the differential Rayleigh cross-section (equation 2.2) variation with combustion must be known.

Spontaneous Raman scattering is the emission of light by the molecules at a different wavelength than the excitation wavelength which is made possible by the energy exchange which can take place between the photon impinging the molecule and the molecule in a particular rotational and vibrational state.

The intensity of the Raman signal scattered into a solid angle Ω at 90^o from the incident laser beam is [19]:

$$I_{Raman,zz} \propto I_i N_l \Omega \left(\frac{\partial \sigma}{\partial \Omega} \right)_{zz} \tag{2.4}$$

in which N_l is the number of scatterers in the probed volume, I_i the intensity of the incident laser beam and $\left(\frac{\partial \sigma}{\partial \Omega} \right)_{zz}$ is the differential Raman cross-section for excitation and detection with parallel polarisation for a rotationally unresolved vibrational line [19].

$$\left(\frac{\partial \sigma}{\partial \Omega} \right)_{zz} = \frac{h(\nu_i - \nu_{12})^4}{8mc^4 \left[1 - \exp\left(hc_v \omega_e / kT \right) \right]} \left\{ (a')^2 + \frac{4}{45} (\gamma')^2 \right\} \tag{2.5}$$

in which v_{12} is the Raman transition frequency, a is the average polarisability and γ the polarisability anisotropy and ω_e is the frequency of the harmonic oscillator.

Analysis of Raman spectra can give both the concentration of the species present and the temperature.
However, Raman signals are usually weak and, as a consequence, usually only suitable for the detection of major species. Raman scattering is also not suitable for luminous flames or flames containing particles, phenomena which are often encountered in practical flames [16].
These issues contributed to the design of a new technique in the early 70's [16], namely Coherent Anti-Stokes Raman Spectroscopy (CARS).

2.1.1.2 Coherent Anti-Stokes Raman Spectroscopy (CARS)

In CARS experiments, a pump laser beam of frequency ω_1 and a downshifted Stokes beam of frequency ω_2 are mixed to give rise, in the probed species in the medium, to the CARS signal at $\omega_3 = 2\omega_1 - \omega_2$. The CARS signal may be expressed as follow [16]:

$$I_3 = \frac{\omega_3}{n_1^2 n_2 n_3 c_v^4 \varepsilon_0^2} I_1^2 I_2 \left|\chi_{CARS}\right|^2 l^2 \left(\frac{\sin \frac{\Delta k l}{2}}{\frac{\Delta k l}{2}} \right)^2 \qquad (2.6)$$

in which I_3 is the intensity of the CARS signal, I_1 the intensity of the pump beam, I_2 the intensity of the Stokes beam, ε_0 the permittivity of free space, c_v the speed of light in vacuum, n_1 the index of refraction of the medium at ω_1, n_2 the index of refraction of the medium at ω_2, n_3 the index of refraction at ω_3, χ_{CARS} is the susceptibility, l is the cavity length and Δk the phase mismatch that is $\Delta k = 2k_1 - k_2 - k_3$.

The shape of the spectrum of the probed species at a given temperature is indicative of its concentration. Comparison between computed CARS spectra and experimental spectra provides the concentration measurement [18].

The susceptibility, χ_{CARS}, is proportional to the population difference between the two energy levels coupled by the mixing process. As a consequence, the CARS signal is temperature-dependent. The CARS spectra recorded in CARS experiments are usually compared with a library of spectra which allow the determination of the temperature.

The CARS signals are usually much stronger than spontaneous Raman scattering signals which make CARS a better technique. However, CARS is only a point-measurement technique. This technique is also very computationally demanding.

2.1.1.3 Resonantly Enhanced Multiphoton Ionisation (REMPI)

In a REMPI experiment, an atom or a small molecule is excited to an excited intermediate state by absorption of two or more photons. It is, then, ionised by another photon [18]. The electrons ejected from the probed species give the concentration measurement. By scanning the laser wavelength, one can even obtain an absorption spectrum.

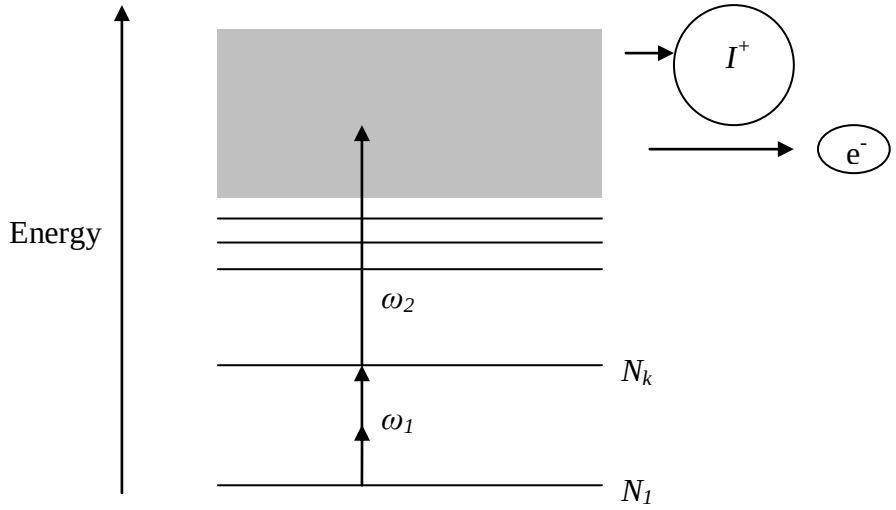

<u>Figure 2.1</u>: Physical processes involved in a REMPI experiment [19].

In Figure 2.1, I^+ is the ionised probed species and e^- is the electron ejected from the probed species. N_k corresponds to the excited intermediate state of the probed species while N_l is the initial state of the probed species.

The REMPI signal rate (counts/s) can be expressed as follow [19]:

$$S_{REMPI} = N_{GS}\left(\frac{\sigma_{lk} n_{L1}^2}{1+\frac{A_k}{\sigma_{kI} n_{L2}}}\right) \tag{2.7}$$

in which N_{GS} is the density of molecules in the ground state, σ_{lk} is the absorption cross-section for the transition l→k, σ_{kI} is the ionisation cross-section, n_{L1} is the number of incident laser photons, n_{L2} is the number of photons per pulse for the ionisation laser and A_k is the transition probability for multiphoton transition l→k.

REMPI experiments are species-specific and time-resolved [18]. However, REMPI is a point measurement technique. Moreover, the electrons are detected by an anode placed in the flame so REMPI is not a truly non-intrusive technique [18].

2.1.1.4 Degenerate Four-Wave Mixing (DFWM)

DFWM involves two monochromatic counterpropagating linearly polarised pump beams with the same strong intensity and a weaker co-planar linearly polarised probe beam [19]. The probe beam interferes with one of the pump beams. This interference pattern gives rise to a non-linear response in the medium thus producing an induced grating. The remaining pump beam is then scattered by this induced grating and gives the signal beam.

In the weak saturation regime, i.e. when $I_{pump} << I_S(0)$, the following equation is valid [18]:

$$I_{sig}^{\text{int}} \propto \frac{\left|\mu_{12}\right|^8 N_{at}{}^2 k^2 T_1^2 T_2^3}{\left[1+4I_{pump}/I_S(0)\right]^{5/2}} I_{pump}^2 I_{probe} \tag{2.8}$$

In the strong saturation regime, i.e. when $I_{pump} >> I_S(0)$, the following equation is valid [18]:

$$I_{sig}^{\text{int}} \propto \left|\mu_{12}\right|^3 N_{at}{}^2 k^2 T_1^{-1/2} T_2^{1/2} I_{pump}^{-1/2} I_{probe} \tag{2.9}$$

where

$$I_S(0) = h^2 / \left(T_1 T_2 \left| \mu_{12} \right|^2 \right) \tag{2.10}$$

is the so-called line-centre saturation intensity, μ_{12} is the atomic dipole moment, T_1 and T_2 the longitudinal and transverse relaxation times and N_{at} is the atomic number density.

Because the signal is dependent on N_{at}, it allows concentration measurement. A DFWM spectrum allows also the estimation of the temperature, N_{at} being determined by a Boltzmann distribution which states that, at temperature T, the number N_i of molecules in the state with energy E_i is [20]:

$$N_i = \frac{N e^{-\frac{E_i}{kT}}}{\sum_i e^{-\frac{E_i}{kT}}} \tag{2.11}$$

with N the total number of molecules and k the Boltzmann constant ($k=1.381*10^{-23}$ J/K).

2.1.1.5 Cavity Ringdown Spectroscopy (CRD)

CRD is an absorption spectroscopy technique. In CRD experiments, a short light pulse is coupled into a cavity formed by two highly reflective mirrors. The portion of light entering the cavity bounces between the two mirrors many times. Another small portion of the light is transmitted through the other mirror. It is the intensity of the light transmitted through the second mirror that is recorded.

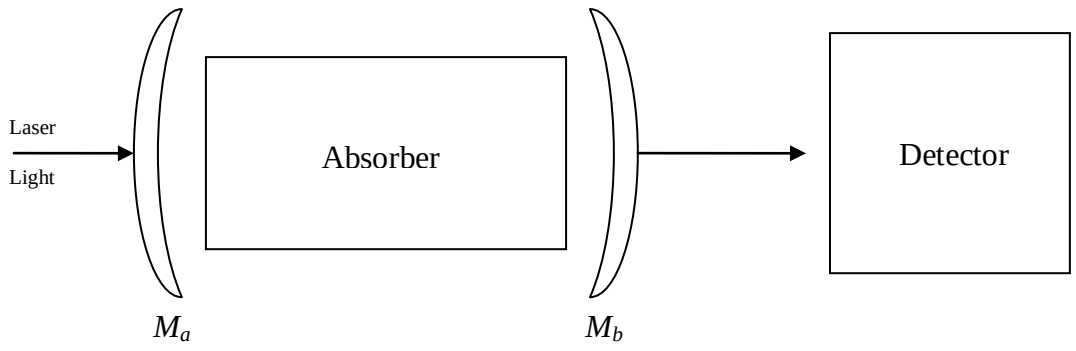

Figure 2.2: Principle of a CRD experiment [18]

The behaviour of this signal with time gives information on the absorbing species present and their concentration [18]:

$$I = I_0 e^{-[(1-R)+\sigma\rho_{abs}d]c_v t/l} \tag{2.12}$$

where I_0 is the initial intensity, R is the reflectivity of the mirrors, c_v is the speed of light, t the time, l the cavity length, σ is the absorption cross-section at the laser wavelength, ρ_{abs} is the absorber density and d is the absorbing length.

CRD is a sensitive technique which allows the detection of minor species. However, it is also a line-of-sight technique and as a consequence usually has a poor spatial resolution. It usually also has a poor temporal resolution.

2.1.1.6 Tunable Diode Laser Absorption Spectroscopy (TDLAS)

Tunable Diode Laser Absorption Spectroscopy (TDLAS) allows measurement of concentrations and temperature.
A tunable diode laser is tuned to an absorption line in the species of interest. The transmitted signal is then measured. The intensity of the transmitted signal is given by the Beer-Lambert law [19]:

$$I = I_0 \exp(-\varepsilon c_i l) \tag{2.13}$$

In which l is the path length, ε is the molar absorptivity and c_i the concentration of the species i.
ε depends on the temperature. As a consequence if the temperature is known, the concentration of the species probed can be determined.
However, it is easy to measure temperature by this method as well. The laser needs to be tuned at a second absorption line. The ratio of the two transmitted signals depends solely on the temperature [19]:

$$R = \left(\frac{I_1}{I_2}\right)_{T_0} \exp\left(\frac{-hc_v(E_1 - E_2)}{k}\left(\frac{1}{T} - \frac{1}{T_0}\right)\right) \quad (2.14)$$

T_0 is a reference temperature and S_1 and S_2 the reference signals at both absorption lines. E_1 and E_2 are the energies involved in the two transitions.

2.1.1.7 Laser Induced Fluorescence (LIF)

The principle of a laser-induced fluorescence experiment [16] is to tune in frequency a laser to an allowed transition in a tracer. As a consequence, the electrons of the tracer are excited from a lower to an upper energy state. Subsequently, the species probed can fluoresce i.e. emit light to return to its ground electronic state.

The fluorescence signal emitted by the probed species is proportional to the intensity of the laser, the population of the lower energy state, the concentration of the probed species and the fluorescence quantum yield.

LIF experiments allow the measurement of both concentrations and temperature. Indeed, as explained above, the fluorescence signal is proportional to the concentration of the probed species and depends also on temperature via its fluorescence quantum yield and the population of the lower energy state of the probed species which follows a Boltzmann distribution (2.11).

It allows field measurements if the excitation of the probed species is achieved with a laser sheet.

2.1.2 Velocity Measurements

In combustion, flow velocity measurements can be performed using various techniques such as:

- Phase Doppler Anemometry (PDA),
- Laser Doppler Velocimetry (LDV) also called Laser Doppler Anemometry (LDA),
- Particle Image Velocimetry (PIV).

The principle of the measurement of the velocity in a PDA experiment is essentially the same as in a LDV experiment. But PDA allows also the measurement of the size of the particles.

In this section, we will briefly describe the principles of LDV and PIV. The PIV technique and in particular the Stereoscopic Particle Image Velocimetry (SPIV) technique will be explained in more depth in section 2.3.

2.1.2.1 Laser Doppler Velocimetry (LDV)

LDV experiments [21] allow point-measurements of the velocity of a gas or liquid flow. They make use of the Doppler effect. The Doppler effect states that there is an apparent change in frequency (or wavelength) of a wave when its source and its observer move relative to one another. The change in frequency (Δf) is related to the velocity (v) at which the source and the observer move toward ($v>0$) or away from ($v<0$) another:

$$\Delta f = \frac{fv}{c_v} \tag{2.15}$$

with c_v the speed of light and f the original frequency of the wave emitted.

The following scheme describes the arrangement of a typical LDV experiment.

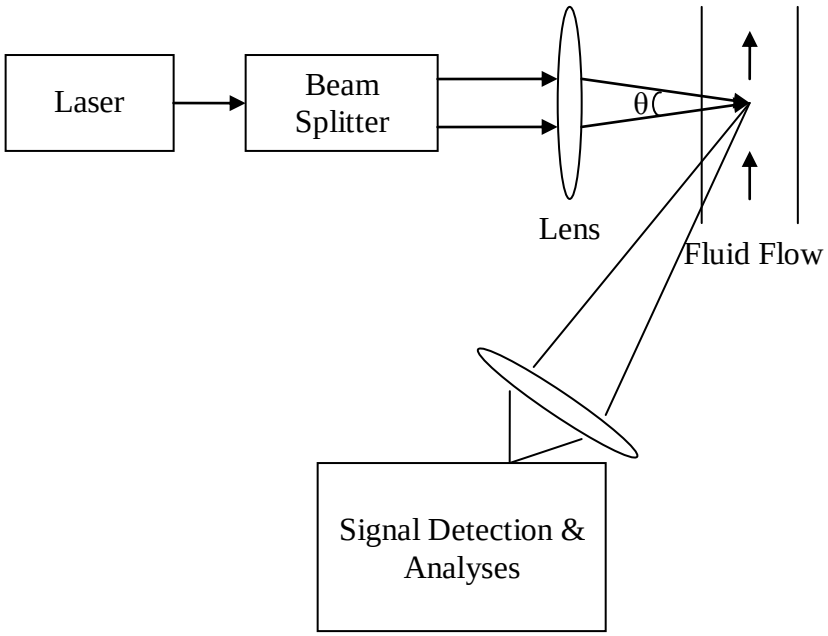

Figure 2.3: Scheme of the experimental arrangement of a typical LDV experiment

The fluid flow (gas or liquid) is usually seeded with particles of diameter around a micron. A laser beam is splitted in two beams which are then focused by a lens onto the probe volume. They interfere and the resulting fringes are spaced by [21]:

$$d_f = \frac{\lambda}{2\sin\left(\frac{\theta}{2}\right)} \tag{2.16}$$

Light is, then, scattered by the seeding particles. The scattered light is then recorded and analysed.

The velocity component perpendicular to the plane in which the two laser beam intersect can, then, be determined [21]:

$$v = d_f \cdot f_{SL} \tag{2.17}$$

in which f_{SL} is the frequency of the scattered light.

However, in that configuration, it is impossible to tell the direction of the velocity vector: the frequency of the scattered light will be the same if the velocity vector is reversed. This is called the directional ambiguity [21]. This ambiguity on the direction of the velocity component can be removed by using two laser beams in which we introduce a frequency shift in one of them. This will cause the fringe pattern with spacing s to move at constant speed V_p. Depending on whether the particles move with or against the fringe pattern, the frequency of the scattered light will be either greater or smaller than $\Delta_p = \frac{V_p}{s}$ thus removing the directional ambiguity.

Adding more laser beams (two or four) allows the measurement of the other components of the velocity of the fluid flow (one or two).

However, the LDV technique remains essentially a point-measurement technique.

2.1.2.2 Particle Image Velocimetry (PIV)

In Classical PIV (2D-PIV), a laser sheet is directed along a plane in the flow. Tracer particles are illuminated and scatter light mostly in the forward direction. Usually, the particles are imaged at right angles to the sheet because the scattered light in this region does not depend so strongly on the observation angle as in the forward direction where the light is concentrated in a narrow lobe. The laser source is pulsed repeatedly and images of these particles are recorded. With the knowledge of the period of the pulses, the velocity can be determined using the displacement of the images [22]:

$$D(X;t,t') = \int_{t}^{t'} v(X(t),t)dt \tag{2.18}$$

with *v(X(t),t)* the velocity of the tracer particle, *D(X;t,t')* their displacement during the time interval [t,t'].

The PIV technique allows the determination of the velocity/strain rates fields, whereas the LDV technique only allows point-measurement of the velocity. That is why, the PIV technique was selected.

2.1.3 Chosen techniques

The choice of a diagnostic for imaging velocities was quite straightforward: only two well established laser methods are available. LDV being only a point measurement technique, PIV was, as a consequence, the only option that could serve our purpose. Moreover, LDV would not have allowed us an access to the velocity gradients and as a consequence to the strain rate fields.

The choice of the diagnostic to implement to get an access to progress variable fields was less straightforward: there exist various scalar measurement techniques. The criteria for the choice of the second technique were:

- it needed to be a field measurement technique,
- the compatibility with SPIV,

- the availability of the equipment,
- the strength of the signal,
- the resolution (spatial and temporal)
- it should not perturb the system studied.

As mentioned in the previous sections, only a few available laser techniques allow field measurements of the temperature or of the concentrations. For instance, CARS, REMPI, CRD and TDLAS do not allow field measurements. Some techniques are not compatible with the PIV technique as, for instance, Rayleigh scattering. The strength of the signal to be studied to get an access to the progress variable fields may be expected to be too weak as, for instance, with spontaneous Raman scattering. Some techniques are not truly non-invasive so they might perturb the system studied as, for instance, with REMPI. The difficulty in processing the data might also be regarded as an issue as, for instance in DFWM or CARS. Sometimes, the equipment was just not available (CARS and TDLAS).
The LIF technique seemed to be the more appropriate technique to use to get an access to progress variable fields: it allows field measurements, it is compatible with the PIV technique, it does not perturb the system studied and the equipment was available.

2.1.4 Comparison between radicals for PLIF experiments

The choice of a species with which to perform PLIF in a combustion system is very important. Numerous molecules can be chosen to perform PLIF experiments [23]: atoms, diatomic molecules such as OH, NO and CH or larger such as acetone, biacetyl, 3-pentanone or toluene. Their spectroscopy must be well understood and their LIF signal must be strong enough and have a good temporal resolution. In the present work, it was necessary to add a tracer because the components of the mixtures of the flames only weakly fluoresce (H_2O, air, H_2, N_2). The tracer added must not perturb the system studied so it should be chosen carefully and used in minimal concentrations.

Organic dyes [23] are not well suited to gaseous flow because they usually have low vapour pressure or they break down before being vaporised. Biacetyl has also a low vapour pressure at room temperature and as a consequence, that makes it not very well suited to gaseous flows. Acetone has a higher vapour pressure at room temperature; however it is not as easy to use as OH or NO. In the case of hydrogen-air flames, two potentially suitable tracers were OH and NO. The radical OH is not very well suited because it occurs naturally in the flame and as a consequence, its concentration varies dramatically. On the other hand, the concentration of NO is much more stable in the flame and as a consequence much more adapted to measure the progress variable.

2.2 Laser Induced Fluorescence of the radical NO

Laser induced fluorescence (LIF) of the radical NO has been extensively studied [24-31]. In 1980, Grieser et al. [24] were able to detect nitric oxide in the ppm range in an atmospheric pressure flame using laser-induced fluorescence measurements. In 1984, Kychakoff et al. [25] were able to visualise NO in combustion flowfields using planar laser-induced fluorescence and concluded that it should, in principle, be possible to detect concentrations as low as 10 ppm and that the technique should be able to resolve temperature as well. In 1989-90, Westblom et al. [26-27] performed simultaneous laser-induced detection of NO, OH and O in flames. However, they made no attempt to quantify their measurements. In 1992, Heard et al. [28] used laser-induced fluorescence to measure the concentrations of NO, OH and CH. They were successful in measuring the absolute NO and OH concentrations but not the CH concentration. In 1993, Reisel et al. [29] were able to measure NO concentrations down to 1ppm in high pressure flames up to 9 atm. In 1993, Lee et al. [30] compared the one-line and two-line NO-PLIF techniques to measure temperature in gases. They concluded that the two-line technique could be applied to a broader range of flows but that the one-line technique was a simpler method. They also developed a model to predict the variation of the NO fluorescence signal as a function of temperature. In 1998, Tamura et al. [31] performed a similar study in flames. They drew similar conclusions. They also gave guidelines to optimise the one-line technique. In particular, they stressed the importance of taking into account the laser lineshape and

bandwidth, the collisional broadening effects and the collisional quenching to measure temperature using the one-line technique.

In order to be able to perform quantitative measurements using planar laser induced fluorescence of nitric oxide, it is necessary to understand the spectroscopy of NO and how it affects the measurements.

A quick introduction on the spectroscopy of the NO radical can be found in [32]. Scholz briefly introduces the radical NO, its different electronic states, its selection rules of transition and their nomenclature.

Bessler et al. [33-35] compare different strategies for NO-PLIF i.e. they compare different excitation mode in the γ-band which has been particularly studied because of its easy accessibility to current commercial laser excitation and because the fluorescence signals are strong. They also evaluate their advantages and drawbacks in different situations.

Reisel et al. [36] give all the equations needed to calculate the transition energies and the Einstein A and B coefficients. These data allow the comparison of the intensity of the different transitions in the γ-band available for the NO-PLIF diagnostic.
P. H. Paul [37] gives an update of the same spectroscopic parameters which agrees well with the previous study.

In order to evaluate the behaviour of the fluorescence signal of NO as a function of temperature, specific spectroscopic aspects of the interesting excitation transitions and of the fluorescence signal in itself had to be studied.

Chang et al. give details [38] about the dependency on temperature of the collision broadening and shift of the γ(0,0)-band of NO in the presence of nitrogen. Results concerning the collisional broadening and shift of the excitation lines of NO in the γ(0,0)-band by O_2 and H_2O were reported by DiRosa et al.. [39].

The line broadening of NO in the γ(0,0)-band was studied by Dodge et al..[40].

Corrections for the collisional quenching of the NO fluorescence signal must also be made to be able to calculate the behaviour of the fluorescence signal as a function of temperature. Paul et al. [41] gave empirical correlations which are useful to correct the fluorescence signal and predict the real fluorescence signal as a function of temperature.

The excitation spectrum of O_2 overlaps partly the excitation spectrum of NO as a consequence, one must be careful in choosing the excitation wavelength for NO so as to avoid a simultaneous excitation of O_2. DiRosa et al. [42] presented interesting results showing that in the region between 225.9 nm and 226.1 nm, no excitation of O_2 occurred.

Another important parameter to fully describe, predict and calculate the behaviour of the fluorescence signal as a function of temperature is the overlap fraction between the laser signal and the chosen excitation line. Partridge et al. [43] formulated a dimensionless overlap fraction to account for the overlap between the laser signal and the excitation line.

Those articles contributed to the choice of a suitable excitation strategy for the NO-PLIF experiments described in the present work. They also allowed the calculation of the behaviour of the fluorescence signal as a function of temperature.

Further explanation and justification derived from these articles will be given in the next sections.

2.2.1 Spectroscopy of the NO radical

The electronic configuration [32] of the NO molecule in the ground electronic state, if we refer to the Molecular Orbital Theory, can be written:

K K $(\sigma_{(g)}2s)^2$ $(\sigma^*_{(u)}2s)^2$ $(\sigma_{(g)}2p)^2$ $(\pi_{(u)}2p)^4$ $(\pi^*_{(g)}2p)$

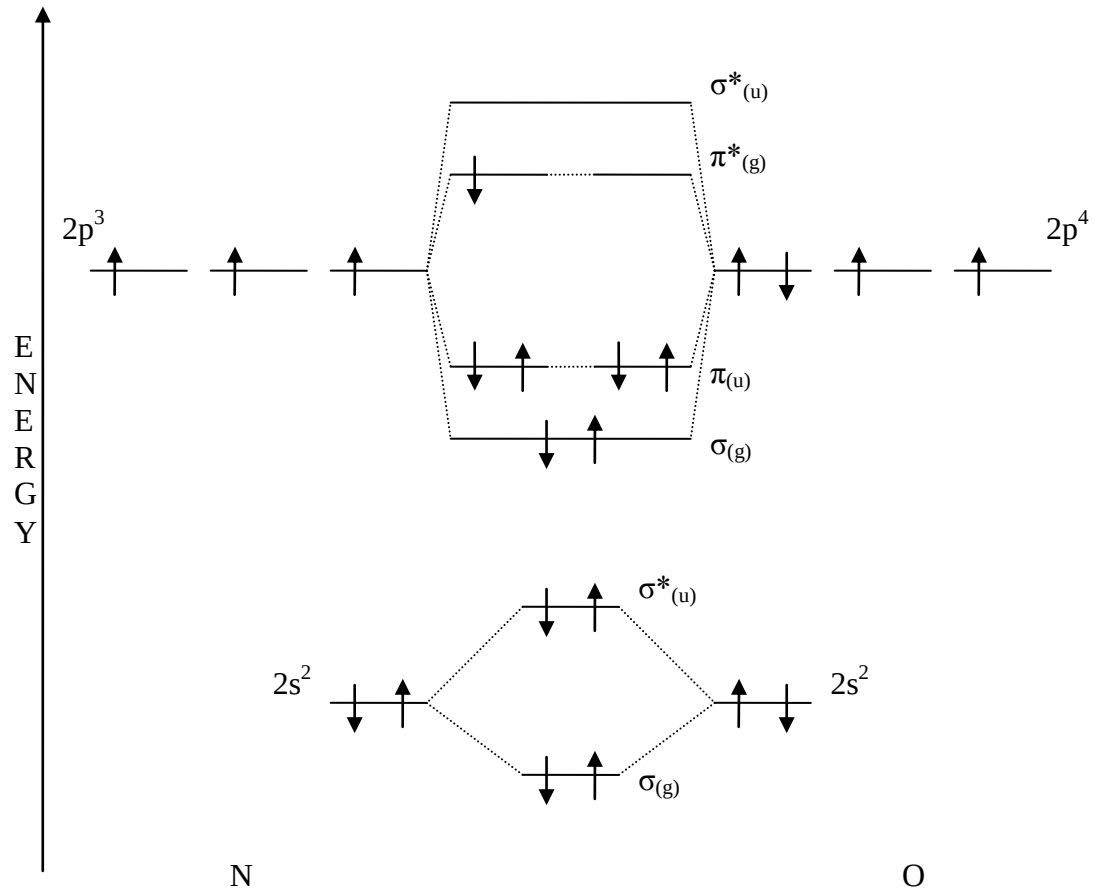

Figure 2.4: Electronic configuration of NO

14 Electrons are in closed orbitals and form the electronic configuration of the NO^+ in the ground electronic state. The 15^{th} electron lies in a non-closed anti-bonding orbital: $\pi^*_{(g)}$.

As a consequence, the ground state of the NO molecule possesses the electronic orbital angular momentum $\Lambda=1$ and the total spin quantum number S=1/2. The ground state is therefore a $^2\Pi$ state (the upper prefix means that this state is a doublet because its multiplicity is 2S+1=2) split in a $^2\Pi_{1/2}$ state and a $^2\Pi_{3/2}$ state (the subscript refers to the total electronic quantum number $\Omega=|\Lambda+\Sigma|=|1 \quad +/- \quad 1/2|$ where Σ is the spin quantum number associated with the vector which is the axial component of the total spin momentum along the internuclear axis). The $^2\Pi_{1/2}$ and $^2\Pi_{3/2}$ states are separated in wavenumber by ~123cm^{-1}.

By absorption of a photon, the NO molecule can be electronically excited. In particular, the electron in the $\pi^*_{(g)}$ can be excited and be brought into the $3s\sigma_{(g)}$ orbital,

$3p\pi_{(u)}$ orbital or the $3p\sigma_{(u)}$ orbital. Table 2.1 contains a description of the electronic configurations of the ground state and the first four excited states of the NO molecule as well as their relative electronic energies T_{el} (in terms of wavenumber):

Electronic configuration	Electronic state	T_{el} (cm^{-1})
$\ldots(\pi_{(u)}2p)^4\ 3p\sigma_{(u)}$	$D^2\ \Sigma^+$	53291
$\ldots(\pi_{(u)}2p)^4\ 3p\pi_{(u)}$	$C^2\Pi$	52373
$\ldots(\pi_{(u)}2p)^3\ (\pi^*_{(g)}2p)^2$	$B^2\Pi$	45482
$\ldots(\pi_{(u)}2p)^4\ 3s\sigma_{(g)}$	$A^2\Sigma^+$	44199
$\ldots(\pi_{(u)}2p)^4\ \pi^*_{(g)}2p$	$X^2\Pi$	0

Table 2.1: Electronic configurations and electronic energies of the ground state and the first four excited electronic states of the NO molecule

The ground electronic state of NO is characterised by spin-splitting as previously mentioned and Λ-doubling.

An uncoupling Phenomenon: *Λ-type doubling*

We observe a Λ-type doubling when the interaction between the rotation of the nuclei and L cannot be neglected anymore (usually for larger speed of rotation). This interaction causes a splitting into 2 components for each J value (when $\Lambda \neq 0$).

In real molecules, rotation, vibration and electronic motions take place simultaneously and influence one another [44]. The interaction between rotation and vibration is taken into account in the vibrating rotator model or the vibrating symmetric top model. The interaction between vibration and electronic motions is taken into account in the potential curve, which is a representation of the electronic energy as a function of the internuclear distance. The interactions between rotational and electronic motions were first studied by Hund [45].

There exist different angular momenta in a molecule:

- the electron spin S
- the electronic orbital angular momentum Λ
- the angular momentum of nuclear rotation N
- the nuclear spin

The three first form the total angular momentum J.

Except in the case of a $^1\Sigma$ state, where J is equal to the angular momentum of nuclear rotation and for which the simple rotator model can be used, different coupling cases have to be distinguished.

Coupling case	Assumptions	"Good" Quantum numbers	Consequences
Hund's case (a)	1) Weak interaction between nuclear rotation and electronic motion (spin and orbital) 2) Strong coupling of the electronic motion to the internuclear axis	- Electronic angular momentum Ω well defined - Angular momentum of nuclear rotation N - J= Ω+N	- J constant in magnitude and direction - Ω and N rotate about this vector (nutation) - L and S precesse about the internuclear axis - Precession is much faster than nutation (assumption) - // symmetric top model $F_v(J)=B_v[J(J+1)- \Omega^2]$
Hund's case (b)	1) Very weak (zero) coupling between S and the internuclear axis	- Electronic orbital angular momentum Λ - Angular momentum of nuclear rotation N - Total angular momentum apart from spin K= Λ+N	- A level with a given K has 2S+1 components - molecular rotation produces a small magnetic moment in the direction of K which causes slight magnetic coupling between S and K→ slight increasing splitting of the levels with different J and equal K - precession of K and S about J slow compared to the nutation
Hund's case (c)	1) Interaction between L and S stronger than the interaction with the internuclear axis	- Λ and Σ not defined - L and S form a resultant J_a coupled to the internuclear axis with a component Ω - Ω and N form the resultant J	Rotational energy level and their J values are given by the formula of Hund's case (a)

Hund's case (d)	1) Very weak coupling between L and the internuclear axis 2) Strong coupling between L and the axis of rotation	- The angular momentum of nuclear rotation is called R and quantised - R and L add vectorially giving K the total angular momentum apart from the spin - K and S form the total angular momentum J - Usually, small coupling between K and S that S is disregarded (possibly J: case (d'))	- First approximation for the rotational energy in case (d): $F(R)=B_vR(R+1)$ - Each term is split into 2L+1 components further split into 2S+1 components
Hund's case (e)	1) Strong coupling between L and S 2) Weak interaction of L and S with the internuclear axis	- L and S form a resultant J_a - J_a combine with R to form J	

Table 2.2: Summary of the different Hund's cases

*Hund's case (a) and Hund'scase (b) are the most frequent cases encountered.

*For Singlet states, Hund's case (a) and Hund's case (b) are not distinct, the singlet states follow the symmetrical top.

There exist sets of equations describing each of the four spin-split Λ-doubled levels [36-37].

The ground electronic state of NO goes from Hund's coupling case (a) to Hund's coupling case (b) through intermediate cases when the nuclear rotation increases.
The values of the energies for the ground electronic state are given in Appendix Chapter II.

The first excited electronic state is a $^2\Sigma^+$ and belongs to Hund's case (b).
The values of the energies for the first excited electronic state are given in Appendix Chapter II.

Notations:

The lines arising from ΔJ=-2, -1, 0, +1, +2 are respectively called O, P, Q, R, S.

Transition rules:

For the NO molecule, transitions are allowed only if the following transitions rules are observed:

ΔJ=J'-J''=0, **±1** except the transition **J=0→J=0** which is **not allowed**

Transitions are allowed only if the parity of the upper state is different from the parity of the lower state, that is:

+↔+ and -↔- are not allowed only +↔-

For the Hund's coupling cases (a) and (b), in order to be allowed the transitions must follow 2 further rules:

ΔΛ=0, ±1 i.e. only such transitions are allowed: **Σ↔ Σ , Σ ↔ Π, Π ↔ Π…**

ΔS=0 i.e. transitions are only possible between states having the **same multiplicity**.

Transition	Ground rotational state: $^2\Pi$			1^{st} excited rotational state $^2\Sigma^+$	
$P_{11}(J'')/P_1(J'')$	1/2	c	J''	-1/2	J''-1
$^{Q}P_{21}(J'')/Q_{21}(J'')$	1/2	d	J''	1/2	J''-1
$Q_{11}(J'')/Q_1(J'')$	1/2	d	J''	-1/2	J''
$^{R}Q_{21}(J'')/R_{21}(J'')$	1/2	c	J''	1/2	J''
$R_{11}(J'')/R_1(J'')$	1/2	c	J''	-1/2	J''+1
$^{S}R_{21}(J'')/S_{21}(J'')$	1/2	d	J''	1/2	J''+1
$^{O}P_{12}(J'')/O_{12}(J'')$	3/2	d	J''	-1/2	J''-1
$P_{22}(J'')/P_2(J'')$	3/2	c	J''	1/2	J''-1
$^{P}Q_{12}(J'')/P_{12}(J'')$	3/2	c	J''	-1/2	J''
$Q_{22}(J'')/Q_2(J'')$	3/2	d	J''	1/2	J''
$^{Q}R_{12}(J'')/Q_{12}(J'')$	3/2	d	J''	-1/2	J''+1
$R_{22}(J'')/R_2(J'')$	3/2	c	J''	1/2	J''+1

Table 2.3: Notations corresponding to the different transitions observed between the ground electronic state and the first excited state [24]

2.2.2 Spectroscopic models for NO-LIF

Some species are luminescent, that is they are able to emit UV, visible or IR light when decaying from an electronically excited state into the ground electronic state. Luminescence can be achieved by different ways. For instance, a chemical reaction

can produce a species in an electronically excited state which is able to return in the ground state by emitting a photon (chemiluminescence). Photoluminescence is the emission of photons by a species that was electronically excited by absorption of light. Fluorescence and Phosphorescence are two particular cases of photoluminescence. Fluorescence can provide information concerning temperatures because it is dependent on the environment of the emitting molecule.
However, photoluminescence is not the only de-excitation pathway for a species which has absorbed photons to return to its ground state [16]:

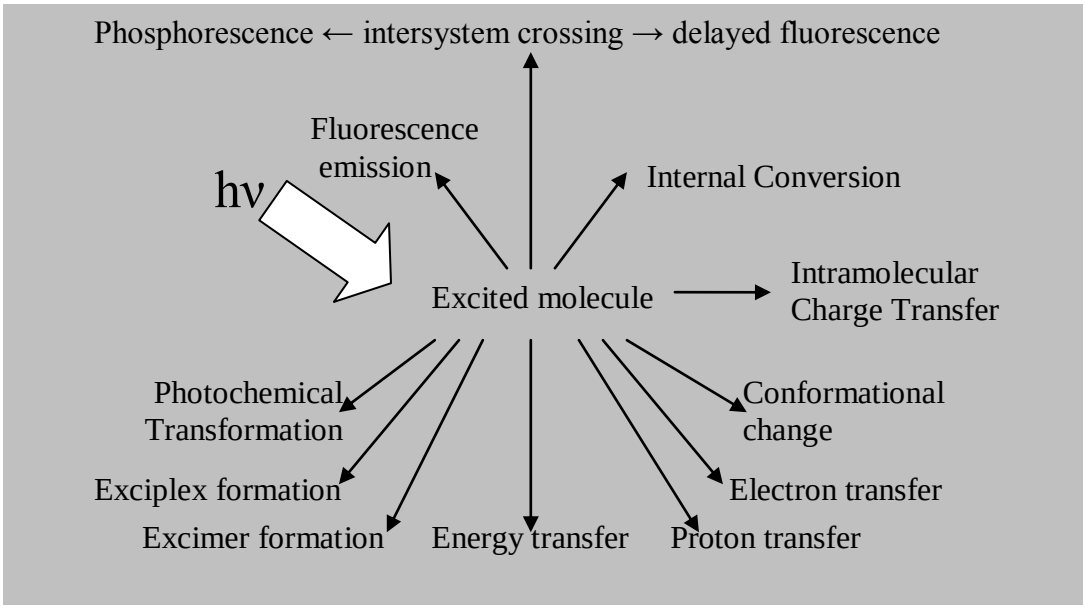

Figure 2.5: De-excitation pathways for a species having absorbed photons

To be able to analyse the information gained from LIF experiments, it is important to understand the different de-excitation pathways of the molecule.

The principle of a laser-induced fluorescence experiment is to tune in frequency a laser to an allowed transition in a tracer. As a consequence, the electrons of the tracer are excited from a lower to an upper energy state. The de-excitation processes through which the molecule can relax include:

- collisional quenching,
- stimulated emission,
- rotational energy transfer,
- vibrational energy transfer,
- predissociation,

- photoionisation,
- spontaneous emission or radiative decay or *fluorescence*…

Many models, using rate equations, have been developed to describe the energy transfers in LIF, simple two-level models or more complex ones.
At first, we will describe the two-energy level diagram [16]:

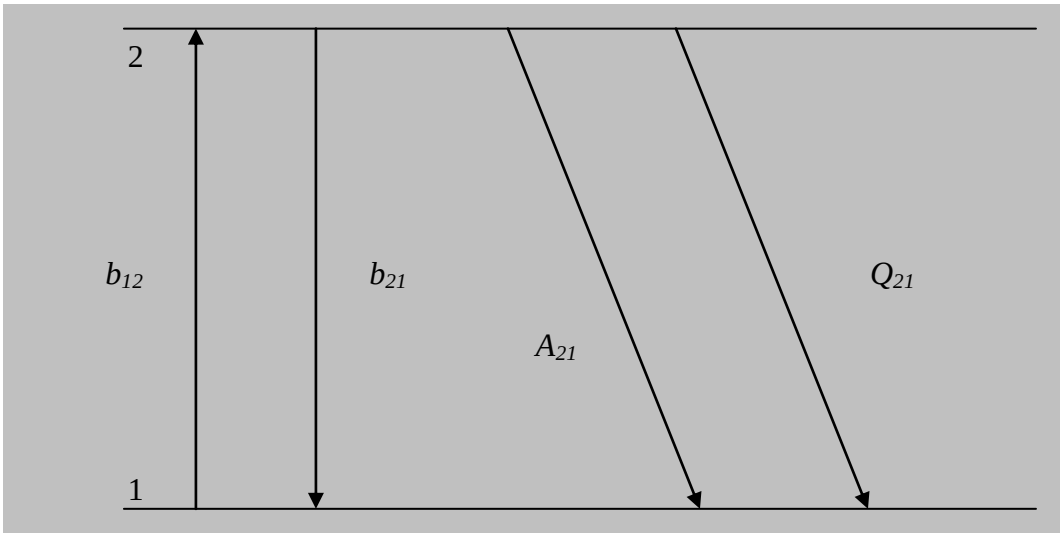

Figure 2.6: Representation of the two-level model

b_{12} is the stimulated absorption rate and b_{21} is the stimulated emission rate. A_{21} is the spontaneous emission rate and Q_{21} is the collisional quenching rate.
We obtain the following rate equations:

$$\frac{dN_1}{dt} = -N_1 b_{12} + N_2(b_{12} + A_{21} + Q_{21}) \tag{2.19}$$

$$\frac{dN_2}{dt} = N_1 b_{12} - N_2(b_{21} + A_{21} + Q_{21}) \tag{2.20}$$

and the population conservation equation may be written:

$$N_1^0 = N_1 + N_2 \tag{2.21}$$

The solution of these equations assuming that $N_2(t=0)=0$ is:

$$N_2(t) = \frac{b_{12}N_1^0}{r}\left(1-e^{-rt}\right) \tag{2.22}$$

with $r=b_{12}+b_{21}+A_{21}+Q_{21}$.

- For $rt<<1$, $N_2(t)=b_{12}N_1{}^0t$ i.e. the upper level population initially builds up linearly with time.
- For $rt>1$, $N_2 \sim \frac{b_{12}N_1^0}{r}$.

The saturation spectral intensity is defined as follow:

$$I_{sat}^{\upsilon} = \frac{\left(A_{21}+Q_{21}\right)c_v}{B_{12}+B_{21}} \tag{2.23}$$

Then we can express the fluorescence signal F:

$$F = h\upsilon A_{21}\frac{\Omega}{4\pi}lSN_2 \sim N_1^0\frac{B_{12}}{B_{12}+B_{21}}\frac{A_{21}}{1+\frac{I_{sat}^{\upsilon}}{I_{\upsilon}}} \tag{2.24}$$

with v the frequency of the emitted fluorescence, Ω the collection solid angle, S the focal area of the laser beam, l the axial extent along the beam from which the fluorescence is observed and knowing that the relation between the Einstein coefficient and the absorption and stimulated emission rates is:

$$b = \frac{BI_{\upsilon}}{c_v} \tag{2.25}$$

The fluorescence is said to be in the linear regime when:

$$I_{\upsilon} << I_{sat}^{\upsilon} \text{ because in that case } F \sim N_1^0\frac{B_{12}I_{\upsilon}}{B_{12}+B_{21}}\frac{A_{21}}{A_{21}+Q_{21}} \tag{2.26}$$

i.e. the fluorescence signal is proportional to the input laser intensity. So at low laser excitation intensities, we have to know the collisional quenching rate which is composition and temperature dependent.

On the other hand, if the saturation regime is achieved i.e. if

$$I_\upsilon >> I_{sat}^\upsilon \text{ then } F \sim \frac{N_1^0 B_{12} A_{21}}{B_{12} + B_{21}} \tag{2.27}$$

However, saturation is not usually easily achieved.

Moreover, in order to study more realistic fluorescence situations i.e. situations where rotational relaxation takes place, one must use multi-level models.

Multilevel rate equation models -necessary to predict accurately fluorescence signals- require a precise knowledge of the spectroscopy of the species studied.

Hereafter, a three-level model used to model the A-X transitions of NO is presented [46]:

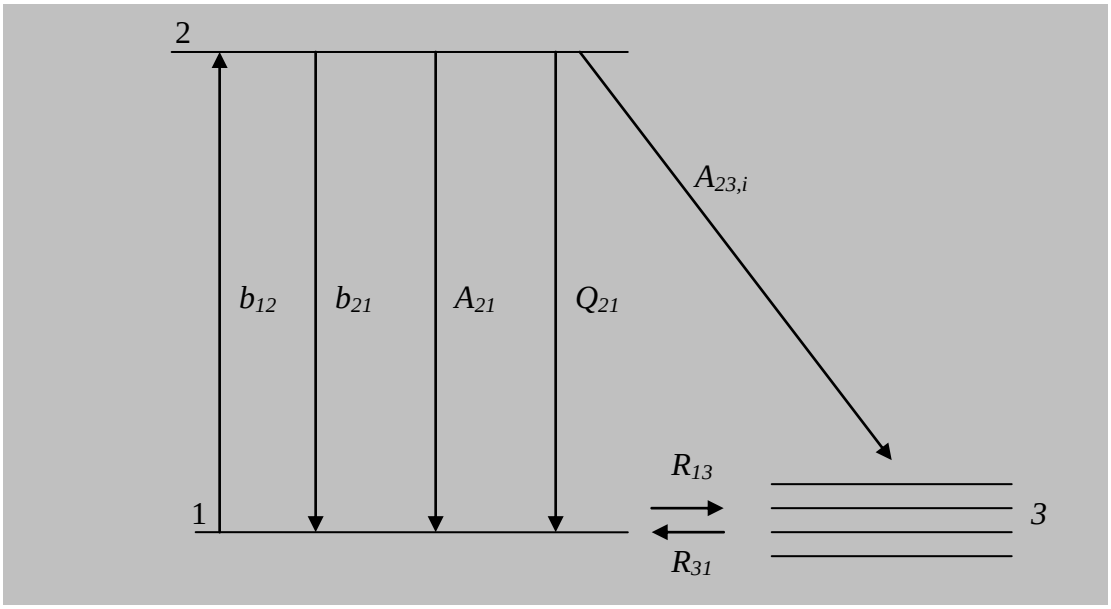

Figure 2.7: Representation of the three-level model

Where the R's are rotational energy transfer rates.

In the linear regime, if we assume $A<<Q$ and use the steady-state rate equation approach, the following expression for the LIF signal of one single transition may be written:

$$I_{LIF}\left(p,T,\nu_{laser},x_{gas}\right)\sim\ f_B(T)N_{NO}I_\nu^0\Gamma\left(p,T,\nu_{laser},x_{gas}\right)B\sum_i\frac{A_i}{Q\left(p,T,x_{gas}\right)} \qquad (2.28)$$

Bessler et al. [46] used the previous three-level non transient linear model to design a software tool, LIFSim, allowing the simulation of absorption spectra as well as excitation and emission LIF spectra for NO and O_2 for given experimental conditions. This program is available through the following address: http://www.pci.uni-heidelberg.de/pci/lifsim. The database includes spectroscopic data of the NO A-X band and O_2 B-X band. The simulations performed by this software take into account such effects as pressure line broadening and shifting as well as quenching. A full description of the functionality of this software as well as the spectroscopic background can be found in [46]. This software was used, in the present work, to simulate excitation LIF spectra of NO. These spectra were then compared with the experimental spectra in order to calibrate the LAMBDA PHYSIK dye laser used in this work (see section 2.2.5)

Following is a five level model describing the NO-LIF in the A-X (0,0) band [30]:

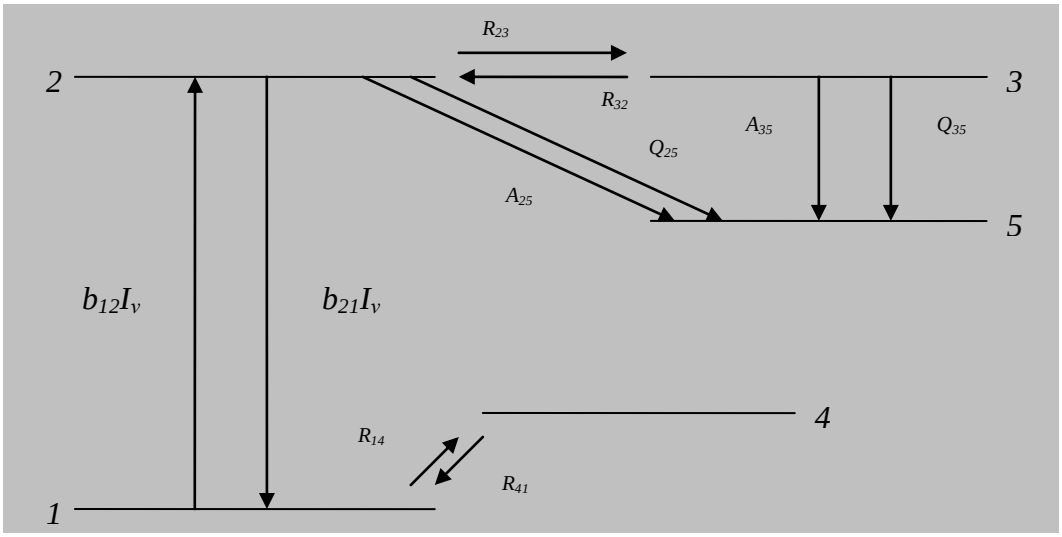

Figure 2.8: Representation of the five-level model for NO-LIF

$b_{12}I_v$ represents the stimulated absorption, $b_{21}I_v$ represents the stimulated emission, R_{ij} represents the rotational energy transfer rates associated with the transition from level i to level j. Q_{ij} represents the collisional quenching rates. A_{ij} is the spontaneous emission rate.

In this model, all energy states that are not directly coupled by the laser excitation are grouped into – approach of Berg and Shackleford [47] – bath levels i.e. levels 3,4,5 are bath levels.

The following assumptions are made:

- collisional quenching and radiative decay rates from levels 2 and 3 to levels 1 and 4 negligible,
- $\frac{R_{41}}{R_{14}} = \frac{N_1^0}{N_4^0}$ *and* $\frac{R_{32}}{R_{23}} = \frac{N_1^0}{N_4^0}$, which means that the ratio of the RET rates between level 1 and 4 (and 2 and 3) is equal to the initial Boltzmann fraction in the pumped state [30], [47],
- $A_{25}=A_{35}=A$, because it was found that the radiative decay rates did not vary much in the upper state [30],
- $Q_{25}=Q_{35}=Q$, because it was found that the collisional quenching cross-section did not vary much with rotational level [30].

It is now possible to write down the rate equations. To analyse the fluorescence signal, time dependent analysis of the rate equations is usually required but they can also be solved explicitly in some cases:

<table>
<tr><td>Weak laser excitation</td><td colspan="2">Strong laser excitation</td><td></td></tr>
<tr><td></td><td colspan="2">All energy transfer processes slow compared with stimulated absorption and emission, no significant RET -> two-level model</td><td>RET and collisional quenching rates not negligible with respect to the laser excitation rate -> saturation may or may not be reached -> time-dependent analysis -> six-level model</td></tr>
<tr><td></td><td>Fluorescence lifetime short compared with the laser pulse duration</td><td>Fluorescence lifetime not negligible compared with the laser pulse duration</td><td rowspan="3">Observation: the six-level model gives the same results as the two-level model in case of weak laser excitation.</td></tr>
<tr><td>Ground-state population not significantly perturbed</td><td>Insignificant fluorescence after the laser pulse</td><td>Fluorescence emitted after the laser pulse=$S_2 \sim N_1^0 b_{12} A/((A+Q)(b_{12}+b_{21}))$</td></tr>
<tr><td>Fluorescence emission rate=$S_f(t) \sim N_1^0 b_{12} I_v A/(A+Q)$</td><td>$S_1 \sim N_1^0 A \tau b_{12}/(b_{12}+b_{21})$</td><td>Total fluorescence=S_1+S_2</td></tr>
</table>

Table 2.4: Expression for the fluorescence signal in different cases of laser-excitation when considering the five-level model

Spectroscopic models such as presented above are necessary to be able to convert measured LIF intensities to concentrations, temperatures or pressures.

The fluorescence signal may be expressed as follow [48]:

$$I_{LIF} = c_{cal} I_{laser} N_{NO} \sum_i f_{B,i}(T) B_{i,k} g_{\lambda,i}(p,T,X) \sum_{k,j} \frac{A_{k,j}}{\sum_l A_{k.l} + Q_k(p,T,X)} \qquad (2.29)$$

The fluorescence signal depends on parameters such as the intensity I_{laser} of the laser, the density N_{NO} of the tracer, the Boltzmann function $f_{B,i}$ which gives the population of the lower energy level (level i) of the transition, the Einstein $B_{i,k}$ coefficients for absorption corresponding to the transition, the overlap factor $g_{\lambda,i}$ between the transition and the laser and the fluorescence quantum yields in which appear the Einstein $A_{k,j}$ and $A_{k,l}$ coefficients and the quenching rate Q_k corresponding to the level k.

There exist 4 major problems [46, 49] with LIF measurements using NO as a tracer:

- interference with other species
- laser and signal attenuation
- complex temperature dependence
- variation of the collisional quenching with pressure and temperature.

Although interferences with polycyclic aromatic hydrocarbons, aldehydes, ketones and with laser-generated C_2 in sooting flames have been reported; in the present work, the interferences come entirely from the fact that the O_2 B-X band overlaps the NO A-X band. To avoid interferences with O_2, it is possible to choose transitions in NO which are not overlapped by the O_2 band. The region between ~225.920nm and ~226.120nm is free from O_2-overlapping. As a consequence, the chosen lines should be chosen in this region [32].
The laser and signal attenuation is mainly due to an absorption by CO_2 and H_2O. This attenuation increases with pressure and temperature. However, it is not an issue in the present atmospheric pressure relatively low temperature experiments.

2.2.3 Calculation of the predicted behaviour of the fluorescence signal as a function of temperature

Concerning the temperature dependence, many factors are temperature dependent:

- the population distribution in the energy levels,
- the overlap fraction,
- the quenching rate/fluorescence quantum yield.

In order to be able to choose a suitable transition, it is necessary to understand a little more the spectroscopy of NO. The following sections will review all the parameters needed to determine the most suited transition for this work and to calculate its corresponding fluorescence signal behaviour with temperature.

Einstein $B_{i,k}$ coefficients for absorption and Einstein $A_{k,j}$ coefficients for spontaneous emission

The equations for those coefficients can be found in the literature [36] which also gives their values for the $\gamma(0,0)$ band of NO.
Tables containing the values of the Einstein $B_{i,k}$ coefficients for absorption for the $\gamma(0,0)$ band of NO originating from $\Pi_{1/2}$ and $\Pi_{3/2}$ and the values of the Einstein $A_{k,j}$ coefficients for spontaneous emission can be found in [36] and appendix chapter II.

Comparing the values of the Einstein coefficients for absorption and spontaneous emission allows the comparison of the relative strength of various transitions.

Boltzmann population distribution

Using the equation found in the literature [50], the population distribution in the ground level was calculated as a function of *J* (or *N*) and temperature.
The variation of the population distribution as a function of temperature will help choose a transition which will present no ambiguity when determining the progress variable.

The following curves - shown in figures 2.9, 2.10, 2.11 & 2.12 - were calculated using the values of the energy levels obtained using the equations found in [37] and assuming Hund's case (b) throughout.

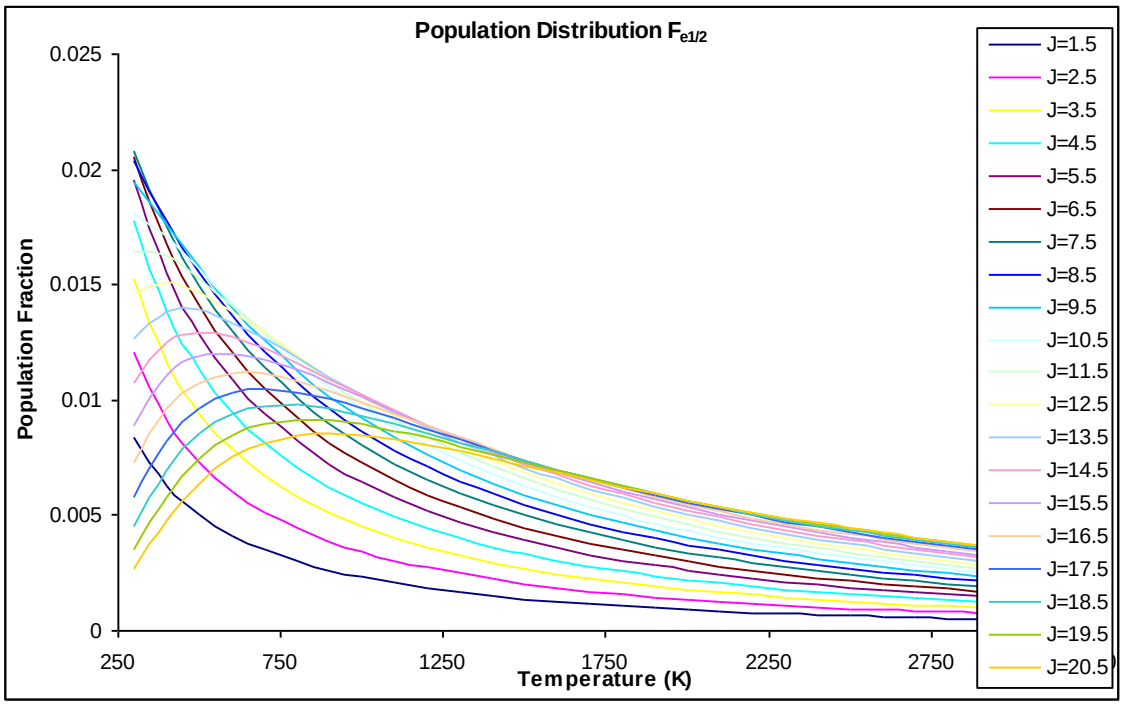

Figure 2.9: Population fraction as a function of temperature for the state $2\Pi_{1/2e}$ and for J between 1.5 and 20.5

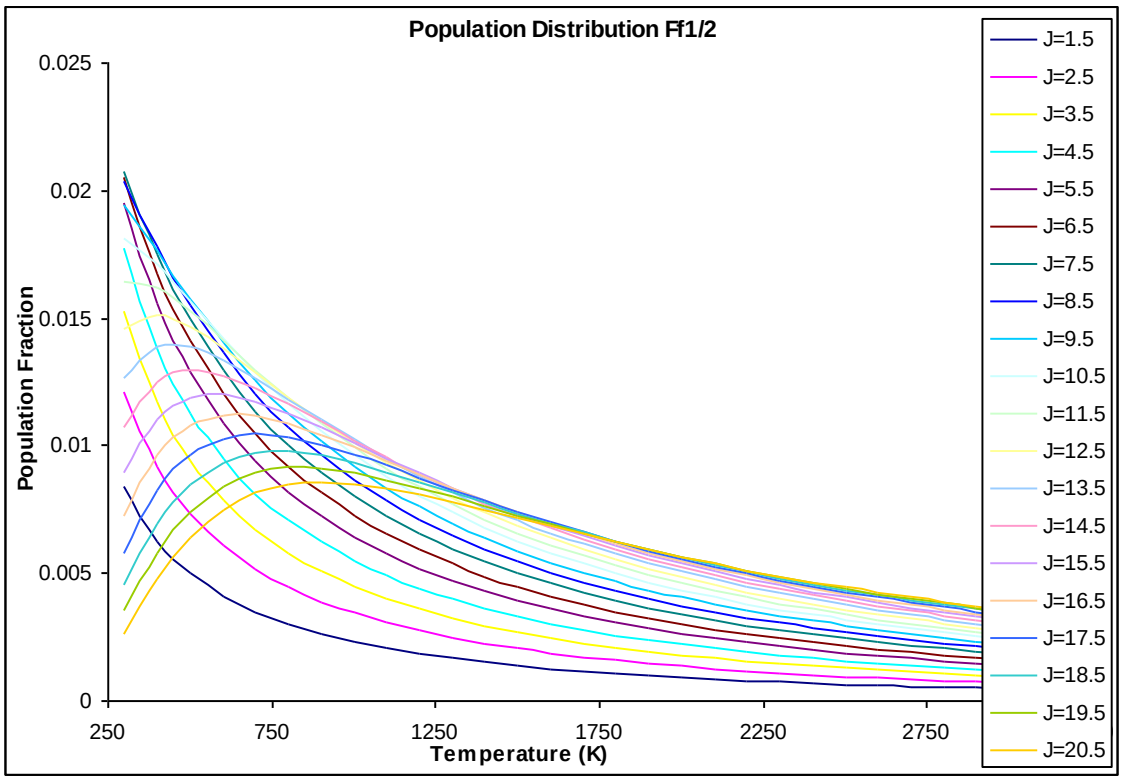

Figure 2.10: Population fraction as a function of temperature for the state $^2\Pi_{1/2f}$ and for J between 1.5 and 20.5

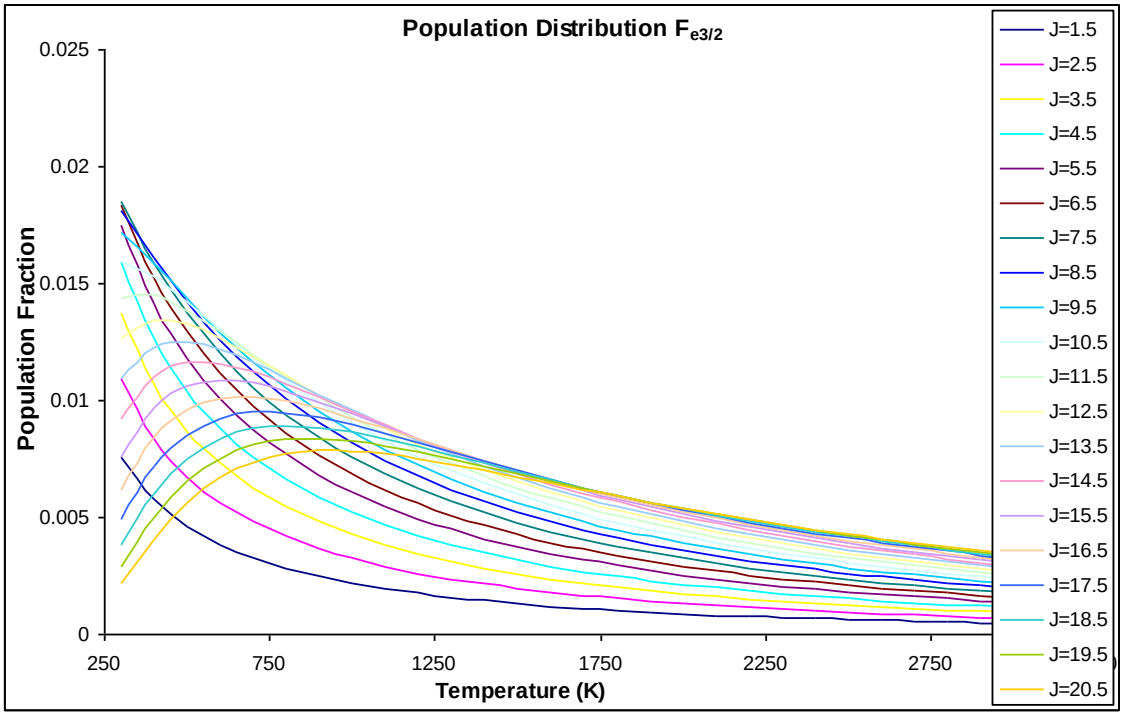

Figure 2.11: Population fraction as a function of temperature for the state $^2\Pi_{3/2e}$ for J between 1.5 and 20.5

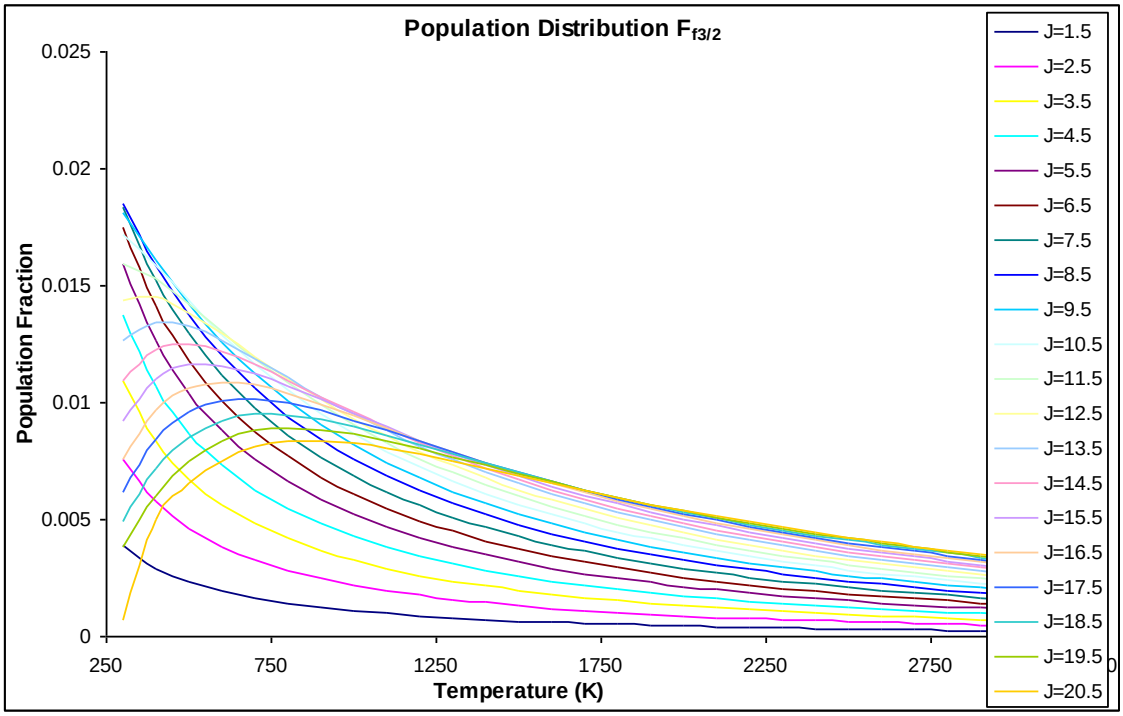

Figure 2.12: Population fraction as a function of temperature for the state $^2\Pi_{3/2f}$ for J between 1.5 and 20.5

Figures 2.13 and 2.14 show the population fraction of the NO molecule in various rovibrational levels as a function of temperature. The values used for these graphs were found in the LIFBASE software [51] available at the following address http://www.sri.com/psd/lifbase/. LIFBASE is a software which is a comprehensive database of the spectroscopic parameters of diatomic molecules such as NO: it contains the absolute rovibrational absorption and emission coefficients, the frequencies of the rovibrational transitions, their probabilities as well as the rotational radiative lifetimes and predissociation rates of diatomic molecules in the rovibrational states studied. This program also allows the simulation of absorption, emission and excitation spectra.

The population distribution as a function of temperature for the LIFBASE [51] and calculated [37] curves shows similar trends.

Minor differences were found between the calculated curves (figures 2.9, 2.10, 2.11 and 2.12) and the curves from LIFBASE [51] (figures 2.13 and 2.14).

For instance, no differences can be seen in the curves showing the population fraction as a function of temperature between the lambda-doubled levels e and f in the LIFBASE graphs (figures 2.13 and 2.14) while differences were obtained in the calculated curves especially as J increases.
Theoretically because of the lambda-doubling, there is an energy difference between the lambda doubled levels e and f so the population fraction should theoretically be different which is what was found in the calculated curves. However the energy difference between two corresponding lambda-doubled levels is very small which may be why the population fraction differences do not show on the LIFBASE graphs. The differences in the population fraction for two corresponding lambda-doubled levels may have been slightly overestimated in the calculated curves. The real population distribution over the lambda-doubled levels is probably in between the calculated and the LIFBASE graphs.
The differences between the spin-split levels (1/2 and 3/2) are a little more marked in the LIFBASE graphs than in the calculated graphs. This could come from differences in the calculation of the value of energy levels. However, the values are of the same order.

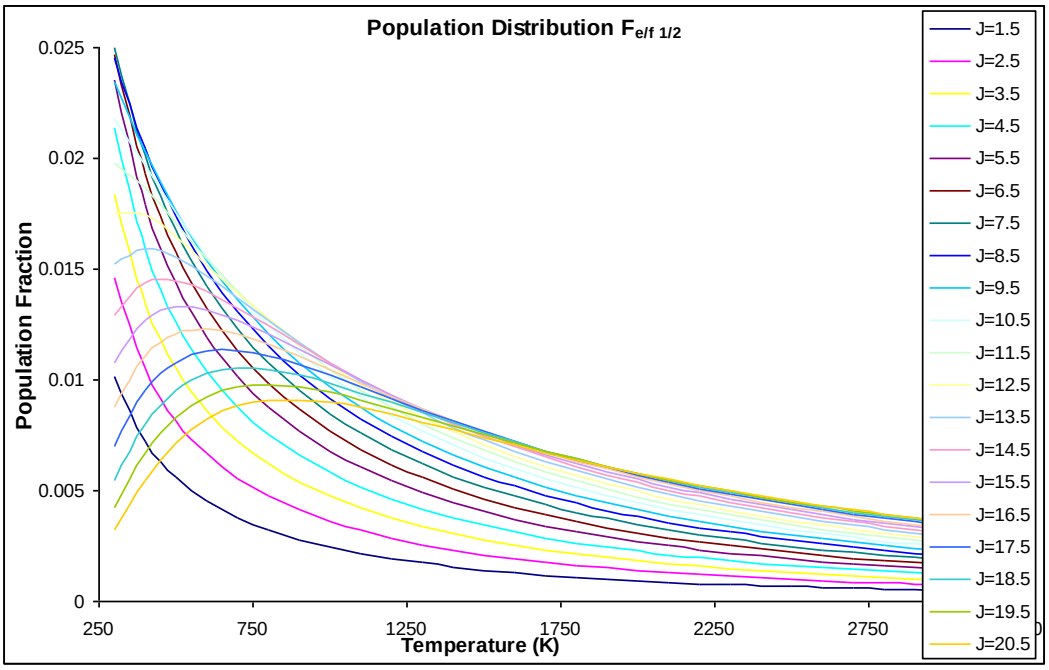

Figure 2.13: Population fraction as a function of temperature for the state $^2\Pi_{1/2}$ for J between 1.5 and 20.5

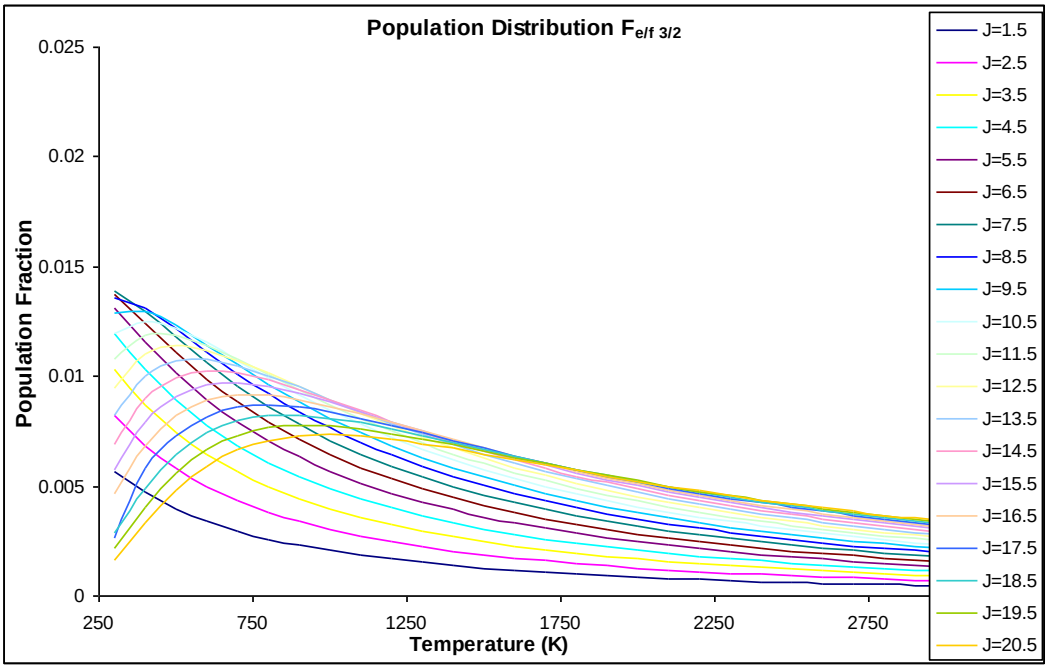

Figure 2.14: Population fraction as a function of temperature for the state $^2\Pi_{3/2}$ for J between 1.5 and 20.5

The $R_{11}+{}^{R}Q_{21}(9.5)$ line lies at 225.980 nm so it is free from interferences with O_2. The population decreases with increasing temperature over the range 300K – 3000K so there will not be any uncertainties on the value of the progress variable determined from the intensity of the fluorescence signal. The J number is sufficiently high so that the fluorescence signal should stay high enough over the temperature range probed.

Overlap fraction

We suppose the laser profile is Gaussian and concerning the line shape, we only consider Doppler broadening.

The line shape for Doppler broadening may be expressed as follow:

$$f_D(\nu-\nu_0)=\frac{1}{\alpha_D\sqrt{\pi}}\exp\left[-\frac{(\nu-\nu_0)^2}{\alpha_D^2}\right] \tag{2.30}$$

and with

$$\alpha_D=\nu_0\sqrt{\frac{2k_BT}{mc_v{}^2}} \tag{2.31}$$

where v represents the frequencies and v_0 is the nominal position of the absorption line considered, m is the mass per molecule (=molar mass/Avogadro number), c_v the speed of light and k_B the Boltzmann constant.
A variable which has a Gaussian distribution (= is normally distributed) has the following distribution:

$$f(x)=\frac{1}{\sigma_{st}\sqrt{2\pi}}\exp\left(-\frac{1}{2}\left(\frac{x-\mu}{\sigma_{st}}\right)^2\right) \tag{2.32}$$

μ is the mean i.e. in our case, it is the frequency at which the laser is tuned during the experiments. σ_{st} is the standard deviation of the distribution. In the case of a laser, we do not usually know the standard deviation but the Full Width at Half Maximum (*FWHM*).
In the case of the normal distribution, one has the relation:

$$FWHM=2\sqrt{-2\log\left(\frac{1}{2}\right)}\sigma_{st}\approx 2.3548\sigma_{st} \tag{2.33}$$

The FWHM of the laser signal used here assumes the value 0.1cm^{-1} according to the specifications of the laser used.

Both functions were normalised before the overlap factor was calculated.

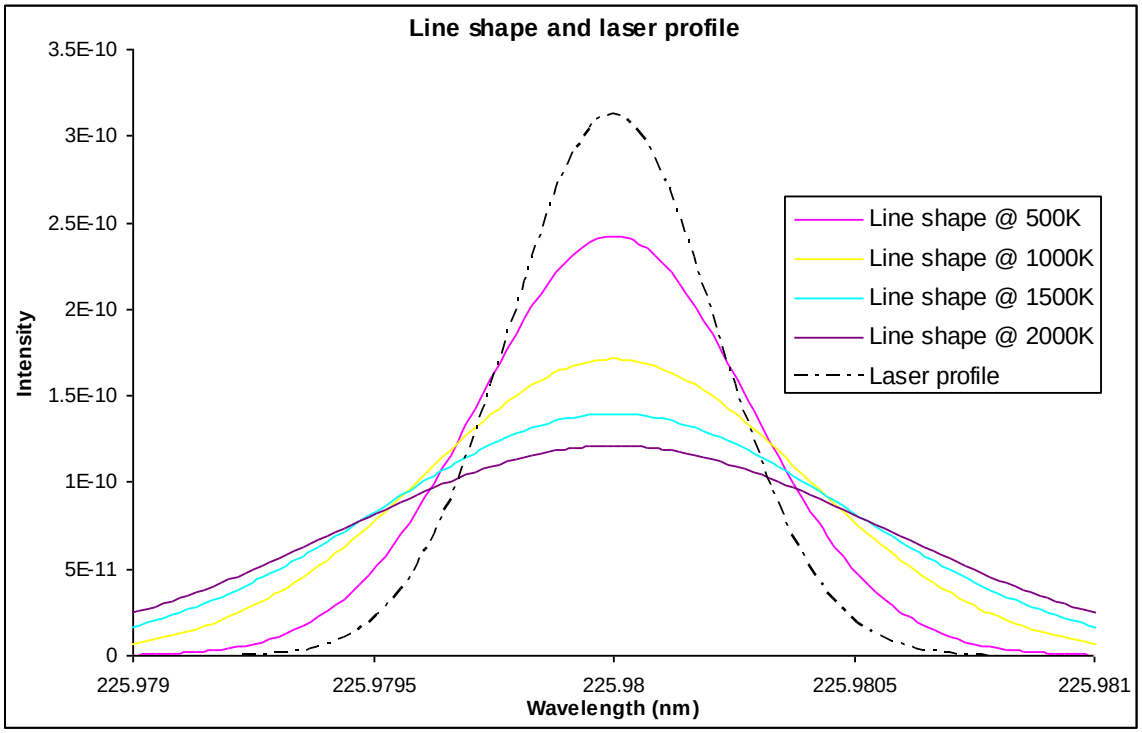

Figure 2.15: $R_{11}+{}^{R}Q_{21}(9.5)$ line shape as a function of temperature and laser profile at 225.980nm

The overlap factor was determined by integrating the product of the normalised line shape function by the laser profile function.

The overlap factor was arbitrarily given the value 1 at 300K.

Figure 2.16 shows the variation of the overlap factor as a function of temperature for the transition $R_{11}+{}^{R}Q_{21}(9.5)$ and the laser tuned at 225.980nm.

As could be expected, the overlap fraction decreases with temperature, going from 1 to 0.43 between 300K and 3000K. As the temperature increases the line corresponding to the transition $R_{11}+{}^{R}Q_{21}(9.5)$ becomes broader due to Doppler broadening. In other words, as the temperature increases, the NO molecules have a broader range of velocity available as a consequence their absorption line broadens. Increasing parts of the absorption line will not be excited any longer by the laser light whose profile is not temperature dependent.

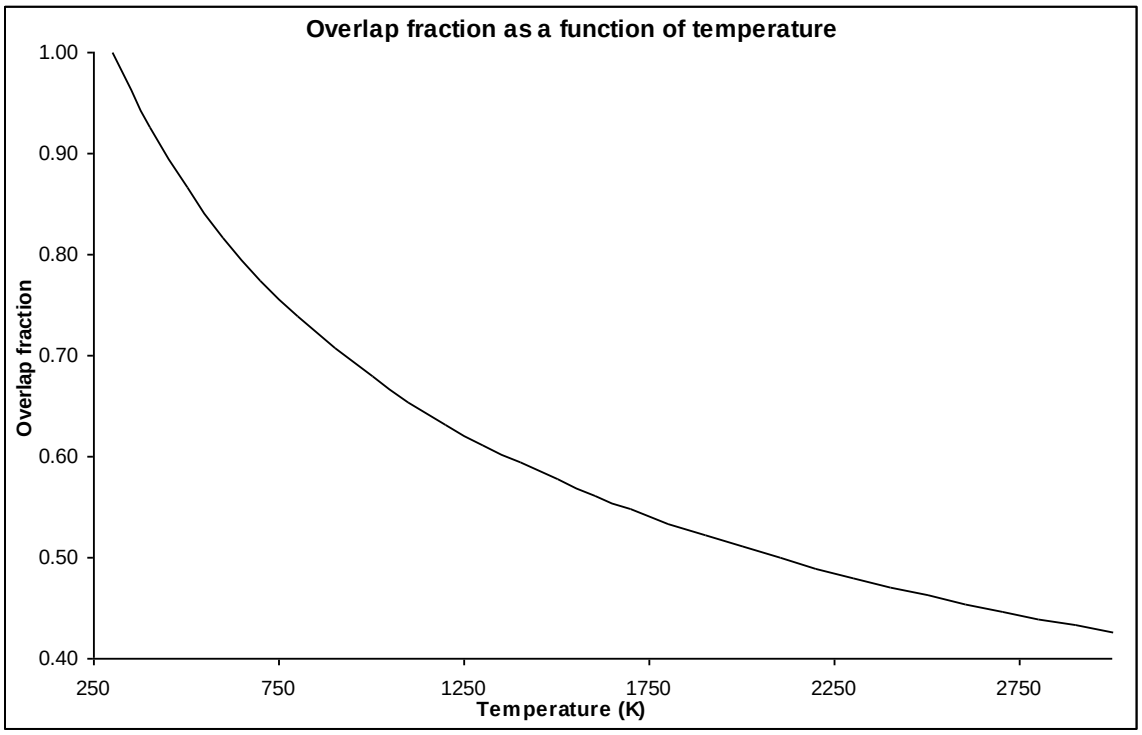

Figure 2.16: Overlap Factor between the transition $R_{11}+{}^{R}Q_{21}(9.5)$ and the laser tuned at 225.980nm as a function of temperature

Collisional quenching rate

Empirical equations to evaluate the variation of the collisional quenching rate as a function of temperature can be found in the literature [41].

The calculation of the collisional quenching rate consists in:

- calculating the expected concentrations of all expected species (for instance, using the Chemkin 4.1 software [15])
- calculating for each species the "thermally averaged electronic quenching cross-section" which may be temperature dependent. Equations for many perturbing species can be found in [41]
- with the help of the previous quenching cross-sections, calculating the total electronic quenching cross-section
- eventually calculating the quenching rate Q which is concentration (mole fraction), temperature and pressure dependent

The Chemkin 4.1 software [15] was used to determine the concentrations of the species present in premixed hydrogen/air flames as a function of temperature. The Chemkin 4.1 software [15] is a software which enables the incorporation of chemical kinetics into the simulation of reacting flows.

The species present in the flames studied here are:

- the reactants: H_2, O_2, N_2,
- the product: H_2O,
- the probed species which is seeded in the flames: NO
- intermediary species: H, O, OH, HO_2 & H_2O_2.

The Chemkin 4.1 software [15] is able to estimate their concentrations as a function of temperature.

According to the above mentioned article [41], each quenching species can be classified into one of four categories.

The first category corresponds to species which do not quench significantly the fluorescence signal. Their electronic quenching cross-section is ~0. This is the case for H_2.

The fourth category corresponds to species whose electronic quenching cross-section is not temperature dependent i.e. it is a constant. This is the case of O_2, OH, H, O, and NO. The electronic quenching cross-sections of O_2, OH, H, O, and NO are respectively 25.1, 82.0, 12.0, 32.0 and 43.0.

The second category corresponds to species whose electronic quenching cross-section is temperature dependent and for which the following equation applies [41]:

$$cross-section = C_0 + C_1 \exp\left(\frac{-C_2 T_R}{T}\right) + C_3 \exp\left(\frac{-C_4 T_r}{T}\right) \qquad (2.34)$$

in which C_0, C_1, C_2, C_3 and C_4 are constant for one species and T_r is a reference temperature which was chosen at 300K. N_2 belongs to this group. Its constants are C_0=0, C_1=0.88, C_2=4.8 C_3=3.1 and C_4=16.0.

The third category corresponds to species whose electronic quenching cross-section is temperature dependent as well and for which the following equations apply [41]:

$$cross-section = C_0\left\{(1+\eta)\exp(-\eta) + C_1\eta^{\frac{1}{3}}\gamma\left(\frac{5}{3},\eta\right)\right\} \tag{2.35}$$

and

$$\eta = C_2\left(\frac{T_r}{T}\right) + C_3\left(\frac{T_r}{T}\right)^2 \tag{2.36}$$

γ refers to the lower incomplete gamma function. H_2O belongs to this category. Its constants are C_0=28.2, C_1=3.39, C_2=0.15 and C_3=2.95.

The effects of HO_2 and H_2O_2 were neglected; their concentrations were too low (molar fraction ~10^{-6}) to have a significant effect, if any, on the quenching.

The total electronic quenching cross-section was calculated using [41]:

$$cross-section_{TOTAL} = \sum_p cross-section_p * \chi_p\left(1+\frac{m_{NO}}{m_p}\right)^{\frac{1}{2}} \tag{2.37}$$

in which $cross-section_p$ is the individual quenching cross-section of all quenching species, χ_p is the mole fraction of the species p and $\frac{m_{NO}}{m_p}$ is the ratio of the molecular masses of NO and the quenching species p.

As will be explained later in chapter 4 (section 4.1.2), it was not possible to directly compute our nitrogen diluted hydrogen/air flames with the Chemkin 4.1 software [15]. The following calculation refers to a hydrogen/air flame with an equivalence ratio of 0.35.

Figure 2.17 shows the variation of the total electronic quenching cross-section as a function of temperature.

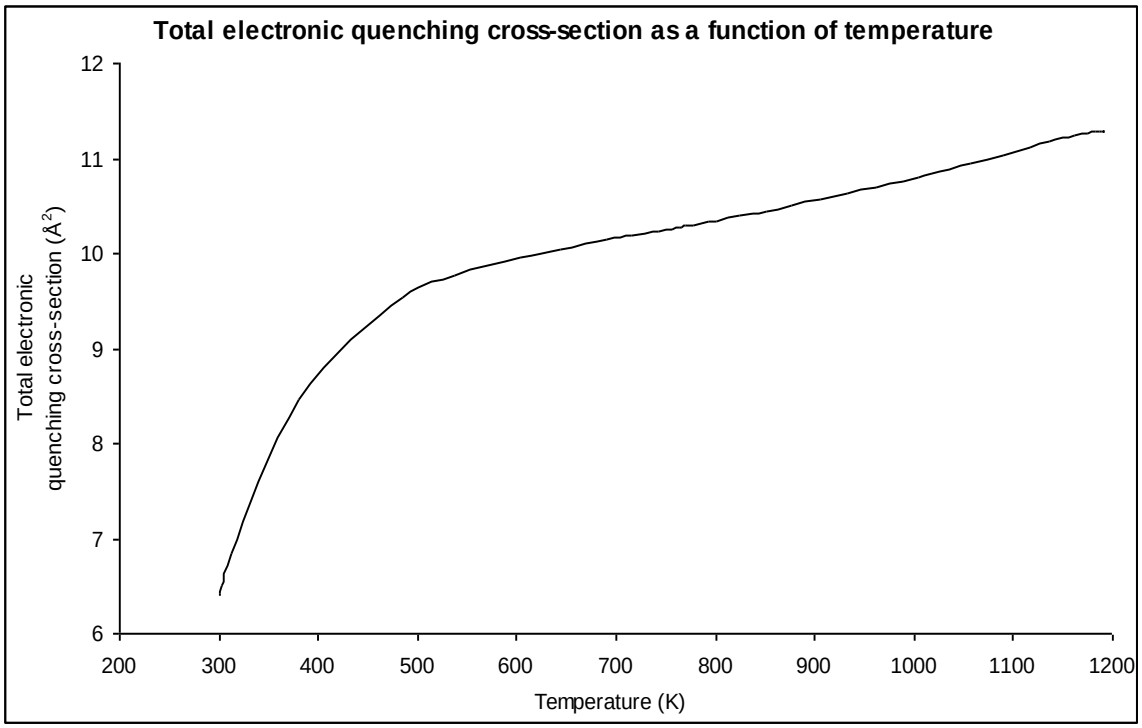

Figure 2.17: Variation of the total electronic quenching cross-section as a function of temperature

The total electronic quenching cross-section increases steeply between 300K and 500K and then keeps on increasing between 500K and 1200K. The main contributors to the total electronic quenching cross-section are (N_2,) O_2 and H_2O. They contribute to at least 99.5% of the total collisional quenching cross-section at all temperature.

Between 300K and 400K, O_2 is the main contributor to the total collisional quenching cross-section. It contributes to 99.8% of the total collisional quenching cross-section at 300K. Its contribution drops to 77.5% at 400K, 50% at ~980K and 42.4% at ~1200K.

H_2O contribution to the total collisional quenching cross-section increases steeply from 0% at 300K to 31.7% at 485K and then keeps increasing to reach 53.8% contribution at 1200K.

The steep rise in the value of the total electronic quenching cross-section between 300K and 500K is due to H_2O which is being produced and whose contribution to the total electronic quenching cross-section increases sharply and is not compensated by the consumption of O_2. From 400K/500K to 1200K, the total electronic quenching cross-section increases less because O_2 is being consumed and the rise of the contribution of H_2O to the total electronic quenching cross-section is less sharp.

The collisional quenching rate was calculated using the equations found in [41]:

$$Q = \sqrt{\frac{8k_BT}{\pi m_{NO}}} * \frac{P}{k_BT} * cross - \sec tion_{TOTAL} \qquad (2.38)$$

The term $\sqrt{\frac{8k_BT}{\pi m_{NO}}}$ (m.s^{-1}) is a measure of the velocity of the NO molecules. This term increases as $\sqrt{T}$ when T increases.

The term $\frac{P}{k_BT}$ (m^{-3}) correspond to the molecular density and decreases as $\frac{1}{T}$ when T increases.

Figure 2.18 shows the variation of the collisional quenching rate as a function of temperature for a premixed laminar hydrogen/air flame with an equivalence ratio of 0.35.

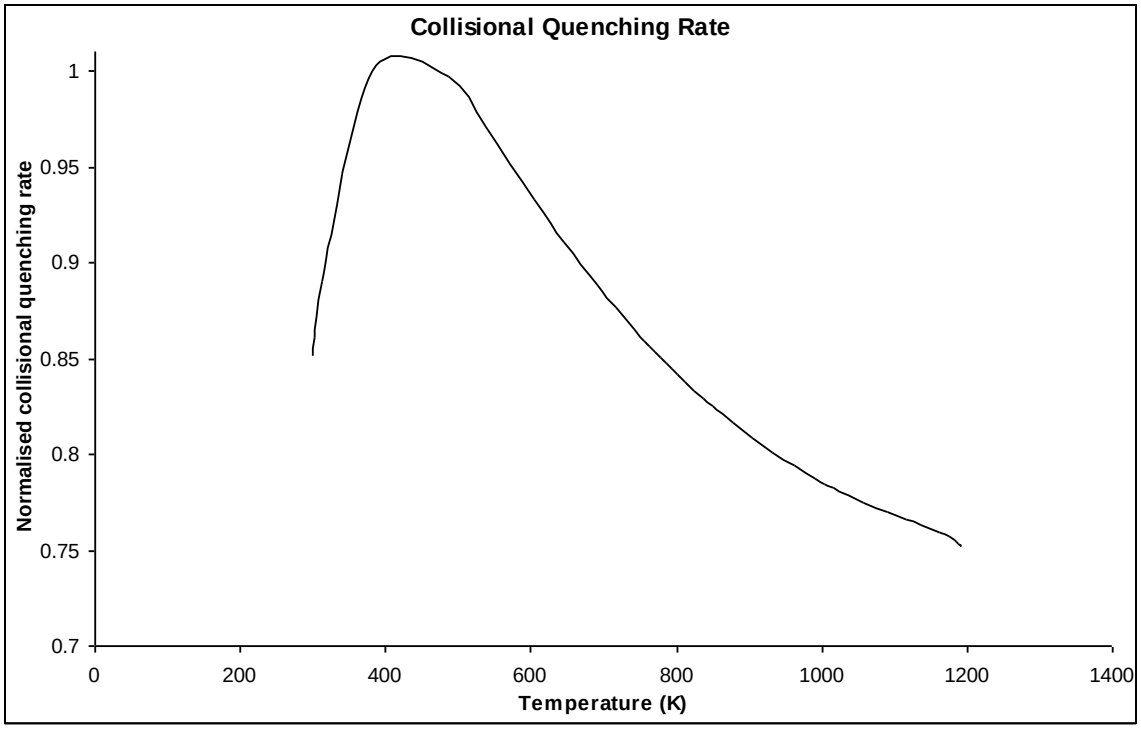

Figure 2.18: Variation of the normalised collisional quenching rate as a function of temperature for a premixed laminar hydrogen/air flame with an equivalence ratio of 0.35

The collisional quenching rate increases between 300K and 400K and then decreases between 400K and 1200K. The initial increase is due to the combination of the term $\sqrt{\frac{8k_BT}{\pi m_{NO}}}$ and the total electronic quenching cross-section which both increase, the latter of which increasing sharply as seen in figure 2.17, while the term $\frac{P}{k_BT}$ decreases. The decrease after 400K is due to the fact that after 400/500K the total electronic quenching cross-section increases as a function of temperature is not enough combined with the term $\sqrt{\frac{8k_BT}{\pi m_{NO}}}$ to compensate for the decrease of the term $\frac{P}{k_BT}$.

Expected behaviour of the NO-PLIF signal as a function of temperature

Following the equations given in [41], when A<<Q, which is the case here, the expected behaviour of the fluorescence signal follows the equation:

$$S_F = \frac{f_B * g}{\sqrt{\frac{8k_B * T}{\pi m_{NO}}} * \sigma_T} \tag{2.39}$$

in which σ_T is the total electronic quenching cross-section.

Figure 2.19 shows the expected behaviour of the NO-PLIF signal as a function of temperature following excitation of the $R_{11}+^{R}Q_{21}(9.5)$ transition line in a premixed laminar hydrogen/air flame of equivalence ratio 0.35.

The fluorescence signal was arbitrarily given the value 1 at 300K.

As can be seen in figure 2.19, the fluorescence signal is expected to decrease as the temperature increases.

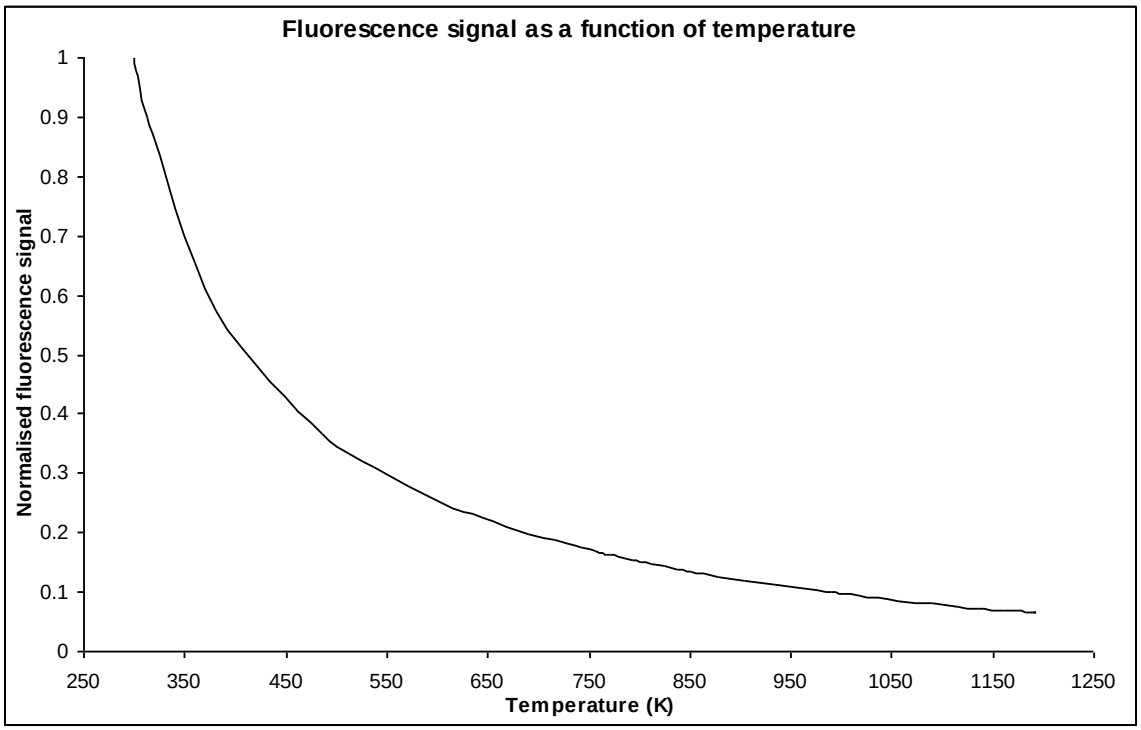

Figure 2.19: Expected variation of the fluorescence signal as a function of temperature

Figure 2.20 compares the progress variable calculated using the NO-PLIF signal and the progress variable calculated using the temperature i.e. using respectively the following equations:

$$c_{NO\_PLIF} = \frac{NO-PLIF - NO-PLIF_{unburnt}}{NO-PLIF_{burnt} - NO-PLIF_{unburnt}} \tag{2.40}$$

and

$$c_T = \frac{T - T_{unburnt}}{T_{burnt} - T_{unburnt}} \tag{2.41}$$

Ideally, if the two definitions for the progress variable were perfectly equivalent, one would obtain a straight line joining the points (0, 0) and (1, 1). As can be seen on the following graph, this is not the case. When using the definition using the NO-PLIF signal, the progress variable is overestimated.

Although it is expected that the trend observed for the particular flame studied here is similar to what happens in the flames experimentally investigated in this work and because it was not possible to obtain specific data for the flames used in this work, it

is not possible to theoretically calculate a correcting factor to account for the differences observed here.

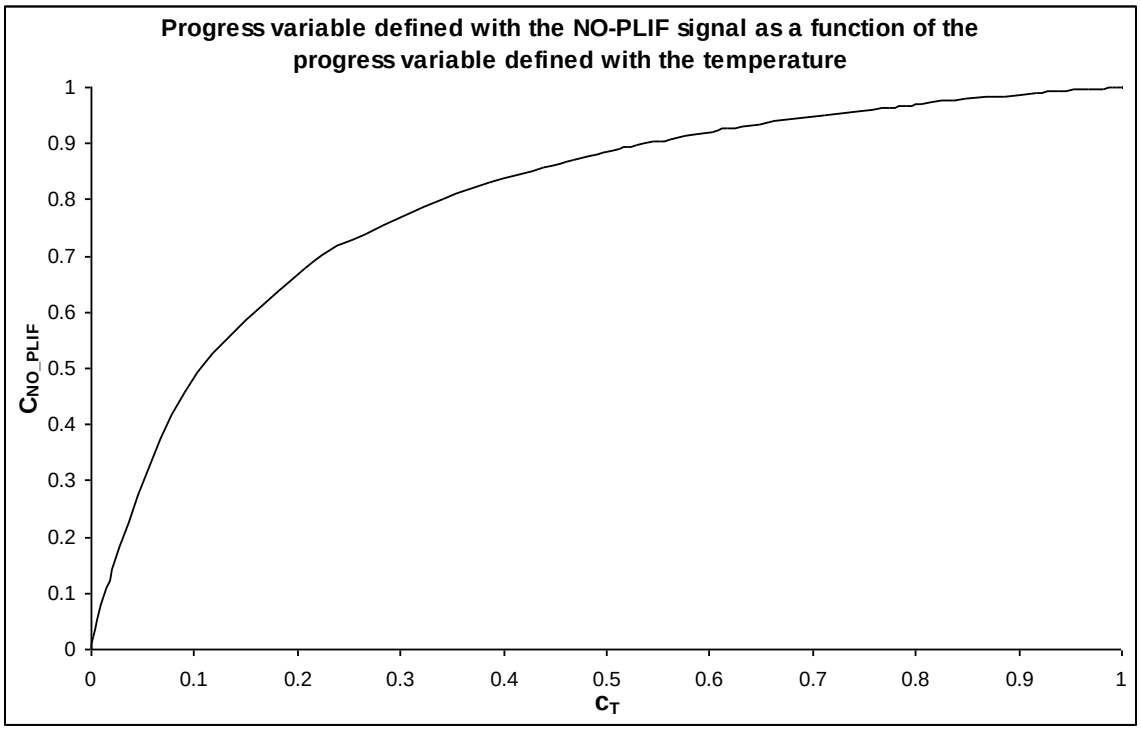

Figure 2.20: Curve comparing the progress variable calculated using the NO-PLIF signal and the progress variable calculated using the temperature

As is demonstrated above, in this work, the main difficulty in theoretically calibrating the NO-PLIF fluorescence signal as a function of temperature was the determination of the precise concentration of the species present in the flame as a function of temperature, as the Chemkin 4.1 software [15] was not able to simulate the particular flames studied here (for more details see section 4.1.2). However, it should be possible to overcome this difficulty, in the future, by choosing to study more conventional flames i.e. less nitrogen-diluted hydrogen-air flames or hydrocarbon flames which could be simulated using, for instance, the Chemkin 4.1 software [15]. Of course, an experimental calibration could theoretically permit the calibration of the fluorescence signal with temperature. However, calibrating the signal at high temperature is challenging and an experimental calibration was not possible altogether in the present work. As a consequence of these issues, it was not possible to directly measure the temperature with the help of the fluorescence signal. However, although the definitions of the progress variable (2.40 & 2.41) are different, one can observe in figure 2.20 that an isoscalar surface defined with the traditional definition of the

progress variable (2.41) is also an isoscalar surface with the definition used here (2.40) and conversely. The localisation of isoscalar surfaces will, hence, be possible. Various isoscalar surfaces were studied, as will be explained later (see chapter V) in order to identify the consequences of the choice of the isoscalar surface on the results.

2.2.4 Calibration of the dye laser grating

As explained earlier in section 2.2.2, the dye laser (LAMBDA PHYSIK dye laser) grating was calibrated against spectra created using the LIFSim software [46].

In order to identify the transition $R_{11}+{}^{R}Q_{21}(9.5)$, we scanned a region of the NO spectrum between 225.880 and 226.110 nm in 0.005 nm steps in a test cell containing 1000ppm NO in nitrogen at room temperature.

The fluorescence signal (in counts per pixel) was recorded as a function of the excitation wavelength (red curve in figure 2.21).

The green curve in figure 2.21 corresponds to the red curve shifted by -0.01nm.

The black curve in figure 2.21 was obtained using the LIFSim software [46] also between 225.880 and 226.110.

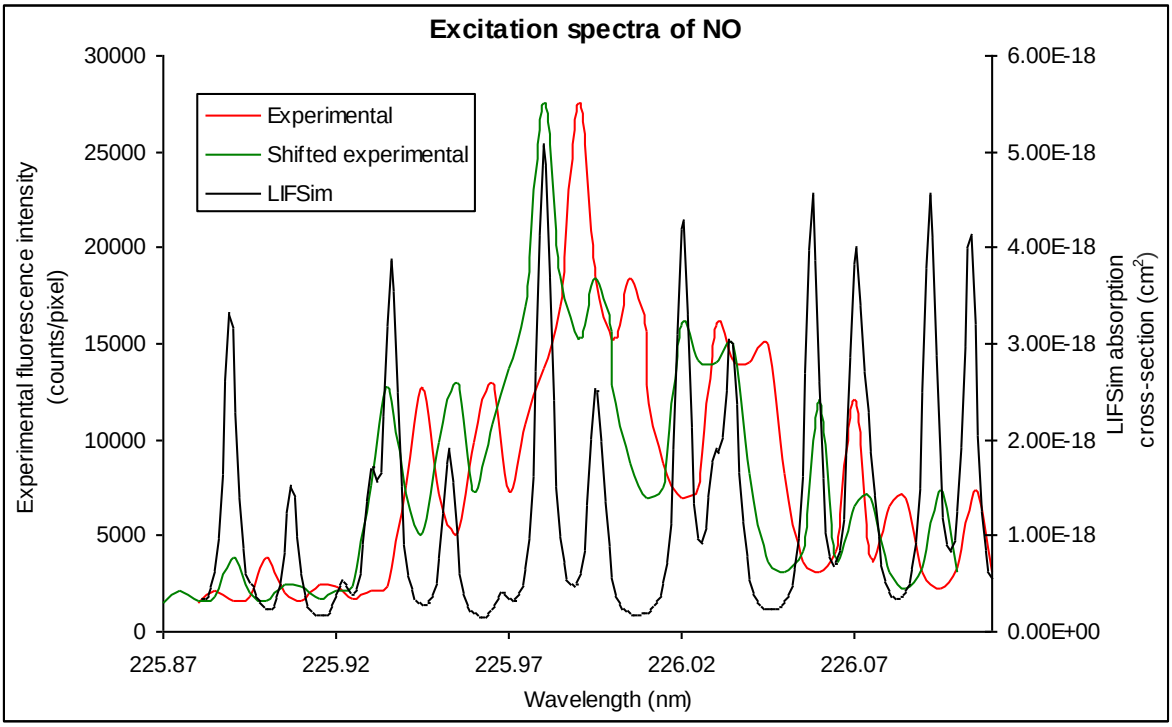

Figure 2.21: First calibration spectra

It was also possible to obtain from the LIFSim software [46] a list of the transitions present in the spectrum and their wavelength.

44272.105	225.875862	0.481023	S21(7.5)
44269.480	225.889256	0.643411	Q21(11.5)
44269.445	225.889435	0.634089	R1(11.5)
44268.152	225.896033	0.063622	Q2(22.5)
44265.996	225.907037	0.086180	P21(17.5)
44265.949	225.907276	0.488787	Q1(17.5)
44263.102	225.921810	0.149184	R2(16.5)
44261.453	225.930224	0.532530	S21(6.5)
44260.293	225.936146	0.747248	Q21(10.5)
44260.262	225.936305	0.699434	R1(10.5)
44257.070	225.952598	0.112156	P21(16.5)
44257.027	225.952817	0.605716	Q1(16.5)
44254.043	225.968055	0.088034	Q2(21.5)
44251.727	225.979883	0.833685	Q21(9.5)
44251.699	225.980023	0.741312	R1(9.5)
44251.426	225.981419	0.528677	S21(5.5)
44248.762	225.995025	0.142525	P21(15.5)
44248.719	225.995244	0.732690	Q1(15.5)
44248.312	225.997319	0.180799	R2(15.5)
44243.781	226.020465	0.905858	Q21(8.5)
44243.758	226.020584	0.765261	R1(8.5)
44241.074	226.034295	0.177485	P21(14.5)
44241.035	226.034494	0.868209	Q1(14.5)
44240.480	226.037328	0.118395	Q2(20.5)
44236.461	226.057867	0.954110	Q21(7.5)
44236.441	226.057967	0.766142	R1(7.5)
44234.066	226.070104	0.212881	R2(14.5)
44234.000	226.070444	0.214894	P21(13.5)
44233.961	226.070643	1.000000	Q1(13.5)
44232.809	226.076533	0.063209	P1(22.5)
44229.766	226.092087	0.928858	Q21(6.5)
44229.746	226.092186	0.708820	R1(6.5)
44227.512	226.103609	0.150064	Q1(12.5)

Table 2.5: List of the transitions shown in the LIFSim curve between 225.880 and 226.100 nm

Some transitions always appear together:

- $P_{22}(J'')$ and ${}^{P}Q_{12}(J'')$,
- $Q_{22}(J'')$ and ${}^{Q}R_{12}(J'')$,
- $Q_{11}(J'')$ and ${}^{Q}P_{21}(J'')$,
- $R_{11}(J'')$ and ${}^{R}Q_{21}(J'')$.

The most intense signal in the LIFSim curve (black curve in figure 2.21) is due to $R_{11}(9.5)+{}^{R}Q_{21}(9.5)$ expected to be at around 225.980 nm. Assuming the most intense signal in our experimental spectrum is also due to those transitions, then, our observed shift would be of 0.01nm since the most intense signal in our spectrum appears around 225.990 nm.

As can be seen in figure 2.21, the spectra match each other:

- next signal at respectively 226.005 and 225.995 for the experimental spectrum (red) and the LIFSim spectrum (black),
- then at 226.030 and 226.020 nm,
- then at 226.045 and 226.034 nm

etc…

The positions of the transitions seem to fit. The relative intensity of the signals, however, is different in the two spectra.

This may have been due to the frequency doubling crystal. It did not seem to move with the grating as a consequence the laser signal was most intense at one particular wavelength – where the angle of the crystal and the position of the grating corresponded- and its power decreased on each side of it. (In this case, it seemed to be around 225.985 nm). This issue was overcome by manually tuning the frequency doubling crystal at the right position during the experiments.

The second calibration curve was obtained by scanning a region of the NO-spectrum between 225.900 and 226.000 nm in 0.0025 nm steps in a test cell containing 1000ppm NO in nitrogen at room temperature.

In the previous calibration, we supposed a shift of 0.01nm between the experimental spectrum (red curve in figure 2.21) and the theoretical spectrum (black curve in figure 2.21). So in the second calibration, the spectrum obtained with the LIFSim software [46] between 225.890 and 225.990 nm was compared with the second experimental calibration curve.

Figure 2.22 shows that there is a very good agreement between the simulated spectrum (black curve) and the experimental spectrum (red curve) when the experimental curve (red curve) is shifted by -0.012 nm (green curve).

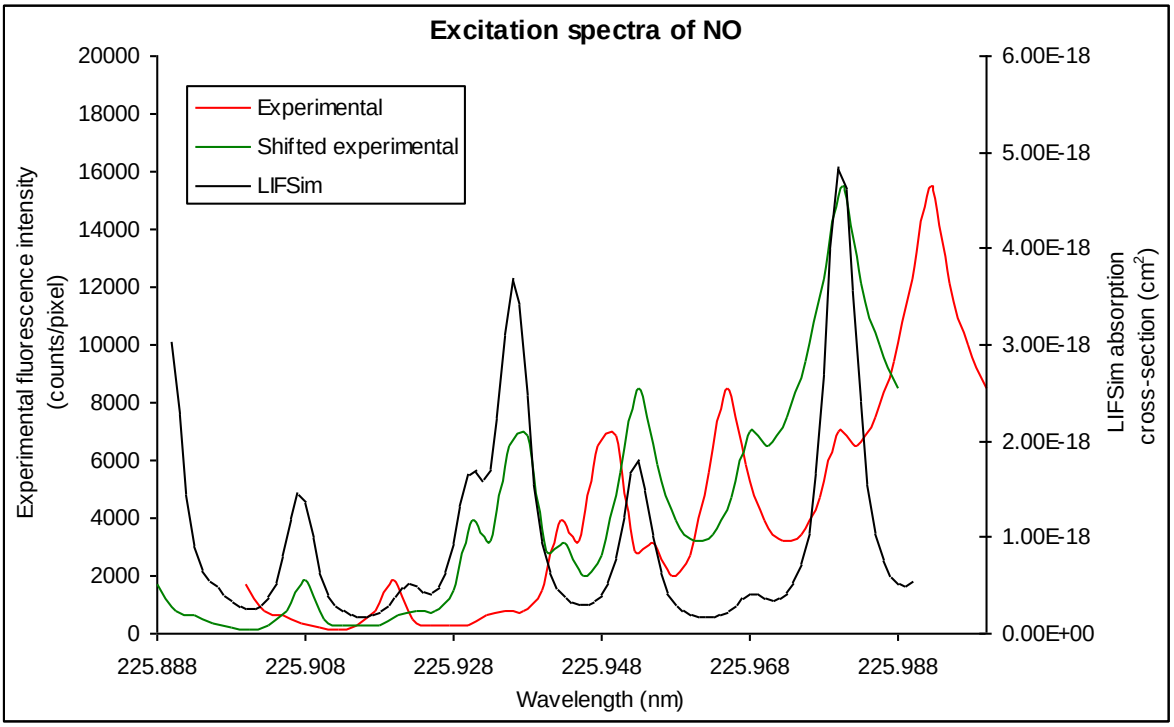

Figure 2.22: Second calibration spectra

44251.426	225.981419	0.629175	S21(5.5)
44261.453	225.930224	0.662874	S21(6.5)
44251.727	225.979883	1.000000	Q21(9.5)
44251.699	225.980023	0.888545	R1(9.5)
44260.293	225.936146	0.932048	Q21(10.5)
44260.262	225.936305	0.872357	R1(10.5)
44269.480	225.889256	0.317556	Q21(11.5)
44269.445	225.889435	0.335254	R1(11.5)
44248.719	225.995244	0.076378	Q1(15.5)
44257.070	225.952598	0.139286	P21(16.5)
44263.102	225.921810	0.185220	R2(16.5)
44257.027	225.952817	0.752136	Q1(16.5)
44265.996	225.907037	0.105910	P21(17.5)
44265.949	225.907276	0.601016	Q1(17.5)
44254.043	225.968055	0.108468	Q2(21.5)
44268.152	225.896033	0.074615	Q2(22.5)

Table 2.6: List of the transitions shown in the LIFSim spectrum between 225.890 and 225.990 nm

The dye laser grating was further calibrated against a spectrum obtained with the LIFSim software [46] to determine exactly the position of the transition $R_{11}+{}^{R}Q_{21}(9.5)$.

Again, the experiments were conducted in the test cell containing 1000ppm NO in Nitrogen at room temperature.

We scanned between 225.980 and 226.000 nm in 0.001 nm steps.

The experimental spectrum (red curve in figure 2.23) was compared with the LIFSim spectrum of the region [225.970 nm, 225.990nm].

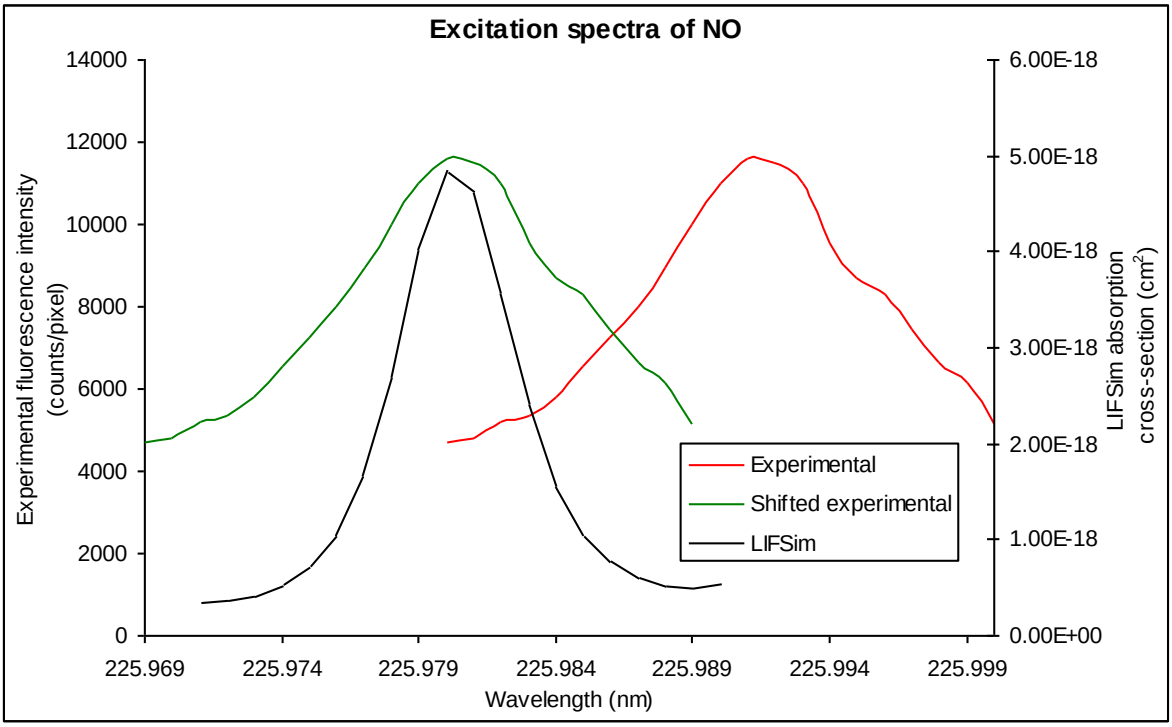

Figure 2.23: Third calibration spectra for the dye laser grating

44251.727	225.979883	1.000000	Q21(9.5)
44251.699	225.980023	0.889360	R1(9.5)

Table 2.7: List of the transitions shown in the LIFSim spectrum between 225.970 and 225.990 nm

The green curve corresponds to the experimental curve (red curve) shifted by 0.011nm. As a consequence, the line $R_{11}+{}^{R}Q_{21}(9.5)$ lay experimentally at 225.991nm (unshifted).

The transition $R_{11}+{}^{R}Q_{21}(9.5)$ was eventually chosen for different reasons. Its behaviour with temperature is quite simple and quite suitable to determine the progress variable. The NO-fluorescence emitted after excitation of the line $R_{11}+{}^{R}Q_{21}(9.5)$ is quite strong compared to other transitions. It lies in a region free from interferences with O_2.

2.3 Particle Image Velocimetry (PIV)

Because PIV allows instantaneous three-dimensional measurements of the velocity fields in increasingly complex experiments in a rather straightforward manner, it has been developed, used and reviewed in numerous articles and books.

An introduction to particle image velocimetry – its principles and governing equations - was given by Westerweel [22] while Stanislas et al. focused on its practical aspects [52] and gave guidelines on the formation of the laser sheet for the experiments.

The seeding was reviewed by Melling [53]. He particularly studied the tracking capability of seeding particles as a function of their sizes. Part of the article is dedicated to the generation of those particles and their seeding. He also reviewed the different sorts of particles which have been used in previous studies for both liquid and gas flows and their characteristics.

Three-dimensional PIV systems, including stereoscopic PIV and holographic PIV, were reviewed by Hinsch [54].

Effects of distortion were studied by Soloff et al. [55]. They particularly reviewed the sources of inaccuracies in PIV measurements and described the way to account for them especially through careful calibration of the experiments.

Stereoscopic PIV was more particularly referenced by Prasad [56] and by Willert [57]. Prasad [56] reviewed the different eligible configurations, compared the different possible ways of reconstructing the information and gave a specific error analysis for each.

Specific experimental error analyses were given by Lawson et al. [58] and [59].

The following sections, which will concentrate on the optimisation of the PIV technique with regard to our experiments, will give a more thorough description of these data and an explanation of the experimental choices made.

2.3.1 Principle

As explained in 2.1.2.2, in classical Particle Image Velocimetry (2D-PIV), a laser sheet is directed along a plane in the flow. The laser source is pulsed repeatedly and the light scattered by the illuminated particles are recorded. With the knowledge of

the period of the pulses, the velocity can be determined using the displacement of the particles [22]:

$$D(X;t,t') = \int_{t}^{t'} v(X(t),t)dt \tag{2.18}$$

With *v(X(t),t)* the velocity of the tracer particles, *D(X;t,t')* their displacement during the time interval [t,t'].

In the case of ideal tracer particles [53] i.e. particles that follow the motion of the fluid, do not alter the flow or the fluid properties and do not interact with each other, the velocity of particle i, v_i, is equal to the local fluid velocity *u(X,t)*.

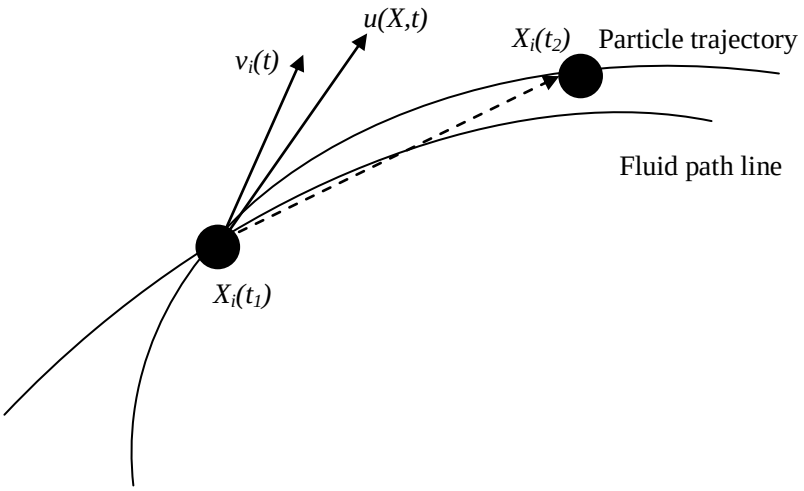

Figure 2.24: Sketch of the PIV principle

In fact, *v* is an approximation of *u* because *v* is an average velocity along the trajectory over a time Δt but the error is considered to be negligible when the spatial and temporal scales of the flow are large with respect to the spatial resolution, the exposure time delay and the dynamics of the tracer particles.

2.3.2 Seeding

The tracking capability of the tracer particles [53] depends on their shape, their diameter, their density as well as the fluid density and the fluid viscosity. A compromise has to be found concerning the particle size: the smaller the particle size

the more adequate is the tracer response of the particles in the fluid but the larger the particle size the higher the signal-to-noise ratio of the scattered light signal. Seeding particles should also possibly be non-toxic, non-corrosive, non-abrasive, non-volatile and chemically inert. Ideally, the particle size distribution should be monodisperse. It is possible to seed gas flows either with liquid droplets or solid particles.

Liquid droplet		Solid particle	
Advantages	Drawbacks	Advantages	Drawbacks
Steadier production rate	Can form liquid films on windows in internal flows → loss of signal	May be used at high concentration	At high concentration → tendency for coagulation
Spherical shape		Consequences of solid particle deposit less serious than for liquid deposit	Beam attenuations as a consequence of solid particle deposits
Information on the refractive index more readily available			

Table 2.8: Liquid droplet vs solid particles for seeding in fluid flows

Ideally, the particle concentration should be sufficient and stable, the particle should be distributed uniformly and coagulation and deposition should be avoided.

The seeding concentration must be high enough to match the smallest length scale of the spatial variations of *D*.

However, the seeding concentration must not be too high because it is not possible to determine the tracer particle pairs if the distance between the tracer particles is larger than the displacement of the paired particles.

In the present work, it was chosen to use solid particles because they would interact less with the reacting flow and are easier to implement. ZrO_2 particles were used as seeding particles. The particles were supplied by Goodfellow Cambridge Limited. The zirconia particles were stabilised with 5.4 % yttria. Their mean particle size was comprised between 0.1 and 2 µm. The density of the particles was 5.9 $g.cm^{-3}$. Their melting point is 2700°C. So they were quite suitable for the experiments in the present work.

Before use, the particles were kept in an oven at ~100°C so as to prevent their coagulation.

The yttria-stabilised zirconia particles were supplied to the gas flow via the seeder pictured below.

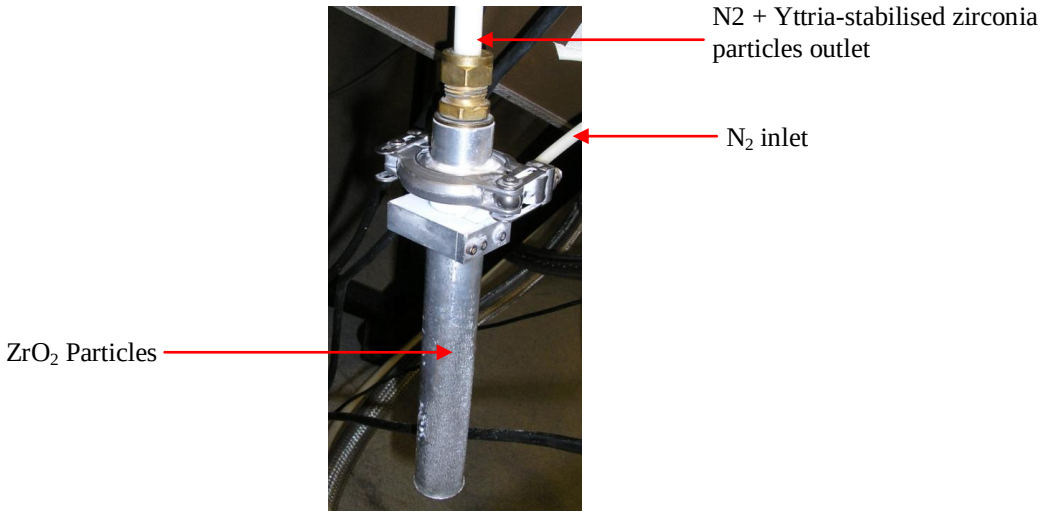

Figure 2.25: The seeder

The seeder consists of a metallic cylinder with a nylon tube on its side acting as an inlet for nitrogen and another nylon tube on top acting as an outlet for the particles and nitrogen. The concentration of the particles was controlled by the nitrogen flow. The nitrogen flow could be varied with a flow-regulating valve. The concentration was experimentally determined so that it was uniform and it allowed maximum resolution of the velocity and no uncertainties on the pairing of the particles.

In the present work, coagulation of the particles did not occur and neither was the deposition of the particles an issue.

2.3.3 Limitations of two-dimensional PIV systems

In classical 2D-PIV, two pulsed images can be recorded on a single frame. The distance between paired particles can be evaluated and thus the magnitude of the velocity known but there remains a difficulty to determine the direction of the vector which is usually called *the 180^0 ambiguity*. To remedy this problem, the images can be recorded on separate frames.

With the 2D-PIV technique, only the in-plane components of the velocity can be determined, moreover those in-plane components are slightly incorrect due to the displacement of the particle along the *z*-axis, error called the perspective error [58].

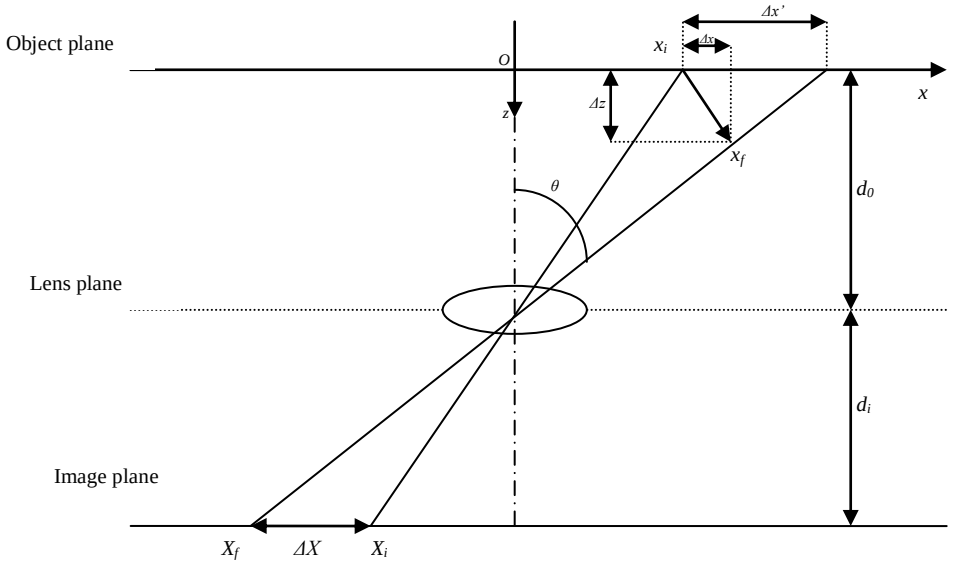

Figure 2.26: Sketch of the perspective error [58]

Let us consider a particle with initial position $x_i=(x,y,0)$. The image of the particle is initially at $X_i=(-M_n x,-M_n y,0)$ where M_n is the nominal magnification and is equal to d_i/d_0. When the particle moves to the position $x_f=(x+\Delta x, y+\Delta y, z+\Delta z)$, the image of the particle moves to the position $X_f=(-M_f(x+\Delta x), -M_f(y+\Delta y),0)$ with $M_f=d_i/(d_0-\Delta z)$ Thus the resulting image displacement is:

$$\Delta X = X_f - X_i = \left(-M_n \frac{\Delta x + x\Delta z / d_0}{1-\Delta z / d_0}, -M_n \frac{\Delta y + y\Delta z / d_0}{1-\Delta z / d_0}, 0 \right) \qquad (2.42)$$

which leads to an apparent in-plane displacement of $\Delta x' = \frac{\Delta X}{-M_n}$ which is not the real in-plane displacement. The perspective error i.e. the relative error between the real and the apparent in-plane error ε is:

$$\varepsilon = \left(\frac{\Delta z \tan\theta_x}{\Delta x}, \frac{\Delta z \tan\theta_y}{\Delta y} \right) \qquad (2.43)$$

with θ_x and θ_y are projections of θ on the *x*-*z* and *y*-*z* planes.

To remedy this problem that is to obtain the correct in-plane displacement and to gain the out-of-plane component of the velocity, other PIV configurations were developed.

Hinsch proposed [54] a classification which labels the measurement techniques as (k,l,m) where k indicates the number of velocity components measured ($1 \leq k \leq 3$), l the number of spatial dimensions of the measurement domain($0 \leq k \leq 3$) and m indicates if it is an instantaneous (=0) or continuous (=1) time recording. Classical PIV is usually a (2,2,0) technique. Here, the goal was to implement a (3, 2, 0) technique. As a consequence, classical PIV could not be used. Instead, a three-dimensional technique had to be used.

2.3.4 Three-dimensional Particle Image Velocimetry (3D-PIV)

The most direct extension of the previous method in three dimensions is to scan the sheet in depth. The scanning time and sheet separation depend on the temporal and spatial scales of the flow. The laser sheet has to be directed so that the main flow direction falls in the plane in order to avoid too great a number of unpaired particle images which would decrease the signal-to-noise ratio. Another way to get the third component of the particles velocity is to infer from the brightness of the particle image its depth coordinate.

However, Stereoscopic PIV seems to be the more commonly used method to measure the three components of the velocity.

Stereoscopic PIV uses two cameras to obtain depth-perception, but still measures on a planar domain therefore it is a (3, 2, 0).

The two most commonly used stereoscopic PIV configurations are the translation systems/lateral displacement system and the rotational systems/angular displacement system which are described in the following sections.

2.3.4.1 Lateral displacement system

In the lateral displacement system, the axes of both cameras are parallel to each other and both orthogonal to the light sheet. (see figure 2.27)

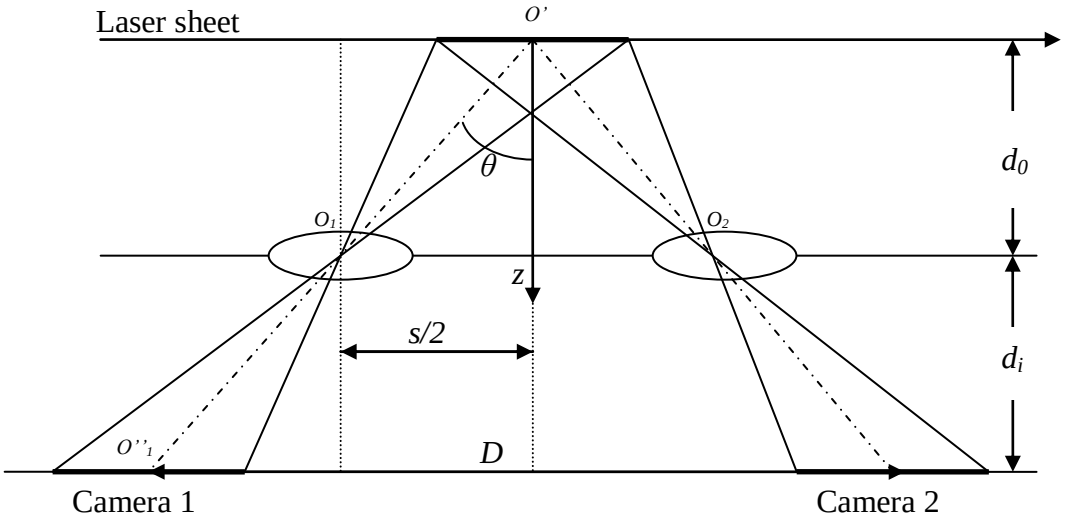

Figure 2.27: Sketch of the SPIV arrangement in the lateral displacement system

The true particle displacement and the apparent displacements measured by cameras 1 and 2 are related as follow [56]:

$$\Delta z = \frac{-d_0\left(\Delta X_1 - \Delta X_2\right)}{M_n S - \left(\Delta X_1 - \Delta X_2\right)} \tag{2.44}$$

$$\Delta x = \frac{\Delta X_1\left(x - s/2\right) - \Delta X_2\left(x + s/2\right)}{M_n S - \left(\Delta X_1 - \Delta X_2\right)} \tag{2.45}$$

$$\Delta y = \frac{-y\Delta z}{d_0} + \frac{\Delta Y_1 + \Delta Y_2}{2M_n}\left[\frac{\Delta z}{d_0} - 1\right] \tag{2.46}$$

Translation system	
Advantages	Drawbacks
Simplicity	Small "common area"
Uniform magnification	Upper limit to θ
Good particle image quality	
Good image focus	
Two views readily superposable	
Spatial resolution of the combined views identical to that of the two individual views	

Table 2.9: Table of the advantages and drawbacks of the lateral displacement system

The angle θ has to be kept under a limit value because if the lenses are separated by too large a value for a given d_o, the performance of the lenses degrades. There is no longer such a restriction in the angular displacement system.

The uncertainties in the calculated displacement are usually considered to be consequences of the uncertainties in the geometric parameters of the stereocameras. This includes uncertainties arising from the interrogation of the PIV photograph ($\sigma_{\Delta X_1}$, $\sigma_{\Delta X_2}$, $\sigma_{\Delta Y_1}$, $\sigma_{\Delta Y_2}$) and uncertainties due to errors in measuring the distance in the stereocamera.

In the case of the translation system, considering only the uncertainties resulting from PIV interrogation errors and assuming that $\sigma_{\Delta X_1} = \sigma_{\Delta X_2} = \sigma_{\Delta Y_1} = \sigma_{\Delta Y_2} = \sigma_{\Delta X}$ and $x=0$ and $y=0$, we obtain the following relations:

$$\sigma_{\Delta z} \approx \sqrt{2}\left[\frac{d_0}{M_n S}\right]\sigma_{\Delta X} \tag{2.47}$$

$$\sigma_{\Delta x} \approx \frac{1}{\sqrt{2}}\left[\frac{1}{M_n}\right]\sigma_{\Delta X} \tag{2.48}$$

$$\sigma_{\Delta y} \approx \frac{1}{\sqrt{2}}\left[\frac{1}{M_n}\right]\sigma_{\Delta X} \tag{2.49}$$

so that the relative error in the out-of-plane component is:

$$\frac{\sigma_{\Delta z}}{\sigma_{\Delta x}} = \frac{\sigma_{\Delta z}}{\sigma_{\Delta y}} = 2\frac{d_0}{s} = \frac{1}{\tan\theta} \tag{2.50}$$

2.3.4.2 Angular displacement system

In the angular displacement system, the two camera axes are not parallel to each other but rotated in a way that the two axes intersect the object plane at the system axis [56].

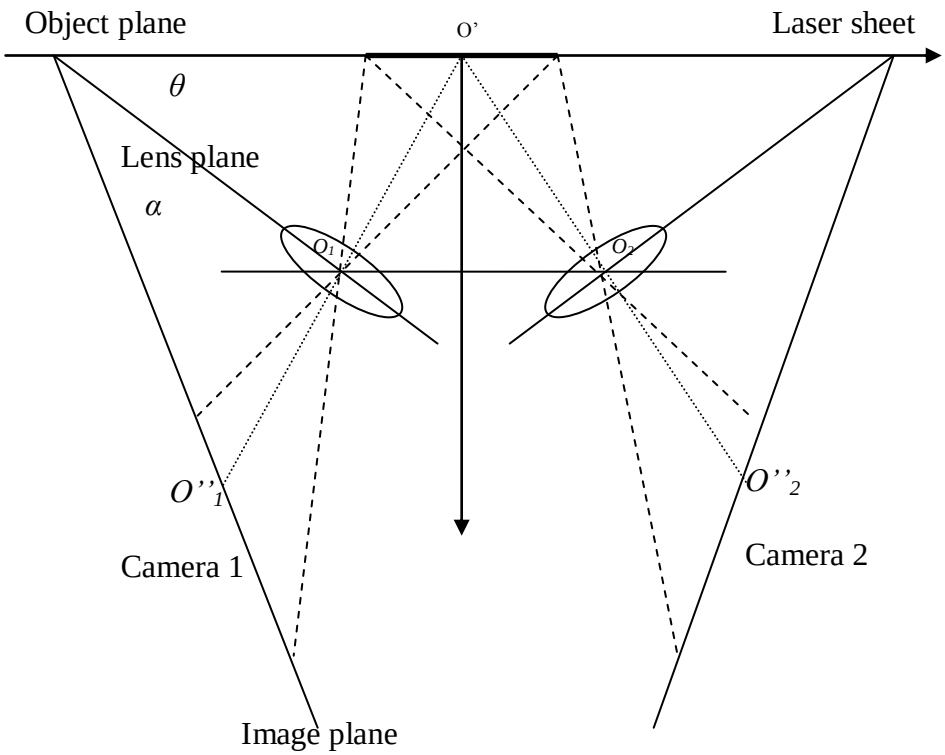

Figure 2.28: Sketch of the SPIV arrangement in the angular displacement system

In this system, the value of θ can be increased without loss of lens performance. However, the object plane, the lens plane and the image plane have to intersect precisely along a line. This requirement known as the Scheimpflug condition is achieved by rotating the image plane with respect to the lens plane (angle α). The Scheimpflug condition need not be observed if the depth-of-field δz of the system is large enough [56].

$$\delta z = 4(1 + M_n^{-1}) f^{\#2} \lambda \tag{2.51}$$

with M_n the camera magnification and λ the wavelength of the illuminating laser.

Rotational systems	
Advantages	Drawbacks
No upper limit for θ	Non-uniform magnification exacerbated by the Scheimpflug condition
	Image fields stretched in opposite directions

Table 2.10: Table of the advantages and drawbacks of the angular displacement system

With ($\alpha \neq 0$) or without ($\alpha = 0$) observing the Scheimpflug condition, different configurations of rotational systems have been employed.
For instance, the two cameras can be placed on either side of the light sheet. This variation of the Scheimpflug angular displacement systems was first used by Willert [57]:

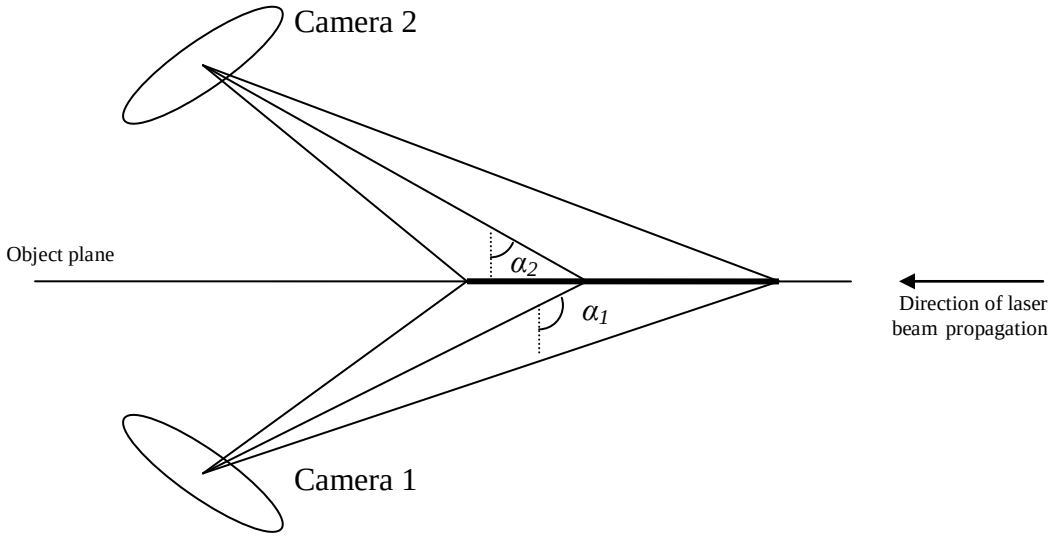

Figure 2.29: Sketch of the Scheimpflug angular displacement system

The equations for such systems are similar to the equations 2.44, 2.45 and 2.46 for the translation system.

In the present work, a rotational configuration was chosen. For practical reasons, the cameras were placed on the same side of the light sheet.
The angle between the two cameras was 90°. The Scheimpflug angle was determined experimentally as recommended in [60-61] so that the magnification stays constant across the whole image.

Concerning the uncertainties in the calculated displacement, the same relation as the one obtained for the lateral displacement system was obtained by Zang and Prasad for the Scheimpflug angular displacement system [62].

2.4 Simultaneous measurements of velocity fields and scalar fields in reacting flows in the literature

Joint measurement of velocities on the one hand and scalars like concentrations or temperature on the other hand are vital in combustion because they allow the assessment of the interactions between the thermodynamic, chemical and fluid mechanical aspects of flames. As previously mentioned, a DNS of the Navier-Stokes equations is usually too computationally demanding in most cases and, whether in a RANS approach or a LES approach, models need to be introduced to solve these equations. A large number of these models deal with turbulent scalar fluxes: species turbulent fluxes, temperature turbulent fluxes or progress variable fluxes, for instance. In that context, simultaneous measurements of velocity fields and scalar fields are extremely important allowing an insight into the physical phenomena occurring in flames and also allowing the trial of the validity of proposed models.
In this section, some of the experiments which have been previously undertaken and reported in the literature to simultaneously measure velocity fields and scalar fields will be reviewed.

In 1996, Frank et al. [63] reported simultaneous measurements of scalar fields and velocity fields in gas-phase flows using PIV and PLIF of biacetyl. They developed the diagnostic in a non-reacting air jet and subsequently applied it to a premixed propane/biacetyl/air flame. They performed two sets of measurements with different resolutions. The low resolution measurement allowed them to approximate the location of the flame front of their premixed propane/biacetyl/air flame using the PLIF of biacetyl images and superimpose it with the velocity fields which they computed from the PIV images. The high resolution measurement allowed them to image more precisely specific regions of the flame, in particular the flame front region where they observed a neat acceleration of the burnt gases associated with the heat release. They were also able to locate more precisely the flame front, to calculate the mean velocity of the reactants and of the products and the velocity fluctuations and to determine the velocity distribution and velocity fluctuations along a contour which gave them an insight into the interactions between turbulence and flame.

In 1997, Hasselbrink et al. [64] reported simultaneous velocity measurements and OH imaging using PIV and PLIF of OH in a lifted, non-premixed methane jet flame. They calculated the location of the flame front using the OH imaging and compared it with the location they calculated using arguments on the density of particles which they could see on the PIV images. They concluded that the flame front localisation using arguments concerning the density of the particles could be accurate provided that the flow is quite simple, the seeding is uniform and the temperature gradients are large.

In 1998, Carter et al. [65] reported simultaneous PLIF of CH and PIV measurements in turbulent non premixed methane/air flames. They used PLIF of CH to compute the flame front location and superimpose it with the velocity field data obtained with PIV. They were able to observe the effects of turbulence on the flame front and on the structure and thickness of the CH layer. They were also able to calculate the strain rates and noticed the survival of the flame even at large compressive and extensive strain rates.

In 1999, Frank et al. [66] reported simultaneous OH-PLIF and PIV in a turbulent premixed natural-gas/air flame. They wanted to investigate the turbulent flux of the mean progress variable. They determined the mean velocity of both reactants and products. They studied five flames with different $\frac{u'}{S_L}$ and observed a transition from counter-gradient to gradient diffusion as the ratio increases, phenomena which had been forecast in DNS but had not been experimentally observed before.

In 2001, Welle et al. [67] reported simultaneous temperature field measurements and velocity field measurements using two-line OH-PLIF and PIV in propane/air counterflow diffusion flames. They used PIV to calculate the flame strain rates and OH-PLIF to determine the temperature at the flame front and the reaction zone width. They wanted to study the frequency response of their flames and the validity of the steady-flamelet model.

In 2005, Filatyev et al. [68] reported simultaneous CH-PLIF and PIV in a turbulent premixed stoichiometric methane/air Bunsen flame. They used CH-PLIF and PIV to visualise the structure of eddies and to determine their sizes and to observe the effects

of eddies on the strain. They were also able to measure reaction layer thicknesses. They could measure, as well, global turbulent burning velocities, global consumption speeds and turbulence levels and verify the validity of empirical formulas.

In 2008, Hartung et al. [14] reported simultaneous SPIV and OH PLIF in premixed turbulent ethylene/air flames stabilised on a bluff body. They wanted to measure local turbulence intensities and to locate the flame front in order to study the effect of heat release on turbulence and to gain an insight into the scalar-turbulence interaction. They compared cold flow cases and flames. They observed that the characteristics of the eddies after the bluff body were strongly changed by the heat release. They also noticed a change in direction in the radial velocity between the two cases. They also studied the turbulence-scalar interactions by determining the probability density function (pdf) of the alignment of the vectors normal to the flame front with the principal strain rates. They observed a tendency of the vectors normal to the flame front to align with the most extensive strain rate as the isoscalar surfaces are getting further away one from another which allowed to question the classical picture of passive scalar turbulence physics.

CHAPTER III

Structure of turbulent premixed hydrogen-air flames

This chapter briefly reviews the tools most commonly used to study turbulent premixed flames. A literature survey of turbulent premixed hydrogen/air flames highlights the potential benefits of using hydrogen as a fuel and the differences observed between hydrogen-air flames and more conventional hydrocarbon premixed flames. The source of these differences and their implications for both modeling and application are briefly discussed. This chapter concludes with an explanation of the motivation for diagnostic experimental testing as a necessary complement to combustion modeling and outlines the distinctive features of a model recently developed at the University of Cambridge for turbulent hydrocarbon-air flames, which will be evaluated in later chapters for the N_2-diluted hydrogen flames of the present study.

3.1 Turbulent premixed flames

Turbulent premixed flames have been the subject of extensive research over many years and their basic features have been comprehensively reviewed elsewhere e.g. [69-70].
Therefore, in this section, detailed reference is made to only a few key parameters, which will be used later in the thesis (especially in chapter IV) to characterise the particular turbulent premixed flames studied.

3.1.1 Parameters used to characterise premixed flames

The ***equivalence ratio*** is the ratio of the fuel-air ratio of the reacting mixture to the stoichiometric fuel-air ratio:

$$\phi = \frac{n_{fuel} / n_{air}}{\left(n_{fuel} / n_{airl} \right)_s} \tag{3.1}$$

The ***adiabatic flame temperature*** of the reacting mixture is the temperature one would obtain from a complete combustion of the reactants in the absence of any heat transfer and changes in kinetic or potential energy.

The ***laminar flame speed*** S_L (or normal burning velocity) is the speed at which the reaction front propagates into the stationary unburnt gases in a laminar flame.

A measure of the ***flame thickness*** δ_L is provided by:

$$\delta_L \approx \frac{\nu_k}{S_L} \tag{3.2}$$

in which ν_k is the kinematic viscosity of the mixture

The fuel type, the composition of the reacting mixture and the temperature of the reactants as well as the properties of the flow have a strong influence on the characteristics of the flame.

To help understand those influences, a few non-dimensional numbers have been introduced, such as, the *Lewis number* of a species k, which compares thermal and mass diffusivities [7]:

$$Le_k = \frac{\left(\lambda / \rho C_p\right)_k}{D_k} \tag{3.3}$$

where λ_k is the thermal conductivity of the species k, C_{pk} is the specific heat capacity at constant pressure of the species k, ρ_k, is the density of the species k and D_k is the molecular diffusivity of the species k relative to the other species in the mixture.
The Lewis number can also be expressed as the ratio of the Schmidt number of the species k, which compares momentum diffusivity and mass diffusivity, and the Prandtl number of the species k, which compares momentum diffusivity and thermal diffusivity [7]:

$$Le_k = \frac{Sc_k}{\mathrm{Pr}_k} \tag{3.4}$$

In turbulent flame modeling, the Lewis number is usually assumed to be unity because molecular effects are generally considered to be small and the mathematical formulation is greatly simplified. However, in the case of hydrogen, the Lewis number is much smaller than unity [7], which emphasises effects of differential diffusion and may cause thermo-diffusive instabilities which have consequences for flame area and reaction rate. These effects have been widely studied previously as will be explained in section 3.1.4.

3.1.2 Parameters used to characterise turbulent flows

To characterise a turbulent flow, a few further non-dimensional numbers are of extreme importance.

The *Reynolds Number* is the ratio of inertial forces to viscous forces. In turbulent combustion where boundary layer effects are generally small, a turbulence Reynolds number is more instructive and takes the form:

$$\mathrm{Re} = \frac{u' * L}{\nu_k} \tag{3.5}$$

where *u'* is the r.m.s turbulent velocity i.e. a measure of the fluctuating velocity component, *L* is the integral length scale, characteristic of the larger energy-containing eddies and ν_k the kinematic viscosity.

The turbulence Reynolds number can also be defined using characteristic parameters of the flame such as its laminar speed (S_L) and its laminar thickness (δ_L).

$$\mathrm{Re} = \frac{u'}{S_L} \bullet \frac{L}{\delta_L} \tag{3.6}$$

The *Damköhler number* is the ratio of the characteristic fluid motion timescale to the characteristic reaction timescale. The Damköhler number can be defined as:

$$Da = \frac{L}{\delta_L} \bullet \frac{S_L}{u'} \tag{3.7}$$

The *Karlovitz number* is the ratio of the chemical time scale τ_c over the smallest turbulence time scale τ_k and can be defined as:

$$K_a = \frac{\tau_c}{\tau_k} = \frac{\delta_L}{l_k} \bullet \frac{u_k}{S_L} = \left(\frac{u'}{S_L}\right)^{3/2} \bullet \left(\frac{L}{\delta_L}\right)^{-1/2} \tag{3.8}$$

where u_k is the velocity characteristic of the Kolmogorov structures and l_k their size [71-73].

3.1.3 Regime diagrams for turbulent premixed combustion

Depending upon operating conditions, different regimes of turbulence in premixed combustion can be observed. In 1985, Borghi [74] proposed a diagram using the non-dimensional numbers outlined in section 3.1.2 to help define those regimes.

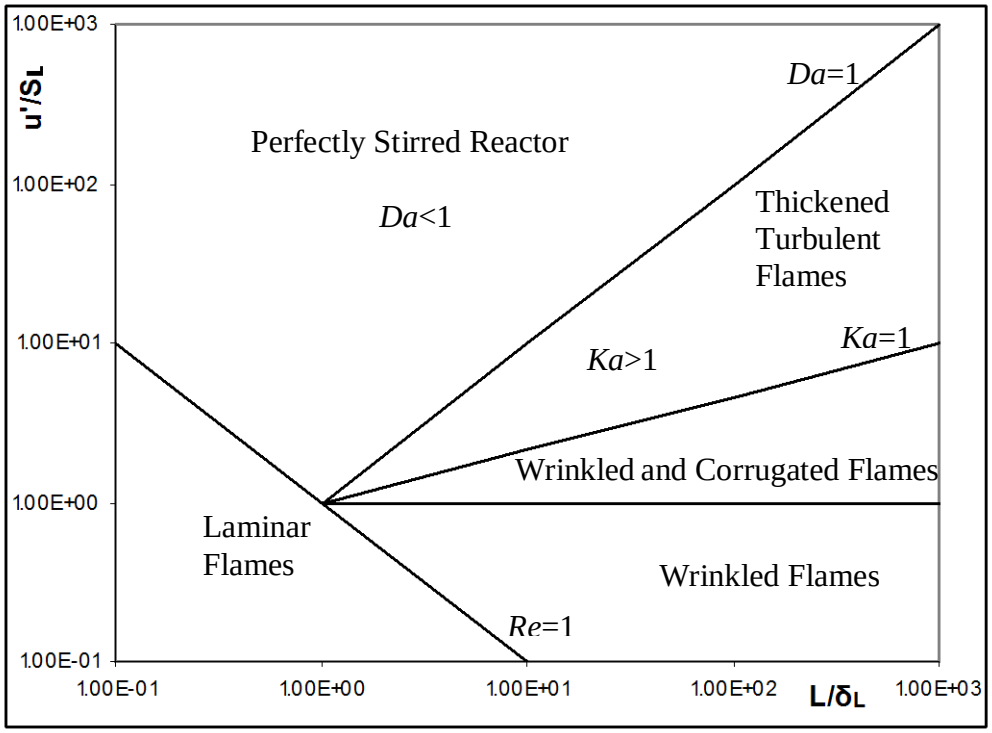

Figure 3.1: The Borghi regime diagram for turbulent premixed combustion [74]

Peters [75] extended this representation of the structure of premixed flames by dividing it into multiple layers. The first layer correspond to the so-called "preheat zone" in which there is no chemical reaction and which is followed by several distinctive reaction layers. The last layer is the so-called oxidation layer and, in between, one can find the so-called "inner layer" or "fuel consumption layer". This layer is of extreme importance but may or may not be affected by reactant turbulence depending on its scale and intensity. The turbulent flame structure will be conditioned by the interactions of the turbulence on this layer.

As a consequence, Peters [75] proposed an updated regime diagram for which he defined a *second Karlovitz number*:

$$Ka_{\delta} = \delta^2 Ka \tag{3.9}$$

The second Karlovitz number is proportional to the first Karlovitz number, scaled with respect to the fraction of the flame thickness corresponding to the inner layer, δ.

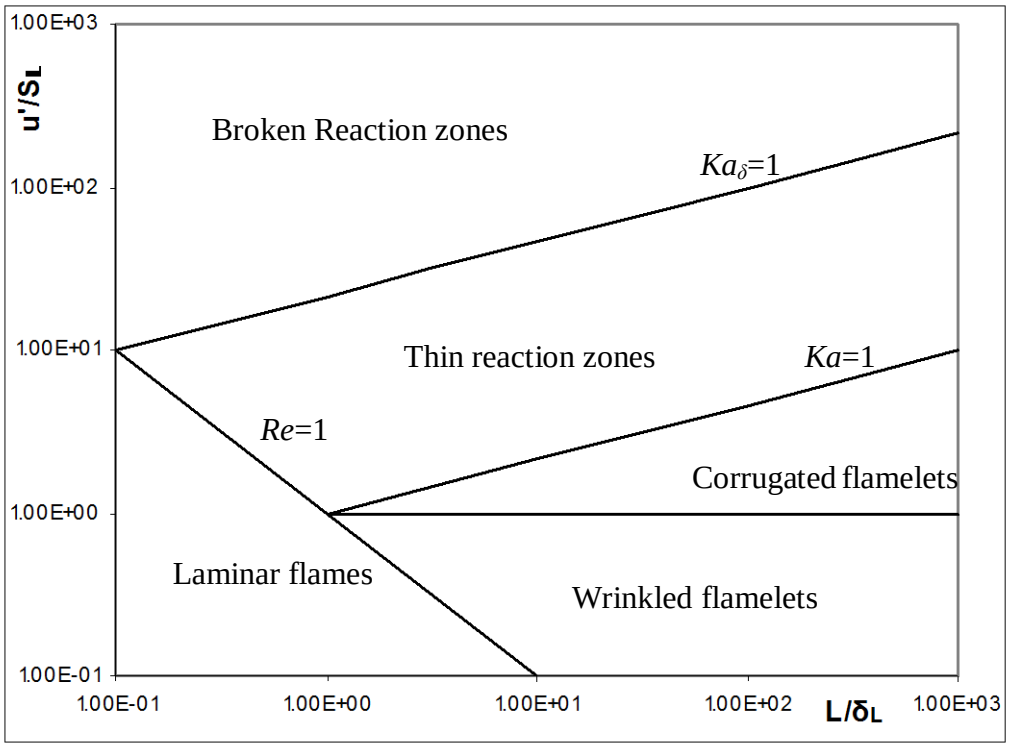

Figure 3.2: The Peters regime diagram for premixed turbulent combustion [75]

Before briefly describing the different turbulent regimes for premixed combustion, one important idea that was put forward by Kolmogorov in 1941 [71-73] is the Eddy Cascade Hypothesis in which large eddies can break into smaller eddies which can in their turn break into even smaller eddies. The kinetic energy of the large eddies is passed onto the smaller eddies which in their turn pass it onto the even smaller eddies… and so on until the size of the eddies is small enough. The kinetic energy is then dissipated by the viscosity forces and transformed into internal energy.

Another important concept in the development of turbulent combustion models is that of the laminar flamelet. Peters defines flamelets [75] as “thin reactive-diffusive layers embedded within an otherwise nonreacting turbulent flow field”.

The wrinkled flamelets regime is characterised by $\frac{u'}{S_L} < 1$ and in this regime, the flame front propagates without being much disturbed even by the largest eddies.

The regime of corrugated flamelets is characterised by Re>1, Ka<1 and $\frac{u'}{S_L} > 1$. In this regime, the largest eddies distort the flame front but there is little interaction with the smallest eddies. The eddies interacting with the flame front are those whose turnover velocity is, at least, equal to the laminar flame speed.

The thin reaction zone regime is characterised by Re>1, Ka>1 and Ka_δ<1. In this regime, some smaller eddies are able to interact with the flame front by transporting preheated gases in front of the reaction zone hence corrugating the flame, but the chemistry remains fast.

The broken reaction zones regime is characterised by Re>1 and Ka_δ>1. In this regime, the smallest eddies are small enough to enter the inner layer of the reaction zone and therefore perturb the chemistry of the process causing local extinction due to increased heat loss.

The overall effect of these modifications is to extend the applicability of the flamelet regime to higher levels of turbulence and to suggest that the approach may be more robust than initially envisaged.

3.1.4 Premixed hydrogen-air flames in the literature

As already mentioned in Chapter I, unlike other fuels, the combustion of hydrogen occurs with much reduced emissions: low emissions of nitrogen oxides under lean-burning conditions and virtually no volatile organic compounds or carbon oxides. Although its large-scale production might still be challenging, this makes hydrogen a

very promising fuel in our environment conscious times. Properties like the higher flame speed and enlarged flammability limits can be exploited to enhance combustion stability in lean mixtures and as a consequence, premixed hydrogen-enriched and pure premixed hydrogen flames have been under scrutiny for a number of years.

The chemical, thermodynamical and physical properties of hydrogen differ substantially from those of other more common hydrocarbon fuels such as propane or methane. Its low molecular weight means that hydrogen has a very high mass-diffusivity and premixed hydrogen-enriched and hydrogen flames show aspects of behaviour that are substantially different from other premixed flames. Whilst hydrogen flames have much higher laminar flame speeds, these are reached at a higher equivalence ratio of ~1.8 instead of ~1 for other fuel-air systems. This may influence the applicability of established relationships, introducing both potential benefits and new problems. As a consequence of the high mass-diffusivity of hydrogen, preferential diffusion of hydrogen occurs and hydrogen-air flames are therefore prone to diffusive-thermal instabilities (Lewis number effects). These may increase the influence of molecular processes which have traditionally been neglected in comparison with turbulence interactions. The differences in behaviour of hydrogen-air flames may therefore have profound implications for combustion models. More and more models [7], for example, now include explicit Lewis number effects and are able to successfully describe/predict the behaviour or the structure of hydrogen-air flames in consequence.

A survey of the literature on premixed hydrogen-air flames was undertaken. A number of experimental and numerical studies on premixed hydrogen-air flames were conducted previously [9, 77-93].

As will be seen shortly (sections 3.2.3 and 3.2.4), the modeling of the reaction rate is one of the most challenging problem in premixed turbulent combustion. The reaction rate is linked to the flame surface area and the burning velocity (see section 3.2.3). As a consequence, the flame surface area and the burning velocity are of particular interest in turbulent premixed combustion. A number of investigations have reported interesting results concerning both flame surface area and burning velocity. They are reported below.

Experimentally, various aspects of premixed hydrogen-air flames have been studied:

- their fractal nature [76-77], which give information on the flame surface area behaviour in particular as a function of the Lewis number
- their flame brush [78-79], which also give information on the flame surface area
- their turbulent burning velocity [80],
- preferential diffusion effects/Lewis number effects [81-89].

Numerically, premixed-hydrogen-air flames have been investigated using, in particular, DNS because of the simple chemistry of such flames. The Lewis number effects have been particularly under scrutiny [9, 80-93].

The influence of the Lewis number on the structure of premixed turbulent propane/air and hydrogen/air stagnation point flames using high speed laser tomography was investigated [77]. Goix et al. studied in particular the flame surface area and the curvature. They found that the flame surface area was sensitive to the Lewis number: they observed a production of flame surface area for the flames with a Lewis number lower than 1. However, they did not observe a strong influence of the Lewis number on the shape of the flame front curvature distribution. The average curvature for their flames was zero.

A full numerical simulation of turbulent premixed flames with varying Lewis numbers (0.8, 1.0 and 1.2) was performed by Haworth et al. [90]. They found that for nonunity Lewis numbers, the local flamelet speed for turbulent premixed flames is different to that of an undisturbed laminar flame and can be correlated with the curvature. The mean flamelet speed was found to assume a higher value than the laminar value for $Le<1$ (conversely for $Le>1$). They also found that the flame area depended on the Lewis number. As a consequence, they concluded that the turbulent flame speed was strongly influenced by the Lewis number and stressed the importance of taking into account the Lewis number effects in combustion models.

The different terms of the evolution equations for the flame surface density were estimated by Trouvé et al. [92] using direct numerical simulations for various Lewis numbers (Le=0.3, 0.8, 1.0 and 1.2). They meant to investigate the relationship

between flame surface density, mean reaction rate and flamelet speed. They also investigated the role of the two components of the flame stretch on the flame surface density. They found that for Le=0.3, both the flame surface density and the flamelet speed needed modeling contrary to cases where the Lewis number is close to unity for which the flamelet speed need not be modelled. They also found that for lower Lewis number the flame surface increased with time. They also described the effect of the stretch on the flame surface area.

The effects of the Lewis number on premixed flames interacting with turbulent Kármán vortex streets were investigated by Lee et al. [84] using OH-PLIF. They found that flame surface area increased with decreasing Lewis number for a fixed turbulent intensity and that the flame surface area increase with the turbulent intensity was more pronounced for small Lewis number. They also stressed the local influence of the curvature on the structure of the flames. However, they found no influence of the Lewis number on the flame curvature pdfs. They concluded that the effects of the turbulence and Lewis number were mainly to increase the flame surface area.

The effects of strain rate and curvature on the different terms of the transport equation of the surface density function σ were investigated by Chakraborty [89] in turbulent premixed methane-air and hydrogen-air flames using DNS.
The surface density function appears to be an important parameter to study as it is related the scalar dissipation rate and the flame surface density (and flame surface area).

The transport equation for σ can be expressed as follow [13]:

$$\frac{\partial \sigma}{\partial t} + \frac{\partial (u_j \sigma)}{\partial x_j} = a_T \sigma + S_d \kappa_m \sigma - \frac{\partial (S_d N_i \sigma)}{\partial x_i} \qquad (3.10)$$

where a_T is the tangential strain rate, S_d the displacement speed which is "the speed at which an isoscalar surface moves in the local flame normal direction with respect to an initially coincident material surface" [13], κ_m is the local flame curvature and N_i is the component in the direction x_i of the flame front normal.

The first term on the right hand side of the equation is called the strain rate term, the second is called, the curvature term and the third term is called the propagation term. They studied the effects of strain rate and curvature on the surface density function and on all three terms of the right hand side of the equations and also they studied the effects of the strain rate and curvature on the displacement speed S_d. They found:

- a positive non linear correlation between the strain rate term and the tangential strain rates for both fuels,
- that for the methane flame, the strain rate term is negatively correlated with curvature while for the hydrogen flame the strain rate term was only weakly correlated with the curvature,
- that for the methane flame and, to a lesser extent, for the hydrogen flame, there exist a negative correlation between the displacement speed and the curvature,
- that the correlation between tangential strain rate and displacement speed is positive toward the reactant side while it is weak toward the product side for the methane flame,
- that the correlation between tangential strain rate and displacement speed is positive toward the reactant side and negative toward the product side for the hydrogen flame,
- that the correlation between tangential strain rate and the curvature term is negative for the methane flame and weak for the hydrogen flame,
- that, for both flames, there could be not be observed any correlation between the curvature term and the curvature,
- that, for the methane flame and the hydrogen flame, the correlation between the propagation term and the tangential strain rate was negative but it became increasingly strong as we approached the product side for the methane flame, while for the hydrogen flame, it became weaker,
- that, for the methane flame, the propagation term was negatively correlated with the curvature toward the reactant side while the correlation became positive toward the product side,
- that, for the hydrogen flame, the correlation between the propagation term and the curvature was always negative.

Those observations allowed them to give guidelines for the modeling of the flame surface density.

The few previous articles aimed at summarising the various influence on the flame surface area which have been reported so far and emphasising the importance of the flame surface area in premixed turbulent combustion modeling.

3.2 Modeling of Turbulent Premixed Flames

3.2.1 Modeling strategies

The starting point of all combustion models is the Navier-Stokes, species and enthalpy equations [7]. They constitute a set of instantaneous local balance equations. They state the conservation of mass, momentum, species and enthalpy. However, except in very simple academic cases, this set of equations cannot be solved directly (Direct Numerical Simulation a.k.a. DNS) i.e. without any model for the turbulent motions. One strategy to solve this set of equations is called Reynolds Averaged Navier Stokes or RANS [7]. Each parameter of the equations is separated in a mean i.e. time averaged component and a deviation from the mean component. The equations are then ensemble averaged, providing us with a new set of equations in which correlations between velocity fluctuations, enthalpy fluctuations, species fluctuations and density fluctuations appear which need to be modeled. Another averaging [7] can be performed: the so-called Favre Averaging which is a density weighted time averaging. With this strategy, again, some unknown quantities appear which have to be modeled, for instance: the Reynolds stresses, the species turbulent fluxes, the temperature turbulent fluxes, the diffusive fluxes and the species reaction rates. Another approach [7] called Large Eddy Simulation or LES consists in modeling only the small eddies which are self-similar and independent of the flow and computing only the large eddies whose behaviour depends on the flow. Instead of averaging the parameters appearing in the set of equations, the parameters are filtered. There exist different types of filters. After filtering the equations, one obtains a set of equation in which appear unresolved Reynolds stresses, species fluxes, enthalpy fluxes and filtered diffusion fluxes and species reaction rates which need to be modeled as well.

3.2.2 Motivations behind experimental testing as a complement of combustion modeling

As explained in section 3.2.1, in the equations obtained using RANS, Favre Averaging or LES, some unknown quantities appear which need to be modelled. Over the years, many models have been proposed and tested [7]. However, they are not always sufficient to describe turbulent flames. In RANS or Favre Averaging, the equations, even when appropriately closed by models, only deliver time-averaged quantities which may be different from instantaneous quantities and as a consequence, they may not satisfactorily describe turbulent flames, especially when unsteady mixing effects occur. LES partially resolve the problem. In LES, the large structures of turbulent flames are simulated and not averaged so one gains access to the instantaneous quantities one may be interested in. However, the small structures in turbulent flames need modeling. It may be easier, however, to model small scales, because they seem to possess a more universal behaviour.

As a consequence, experimental testing is still crucial to turbulent combustion. In particular, simultaneous and instantaneous spatially resolved measurements of temperature, species concentrations and velocities are very important in that they allow an insight into phenomena which cannot be computationally simulated. They also allow the testing of models dealing with unresolved scales.

3.2.3 Turbulence-chemistry interactions in turbulent premixed flames

Turbulence is a common feature in practical combustion. As a consequence, interactions between turbulence and chemistry are also a common feature of practical flames.

Such interactions are explicit in the Reynolds averaged balance equations, the Favre averaged balance equations and the balance equations obtained using LES. For instance, in RANS, the turbulence-chemistry interactions show in the species and temperature turbulent fluxes and also in the species chemical reaction rates. In LES,

the turbulence-chemistry interactions again show in the unresolved species fluxes and enthalpy fluxes and in the filtered chemical reaction rate.

The chemical reaction rate has been under particular scrutiny and its modeling appears to be particularly challenging. The chemical reaction rate depends on temperature and scalar concentrations. However, this dependence is non linear which makes its modeling particularly difficult.

The modeling of the chemical reaction rate is simplified if it is assumed that the reactions zones are thin compared to the Kolmogorov length scale (thin flame assumption). The average reaction rate, then, becomes a function of the unburnt mixture density, the unstretched laminar burning velocity, a quantities representing the effect of stretch on the laminar burning velocity and the flame surface density. As a consequence, the effect of turbulence on the reaction rate is mainly represented by the flame surface density.

The flame surface density (as will be explained in section 3.2.4) can be related to the scalar dissipation rate [8]. Various effects on scalar dissipation have been studied:

- the effects of dilatation [8],
- the effects of strain rate and curvature [9],
- the effects of Damköhler number [11-12],
- the effects of heat release [14].

However, as can already be seen and will be further discussed in the next section and further, the Lewis number effects have not been particularly studied.

The results of the studies [8, 11-12, 14] are presented in section 3.2.4, which also presents the model developed at the University of Cambridge which is under particular scrutiny in this thesis.

3.2.4 Modeling of the scalar dissipation rate of the progress variable

As explained in [7], there exist different models which were developed for premixed combustion.

The features of the model developed and investigated at the University of Cambridge [8-14] will be described in the following pages.

The progress variable was defined in [8] as:

$$c_T = \frac{T - T_{unburnt}}{T_{burnt} - T_{unburnt}} \tag{2.41}$$

where T_{burnt} is the temperature of the burnt mixture and $T_{unburnt}$ the temperature in the unburnt mixture.

The instantaneous equation governing c may be written as [8]:

$$\rho\left(\frac{\partial c}{\partial t} + u_j \frac{\partial c}{\partial x_j}\right) = \dot{\omega} + \frac{\partial \rho\alpha \frac{\partial c}{\partial x_j}}{\partial x_j} \tag{3.11}$$

where α is the diffusivity of c, ρ is the fluid density, $\dot{\omega}$ is the chemical source term, u_j the component of the velocity in the direction j and x_j the coordinate in the direction j.

In the RANS methodology using Favre Averaging, in the balance equation governing $\tilde{c}$, appear the average reaction rate term $\overline{\dot{\omega}}$ and the turbulent flux $u''\tilde{c}''$ which need to be modeled.

Various attempts have been made to model the average reaction rate term. Usually, the reaction rate term is modeled using the flame surface density Σ which, in its turn, needs to be modeled.

One can introduce the scalar dissipation rate of the progress variable N_c which can be defined as [8]:

$$N_c = \alpha(\nabla c.\nabla c) \tag{3.12}$$

in which α is the diffusivity of c.

The scalar dissipation rate is related to the flame surface density Σ via the mean scalar dissipation rate $\tilde{\varepsilon}_c$ which represents the dissipation rate of the progress variable variance in the thin flamelet assumption and which is [8]:

$$\tilde{\varepsilon}_c = K_\Sigma S_L \Sigma = \alpha\left(\nabla c'' \nabla c''\right) \tag{3.13}$$

in which K_Σ is a constant and S_L the laminar flame speed.

In 2005, Swaminathan et al. [8] derived an exact transport equation for the instantaneous scalar dissipation rate N_c:

$$\rho\frac{DN_c}{Dt} = \frac{\partial}{\partial x_j}\left(\rho\kappa\frac{\partial N_c}{\partial x_j}\right) - 2\rho\kappa\kappa\frac{\partial c_{,j}}{\partial x_j}\frac{\partial c_{,j}}{\partial x_j} - 2\rho\kappa c_{,i}e_{i,j}c_{,j} + 2\rho N_c\left(\frac{\partial u_l}{\partial x_l}\right) + 2\kappa c_{,i}\dot{\omega}_{,i} \tag{3.14}$$

where $\frac{D}{Dt}$ corresponds to $\left(\frac{\partial}{\partial t} + u_j\frac{\partial}{\partial x_j}\right)$, $c_{,i}$ is the gradient of scalar c in the direction i, κ is the molecular diffusivity and is weakly dependant on temperature and $e_{i,j}$ is the turbulence strain rate.

The third term on the right hand-side of equation (3.14) represents the turbulence-scalar interaction. As is explicit in equation (3.14), the production of scalar gradient happens when the gradient vector preferentially align with the most compressive vector while dissipation of scalar gradient happens when the gradient vector preferentially align with the most extensive strain rates.

Using this equation and the relationship between $\tilde{\tilde{\varepsilon}}_c$ and N_c which is [8]:

$$\bar{\rho}\tilde{\tilde{\varepsilon}}_c = \bar{\rho}\tilde{\tilde{N}}_c - \overline{\rho\kappa}\left(\nabla\tilde{\tilde{c}}.\nabla\tilde{\tilde{c}}\right) \qquad (3.15),$$

they were also able to derive, in [8], a transport equation for $\tilde{\tilde{\varepsilon}}_c$:

$$\frac{\partial\bar{\rho}\tilde{\tilde{\varepsilon}}_c}{\partial t} + \frac{\partial}{\partial x_j}\left(\bar{\rho}\tilde{u}_j\tilde{\tilde{\varepsilon}}_c\right) = \frac{\partial}{\partial x_j}\left(\overline{\rho\kappa}\frac{\partial\tilde{\tilde{\varepsilon}}_c}{\partial x_j}\right) - 2\overline{\rho\kappa\kappa\left(\frac{\partial c''_{,i}}{\partial x_j}\frac{\partial c''_{,i}}{\partial x_j}\right)} + T_1 + T_2 + T_3 + T_4 \qquad (3.16)$$

Where [8]:

$$T_1 = -\frac{\partial\overline{\rho u''_j\varepsilon_c}}{\partial x_j} - 2\overline{\rho\kappa}\left(u''_j\tilde{\tilde{c}}''_{,i}\right)\frac{\partial^2\tilde{\tilde{c}}}{\partial x_i\partial x_j} \qquad (3.17)$$

$$T_2 = 2\overline{\rho\varepsilon_c\frac{\partial u_l}{\partial x_l}} \qquad (3.18)$$

$$T_3 = 2\overline{\rho\kappa}\frac{\partial\tilde{\tilde{c}}}{\partial x_i}\left(\frac{\partial c''}{\partial x_j}\frac{\partial\tilde{\tilde{u}}''_i}{\partial x_j}\right) - 2\overline{\rho\kappa\left(\frac{\partial c''}{\partial x_i}\tilde{\tilde{e}}''_{ij}\frac{\partial c''}{\partial x_j}\right)} - 2\overline{\rho\kappa\left(\frac{\partial c''}{\partial x_i}\frac{\partial\tilde{\tilde{c}}''}{\partial x_j}\right)}\tilde{\tilde{e}}_{ij} \qquad (3.19)$$

$$T_4 = 2\overline{\left(\kappa\frac{\partial c''}{\partial x_i}\frac{\partial\dot{\omega}''}{\partial x_i}\right)} \qquad (3.20)$$

In [8], they also proposed a model for the mean scalar dissipation rate $\tilde{\tilde{\varepsilon}}_c$, whose predictions compared well with DNS results. They used this model to derive a new model for the mean reaction rate with explicit reference to chemical time scale.

Previous studies (see in [10]) have shown that the turbulence is responsible for the production of scalar gradients in flows in the absence of chemical reaction or with passive chemical reactions i.e. when the dynamics of the flows is not influenced by the heat released by the chemical reactions. However, few such investigations have been dedicated to study of flows in the presence of nonpassive chemical reactions. Swaminathan et al. investigated this aspect [10] using DNS. They found that, contrary to what previous studies had shown, there was a preferential alignment of the scalar gradient with the most extensive strain rates for the flames they studied. They also proposed a model to express the term T_3 which allows the prediction of both production and dissipation of scalar gradients:

$$T_3 = 2C_s\left(1-Da\right)\bar{\rho}\,\varepsilon_c\frac{\tilde{\tilde{\varepsilon}}}{\tilde{\tilde{k}}} \tag{3.21}$$

They further investigated [11] this relationship i.e. the effect of the Damköhler number on the turbulence-scalar interaction using DNS. They observed the production of scalar gradient for their low Damköhler number flame except in regions of intense heat release whereas they observed the dissipation of scalar gradient for their high Damköhler number flame. In a follow-up paper [12], they refined their model and stressed the importance of modeling the Damköhler number effects to accurately describe the turbulence-scalar interactions. They extended their model to the other terms of equation 3.16 in [13].

In 2008, they experimentally investigated the effects of heat release on the turbulence and scalar-turbulence interaction in premixed ethylene-air flame using SPIV and OH-PLIF [14]. In particular, they studied the orientation of the flame front normal with the principal strain rates. Their experiments showed that there was a preferential alignment of the flame front normal with the most extensive strain rate for the flames they investigated which all had a Damköhler number equal or greater than unity from which they inferred that the turbulence dissipated scalar gradients in premixed flames with Damköhler number equal or greater than unity. In this article [14], they also raise the issue of the influence of the Lewis number on this alignment.

In the present work, nitrogen-diluted hydrogen-air flames were investigated using SPIV and NO-PLIF. As a consequence, it was possible to investigate whether or not this preferential alignment remained the same for flames with a different Lewis number. The NO-PLIF data allowed the determination of the flame front normal while the SPIV allowed the determination of the components of the strain rate tensor. The pdfs of the alignment of the flame front normal with the most extensive and the most compressive strain rates were determined and compared with the results shown in [14]. The results are presented and discussed in chapter VIII.

CHAPTER IV

Experimentation

The first part of this chapter contains a description of the burner used in the present work. The simulations performed on the Chemkin 4.1 software [15] to characterise the flames studied in this work are also reported as well as the experimental campaign performed on the burner using hot wire anemometry. The second part of this chapter describes the experimental set-up for the simultaneous NO-PLIF and SPIV experiments.

4.1 Characterisation of the burner

4.1.1 The burner

4.1.1.1 General description

The burner used in this study was a piloted burner. It was mounted on the x, y, and z traverse of a milling machine bed to allow it movements vertically and laterally:

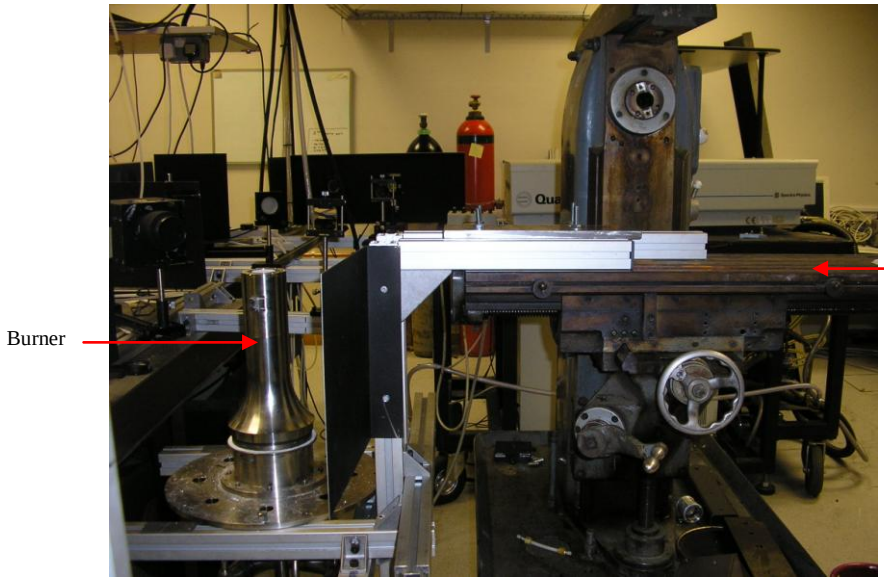

Figure 4.1: The piloted burner mounted on the x, y, z traverse of a milling machine bed

This configuration allowed different areas of the flames to be visualised without having to realign the lasers and the optical elements of the set-up.
The burner was fixed to the milling machine bed which could move in 0.1mm steps in the x, y and z directions.

Figures 4.2, 4.3 and 4.4 give a visual description of the burner used. It consists of:

- a 35mm ID inner tube (shown in figure 4.3),
- a 55mm ID outer tube (shown in figure 4.3),
- a distribution plate (shown in figure 4.3) used to stabilise the pilot flame and which is clamped by a ring screwed on top of the outer tube of the burner,

- various spacer tubes (shown in figure 4.3) which allow the distribution plate to be placed at various depth of the exit (between 10mm and 0 mm),
- a turbulence grid (shown in figure 4.4) placed 300mm down the burner,
- two inlets (shown in figure 4.4), one for the pilot flame mixture and the other for the piloted flames mixtures.

Figure 4.2: The piloted burner

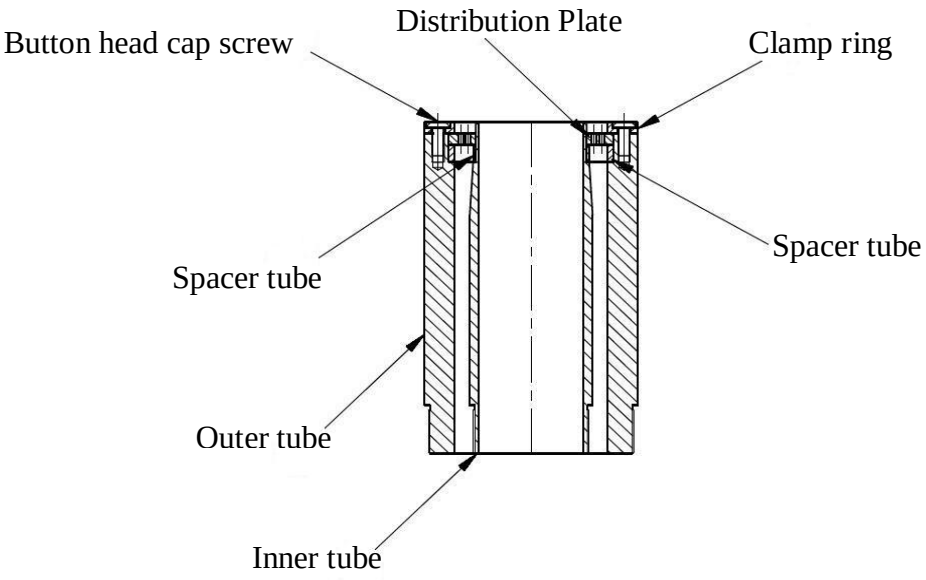

Figure 4.3: Sketch of the top part of the burner

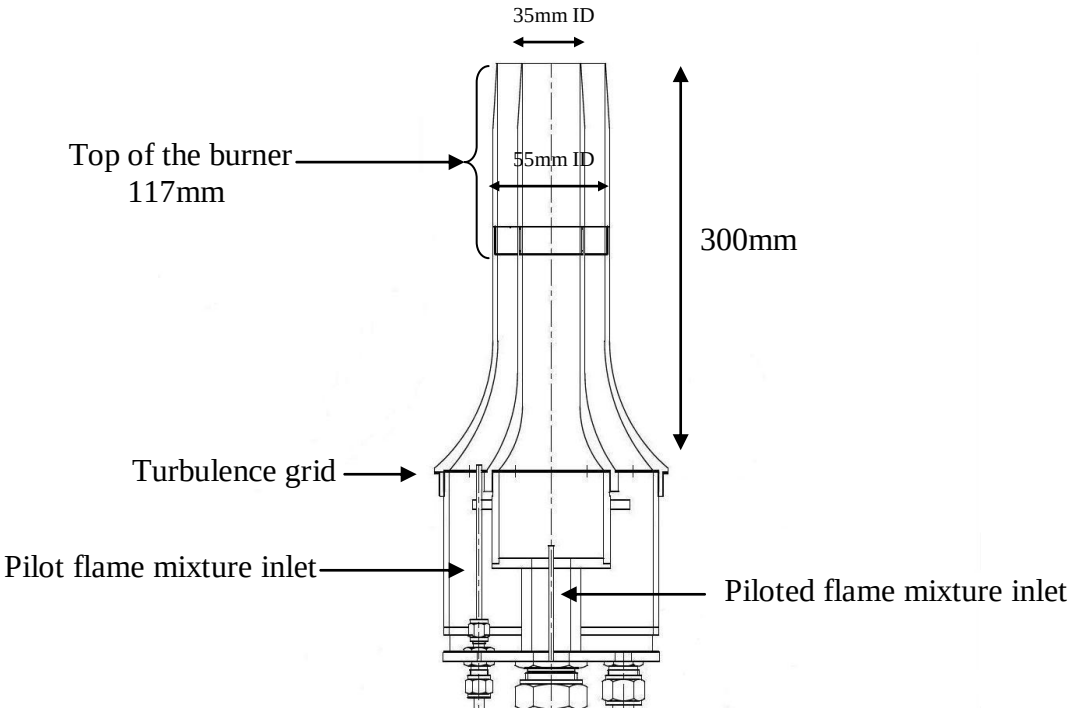

Figure 4.4: Sketch of the burner

The mixing of the gases occurred in two mixing chambers to which were attached the inlet tubes. The tubes had an approximate length of 1m and were attached on their other side to the burner.

The mixing chambers were placed just after the flow meters and sonic nozzles which are further described in the next section.

4.1.1.2 The flow measurement system

The flow meters and sonic nozzles used in the present work were all placed on a so-called control panel which is shown in figure 4.5.

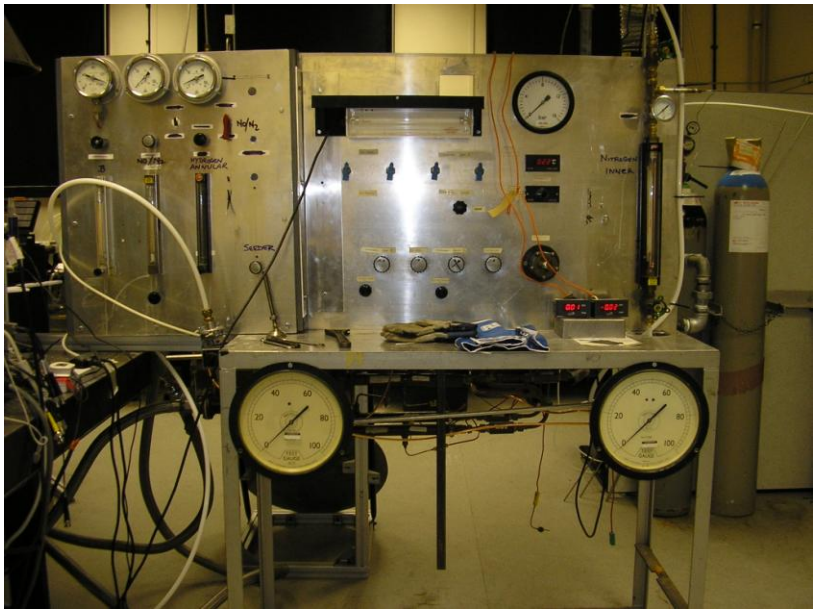

Figure 4.5: The control panel

The flames studied were turbulent premixed nitrogen diluted hydrogen-air flames. The piloted flames were also seeded with NO which is considered inert at the temperature of the flames studied and, if produced, produced in quantities much lower than the seeding concentrations [23-31]. To control the different gas flows, *Fischer & Porter* flow meters and sonic nozzles - designed, manufactured and calibrated at Cranfield University [94] - were used (see table 4.1):

Pilot Flame	N_2	Flow meter:1/4''-G5-25 Float: 1/4''-SS Accuracy:+/-1.875% actual reading , +/- 0.625% full scale reading
	H_2	Flow meter: 1/8''-G5-12 Float: 1/8''-SS Accuracy:+/-1.875% actual reading , +/- 0.625% full scale reading
	Air	Sonic nozzle 0.9mm Accuracy: max. 1%
Piloted Flame	Air	Sonic nozzle 1.8mm Accuracy: max. 1%
	N_2	Flow meter: 1/2''-35-G10/55 Float: 1/2''-GNSVT Accuracy: +/-2% max. flow
	H_2	Sonic nozzle 0.45mm Accuracy: max. 1%
	NO (1% in N)	Flow meter: 1/4''-G5-25 Float: 1/4''-SS Accuracy:+/-1.875% actual reading , +/- 0.625% full scale reading

Table 4.1: Measuring devices on the control panel of the rig

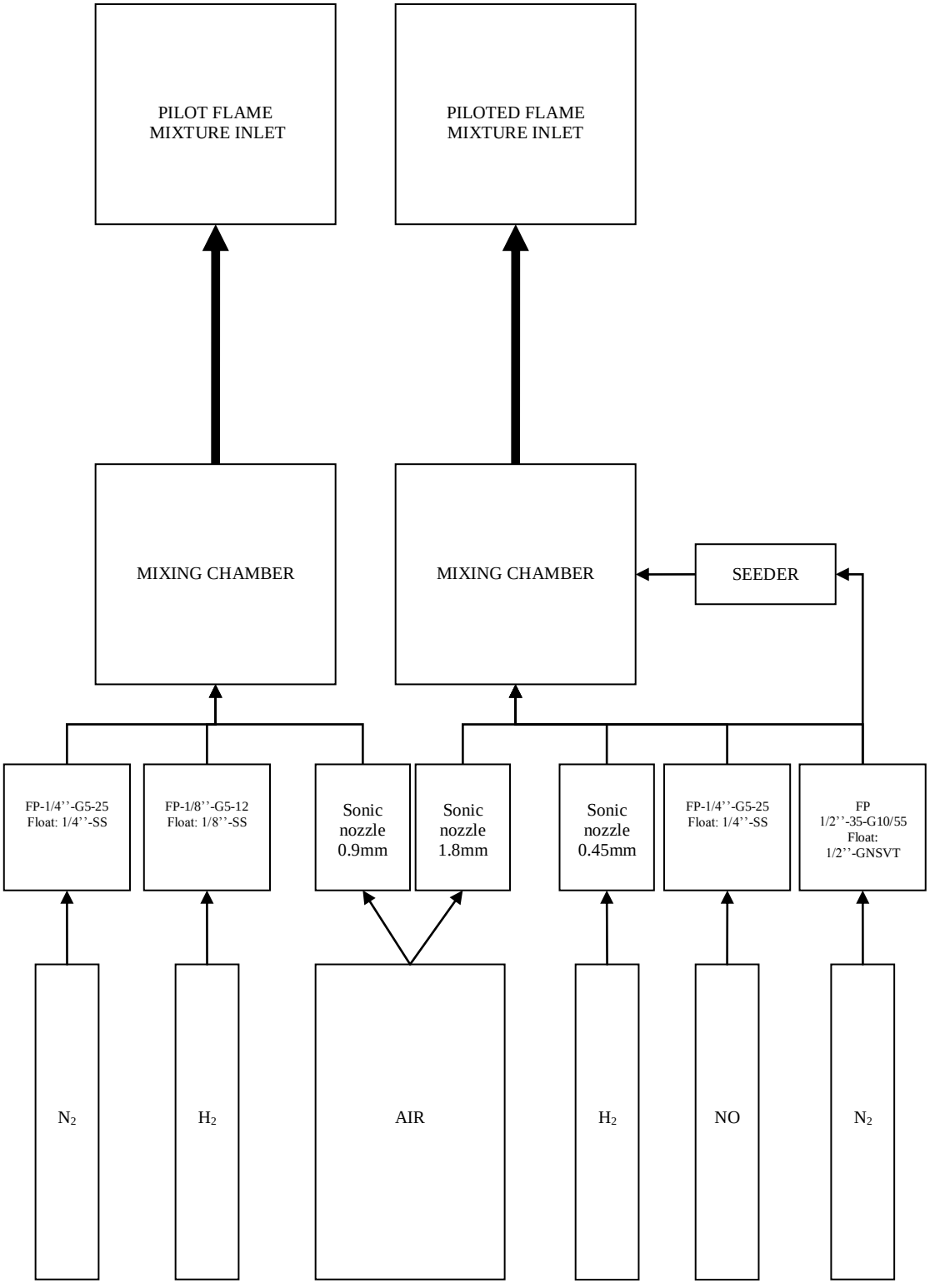

<u>Figure 4.6</u>: Block diagram of the flow measurement system and mixing of the gases

4.1.1.3 The pilot flame

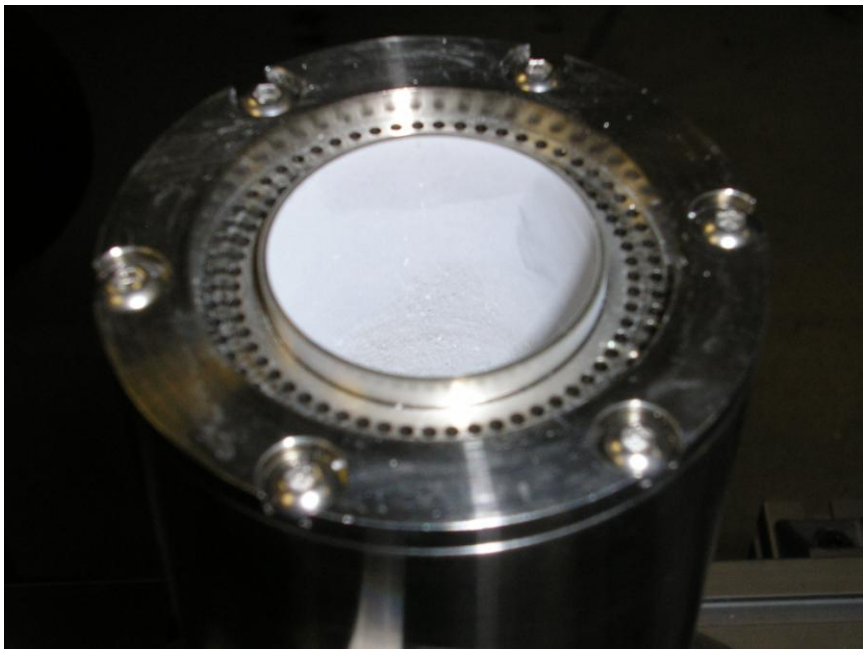

Figure 4.7: View of the top of the burner

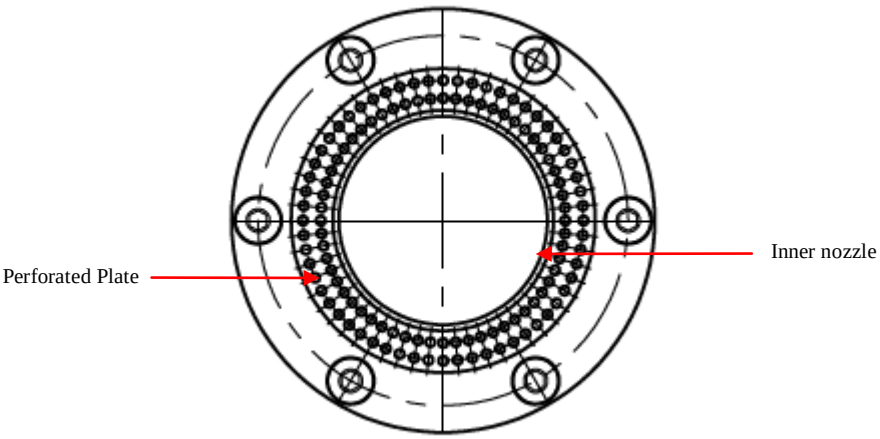

Figure 4.8: View of the top of the burner

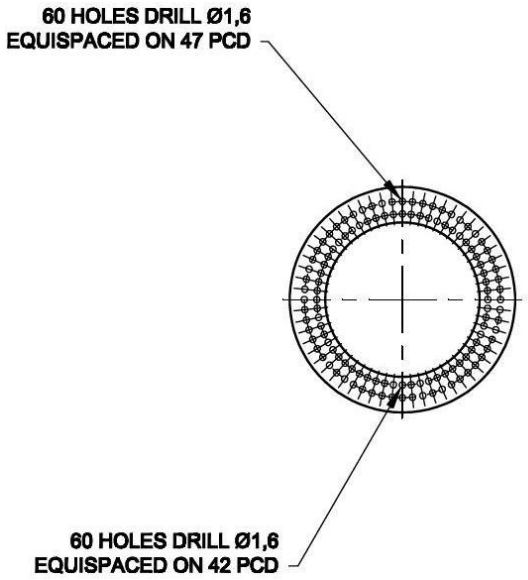

Figure 4.9: Sketch of the perforated plate

The pilot flame sat on a perforated plate which had two rows each of 60 regularly spaced holes. The holes had a diameter of 1.6mm. The perforated plate was placed 4mm down the duct and it is 4 mm thick.

The composition of the pilot flame remained the same throughout the experiments and was as follow: equivalence ratio Φ of 0.52 and $dilution = \frac{n_{O_2}}{n_{O_2} + n_{N_2}}$ (4.1) of 0.131.

Its composition in mole fraction was then: 0.120 O_2, 0.756 N_2, and 0.124 H_2.
Its mass flow rate was: 33.46g/min. Its volume flow rate was 0.525L/s.

This composition and flow rate for the pilot flame were determined experimentally. This composition is the composition that is closest to the composition of the piloted flame and stable. The flow rate is the lowest flow rate that could be achieved with the burner so as to minimise the interaction between the pilot and piloted flames.

Technical drawings of the burner can be found in Appendix Chapter V.

4.1.1.4 The piloted flames

The compositions of the flames studied are summarised in the table 4.2.

The turbulence was created by a turbulence grid placed 300mm down the main duct.

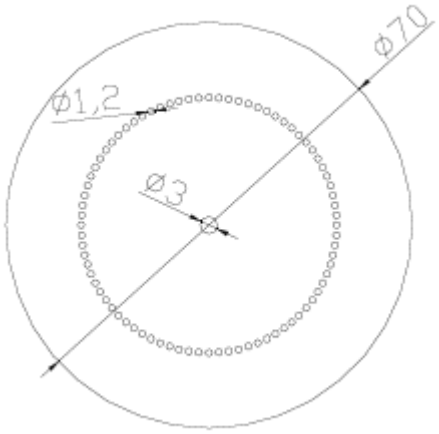

Figure 4.10: Turbulence grid

The turbulence grid is a 70mm diameter disk with a single row of regularly spaced 1.2mm diameter holes.

The experiments were conducted on 9 flames:

Flame	Flow Rate ($L.s^{-1}$)	*Average Speed* ($m.s^{-1}$) =Flow Rate/Duct Section	*Dilution*	Φ	T_{ad} (K)	C_{NO}
A	4.25	4.42	0.106	0.38	906	505
B	4.38	4.55	0.106	0.54	1124	489
C	4.55	4.73	0.106	0.75	1384	470
D	3.27	3.40	0.106	0.54	1124	489
E	3.41	3.54	0.106	0.76	1396	469
F	2.75	2.86	0.098	0.75	1317	494
G	5.30	5.51	0.105	0.38	901	495
H	5.46	5.67	0.105	0.53	1104	480
I	6.33	6.58	0.106	0.38	906	502

Table 4.2: Summary of the flames studied

Φ is the equivalence ratio.

C_{NO} is the molar concentration of NO in the flame in ppm.

T_{ad} is the adiabatic flame temperature determined using the *Gaseq* software [95].

4.1.2 Laminar flame simulations

4.1.2.1 Input data and method used for the laminar flame simulations

In order to establish the turbulence regimes of the flames studied i.e. in order to calculate the Karlovitz and Damköhler numbers (using equations 3.7 and 3.8), the unstrained laminar flame speed and the laminar flame thickness were computed using the Chemkin 4.1 software [15] because their values for the flames studied in this work were not available in the literature.

The input data for the simulation of the combustion of premixed hydrogen-air flames were taken from [96]. It contains all the numerical data available on hydrogen oxidation.

Table 4.3 shows the revised mechanism found in [96] and table 4.4 gives the thermodynamic properties [96] of all species playing a role in hydrogen oxidation. This set of data is the most up-to-date to the author's knowledge.

In table 4.3, A, n and E_a refer respectively to the pre-exponential factor, the exponent of the ratio of the temperature over the reference temperature and the activation energy in the modified Arrhenius equation (equation 4.2) which gives explicitly the temperature dependence of the rate constant k of chemical reactions:

$$k = A\left(\frac{T}{T_0}\right)^n e^{\frac{-E_a}{RT}} \qquad (4.2)$$

In table 4.4, $\Delta H_{f/298K}$ is the standard enthalpy of formation of the species considered at 298K, S is the entropy of the species considered at 300K and C_p is the specific heat capacity under standard constant pressure of the species considered at 300K, 400K, 500K, 800K, 1000K and 1500K.

	Reaction	A	n	E_a
H_2/O_2 Chain Reaction				
1	$H + O_2 = O + OH$	1.91×10^{14}	0.00	16.44
2	$O + H_2 = H + OH$	5.08×10^{4}	2.67	6.292
3	$OH + H_2 = H + H_2O$	2.16×10^{8}	1.51	3.43
4	$O + H_2O = OH + OH$	2.97×10^{6}	2.02	13.4
H_2/O_2 Dissociation/Recombination Reactions				
5	$H_2 + M = H + H + M$	4.57×10^{19}	-1.40	105.1
6	$O + O + M = O_2 + M$	6.17×10^{15}	-0.50	0.00
7	$O + H + M = OH + M$	4.72×10^{18}	-1.00	0.00
8	$H + OH + M = H_2O + M$	4.50×10^{22}	-2.00	0.00
Formation and Consumption of HO_2				
9	$H + O_2 + M = HO_2 + M$ $H + O_2 = HO_2$	3.48×10^{16} 1.48×10^{12}	-.041 0.60	-1.12 0.00
10	$HO_2 + H = H_2 + O_2$	1.66×10^{13}	0.00	0.82
11	$HO_2 + H = OH + OH$	7.08×10^{13}	0.00	0.30
12	$HO_2 + O = OH + O_2$	3.25×10^{13}	0.00	0.00
13	$HO_2 + OH = H_2O + O_2$	2.89×10^{13}	0.00	-0.50
Formation and consumption of H_2O_2				
14(1)	$HO_2 + HO_2 = H_2O_2 + O_2$ $HO_2 + HO_2 = H_2O_2 + O_2$	4.2×10^{14} 1.3×10^{11}	0.00 0.00	11.98 -1.629
15	$H_2O_2 + M = OH + OH + M$ $H_2O_2 = OH + OH$	1.27×10^{17} 2.95×10^{14}	0.00 0.00	45.5 48.4
16	$H_2O_2 + H = H_2O + OH$	2.41×10^{13}	0.00	3.97
17	$H_2O_2 + H = H_2 + HO_2$	6.03×10^{13}	0.00	7.95
18	$H_2O_2 + O = OH + HO_2$	9.55×10^{6}	2.00	3.97
19(1)	$H_2O_2 + OH = H_2O + HO_2$ $H_2O_2 + OH = H_2O + HO_2$	1.0×10^{12} 5.8×10^{14}	0.00 0.00	0.00 9.56

Table 4.3: Revised reaction mechanism for hydrogen oxidation [96]

(1) sum of the two expressions

Species	$\Delta H_{f/298K}$	S_{300K}	C_p(300K)	C_p(400K)	C_p(500K)	C_p(800K)	C_p(1000K)	C_p(1500K)
H	52.098	27.422	4.968	4.968	4.968	4.968	4.968	4.968
O	59.56	38.500	5.232	5.139	5.080	5.016	4.999	4.982
OH	8.91	43.933	6.947	6.992	7.036	7.199	7.341	7.827
H_2	0.00	31.256	6.902	6.960	6.997	7.070	7.209	7.733
O_2	0.00	49.050	7.010	7.220	7.437	8.068	8.350	8.721
H_2O	-57.77	45.154	8.000	8.231	8.446	9.223	9.875	11.258
HO_2	3.00	54.809	8.349	8.886	9.465	10.772	11.380	12.484
$H2O_2$	-32.53	55.724	10.416	11.446	12.346	14.294	15.213	16.851
N_2	0.00	45.900	6.820	7.110	7.520	7.770	8.280	8.620
Ar	0.00	37.000	4.900	4.900	4.900	4.900	4.900	4.900
He	0.00	30.120	4.970	4.970	4.970	4.970	4.970	4.970

Table 4.4: Thermodynamic properties of the species involved in the oxidation of hydrogen [96]

The Chemkin 4.1 [15] *Premixed Laminar Flame Model* was used to compute the unstrained laminar flame speed and laminar flame thickness. With this model, the flames computed are considered to be freely propagating and the transport properties used are mixture-averaged transport properties. A "continuation" technique was employed. The "continuation" technique consists in computing first a stoichiometric hydrogen-air flame and then using the solutions obtained to compute the next continuation which departs slightly from the stoichiometric flame and whose solutions will be used for the next continuation which departs even more from the stoichiometry.

It was not possible to directly calculate the values of the unstrained laminar flame speed and laminar flame thickness for our mixtures. The lean limit for the combustion of H_2 in air is about 4% by volume [97]. However, as the flames we wanted to compute were nitrogen diluted, it is to be expected that the lean flammability limit will be higher than 4% by volume. As a consequence, the flames we wanted to compute may have been very close to the extinction boundary. That may be the reason why the Chemkin 4.1 software [15] did not manage to fully solve the problem.

To obtain an estimation of the unstrained laminar flame speed and laminar flame thickness, the following procedure was applied.
The unstrained laminar flame speed was directly estimated using the Chemkin 4.1 software [15] for undiluted H_2/air flames with equivalence ratio 0.35, 0.40, 0.50, 0.60, 0.70, 0.80, 0.90, 1.00, 1.50, 2.00, 3.00. The unstrained laminar flame speed was also directly calculated using the Chemkin 4.1 software [15] for stoichiometric nitrogen-diluted H_2/air flames with dilution factor (equation 4.1) of 0.21, 0.20, 0.18, 0.16 and 0.14.
The laminar flame thickness was calculated for the same flames using the temperature profile calculated by the Chemkin 4.1 software [15].
The values of the unstrained laminar flame speed and laminar flame thickness for our flames were extrapolated using those data. More details concerning the curves obtained with the Chemkin 4.1 software [15] and the extrapolation procedures are given in the next sections.

4.1.2.2 Results of the simulations

The unstrained laminar flame speed obtained directly from the Chemkin 4.1 software [15] for the undiluted H_2/air flames with equivalence ratio 0.35, 0.40, 0.50, 0.60, 0.70, 0.80, 0.90, 1.00, 1.50, 2.00, 3.00 and for the stoichiometric nitrogen-diluted H_2/air flames with dilution factor of 0.21, 0.20, 0.18, 0.16 and 0.14 are plotted in figure 4.11:

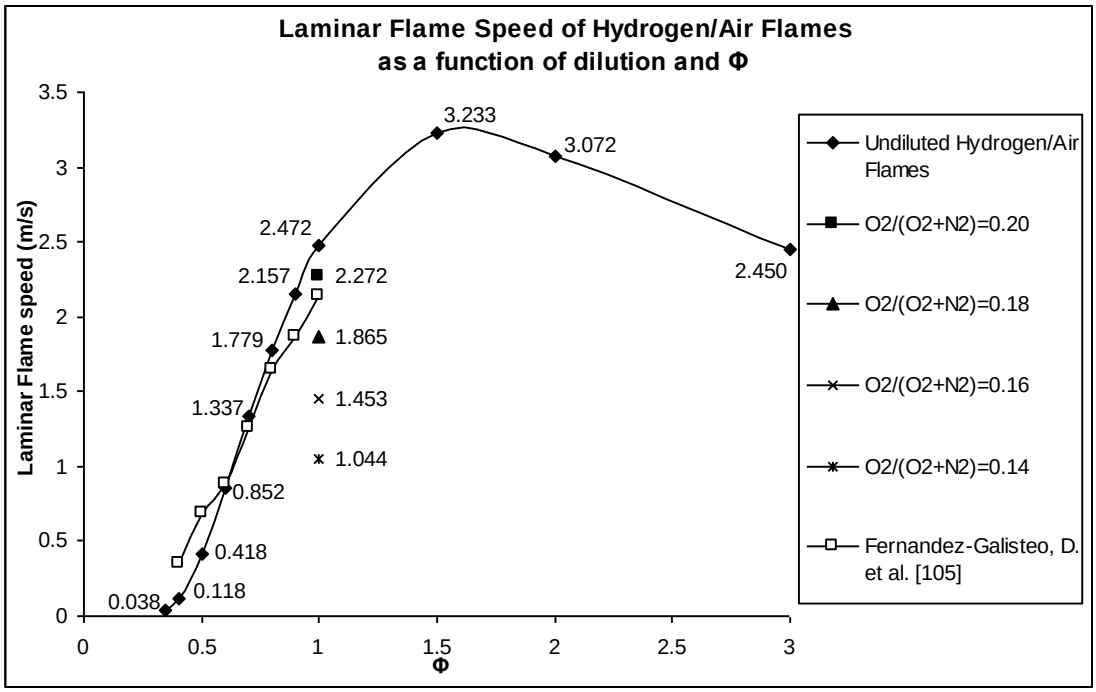

Figure 4.11: Unstrained laminar flame speed as a function of the equivalence ratio and the dilution

The curve showing the unstrained laminar flame speed as a function of the equivalence ratio for undiluted hydrogen-air mixture agrees well with previous experimental and numerical data [98-105]. Both the tendency of the unstrained laminar flame speed to decrease with decreasing equivalence ratio between Φ=0.5 and 1 and the values of the unstrained laminar flame speed agreed well with the literature [98-105].

Figure 4.12 shows the variation of the unstrained laminar flame speed as a function of the dilution factor.

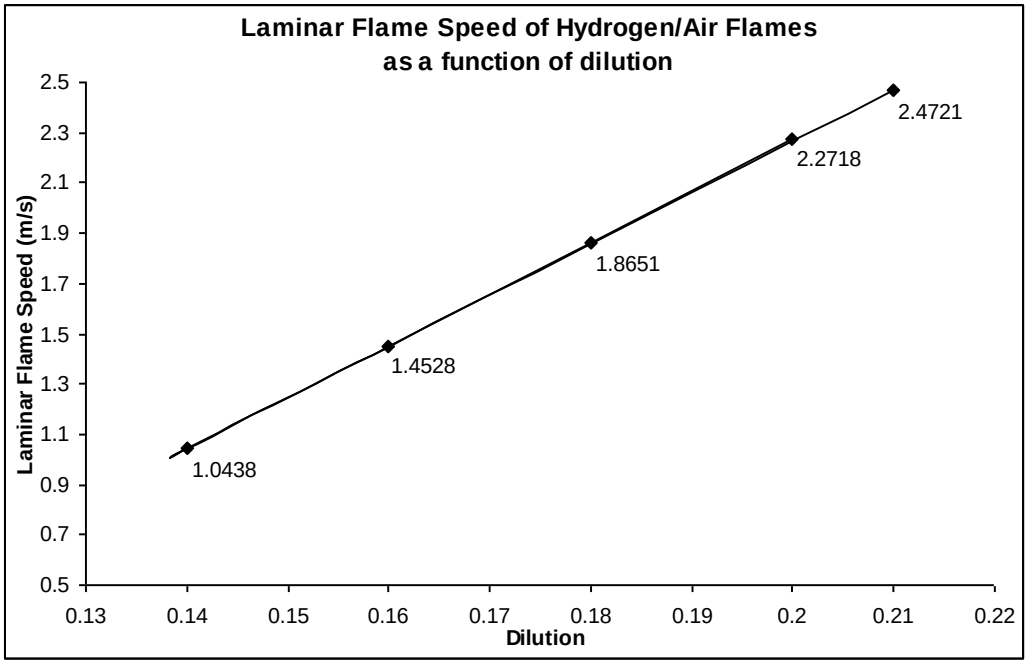

Figure 4.12: Laminar Flame Speed as a function of dilution for Φ=1

It can be observed that the unstrained laminar flame speed varies linearly with the dilution factor. Within the limits of the study i.e. for dilution values between 0.21 and 0.105, the curve above seems to have the following equation:

$$S_L = 20.428 * Dilution - 1.815 \tag{4.3}$$

This equation will be used for the extrapolation of the curves for mixtures with a higher content in nitrogen.

The calculation of the laminar flame thickness is less straightforward. We proceeded as follow. From the Chemkin 4.1 software [15], we can obtain the variation of the value of the temperature in space. The origin for the value of distance is arbitrarily fixed. However, the relative distance between two temperatures is part of the simulation.

The values of the progress variable c_T as a function of distance were calculated from the temperature data using equation 2.41.

Figures 4.13 and 4.14 show the progress variable as a function of distance:

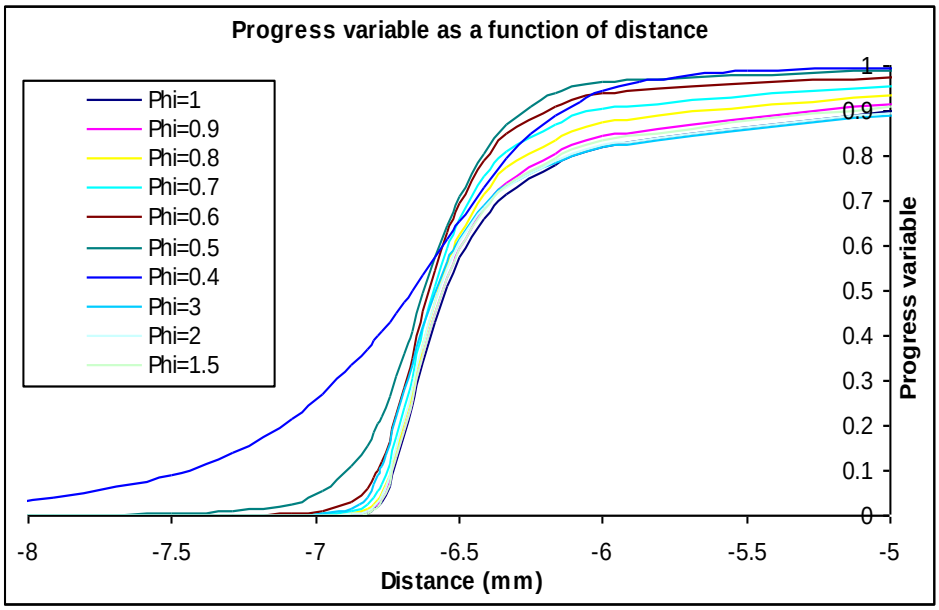

Figure 4.13: Progress variable as a function of distance for undiluted hydrogen-air flames

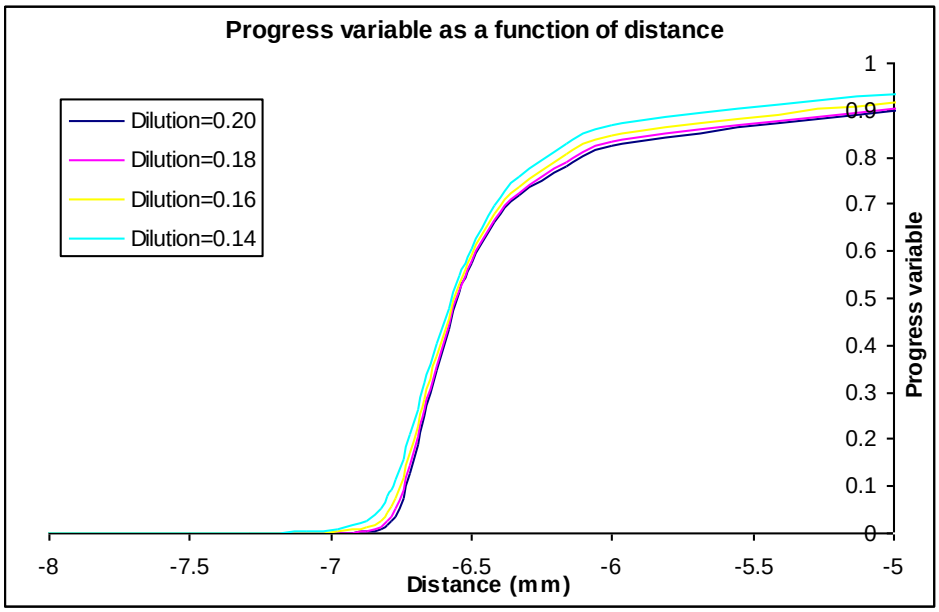

Figure 4.14: Progress variable as a function of distance for values of dilution of 0.20, 0.18, 0.16, and 0.14 and equivalence ratio of 1

The laminar flame thickness was calculated using the following formula:

$$\delta_L = 5 * D\left(c_{T\,0.6} - c_{T\,0.4}\right) \tag{4.4}$$

in which, $D(c_{T0.4} - c_{T0.6})$ is the distance separating in the flame the values of the progress variable c_T of 0.4 and 0.6.

Graph 4.15 shows the laminar flame thickness as a function of the equivalence ratio:

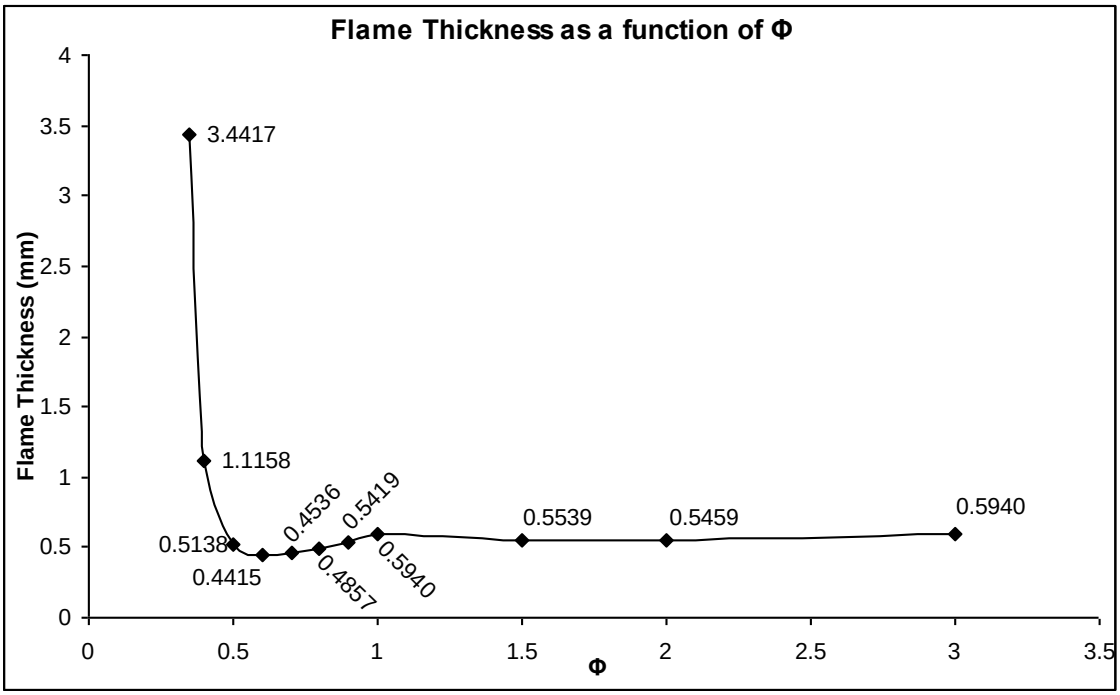

Figure 4.15: Flame thickness as a function of the equivalence ratio

As could be expected, the flame thickness varies with the equivalence ratio. It is maximum for lean mixtures. It steeply decreases until equivalence ratios of 0.6 are reached. Then, the flame thickness stays almost constant for mixtures with an equivalent ratio higher than 0.6.

The following graph shows the flame thickness as a function of dilution. It can be observed that the flame thickness does not vary much with the dilution. It very slowly increases as nitrogen is added to the mixture. Within the limits of the present study, we assumed the behaviour of the flame thickness as a function of the dilution to be linear. We found the following equation:

$$\delta_L = -0.224 * Dilution + 0.645 \qquad (4.5)$$

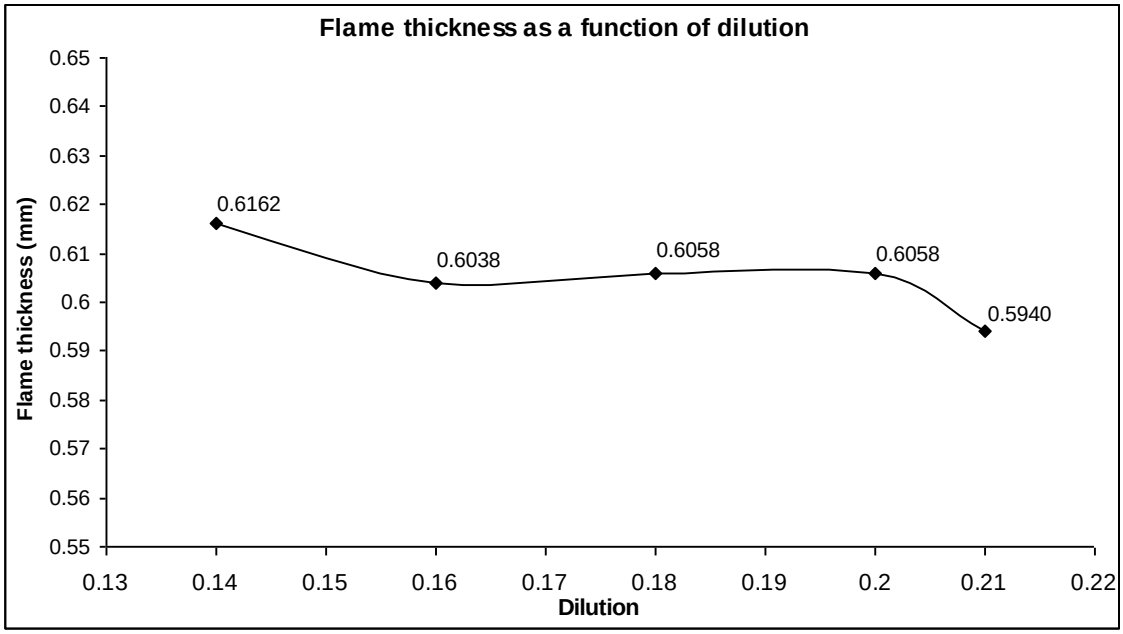

Figure 4.16: Flame thickness as a function of dilution for nitrogen diluted hydrogen/air flames with an equivalence ratio of 1

4.1.2.3 Extrapolation for the flames studied

Figure 4.17 shows the extrapolated curve for the unstrained laminar flame speed as a function of the equivalence ratio for a dilution of 0.105.

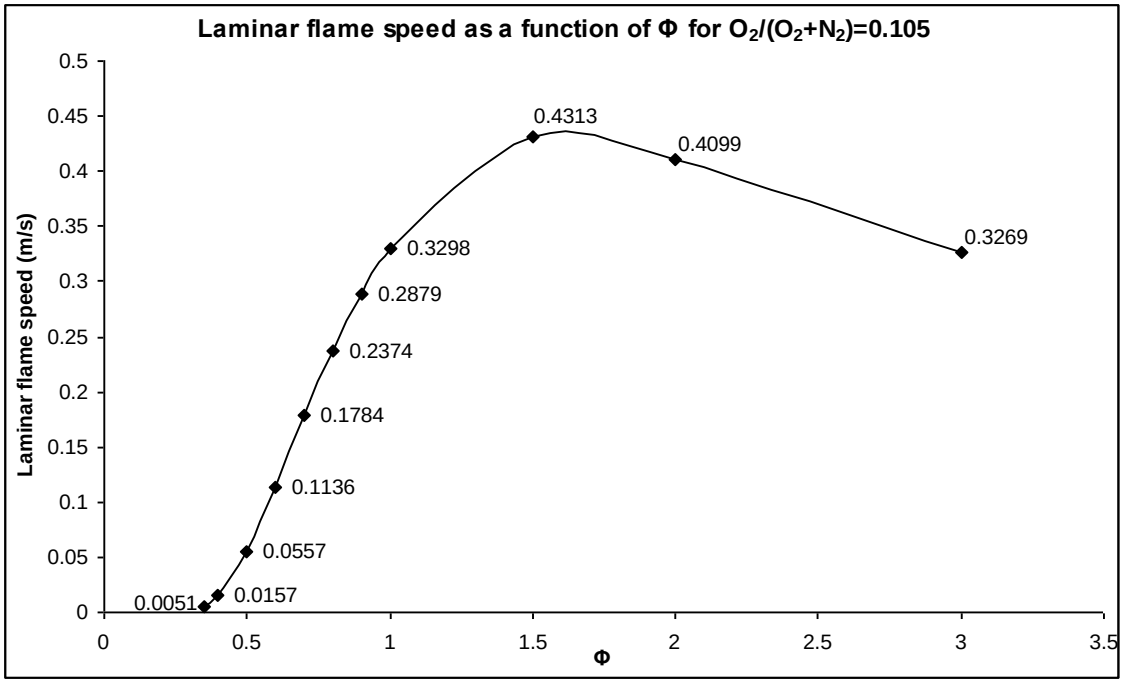

Figure 4.17: Extrapolated values of the unstrained laminar flame speed as a function of the equivalence ratio for a dilution value of 0.105

Figure 4.18 shows the extrapolated curve for the laminar flame thickness as a function of the equivalence ratio for a dilution of 0.105.

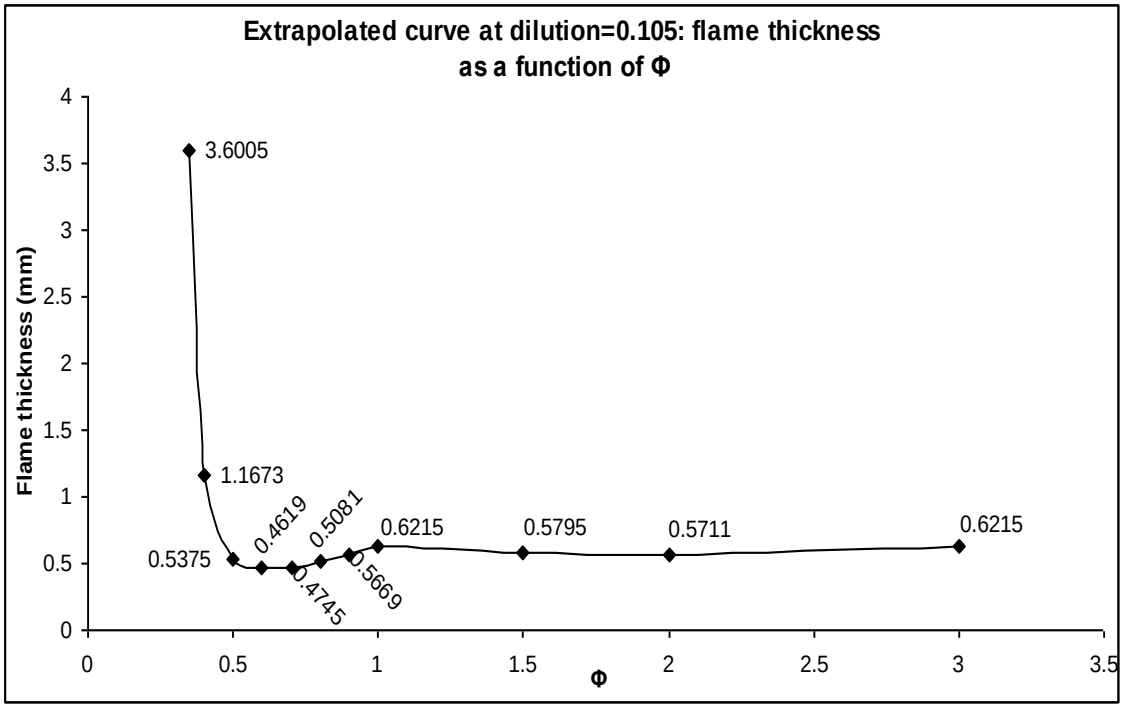

Figure 4.18: Extrapolated values of the flame thickness as a function of the equivalence ratio for a dilution value of 0.105

To sum up, table 4.5 shows the unstrained laminar flame speed and laminar flame thickness of the flames studied in the present work:

Flame	Dilution	Φ	S_L (m.s^{-1})	δ_L (mm)
A	0.106	0.38	0.001	1.17
B	0.106	0.54	0.079	0.54
C	0.106	0.75	0.208	0.49
D	0.106	0.54	0.079	0.54
E	0.106	0.76	0.214	0.50
F	0.098	0.75	0.208	0.49
G	0.105	0.38	0.001	1.17
H	0.105	0.53	0.073	0.54
I	0.106	0.38	0.001	1.17

Table 4.5: Unstrained laminar flame speed and laminar flame thickness for the flames studied

4.1.3 Hot wire anemometry experiments

4.1.3.1 Principles

Constant temperature anemometry also called hot-wire anemometry [106] allows point-measurement of instantaneous fluid flow velocities and flow fluctuations.

A probe, which can be a film or a wire, is electrically heated to a fixed temperature. A measure of the heat loss experienced by the probe gives information on the flow. Indeed, the heat loss depends on the temperature of the fluid, its properties, the probe itself – its properties and its temperature – and the configuration of the probe in the fluid.

On the one hand, the power necessary to maintain a wire at a constant temperature is [106]:

$$W = R_p I^2 = \frac{V^2}{R_p} \tag{4.6}$$

with V the voltage, R_p the resistance of the probe and I the current.

On the other hand, this power is needed for, at first, the storage of the thermal energy in the wire and then, to compensate for the loss of heat of the probe to its environment [106]:

$$W = \frac{dc_w T_p}{dt} + \pi l d_w h(T_p - T_m) \tag{4.7}$$

where c_w is the specific heat of the wire, l is the characteristic length of the wire, d_w is the diameter of the wire, h the coefficient of heat transfer, T_p is the temperature of the probe and T_m is the temperature of the fluid medium.

In the steady-state regime, the power used to keep the wire at a constant temperature compensates the heat loss only [106]:

$$\frac{V^2}{R_p} = \pi\, l\, d_w\, h(T_p - T_m) \tag{4.8}$$

The dimensionless Nusselt number, *Nu*, compares the convective heat transfer and the conductive heat transfer [106]:

$$Nu = \frac{h d_w}{k_f} \tag{4.9}$$

where k_f is the heat conductivity of the fluid medium.
It was found that the Nusselt number could be expressed as a function of the Reynolds number [106].

$$Nu = A + BRe^n \tag{4.10}$$

The Reynolds number compares the inertial forces to the viscous forces in fluid flows.

$$Re = \frac{\rho_{fm} U_f L}{\mu_{fm}} \tag{4.11}$$

where ρ_{fm} is the density of the fluid medium and μ_{fm} its dynamic viscosity.

Hence, readings of the voltage provide us with a measure of the flow velocity [106].

$$\frac{V^2}{R_p} = A' + B' U^n \tag{4.12}$$

which is known as King's Law.

Figure 4.19 shows the experimental apparatus needed to measure both the mean velocity $\bar{U}$ and the fluctuating component of the velocity *u'* i.e. the standard deviation of the velocity over time.

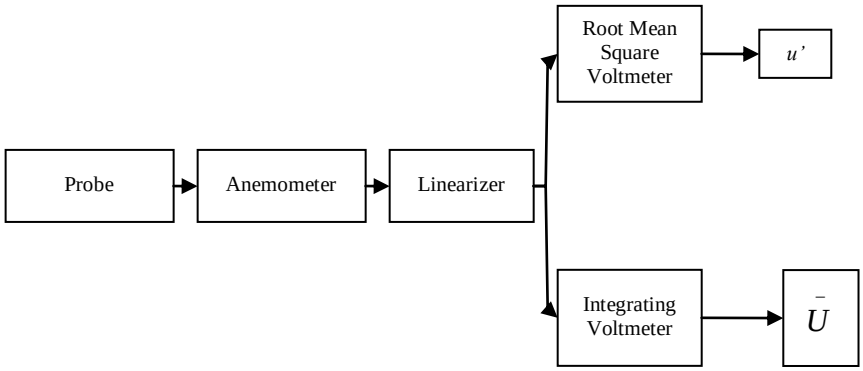

Figure 4.19: Typical measuring chain in a hot wire anemometry experiment

In the present work, the frequency of the velocity fluctuations was unknown. The time constants chosen for the mean velocity and the fluctuating velocity were determined experimentally so as to obtain a stable meter reading.

4.1.3.2 Experiments

In the following experiments, two Dantec Dynamics 55P11 probes were used because the first one was broken during the experiments. They are 5µm diameter Pt-plated tungsten wire of length 1.25mm.

They were calibrated in air between 0 $m.s^{-1}$ and ~20-30 $m.s^{-1}$.

For the experiments, the probes were placed vertically 20 mm over the burner described in section 4.1.1 on the centre line of the inner nozzle.
Air was flushed through the inner nozzle of the burner at different velocities: ~1, 2, 2.5, 3, 5, 6, 8 and 10$m.s^{-1}$. The probes were swept on a diameter across the inner nozzle and measurement occurred every 3 mm between -15 and +15mm. A vertical sweep was also recorded between 0 mm and 45 mm every 5 mm on the centre line of the inner nozzle for an estimated velocity of the air of 3$m.s^{-1}$.

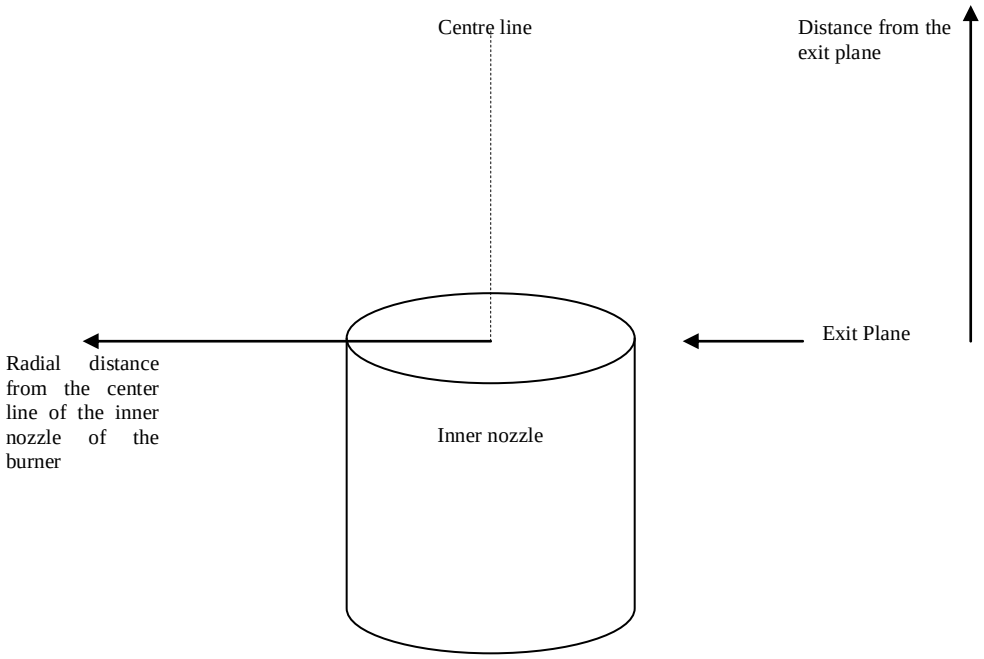

Figure 4.20: Geometry of the experiments

The results of the calibration and of the experiments can be found in section 4.1.3.3.

4.1.3.3 Results

4.1.3.3.1 Calibration curves of the probes

The voltage was given by the integrating voltmeter.

The calibration was performed with pressurised air going through a nozzle. The upstream and downstream static pressures were recorded as well as the temperature before the nozzle. The density of the air was calculated using the perfect gas law. The velocity of the air was calculated using the Bernoulli equation and the continuity equation knowing the ratio of the cross-sections:

$$v = \sqrt{\frac{2*(P_1 - P_2)}{\rho_{air}\left(1-\left(\frac{A_2}{A_1}\right)^2\right)}} \qquad (4.13)$$

with P_1 and P_2 respectively the upstream and downstream pressure and $\frac{A_2}{A_1}$ the ratio of the cross-sections.

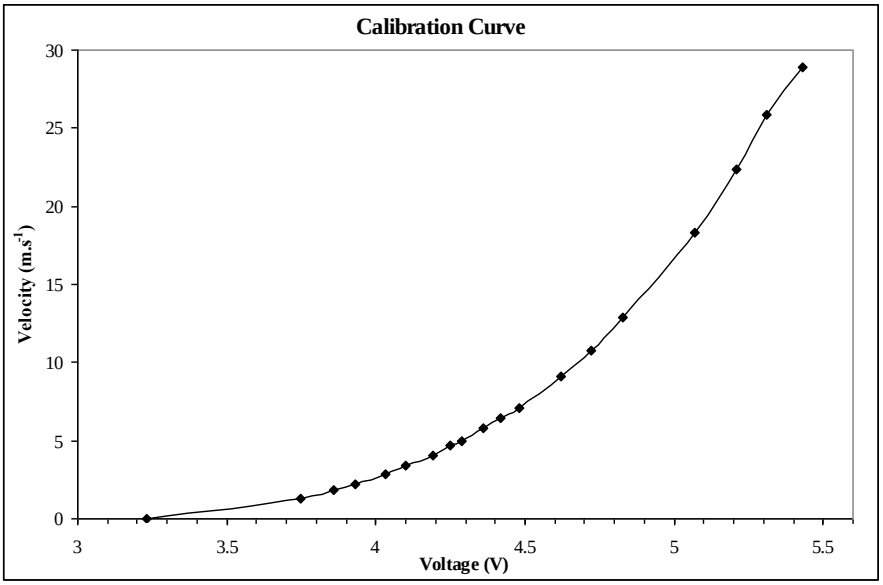

Figure 4.21: Calibration curve of the first probe

The calibration curve for the first probe used was fitted with a third order polynomial:

$$U = 2.1369 * V^3 - 20.1300 * V^2 + 64.8600 * V - 71.484 \qquad (4.14)$$

The curve fitting was good; the value of R^2 is 0.9996.

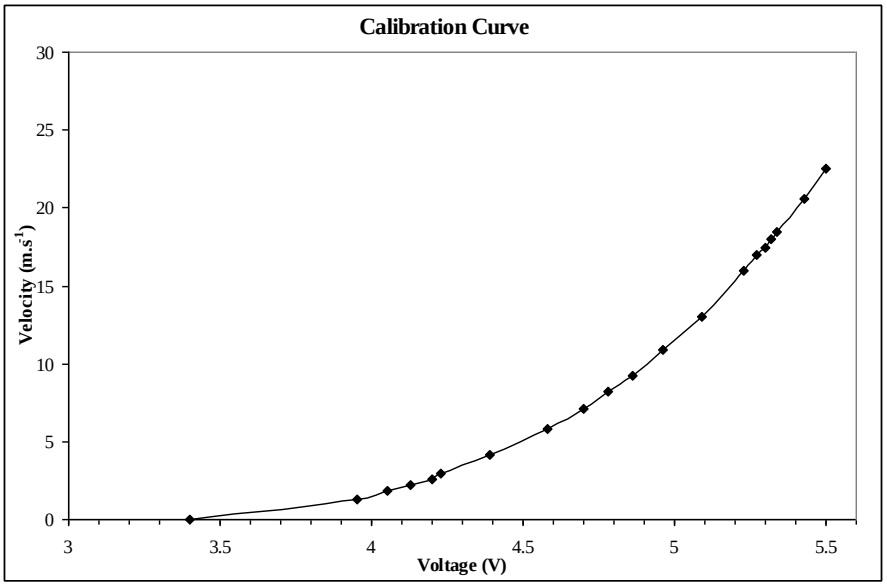

Figure 4.22: Calibration curve of the second probe

As for the first probe, the calibration curve for the second probe was also fitted with a third order polynomial:

$$U = 1.6256 * V^3 - 15.6270 * V^2 + 51.4330 * V - 58.131 \qquad (4.15)$$

The curve fitting was also good with a value of R^2 of 0.9999.

The two previous equations were derived. The plots of the equations $\frac{dU}{dV} = f(V)$ are shown in figure 4.23 and in figure 4.24. They will be used to determine the velocity fluctuations *u'*.

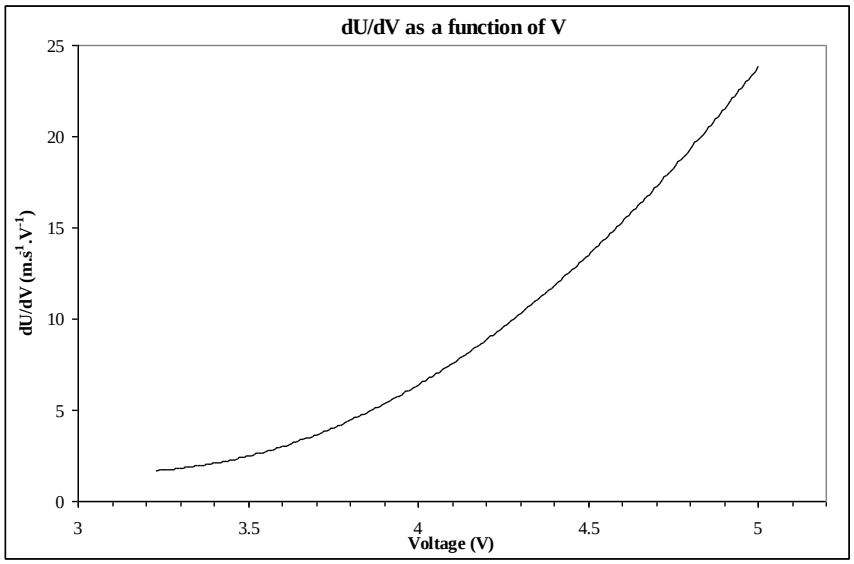

Figure 4.23: Curve linking dU/dV and V for the first probe

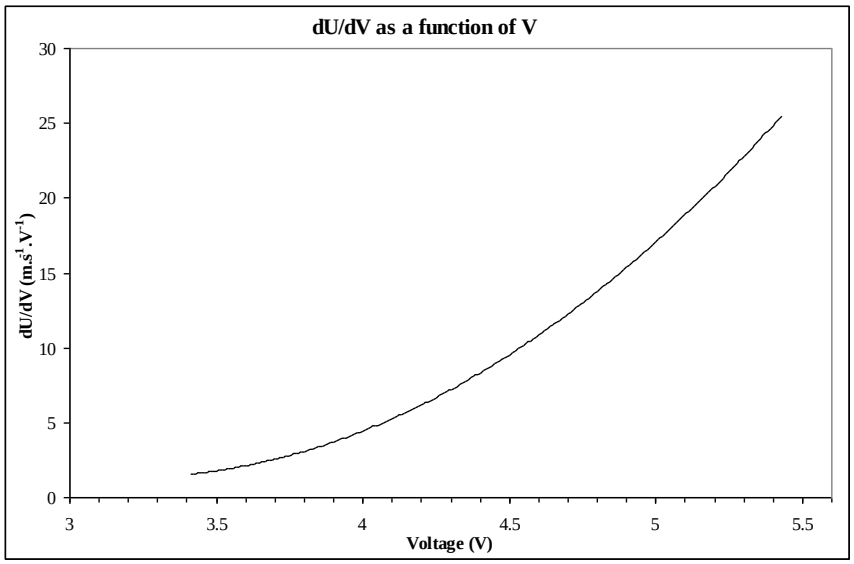

Figure 4.24: Curve linking dU/dV and V for the second probe

4.1.3.3.2 Results

The value of *u'* was calculated using the following formula:

$$u' = e * \frac{dU}{dV} \tag{4.16}$$

where *e* is the value given by the root mean square voltmeter.

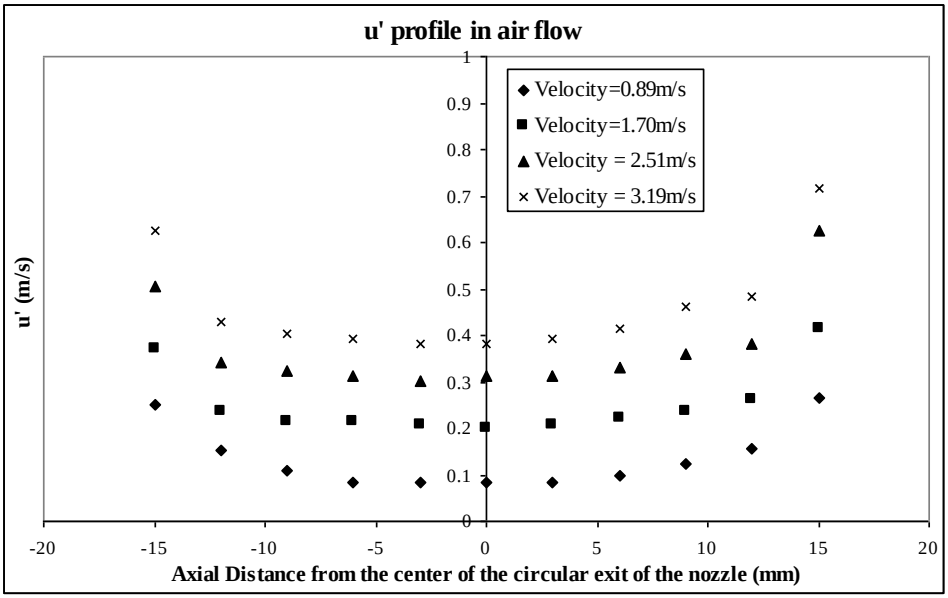

Figure 4.25: Radial profile of the fluctuating component of the velocity in air flows in the inner nozzle of the burner

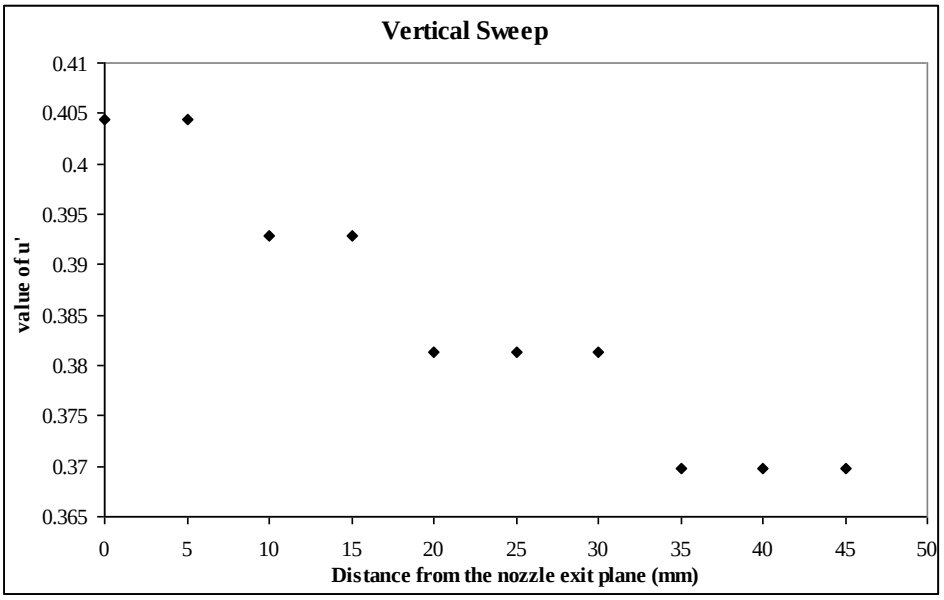

Figure 4.26: Axial profile of the fluctuating component of the velocity in air flows on the centre line of the inner nozzle of the burner

The features of the previous graph (figure 4.26) can be explained by the fact that the measurement of u' has a limited resolution, which is of the order of ~0.01 m/s. That represents an uncertainty of ~3% on the measurement.

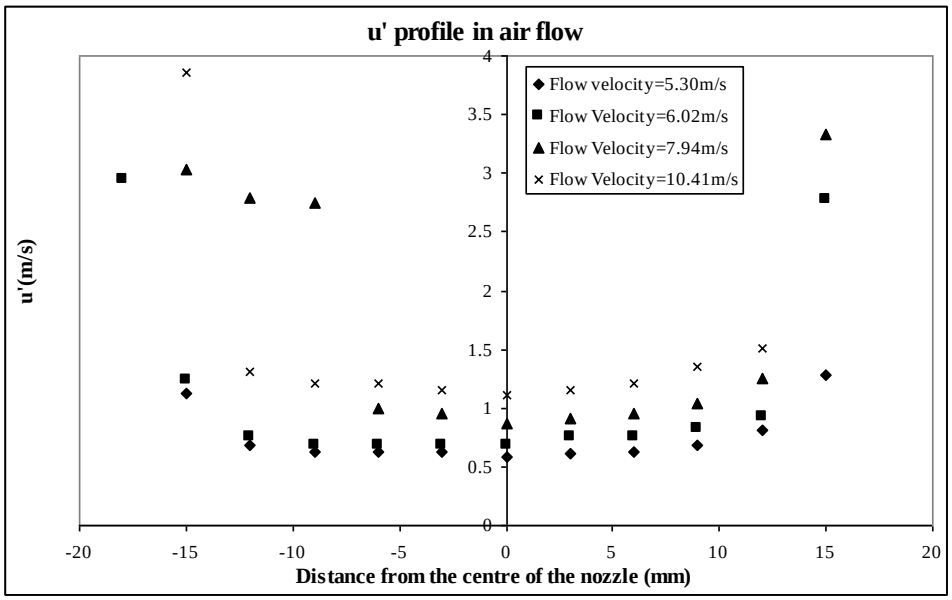

Figure 4.27: Radial profile of the fluctuating component of the velocity in air flows in the inner nozzle of the burner

4.1.3.4 Interpretation of the results

The results shown in paragraph 4.1.3.3.2 were extrapolated for other mixtures.
It was assumed that similar behaviour of the burner as the one observed in air would be encountered for the same Reynolds number. Corrections were applied taking into account the change in kinematic viscosity. The kinematic viscosity values were taken from the *Gaseq* program [95].

Figure 4.28 shows the results obtained:

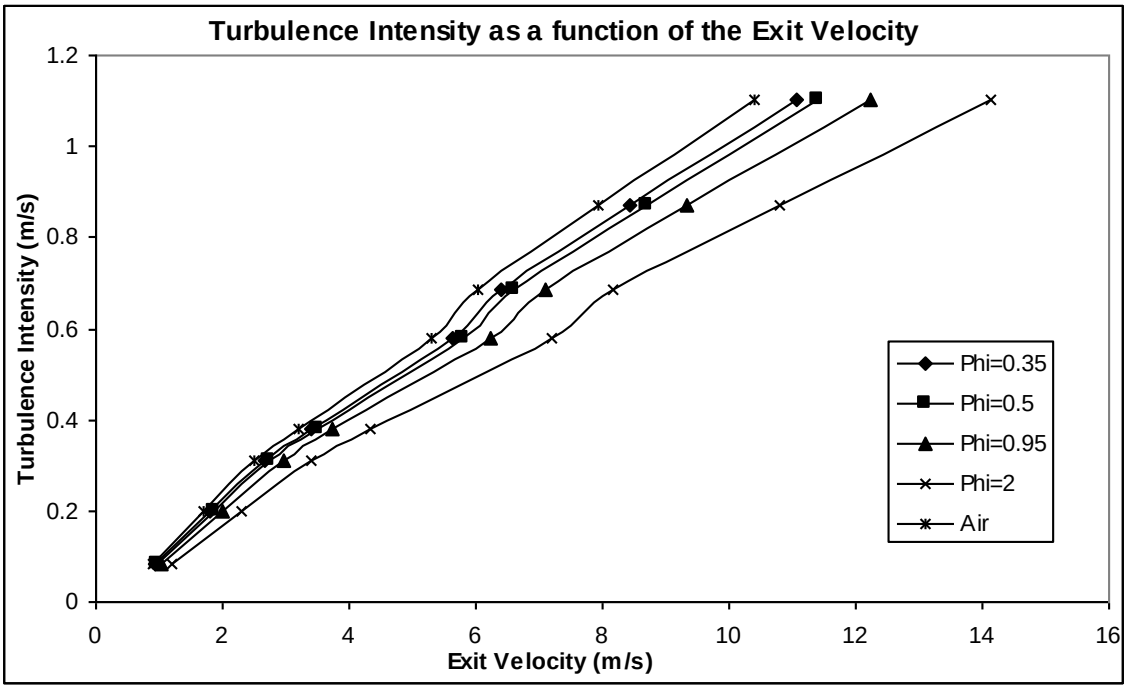

Figure 4.28: Turbulence intensity as a function of the exit velocity for hydrogen-diluted air mixtures corresponding to flames with a dilution ratio of 0.105 and an equivalence ration between 0.35 and 2

The cases studied were diluted air-hydrogen mixtures corresponding to flames with a dilution ratio of 0.105 and equivalence ratios between 0.35 and 2.

A linear regression was performed in each case. The following equations were found:

Fluid	$u' = f(\bar{U})$	
Air	$u' = 0.1058 * \bar{U} + 0.0259$	(4.17)
φ=0.35	$u' = 0.0995 * \bar{U} + 0.0259$	(4.18)
φ=0.50	$u' = 0.0967 * \bar{U} + 0.0259$	(4.19)
φ=0.95	$u' = 0.090 * \bar{U} + 0.0259$	(4.20)
φ=2.00	$u' = 0.0779 * \bar{U} + 0.0259$	(4.21)

Table 4.6: Equations between u' and $\bar{U}$ for air and different mixtures

The turbulence intensity lies around 10% of $\bar{U}$ for the mixtures we are interested in. The values used for *u'* in section 4.1.4 were calculated in the same way.

4.1.3.5 Uncertainties on the measurements

The uncertainties were evaluated following the guidelines given in [106].

The uncertainties on the velocity measurement coming from the calibration procedure account for a relative standard uncertainty of 1%, the linearisation account for 0.5%, the A/D resolution for 0.13%, the uncertainty on the overtemperature of the probe for 0.8% and on the temperature of the fluid medium for 0.2%, the uncertainty on the pressure for 0.6%, the uncertainties on the probe positioning and the humidity of the gases were neglected.

The total uncertainty (2σ i.e. twice the standard deviation) on the velocity and velocity fluctuations lie around 3%.

4.1.4 Theoretical characterisation of the flames

The places of the previous flames on the Borghi diagram were determined and their traditional non-dimensional numbers evaluated.
The integral length scale L was estimated at 15mm, values which was determined in a previous work on the burner [94].

The root-mean-square of the turbulent velocity fluctuations u' was extrapolated using hot wire anemometry results obtained using air through the burner at different flow rates (section 4.1.3).

The laminar flame speed S_L and the flame thickness δ_L were extrapolated from data obtained using the Chemkin 4.1 software [15] (section 4.1.2).

The results are presented in table 4.7:

Flame	L (mm)	u' (m.s^{-1})	S_L(m.s^{-1})	δ_L(mm)	Ka	Da	Regime
A	15	0.45	0.0114	1.17	69.4	0.33	Thin or Broken reaction zones
B	15	0.45	0.0789	0.54	2.7	4.91	Thin reaction zones
C	15	0.45	0.2079	0.49	0.5	14.09	Corrugated flames
D	15	0.34	0.0789	0.54	1.7	0.65	Thin reaction zones
E	15	0.34	0.2138	0.50	0.4	18.75	Corrugated flames
F	15	0.28	0.2079	0.49	0.3	23.85	Corrugated flames
G	15	0.55	0.0114	1.17	93.8	0.27	Broken reaction zones
H	15	0.55	0.0731	0.54	3.8	3.73	Thin reaction zones
I	15	0.66	0.0114	1.17	123.5	0.22	Broken reaction zones

Table 4.7: Summary of the characteristics of the flames studied

The definitions of the Karlovitz and Damköhler numbers were given in chapter III (equations 3.7 and 3.8).

4.2 Experimental set-up for combined NO-PLIF and SPIV measurement

4.2.1 Equipment used for combined NO-PLIF and SPIV measurement

In the present work, NO-PLIF was used to determine the flame front contour and the vectors normal to the flame front and stereoscopic PIV was used to determine the velocity fields and strain rates fields. Care was taken to ensure a high spatial resolution and a good signal to noise ratio. The 3D velocities were measured with a resolution of 256 microns. The resolution of the raw NO-PLIF images was 48 microns. The time resolution of the measurement was 1s.

For the NO-PLIF diagnostic, a LAMBDA PHYSIK dye laser was used with the coumarin 445 dye in methanol. The Coumarin 445 (7-(ethylamino)-4-methyl-2H-1-benzopyran-2-one) was obtained from the Exciton Company.

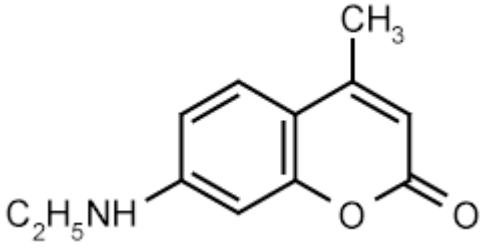

Figure 4.29: The Coumarin 445 molecule

According to the Exciton laser wavelength chart [107], Coumarin 445 emits between 430 and 474 nm. The signal frequency was then doubled using a KD*P crystal. The dye laser was tuned at 225.980 nm to excite the $R_{11}+^{R}Q_{21}(9.5)$ line in the $A^2\Sigma^+$-$X^2\Pi$ $\gamma(0,0)$-band of NO. The dye laser was pumped by a Quanta-Ray GCR Series pulsed Nd:YAG laser system. The 1064nm fundamental was frequency doubled with a KD*P crystal. The resulting 532 nm wave was then mixed with the fundamental to produce a signal at 355 nm which is the excitation wavelength of the coumarin 445 dye in methanol with a Nd:YAG laser. The Nd:YAG laser output was controlled using two delay generators, *Stanford Research Systems'* DG 535.

The NO-PLIF signal was recorded onto a *Princeton Instruments* red-blue enhanced ICCD camera. The camera was controlled by the *Princeton Instruments* Model ST-138 camera controller and detector. The images were recorded using the *WinView95* software, which is a data acquisition software. The images obtained were 576*384 pixel arrays.

For the SPIV diagnostic, a *Spectra-Physics* Quanta-Ray PIV 400 pulsed Nd:YAG laser was used. It consists of two GCR 170 resonators i.e. dual rod oscillators. The 532 nm output was generated using a Type II KD*P crystal in the harmonic generator. The output at 532 nm is specified at 350 mJ per pulse in a standard polarisation configuration i.e. the 532 nm output beam vertically polarised.

The PIV images were recorded using two *LaVision* FlowMaster CCD cameras. Their chip size was 1280*1024 pixels. The images were recorded using the *LaVision* DaVis 7.1 software package [60-61], which is a CCD image acquisition and processing program developed by LaVision. It is also designed to control cameras and lasers.

Figure 4.30 shows a scheme of the experimental set-up and figures 4.31 and 4.32 show photographs of the arrangement of the NO-PLIF and PIV cameras and of the optical set-up.

4.2.2 Experimental set-up

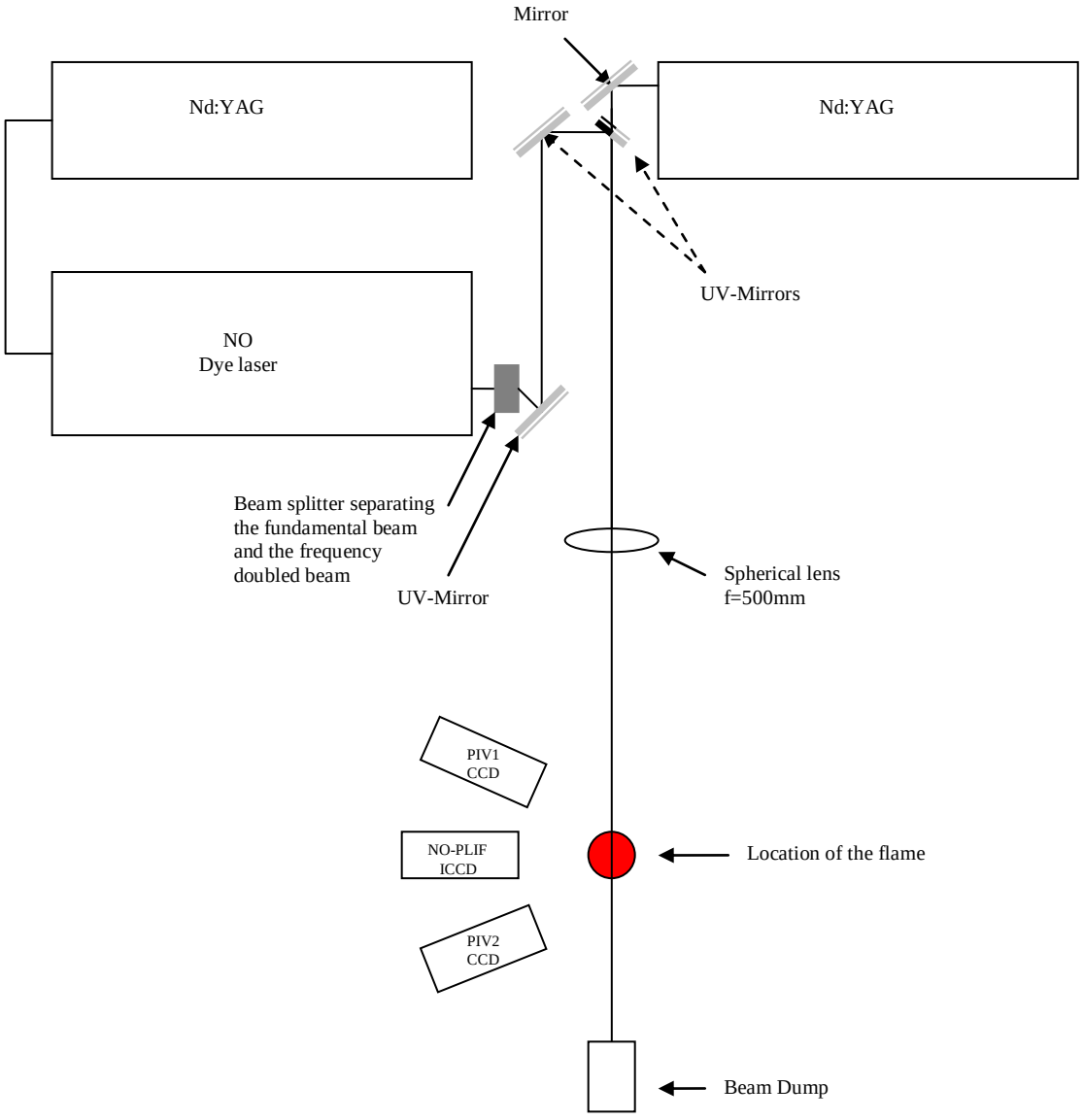

Figure 4.30: Experimental set-up for combined NO-PLIF and SPIV

The NO-PLIF ICCD camera and the two SPIV CCD cameras were placed on the same side of the light sheets. The NO-PLIF ICCD camera was facing the plane of the light sheet. For experimental convenience, the SPIV CCD cameras were on each side of the NO-PLIF camera at an angle of 45˚. As a consequence, both PIV cameras were on the same side of the light sheets in a so-called "Backward-Forward-Scattering" arrangement. The PIV camera on the left hand side in figure 4.31 was recording the light scattered in the backward direction while the PIV camera on the right hand side was recording the light scattered in the forward direction. As could be expected, the intensity of the light scattered in the backward direction was significantly lower than the intensity of the light scattered in the forward direction. As a consequence, the lens of the camera recording the backward scattered light needed a larger aperture. The experimentally chosen f-number for the lens of the camera recording the backward scattered light was 4 while the f-number for the lens of the camera recording the forward scattered light was 5.6. Both SPIV cameras had 532 nm filters with a FWHM of 10 nm. The angle between the two PIV cameras was chosen at 90˚ because the measurement of the out-of-plane component of the velocity is optimal in that configuration.

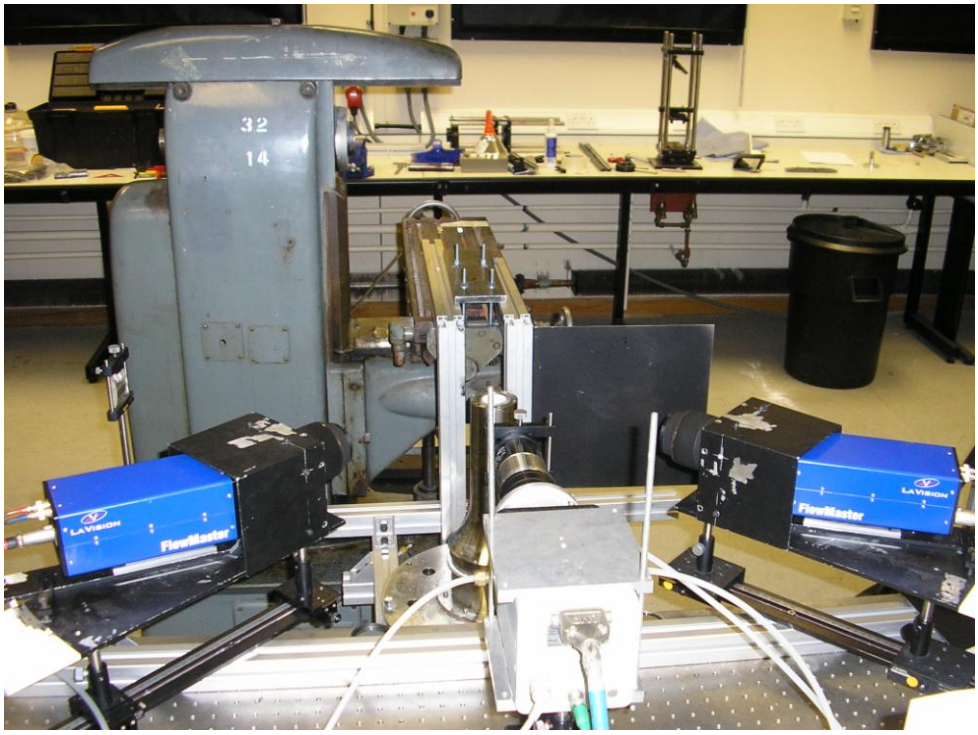

Figure 4.31: Camera arrangement for combined NO-PLIF and SPIV measurements

A disadvantage of the experimental set-up shown in figure 4.31 is that because the PIV cameras are at an angle with regard to the object plane, the recorded images are strongly distorted. The magnification changes across the image. The solution to this problem consists in further tilting the camera on its axis. The angle between the initial position of the camera and the correct position is called the Scheimpflug angle. In the present experiments, the Scheimpflug angle was determined empirically. A calibration plate was placed at the exact position of the light sheet and the cameras were rotated until the area of interest was fully focused for both cameras.

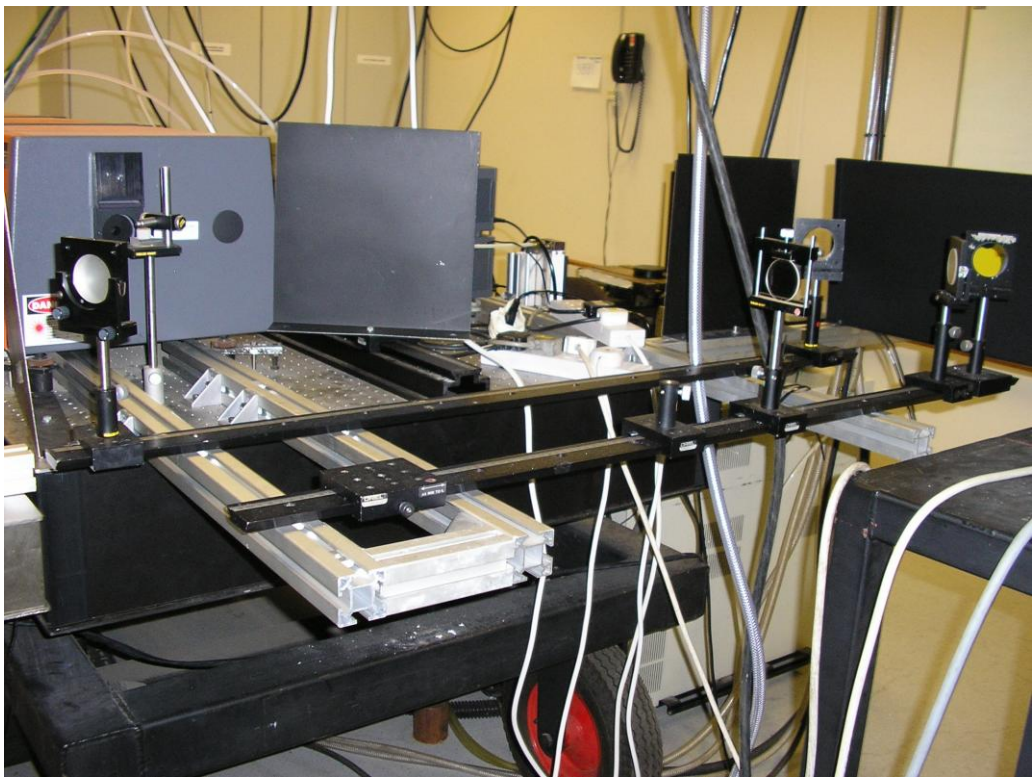

Figure 4.32: Optical arrangement for combined NO-PLIF and SPIV measurements

4.2.3 Timing Configuration

This section describes the timing sequence used for the combined NO-PLIF and SPIV experiments.

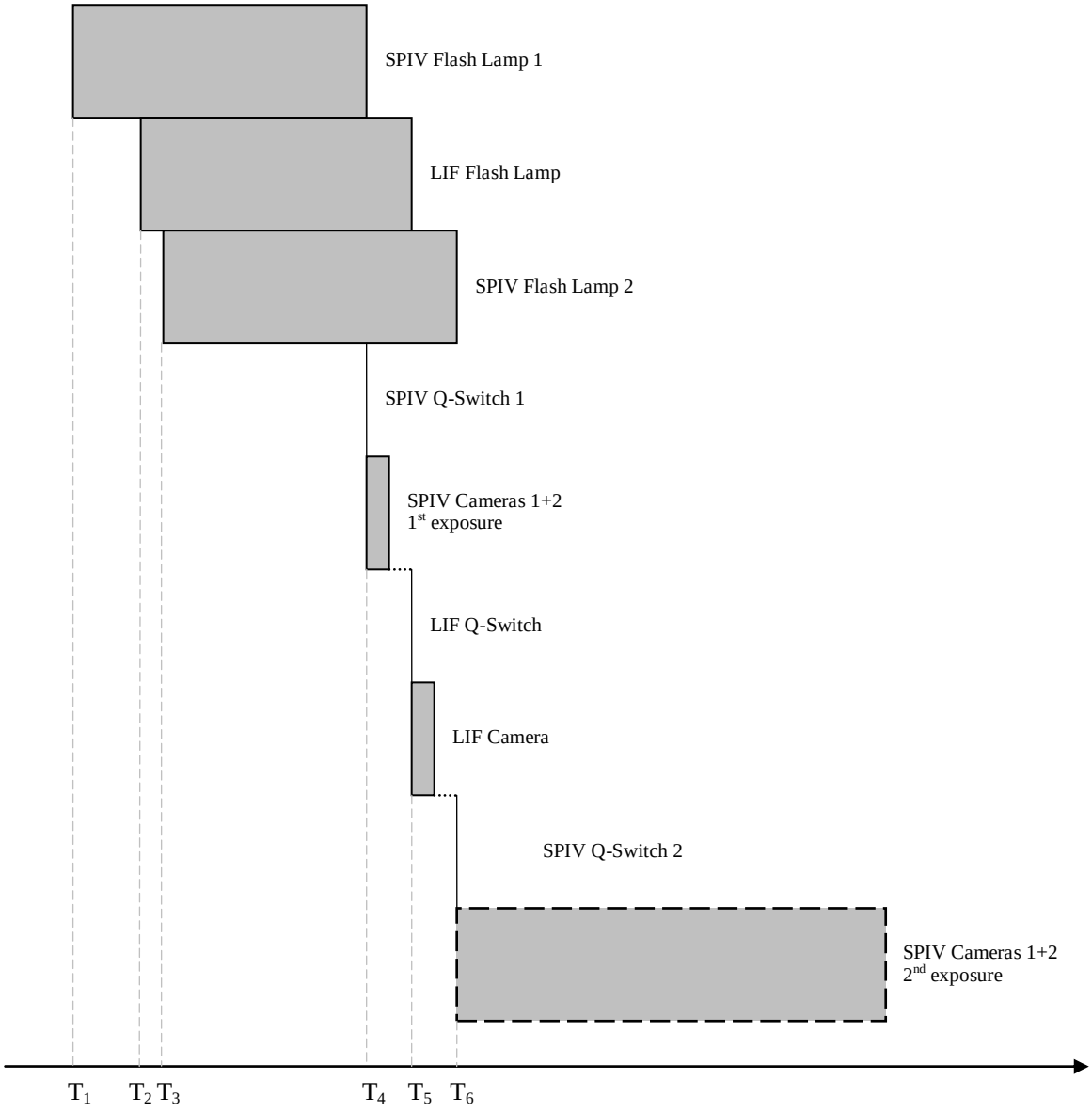

T_1	0	SPIV Flash lamp 1
T_2	23μs	LIF Flash lamp
T_3	25μs	SPIV Flash lamp 2
T_4	186μs	SPIV Q-switch 1
T_4	186μs	SPIV Camera 1+2 First exposure 10μs
T_5	198μs	LIF Q-switch
T_5	198μs	LIF Camera exposure 1μs
T_6	211μs	SPIV Q-switch 2
T_6	211μs	SPIV Camera 1+2 Second exposure 125ms

Figure 4.33: Timing configuration description

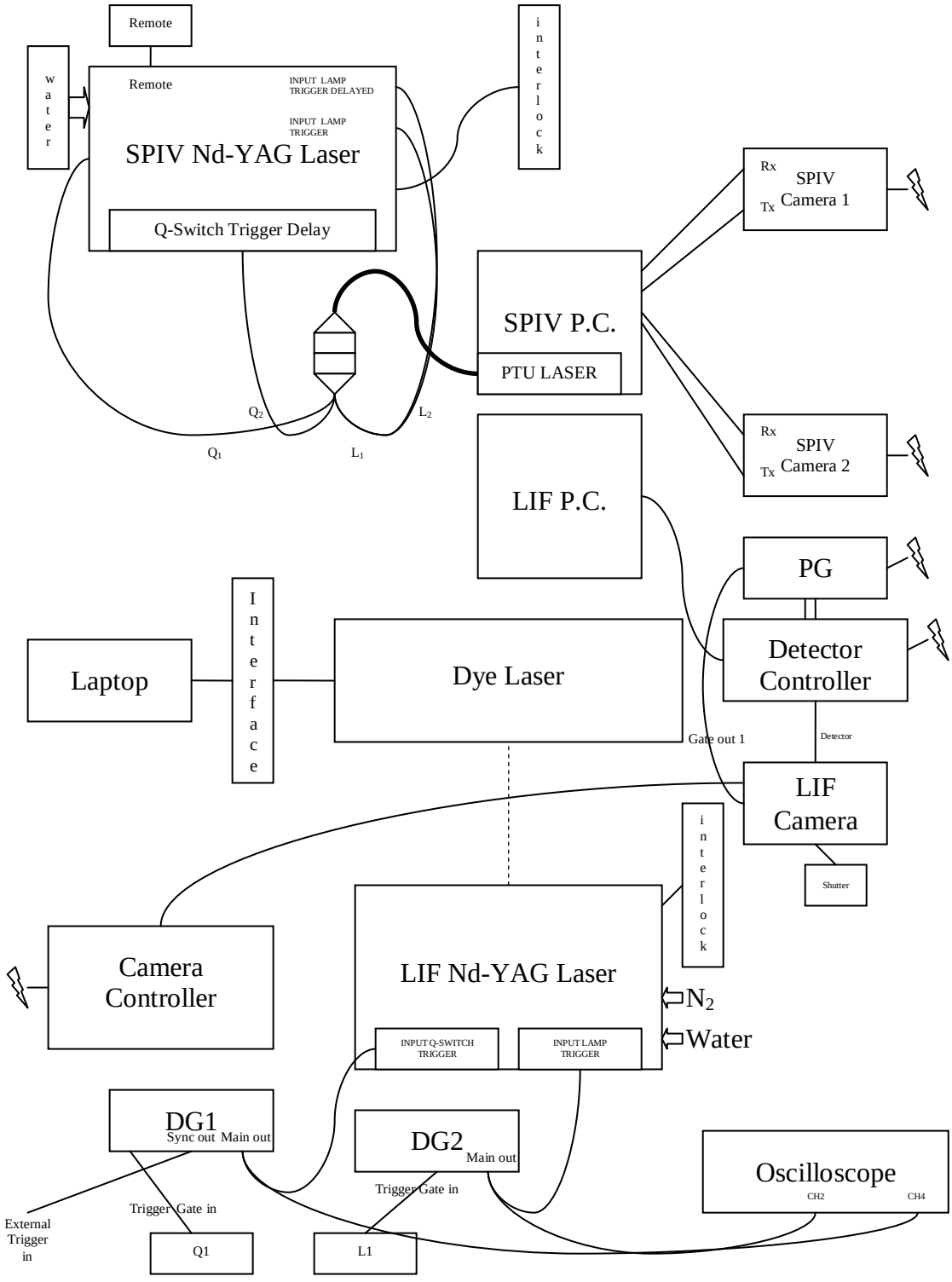

<u>Figure 4.34</u>: Connections between the different pieces of equipment

Figure 4.34 shows the connections between the different pieces of equipment.
Figure 4.33 shows the sequencing of the various signals.

The set-up of the SPIV equipment is quite straightforward. Both cameras are connected to the P. C. The SPIV Nd:YAG laser is also connected to the P.C. The SPIV Nd:YAG laser and both cameras were controlled by the DaVis 7.1 software package [60-61]. The delay between the flash lamp and the Q-switch is optimal at 186μs. The first exposure time can be chosen. In the present work, the first exposure was 10μs long. The second exposure time cannot be changed. The second exposure is always 125ms long. The delay between the two pulses was set at 25μs. This delay allows an optimal resolution of the bulk flow velocities. Both cameras were also simultaneously triggered by the computer at the same time as the Q-switch trigger.

The set-up of the LIF equipment is a little less straightforward. For the LIF experiments, only one pulse is needed and the LIF pulse occurred between the two SPIV pulses.
To synchronise the experiments and to control Nd:YAG laser, as previously mentioned, two delay generators were used: one of them triggers the flash lamp while the other triggers the Q-switch of the laser. The flash lamp is triggered by the first flash lamp TTL signal from the SPIV laser via the delay generator and after a delay of 23μs. The Q-switch is triggered by the first Q-switch TTL signal from the SPIV laser via the delay generator after a delay of 12μs. The delay between the flash lamp and the Q-switch for the LIF Nd:YAG was optimal at 175μs. The signals coming out of the pulse generators and triggering the flash lamp and Q-switch of the LIF Nd:YAG were monitored by an oscilloscope.
The LIF camera needs a considerably shorter exposure time (1μs) to avoid eventual scattering of the light by particles in the flame and to reduce the background signal to its lowest level. The camera was triggered by the Q-switch TTL signal from the SPIV Nd:YAG laser via its controller/pulse generator after a delay of 12μs.

4.2.4 Calibration of the data

4.2.4.1 Calibration of the SPIV images

The calibration device consists in a flat calibration plate with equidistant dots. The dots had a diameter of 1mm and they were spaced by 3mm.

The calibration grid was generated using Microsoft PowerPoint.

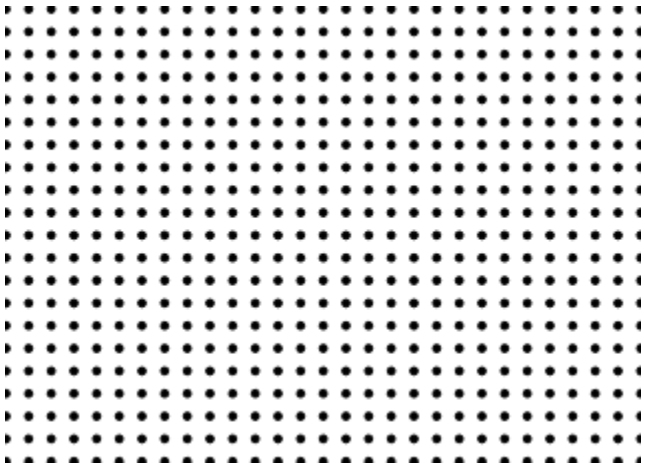

Figure 4.35: Microsoft PowerPoint generated calibration grid

The calibration plate was glued onto a 15mm thick flat aluminium support which was attached at its base to an aluminium rectangle. The support for the calibration plate and the rectangle to which it was attached formed an L. They were screwed onto a translation stage and could move forward and backward. The translation stage was screwed onto a stainless steel cylinder which fitted the top of the burner. The translation stage could be rotated around the axis of the burner. The laser sheet and the calibration plate needed to be perfectly aligned for the calibration. To allow a correct alignment, the rotation of the calibration plate around the axis of the burner could be finely adjusted using a screw which was attached at one side of the translation stage. The screw was stopped against a stainless steel rectangle attached to one side of the burner. The rotation of the translation stage was kept on the chosen position by an elastic rubber band. (figure 4.36)

Figure 4.36: Calibration plate and its support used for the experiments

In the stereo-PIV configuration used and with a flat calibration plate, three calibration images for each camera need to be recorded at three different parallel positions.

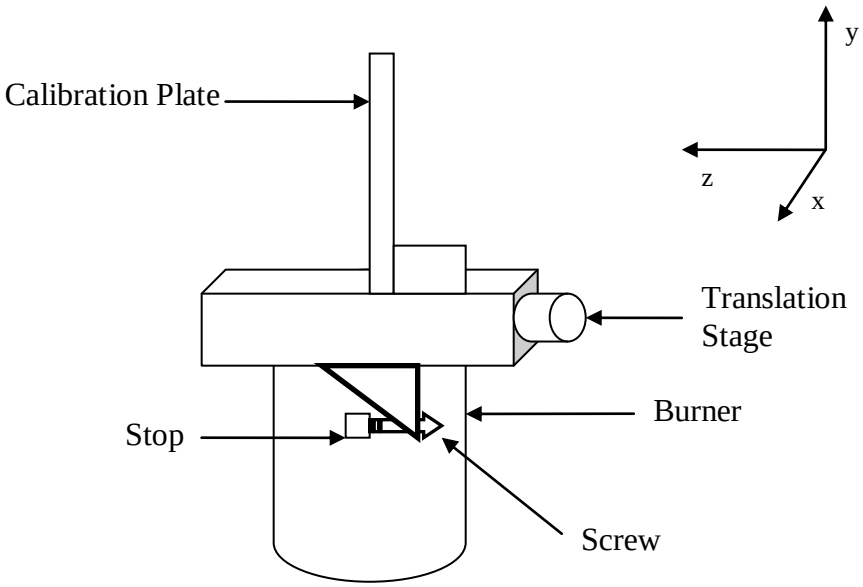

Figure 4.37: Sketch of the calibration device and its orientation

Figure 4.37 shows the orientation chosen for the calibration procedure. The first position for which a calibration image is needed corresponds to the level z=0. The level z=0 corresponds to the case when the calibration grid is perfectly aligned with

the laser sheets. The two other calibration images were recorded at z=-0.5mm and +0.5mm.

Figure 4.38 and 4.39 show a set of calibration images recorded for the stereo-PIV. The first image on the left corresponds to z=+0.5mm, the second to z=0mm and the third to z=-0.5mm. Camera 1 records the forward scattering while camera 2 records the backward scattering.

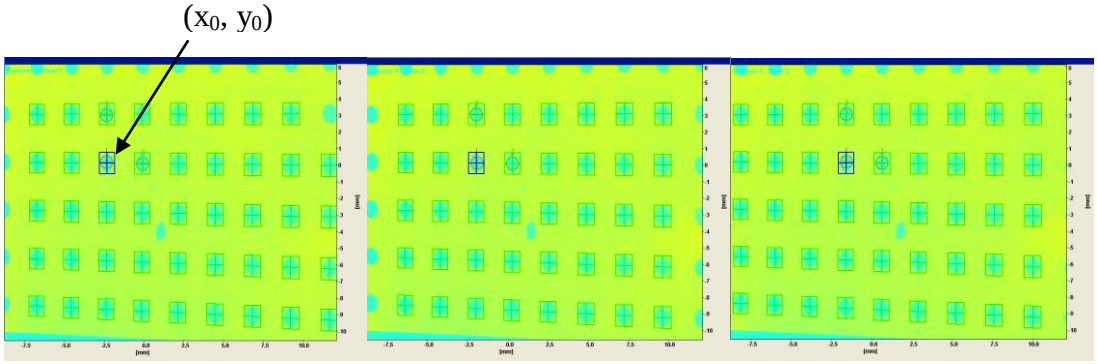

Figure 4.38: Averaged calibration images for the SPIV camera 1

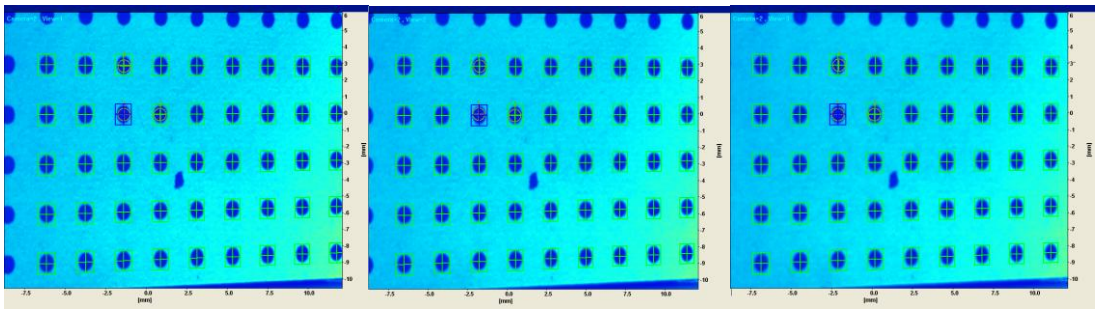

Figure 4.39: Averaged calibration images for the SPIV camera 2

Each of the six calibration images is an average of 5 instantaneous images.

The calibration consists in calculating all the parameters (a_0 to a_9 and b_0 to b_9) in a polynomial of 3rd order for both dimensions x and y to link the raw coordinates (x,y) which are the coordinates in the images to the corrected coordinates (x', y') which are the coordinates in real physical space:

$$(x, y) = (x' + dx(x', y'), y' + dy(x', y')) \tag{4.22}$$

where

$$dx = a_0 + a_1 s + a_2 s^2 + a_3 s^3 + a_4 t + a_5 t^2 + a_6 t^2 + a_7 st + a_8 s^2 t + a_9 st^2 \quad (4.23)$$

$$dy = b_0 + b_1 s + b_2 s^2 + b_3 s^3 + b_4 t + b_5 t^2 + b_6 t^3 + b_7 st + b_8 s^2 t + b_9 st^2 \quad (4.24)$$

with s and t the normalised coordinates defined by the image size (nx and ny) and the origin (x_0, y_0) which is arbitrarily defined:

$$s = \frac{2(x' - x_0)}{nx} \quad (4.25)$$

and

$$t = \frac{2(y' - y_0)}{ny} \quad (4.26)$$

The parameters a_0 to a_9 and b_0 to b_9 are calculated using the marks (dots in this case) of the calibration plate. That is why the number of marks present in the image needs to be sufficient (>20). In the present work, the lowest number of marks detected was 40.

An important parameter to check the quality of the calibration is the average deviation of all marks; it represents how well the position of the marks in the corrected image agrees with the position on a perfect regular grid. This should be well below 1 pixel. In the present case, the average deviation was at worst 0.41 pixel which is completely satisfying.

4.2.4.2 Calibration of the NO-PLIF images

For the NO-LIF experiments, only one calibration image at z=0 is needed as it is two-dimensional and the LIF image will not be distorted as the LIF camera faces the burner.

Figure 4.40 shows an example of the calibration image recorded for the NO-LIF experiments using the Winview95 software which is an image acquisition software.

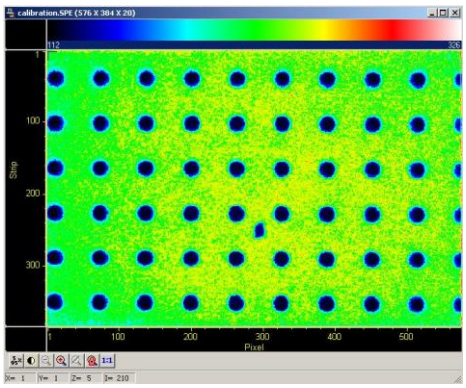

Figure 4.40: Instantaneous calibration image for the Princeton NO-PLIF camera

After acquisition, the images taken with the Winview95 software were imported in the DaVis 7.1 software [60-61] to be calibrated and processed. The calibration, in the case of the NO-PLIF experiments, consisted only in scaling the images in mm instead of pixels.

4.2.5 Position of the images taken

Figure 4.41 shows the position of the images taken with regard to the flames and to the burner.

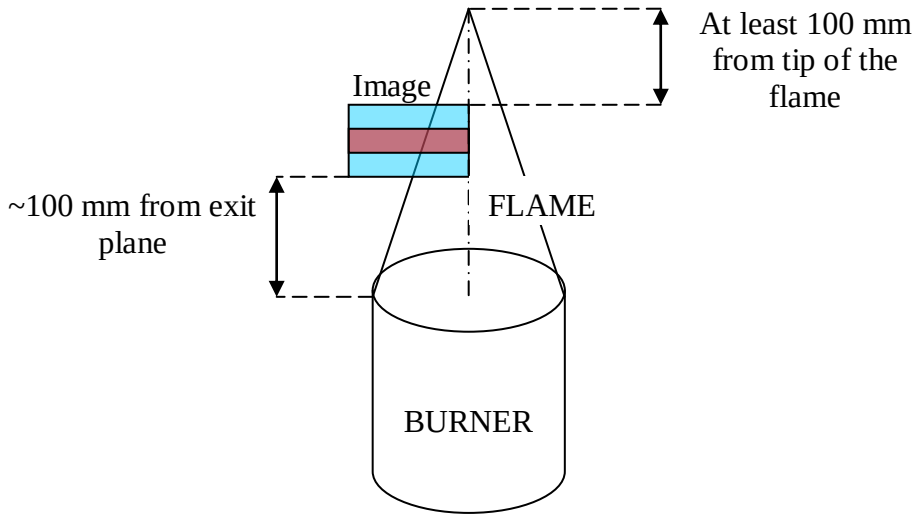

Figure 4.41: Position of the images taken with regard to the burner and the flames

The chosen position ensures that the images taken correspond to parts of the flames far from the tip and also far from the pilot flame so as to represent the general case.

CHAPTER V

Processing and analysis of the NO-PLIF data

This chapter describes the conversion of the NO-PLIF data into progress variable images and the method used to calculate the two-dimensional vectors normal to the chosen isoscalar surfaces. It analyses the influence of the value of c on the isoscalar surfaces and on the orientation of the 2D vectors normal to the isoscalar surfaces. This chapter also gives an analysis of the gradient of the progress variable. Finally, this chapter proposes a new method to calculate, from the progress variable gradients, the three-dimensional vectors normal to the isoscalar surfaces.

5.1 Conversion of the NO-PLIF images into progress variable images

For each set of experiments, a calibration image was recorded as well as a background image, a flat field image and the raw NO-PLIF images of the flames.

5.1.1 The raw NO-PLIF images

The raw NO-PLIF images consist of:

- a background signal which has to be removed and which corresponds to the ambient light possibly recorded by the camera and the dark current of the camera,
- a signal corresponding to the interaction of the laser light with the NO molecules, which has to be corrected to take into account the fact that the laser sheet is not perfectly homogeneous, that the intensity of the laser light might not be perfectly constant over time and that the camera output signal for a same amount of light might vary from one pixel to another (camera's gain).

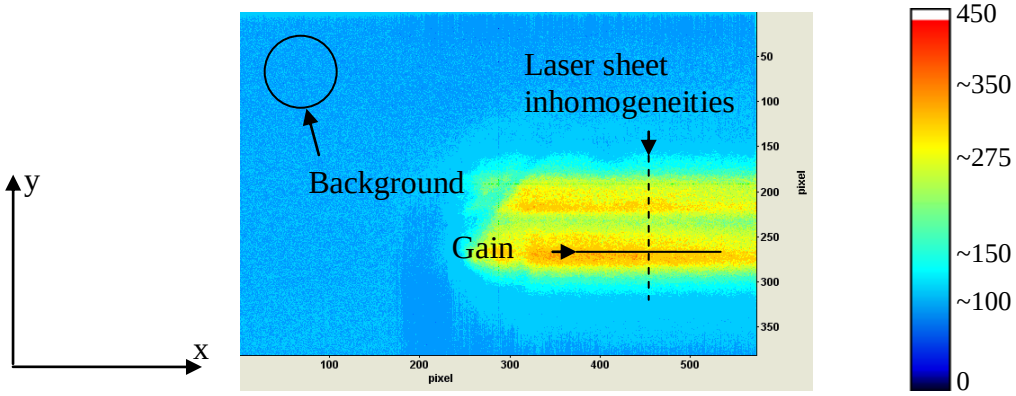

Figure 5.1: Example of an instantaneous raw NO-PLIF image (scale: 48µm/pixel)

The circle shown in figure 5.1 correspond to an example of a region where no laser light is present and also no NO radicals. As a consequence, the signal on the image is due to the dark current of the camera (and possibly ambient light, although, because of the experimental configuration i.e. the fact that the camera's shutter is open for 1µs, this contribution is much reduced). In figure 5.1, the effects of the camera's gain are also visible (horizontal black line). Because of the experimental set-up, the intensity of the laser light in each image is assumed to be constant in the x-direction. If every

pixel of the camera converted the light in exactly the same way, the intensity of the fluorescence signal recorded by the camera should not vary in the x-direction, provided the temperature stays constant. This is not the case: the horizontal black line is in a region of the flame corresponding to the unburnt gases far from the flame; however it is possible to observe that the fluorescence signal recorded by the camera is not perfectly constant in the x-direction. The effects on the raw image of the laser sheet inhomogeneities in the y-direction (vertical dashed line) can also be seen in figure 5.1. The intensity recorded by the camera varies substantially in the y-direction. This variation in the intensity recorded in the y-direction, because of its extent and pattern, cannot be solely attributed to the camera's gain, although the effects of the camera's gain are also present in the y-direction.

5.1.2 The NO-PLIF camera background

The background image is an average of 17 instantaneous shots. They were taken in air with the laser on and tuned at the working wavelength.

The background image accounts for:

- the dark current of the camera,
- and also possibly, the ambient light that the camera could record. However, the ambient light is not a major issue here because the camera's shutter only stays open for a microsecond.

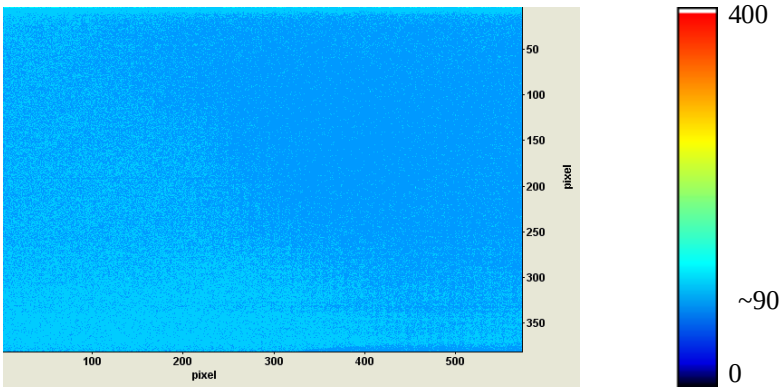

Figure 5.2: Example of an averaged background image for the Princeton NO-LIF camera (scale: 48µm/pixel)

As can be seen in figure 5.2, the background, as can be expected, is a function of the location on the image i.e. is not perfectly constant over the image.

5.1.3 Flat field images

The flat field images are an average of 27 instantaneous shots. They were taken with the laser on and tuned at the working wavelength in the following mixture (percentage in moles): 80% N_2, 8% O_2, 12% NO, Flow rate = 3.08L/s.

The flat field images – an example of which is shown in figure 5.3 - are intended to correct the camera's gain i.e. the possible pixel-to-pixel variation in the output signal for a same amount of light.

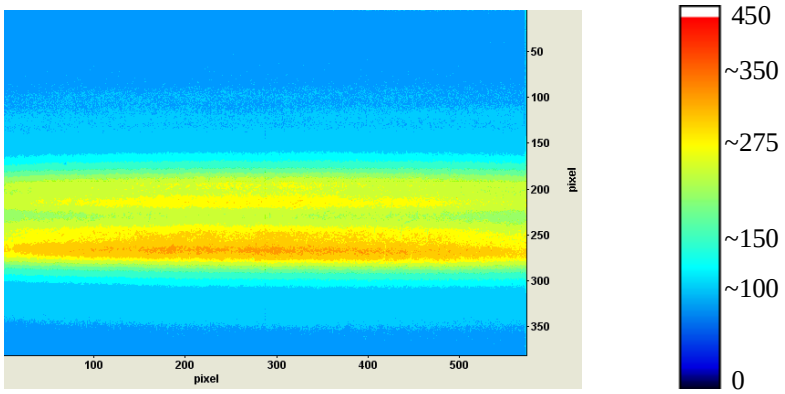

Figure 5.3: Example of an averaged flat field image (scale: 48µm/pixel)

5.1.4 Signal-to-noise ratio

The signal-to-noise ratio was evaluated for each single-shot raw image. The definition used here is the definition that was used in [108]. The signal level is defined as the peak signal intensity with background subtracted while the noise level corresponds to the standard deviation of the background noise fluctuation. The signal-to-noise ratio was averaged over the 400 shots for each flame. The averaged signal-to-noise ratio varies between 52 and 88 which is satisfactory. The signal-to-noise ratio is mainly dependent on the laser light coming from the dye laser as a consequence, no trend could be observed concerning the variation of the signal-to-noise ratio as a function of the flames studied.

5.1.5 Conversion of the raw NO-PLIF into progress variable images

It was chosen to define, in the present work, the progress variable with the help of the NO-PLIF signal:

$$c_{NO\_PLIF} = \frac{NO\_PLIF - NO\_PLIF_{unburnt}}{NO\_PLIF_{burnt} - NO\_PLIF_{unburnt}} \tag{2.40}$$

The raw NO-PLIF image can be expressed as follows:

$$R(x,y,T) = G(x,y) * I_F(y,T) + B(x,y) \tag{5.1}$$

The flat field image can be expressed as follows:

$$F(x,y) = G(x,y) * I_{F'}(y) + B(x,y) \tag{5.2}$$

where B is the background, G the camera's gain and I_F the fluorescence signal due to NO in the flame and $I_{F'}$ the fluorescence signal due to NO in the flat field image conditions (constant temperature and concentration).
As a consequence:

$$\frac{(R(x,y,T) - B(x,y))}{(F(x,y) - B(x,y))} = \frac{I_F(y,T)}{I_{F'}(y)} \tag{5.3}$$

The images corresponding to equation 5.3 were calculated.

A 51 pixel wide stripe from each calculated image was taken from the unburnt gases side (between x=500 and x=550 pixels) and averaged in the x-direction and extended to produce a 576*384 pixel (full size) image. Such an image may be expressed by the following equation:

$$\frac{(R_u(x,y) - B_u(x,y))}{(F_u(x,y) - B_u(x,y))} = \frac{I_{Fu}(y,T)}{I_{F'}(y)} \tag{5.4}$$

The same procedure was applied for the burnt gases side. This time, however, this term was evaluated using a 11 pixel wide stripe between x=56 and x=66 pixels

because, in some images, the burnt gases side is much reduced and only ~20-30 pixels wide:

$$\frac{(R_b(x,y)-B_b(x,y))}{(F_b(x,y)-B_b(x,y))}=\frac{I_{Fb}(y,T)}{I_{F'}(y)} \tag{5.5}$$

Finally, the progress variable images were calculated using the following equation:

$$c(x,y)=MASK*\frac{\frac{(R(x,y,T)-B(x,y))}{(F(x,y)-B(x,y))}-\frac{(R_u(x,y)-B_u(x,y))}{(F_u(x,y)-B_u(x,y))}}{\frac{(R_b(x,y)-B_b(x,y))}{(F_b(x,y)-B_b(x,y))}-\frac{(R_u(x,y)-B_u(x,y))}{(F_u(x,y)-B_u(x,y))}} \tag{5.6}$$

where MASK is a simple mask which filters out the unwanted portions of the images (where no laser light was present).

As is obvious in the previous equations (equations 5.3 to 5.6), the corrections for the camera's gain and the background are directly taken into account in the calculation. Because the value of the burnt gases term and unburnt gases term are re-evaluated for each image, the progress variable images are independent of the overall laser power. Because the progress variable images are evaluated using "stripes", the variation in the laser sheet intensity, which is only in the y-direction, is also corrected.

Figure 5.4 shows an example of such a progress variable image calculated using the NO-PLIF signal:

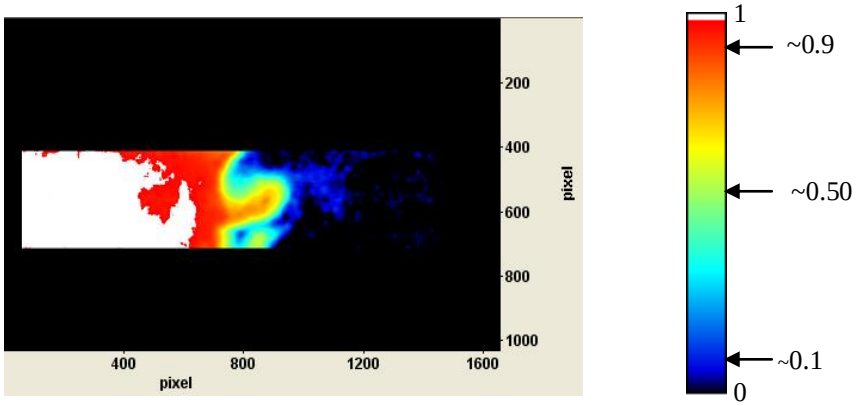

Figure 5.4: Example of a progress variable image (scale: 16μm/pixel)

This progress variable image corresponds to an instantaneous shot of flame A. The contours of the flame can already be seen.

The progress variable images were then calibrated. The resolution of these images (48 μm) is different from the resolution of the raw SPIV images (16 μm) and of the velocity vector fields (262 μm). To allow the correlation of the SPIV data and the NO-PLIF data, the progress variable images needed to be resized i.e. their resolution had to be adjusted to that of the SPIV data and rebuilt to spatially match the SPIV data.

5.2 Mapping of the NO-PLIF data onto the SPIV data

As previously explained, the NO-PLIF and as a consequence the progress variable images have widely different resolutions than the SPIV images. Besides, they also have slightly different fields of view. In order to successfully correlate the NO-PLIF data and the SPIV data, the progress variable images were mapped onto the SPIV images. It was chosen to map the progress variable images onto the SPIV data and not the SPIV data onto the progress variable images because it is easier, quicker and safer to adapt the resolution of a scalar field than a vector field.

To achieve that, a two-step strategy was developed:

- the first step consists in enlarging the progress variable images by a factor of 3 by bilinear interpolation,
- the second step consists in rebuilding the progress variable images, i.e. shifting the images so that pixels with the same coordinates in the progress variable images and the SPIV images correspond to the same physical location. To match, the images must have the same size i.e. 1664*1040 pixels which is the size of the SPIV images. The resized progress variable images had a size of 1676*1117 pixels. So part of the images had to be cut. The pixels to be kept are selected one by one and assigned a new pixel in the final image, this new pixel corresponding to the right physical location.

The error introduced in re-positioning the progress variable images is less than 8μm.

5.3 Selected progress variable images

The progress variable images presented below are meant to give an illustration of the various flames studied in this work.

As a reminder, the tables containing the characteristics of the flames studied are presented again below:

Flame	Flow Rate ($L.s^{-1}$)	*Average Speed* ($m.s^{-1}$) =Flow Rate/Duct Section	*Dilution*	Φ	T_{ad} (K)	C_{NO}
A	4.25	4.42	0.106	0.38	906	505
B	4.38	4.55	0.106	0.54	1124	489
C	4.55	4.73	0.106	0.75	1384	470
D	3.27	3.40	0.106	0.54	1124	489
E	3.41	3.54	0.106	0.76	1396	469
F	2.75	2.86	0.098	0.75	1317	494
G	5.30	5.51	0.105	0.38	901	495
H	5.46	5.67	0.105	0.53	1104	480
I	6.33	6.58	0.106	0.38	906	502

Table 4.2: Summary of the flames studied

Flame	L (mm)	u' ($m.s^{-1}$)	S_L($m.s^{-1}$)	δ_L(mm)	Ka	Da	Regime
A	15	0.45	0.0114	1.17	69.4	0.33	Thin or Broken reaction zones
B	15	0.45	0.0789	0.54	2.7	4.91	Thin reaction zones
C	15	0.45	0.2079	0.49	0.5	14.09	Corrugated flames
D	15	0.34	0.0789	0.54	1.7	0.65	Thin reaction zones
E	15	0.34	0.2138	0.50	0.4	18.75	Corrugated flames
F	15	0.28	0.2079	0.49	0.3	23.85	Corrugated flames
G	15	0.55	0.0114	1.17	93.8	0.27	Broken reaction zones
H	15	0.55	0.0731	0.54	3.8	3.73	Thin reaction zones
I	15	0.66	0.0114	1.17	123.5	0.22	Broken reaction zones

Table 4.7: Summary of the characteristics of the flames studied

Figure 5.5 shows the positions of the flames in the Peters regime diagram [75] for premixed turbulent combustion:

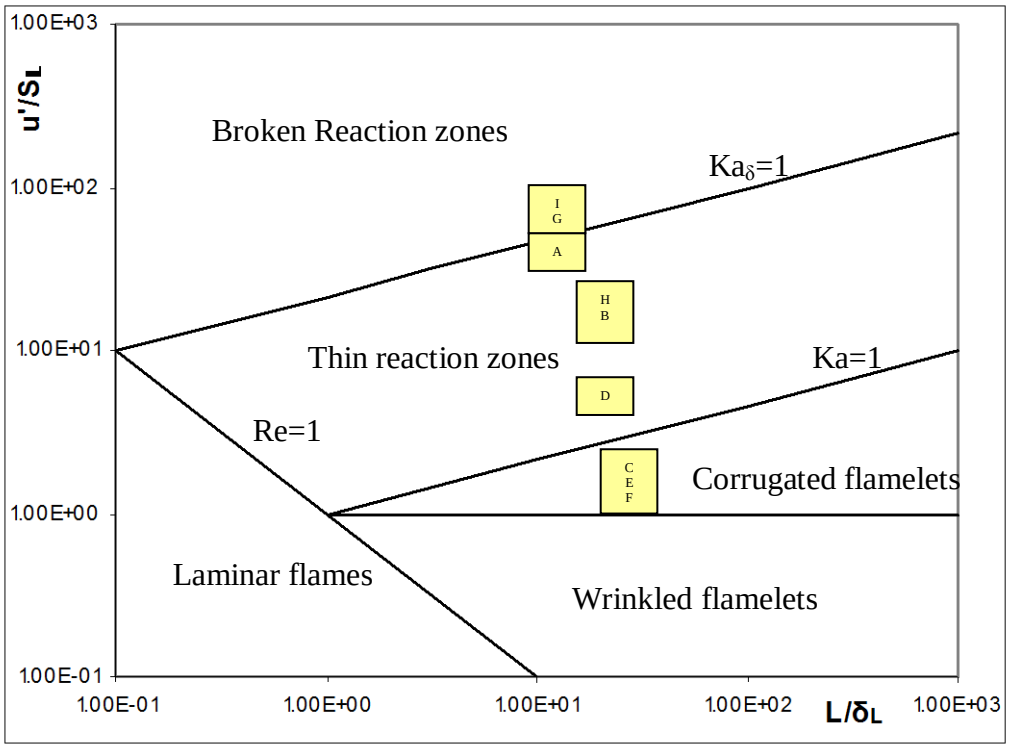

Figure 5.5: Position of the flames studied in the Peters regime diagram for premixed turbulent combustion

The flames A, B, C, E, F and I were studied in more details. They were chosen in particular because:

- They belong to different regimes. Flame C, E and F belong to the corrugated flamelets regime. Flame I belong to the broken reaction zones regime. Flame B belong to the thin reaction zones regime and flame A belong either to the thin reaction zones regime or the broken reaction zones regime.
- Flame A, B and C, although belonging to different regimes, have got similar flow rates (4.28, 4.35, 4.55 $m.s^{-1}$).
- Flame E and F belong to the same regime as flame C; however they have much lower flow rate and similar equivalence ratio (~0.75).
- Flame I has a much higher flow rate than flame A and a similar equivalence ratio.

Flame A:

(scale: 16μm/pixel)

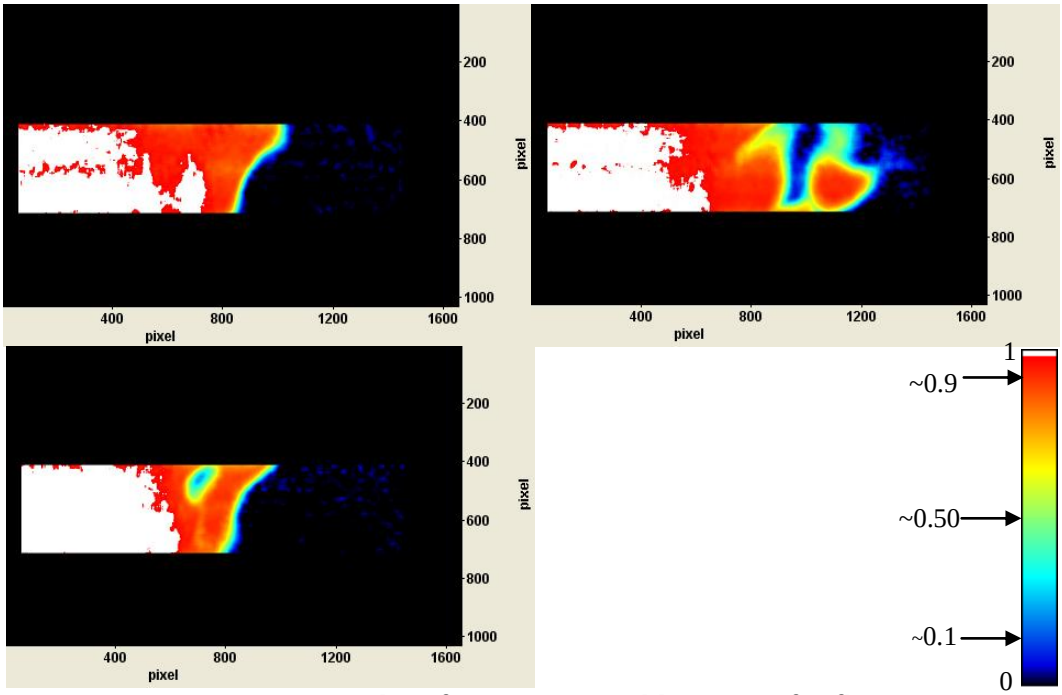

Figure 5.6: Examples of progress variable images for flame A (top left to bottom left: (a), (b) and (c))

Flame B:

(scale: 16μm/pixel)

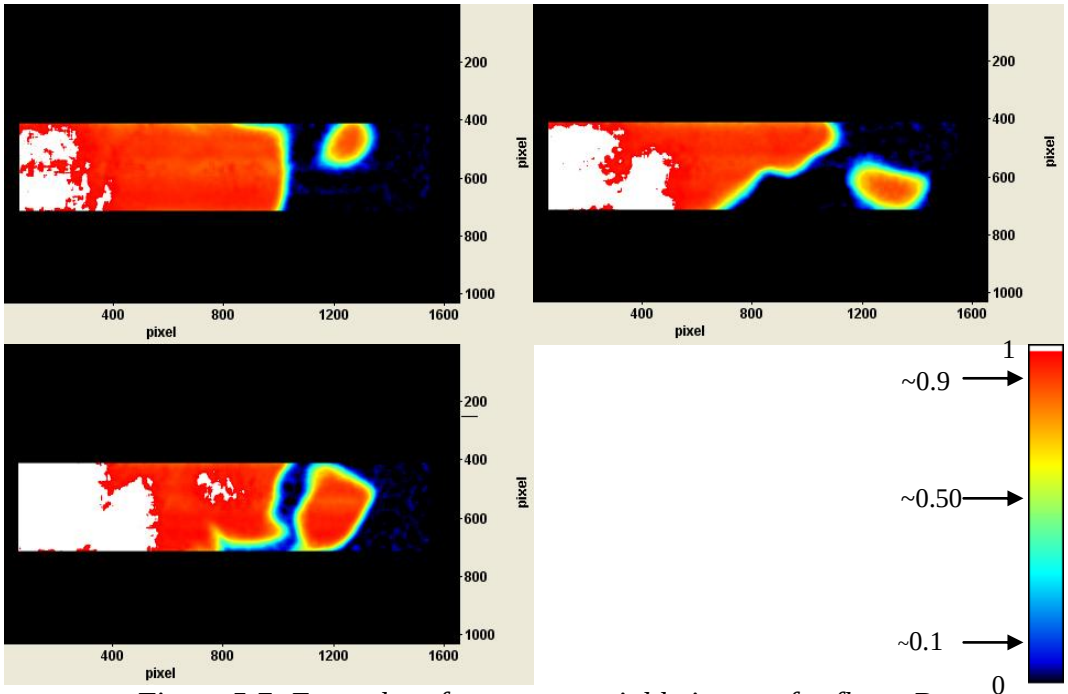

Figure 5.7: Examples of progress variable images for flame B (top left to bottom left: (a), (b) and (c))

Flame C:

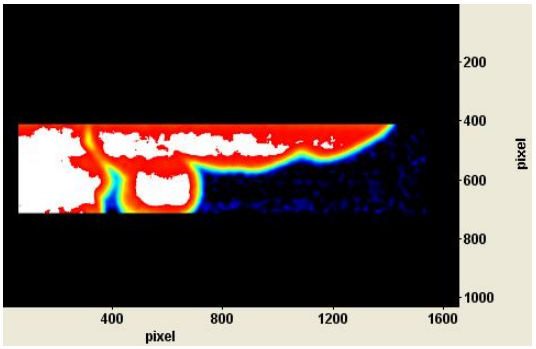

Flame E:

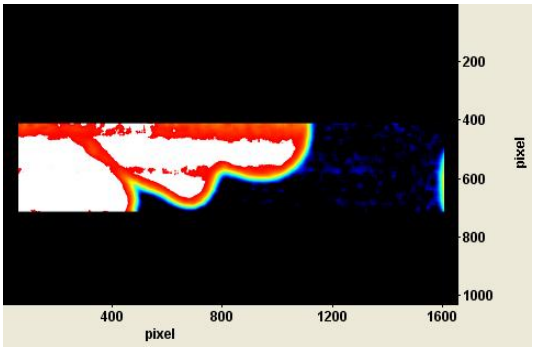

Flame F:

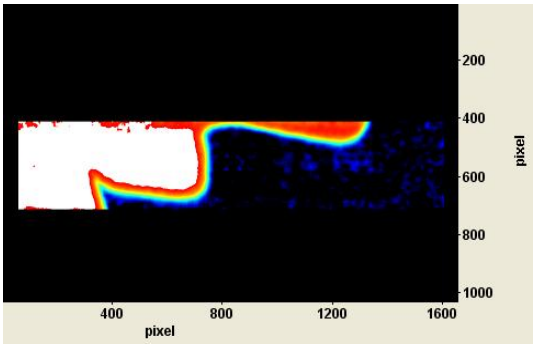

Colour Scale:

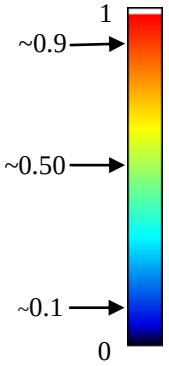

Figure 5.8: Examples of progress variable images for flame C (a), for flame E (b) and for flame F (c) (scale: 16µm/pixel)

Flame I:

(scale: 16µm/pixel)

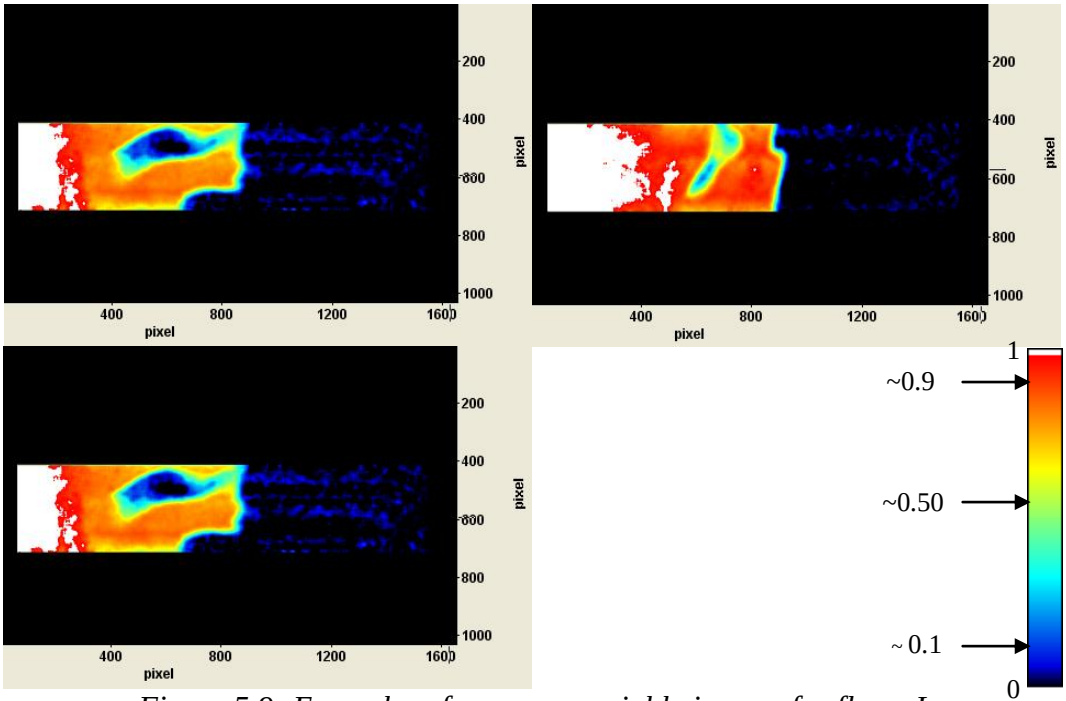

Figure 5.9: Examples of progress variable images for flame I (top left to bottom left: (a), (b) and (c))

Flame A:

Flame A belongs either to the thin reaction zones regime or the broken reaction zones regime. In the thin reaction zones regime, there exist an interaction between the flame front and some eddies and as a consequence the flame should be corrugated and some hot gases should be transported in front of the reaction zone. This phenomenon may be observed for flame A, in particular in figure 5.6 (b). In the broken reaction zones regime, the smallest eddies can interact with the inner layer of the reaction zone and cause local extinction. This phenomenon might also be observed for flame A, in figures 5.6 (c): the pockets of unburnt gases in burnt gases may be an indication that extinction occurred.

Flame B:

Flame B belongs to the thin reaction zones regime as a consequence we should observe hot gases being transported in front of the reaction flame front which we may observe in figure 5.7.

Flame C, flame E & flame F:

Flame C, E and F belong to the corrugated flamelets regime. We should, as a consequence, observe strong distortion of the flame due to the largest eddies. Phenomenon we could observe in figure 5.8.

Flame I:

Flame I belongs to the broken reaction zones regime.
Figure 5.9, as expected, might show local extinction of the flame due to the smallest eddies able to enter the inner layer of the reaction zone and perturb the chemistry of the flame: again pockets of unburnt gases in burnt gases are visible.

However, one must be careful. The pockets of gas burning in the unburnt gas region and the pockets of unburnt gas in the burnt gas region –the latter of which may suggest that local extinction occurred - which were apparently identified on the

previous images may not all be genuine. They may actually be due to distortions of the flame sheet in the plane of the laser. The thickness of the flame fronts may be expected to be of the order of 1 mm. The size of some of the pockets of gas burning in the unburnt gas region and the size of some of the pockets of unburnt gases in the burnt gas region we have identified in the previous images seem larger than one would expect from embedded turbulence.

The occurrence of pockets of gas burning in the unburnt gas region and of the pockets of unburnt gases in the burnt gas region was surveyed. Table 5.1 shows the number of pockets of gas burning in the unburnt gas region (column "A") and the number of pockets of unburnt gases in the burnt gas region (column "B") which were apparently identified in the sets of 400 images recorded for flames A, B, C, E, F and I:

Flame	Turbulence Regime	A	B
A	Broken/Thin Reaction Zones	21	18
B	Thin Reaction Zones	28	21
C	Corrugated Flamelets	16	26
E	Corrugated Flamelets	26	23
F	Corrugated Flamelets	17	17
I	Broken Reaction Zones	36	17

Table 5.1: Table showing the occurrence of pockets of gas burning in the unburnt gas region and of pockets of unburnt gases in the burnt gas region

Given the differences in Da and Ka for the flames investigated, we expected to observe few pockets of burnt gases in the unburnt gas region and few pockets of unburnt gases in the burnt gas region for the flames belonging to the corrugated flamelets regime (flame E, F and C), more pockets of burnt gases in the unburnt gas region for the flames belonging to the thin reaction zones regime (flame B and A) and more of both pockets of burnt gases in the unburnt gas region and pockets of unburnt gases in the burnt gas region for flames belonging to the broken reaction zones regime (flame A and I). Such a tendency could not be observed which suggests that, at least, some of the identified pockets of burning gas in the unburnt gas region and vice versa are not genuine.

Extinction, whether it occurred or not, will be further investigated in chapter VI via the study of the values of the strain rates.

5.4 Calculation of the 2D vector normal to chosen isoscalar surfaces and analyses of the orientation of the 2D vector normal

The methodology presented below was used to calculate the two-dimensional vectors normal to chosen iso-c lines.

5.4.1 Flame front selection

The flame front selection is a crucial step in the analysis of the NO-PLIF images. It will dictate the position where the 2D vectors normal to the flame front will be calculated. Also, the exactitude of the calculation of the 2D vectors normal to the flame front depends on the accuracy of the flame front shape. It follows that the precision of the flame normal alignment with the principal strain rates depends also on the flame front selection.

Previously, as already explained in section 3.2.4, Hartung et al. [14] studied the flame normal alignment with the principal strain rates in ethylene-air flames. They used the OH-PLIF technique to locate the flame front position. They situated the flame front position in the region of maximum gradient of OH. They found, numerically, that this region corresponded also to a region of intense heat release which makes the determination of the flame front, in such a way, very precise. For a hydrogen/air flame with an equivalence ratio of 0.35, the maximum gradient of OH occurs at c_T=0.85 (which corresponds to c_{NO_PLIF}=0.95) while the maximum heat release occurs at c_T=0.75 (c_{NO_PLIF}=0.90). The maximum gradient of OH occurs very close to the burnt gases side which is due to the low adiabatic flame temperature (T=1190K) of the flame studied. Unfortunately, as will be further explained later, it was not possible to work at such high value of c_{NO_PLIF}. Also, the accurate determination of the intense heat release regions in the present flames would have required the exact simulation of the present flames which was not feasible.

The OH-PLIF technique differs widely from the NO-PLIF technique. In the case of OH-PLIF, the fluorescence signal is not so much a function of temperature as a

function of concentration which varies widely in the flame which makes the location of the flame front using a gradient method a necessity. In the case of NO-PLIF, the fluorescence signal varies as a function of temperature. As a consequence, one does not need gradient information to determine the flame front position. One can use a simple threshold technique which consists in selecting a particular value of $c_{NO\text{-}PLIF}$ to define the flame front (or iso-c line or isoscalar surface).

This technique has the advantage of allowing the study of the influence of the choice of the position of the iso-c line on the results obtained. One drawback of the NO-PLIF is that it was not possible to determine which of the iso-c lines were in intense heat release zone because of the partial calibration of the fluorescence signal as a function of temperature (see section 2.2.3).

In the progress variable images calculated as explained in section 5.1, the pixels with an intensity within the interval [0.395, 0.405] (or [0.595, 0.605] or [0.795, 0.805] or [0.895, 0.905] depending on which iso-c was under scrutiny) are assigned the intensity 1 and the pixels with an intensity outside this range are assigned the intensity 0. In figure 5.10, an example of different iso-c lines for flame C are shown.

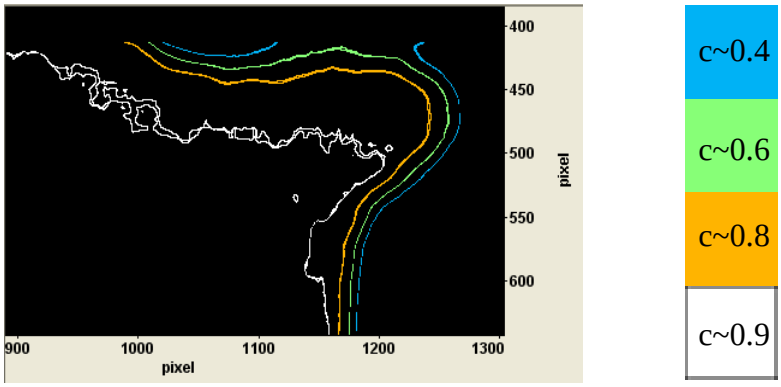

Figure 5.10: Example of different iso-c lines for flame C (scale: 16μm/pixel)

As can be seen in figure 5.10, for flame C, the iso-c lines for values of c between 0.4 and 0.8 are parallel, whereas, the iso-c line corresponding to the value of c of 0.9 is no longer parallel to the other lines. It is also much more convoluted. This feature was present in all flames studied except for flame E and flame I. For flame E, all the iso-c

lines stay parallel, while for flame I, both the is-c line at 0.8 and at 0.9 depart from the other iso-c lines.

This feature can be explained by the fact the resolution of the NO-PLIF technique decreases with temperature as can be seen in figures 2.20 and 2.21 in chapter II i.e. that the variation of the fluorescence signal as a function of temperature is all the greater at relatively low temperature (especially below 1000K). The fact that, for flame E, the iso-c line at 0.9 is still parallel to the other iso-c lines may be explained by the fact that this flame is the flame with the highest adiabatic flame temperature. In this case, the greater temperature gradient counterbalances the limited resolution of the fluorescence signal at high temperature. On the contrary, for flame I, the combination of low adiabatic flame temperature and high turbulence makes both the iso-c lines at c=0.8 and c=0.9 convoluted and non parallel to the other iso-c lines. This feature has for consequence that for most flames, it will not be possible to work with the iso-c line at 0.9 because it may not represent properly the flame front.

Figure 5.11 shows an estimation of the average length of the iso-c lines in pixels as a function of the value of the progress variable calculated using equation 2.40. The average length of the iso-c lines were estimated for c=0.4, c=0.6, c=0.8 and c=0.9. This graph was mainly intended to prove the previous observations.

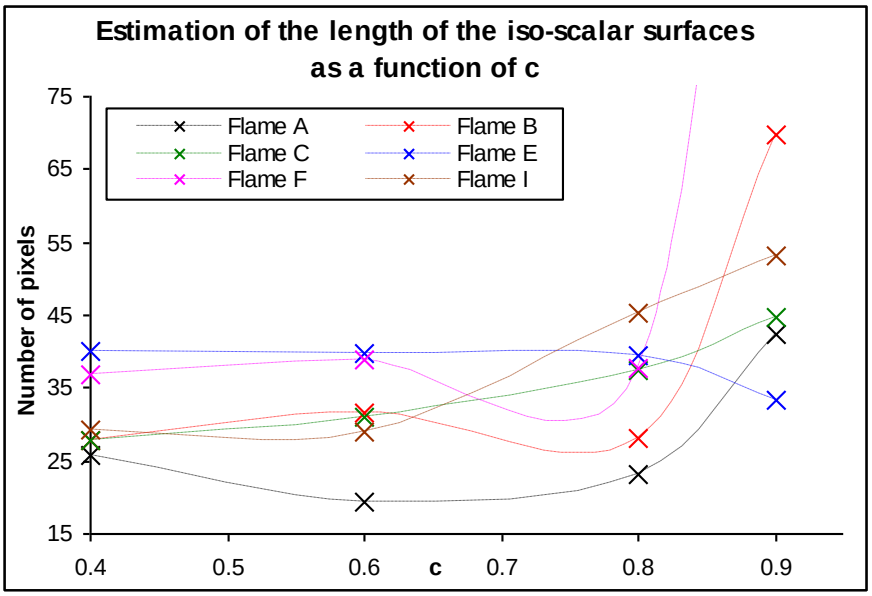

Figure 5.11: Length of the iso-scalar surfaces as a function of c

As can be seen, because the resolution of the NO-PLIF decreases with temperature (especially at T>1000K) the length of the iso-c lines increases dramatically with c especially after 0.8 which suggests that the method used for the flame front selection breaks down for value of c greater than 0.8 .

No obvious correlation between the average length of the iso-c lines and the combustion regime of the corresponding flames or their equivalence ratio or dilution could be found. This might be due to the fact that the average length was only a measure of the portion of the flame contour present on the images and as such depends also on the flame front orientation.

5.4.2 Calculation of the 2D vectors normal to the flame front

The calculation procedure for the 2D flame front normal employed in this work uses a similar approach than the one used in [94].

Figure 5.12 illustrates the first part of the calculation i.e. the calculation of the general direction of the 2D vector normal to the flame front.

Each iso-c line image was divided in interrogation windows of 16*16 pixels (white and yellow squares in figure 5.12). Only the interrogation windows containing parts of the iso-c line considered (white squares) were used for the calculation of the flame front normal. The line tangent to the iso-c line under investigation was approximated by linear interpolation of the pixels defining the iso-c line in the interrogation window considered. The direction of the vectors normal to the iso-c line considered were then calculated using the tangent line.

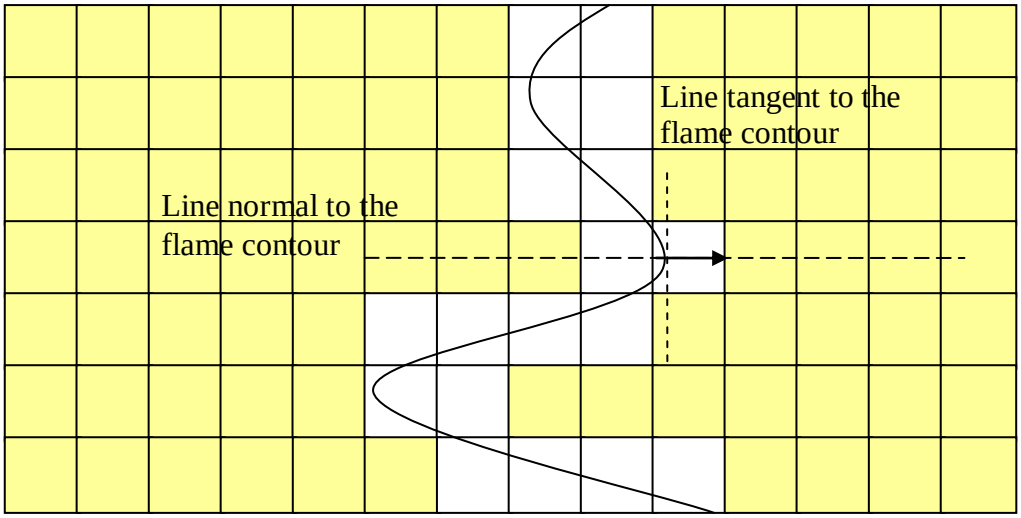

Figure 5.12: Sketch illustrating the calculation of the 2D vectors normal to the flame front

Tests were designed to determine the orientation of the vectors normal to the flame front. Figure 5.13 shows schematically a 16*16 pixel interrogation window in which two rows (x_1 and x_2) and two lines (y_1 and y_2) corresponding to the edges of the interrogation window were highlighted. They allow the calculation of the direction of the components of the vectors normal to the iso-c lines.

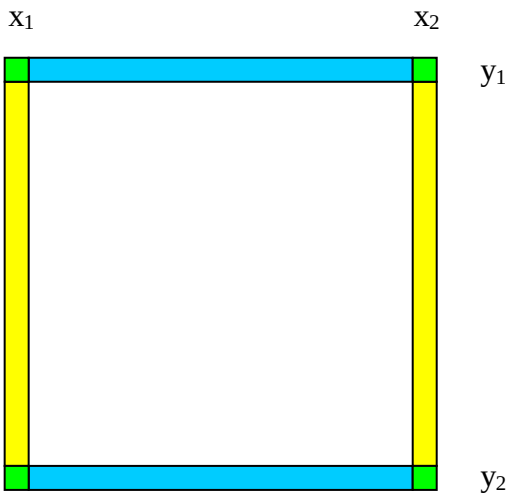

Figure 5.13: Sketch of the orientation test for the vector normal to the iso-c lines

The average value of c in the row x_1 is subtracted from the average value of c in the row x_2. If the subtraction results in a positive figure, the component of the vector normal to the flame front in the x-direction is positive as well. The average value of c in the line y_1 is subtracted from the average value of c in the line y_2. If the subtraction

results in a positive figure, the component of the vector normal to the flame front in the y-direction is negative. The vectors normal to the flame front are, as a consequence, oriented so that they point toward the burnt gases. The procedure for finding the orientation of the flame normal has been checked on 10 images for each flame. In each case, the orientation of the flame normal was found to be consistent with the flame front shape and orientation.

Figure 5.15 show the pdfs of the orientation of the vectors normal to the iso-c lines compared with the y-axis which corresponds to the burner axis and hence to the mean reactant flow direction at the inlet.

Figure 5.14 shows how the angles between the vectors normal to the flame front and the y-axis have been calculated.

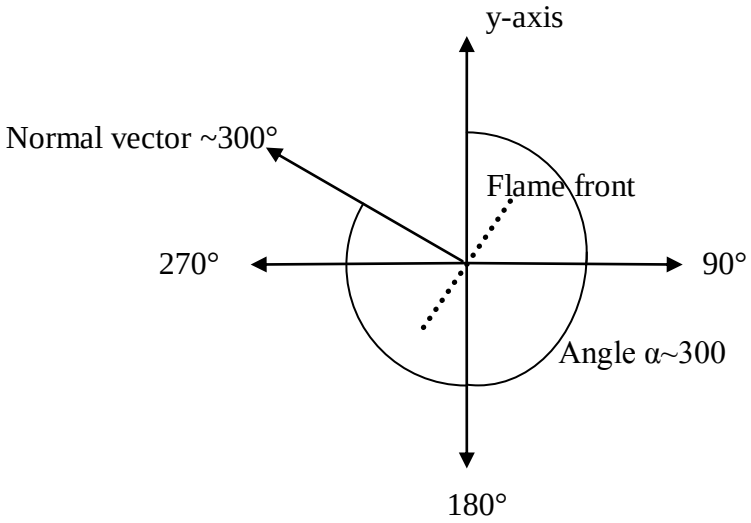

Figure 5.14: Angle between the y-axis and the vectors normal to the flame front

Figure 5.15 shows that the iso-c lines corresponding to c=0.9 departs from the other iso-c lines (except for flame E): the curves corresponding to the orientation of the 2D flame normal overlap one another except the ones corresponding to c=0.9.

The graphs 5.15 (c), (d) and (e) corresponding to flame C, E and F are quite similar, while the graphs 5.15 (a) and (f) corresponding to flame A and I are quite similar.

Graph 5.15 (b) corresponding to flame B represents an intermediate case between the two previous.

The data obtained for the orientation of the 2D flame normal and represented in figure 5.15 was binned; the bin size was 5°.

The data obtained for the iso-c lines at c=0.9 was kept in figure 5.15, for illustration purpose, although it does not have any physical meaning related to combustion. The curves at c=0.9 have similar features for all flames studied: two peaks at 0/360° and 180°.

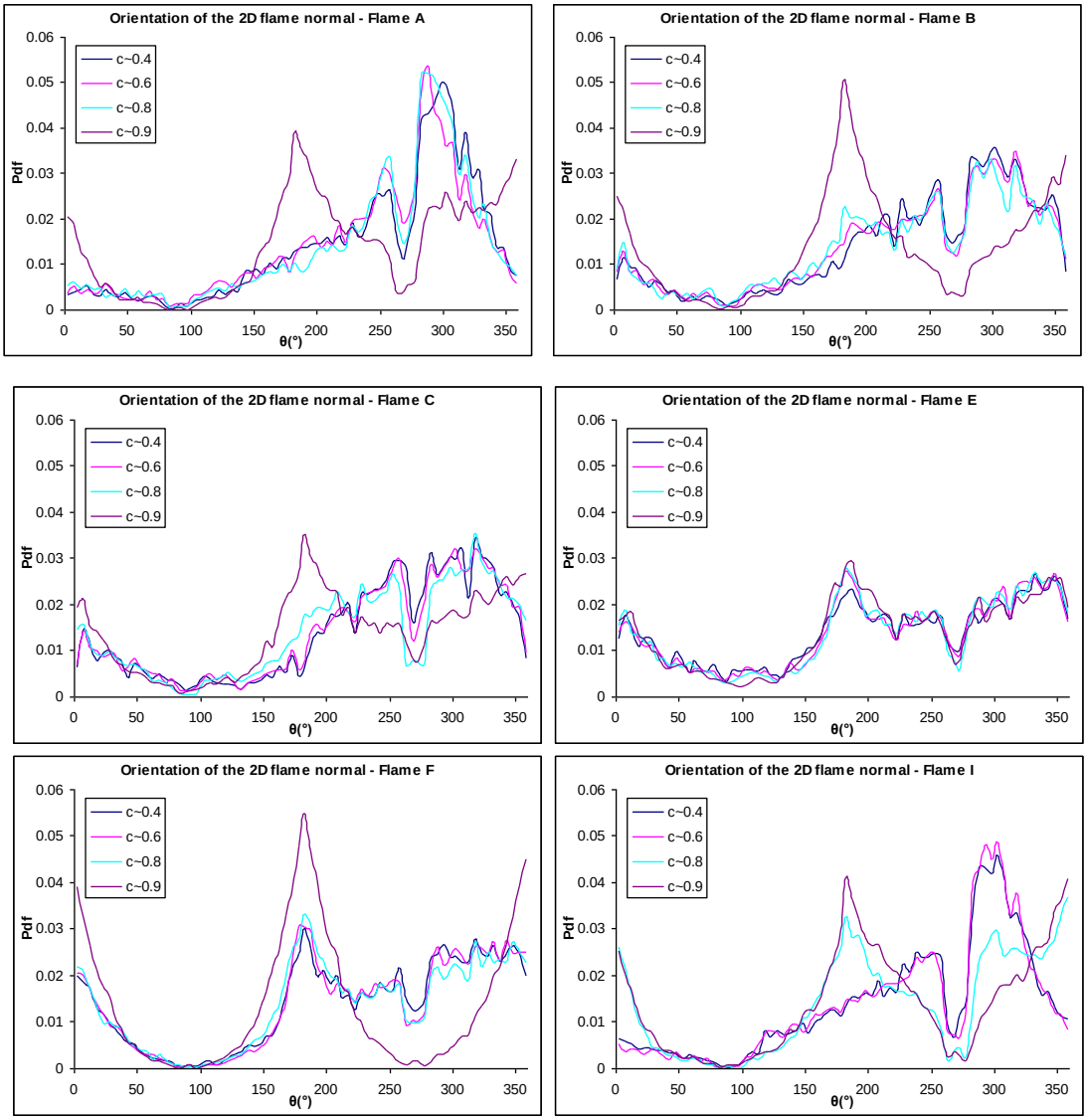

Figure 5.15: Orientation of the 2D flame normal (from top left to bottom right: (a) Flame A, (b) Flame B, (c) Flame C, (d) Flame E, (e) Flame F, (f) Flame I)

Flame C, E and F all belong to the corrugated flamelets regime which is characterised by a strongly disturbed flame front due to the interactions of the largest eddies with the flame front. As we can observe in the previous graphs, there is not a precise main orientation for the vectors normal to the flame front. The value of the angle between the 2D normal vectors and the y-axis spread between the values 150° and 15° (which can be seen as 375°). The flame normal vectors point mainly toward the left hand-side of the image (the burnt gases side) but they can take all values of angle.
The picture is different for flames A and I. The graphs corresponding to these flames show a main orientation of the normal vectors at preferentially an angle of ~300° i.e. the normal vectors mainly point to the top left hand-side of the images. Flames A and I belong to the broken reaction zone regime. The smallest eddies are able to interact with the inner layer of the flame possibly causing extinction but apparently the flames are not so sensitive to the largest eddies and the flame front is not as distorted.
Flame B shows a picture in between the two cases.

5.5 Investigation of the progress variable gradient images

The spatial gradient of c was calculated using the progress variable images calculated as indicated in section 5.1.

The following methodology was used:

- the full 1664*1040 pixel progress variable image was divided in 16*16 pixel (262 µm * 262 µm) interrogation windows,

- the average value of the progress variable within each interrogation window was calculated:

$$Avg(c)_{16*16box} = \frac{\sum c}{16*16} \tag{5.7}$$

- each interrogation window was then divided in four 8*8 pixel boxes as follow:

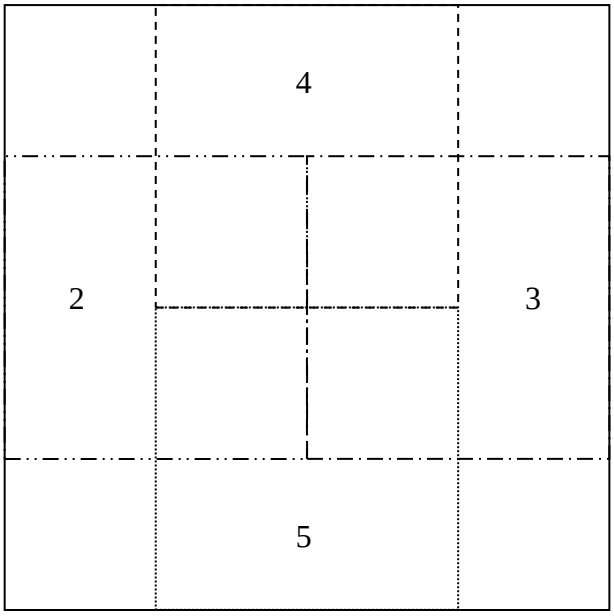

*Figure 5.16: Sketch of the four 8*8 pixel boxes*

- the gradient was then calculated as follow:

$$Gradient = \left|\sum_{4} c - \sum_{5} c\right| + \left|\sum_{2} c - \sum_{3} c\right| \qquad (5.8)$$

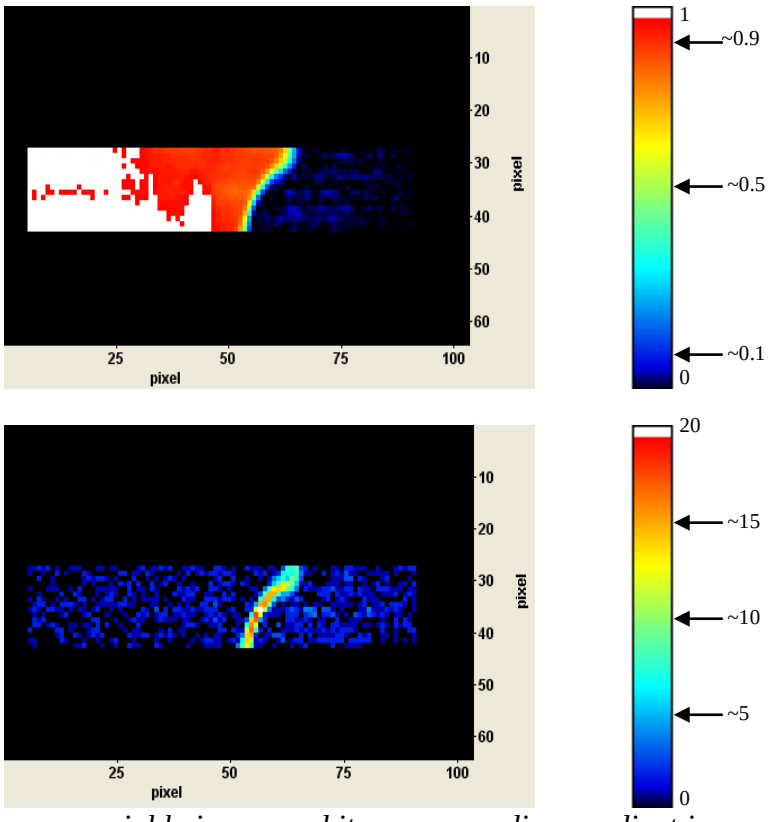

Figure 5.17: Progress variable image and its corresponding gradient image (flame A)

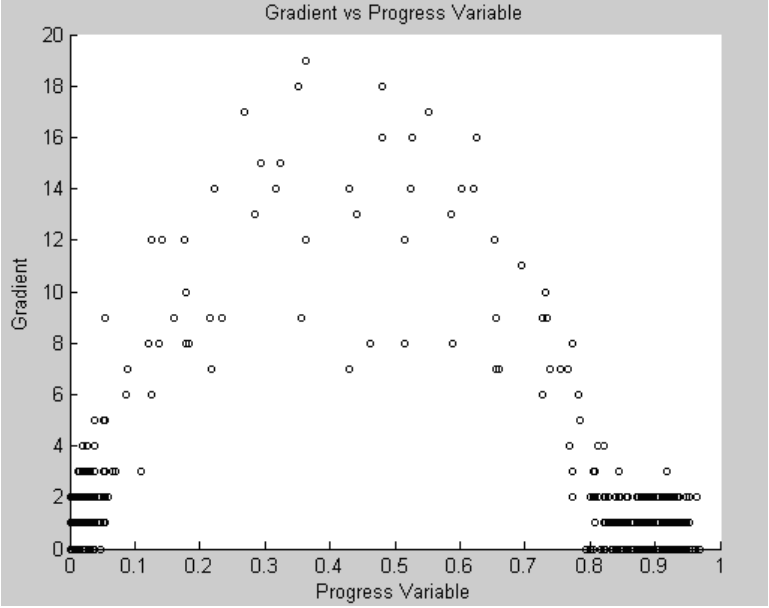

Figure 5.18: Spatial gradient of the progress variable as a function of the progress variable (flame A)

Figure 5.18 shows a typical graph of the spatial gradient of the progress variable as a function of the progress variable for an arbitrary single shot image of flame A. Each data point corresponds to a single pixel in the spatial gradient/progress variable image. There are numerous data points at c=0 and c>0.8: most of the image corresponds to either the burnt gases side or the unburnt gases side and only a small portion of the image corresponds to the flame in itself. These graphs have similar features for all the flames studied here: they have a similar shape and they reach a maximum at c=0.4. However, this maximum reached at c=0.4 is different for each flame. Figure 5.18 shows that there is not a single value of progress variable gradient corresponding to each value of progress variable. This feature can be attributed to the effect of turbulence on the local flame structure and also to the flame orientation relative to the laser sheet. This latter feature will be explained in more details and exploited in section 5.6.

To explain further the experimental graphs representing the spatial gradient of the progress variable as a function of the progress variable (such as the one shown in figure 5.18), simulated graphs using laminar flame computations were studied. They allow the study of tendencies, whether in terms of shape or of value or position of the maximum gradient, as a function of dilution and equivalence ratio regardless of the hydrodynamic field present which simplifies, at first, the analysis.

Figures 5.19 and 5.20 correspond to simulated graphs of the spatial gradient of the progress variable as a function of the progress variable in laminar flames for various equivalence ratios and dilutions. The progress variables and the progress variable gradients were calculated using the data obtained with the Chemkin 4.1 software [15] as described in section 4.1.2 and using equation 4.4.

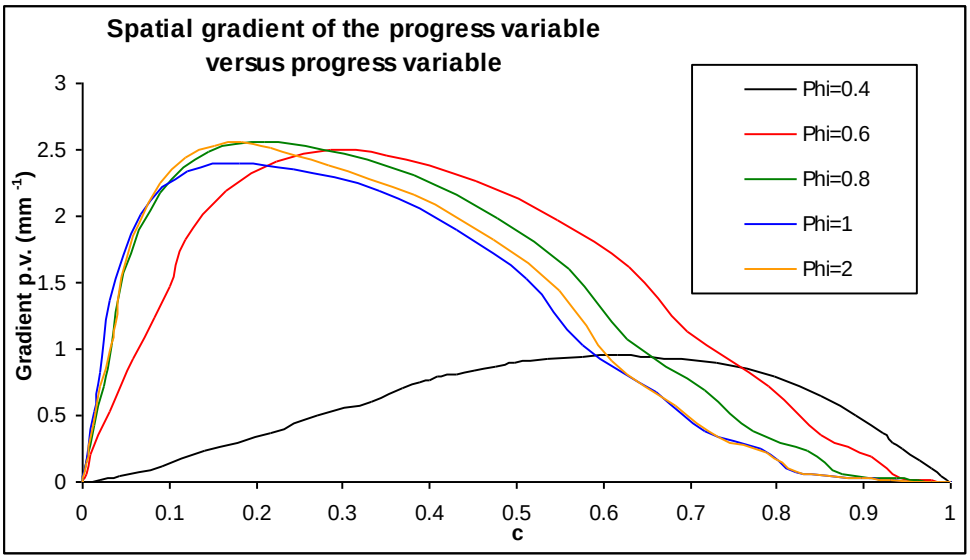

Figure 5.19: Spatial gradient of the progress variable as a function of the progress variable for hydrogen/air flames with an equivalence ratio between 3 and 0.4

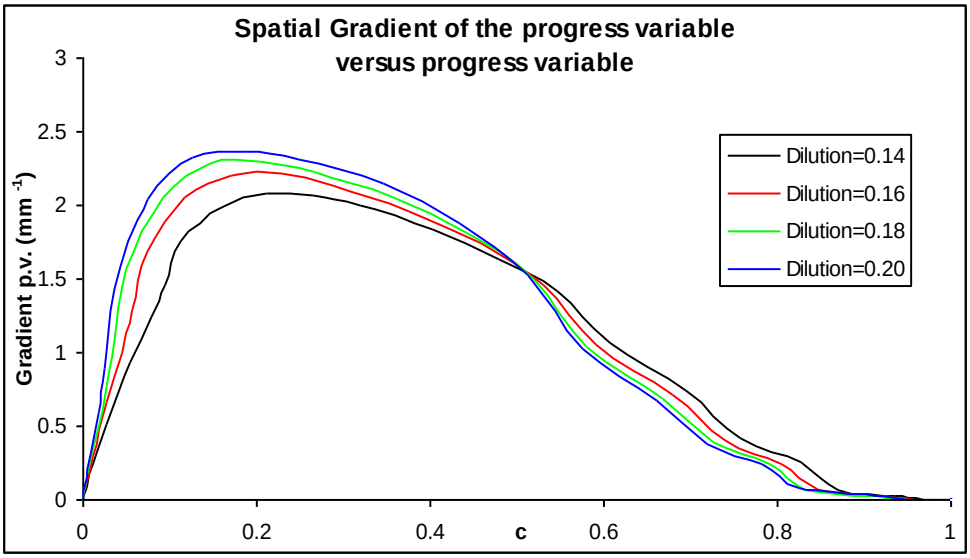

Figure 5.20: Spatial gradient of the progress variable as a function of the progress variable for nitrogen-diluted hydrogen/air flames with an equivalence ratio of 1

- Figure 5.18 and figures 5.19 and 5.20 show that the experimental and the simulated graphs are quite similar in shape.

- While the values on the simulated graphs are in mm^{-1}, the values in figure 5.18 are not because of the way the gradient has been calculated (see equation 5.9). To obtain values in mm^{-1}, one has to divide the progress variable gradient values in figure 5.18 by 134. For instance, in the case shown in figure 5.18, the maximum value for the gradient is, in fact, 0.14 mm^{-1} which appears to be much smaller than the values one would expect for the laminar flames by considering the simulated graphs, which seems reasonable.

- The location of the maximum value of the progress variable gradient differs from the simulated graphs. This is due to differences in flame conditions: the experimental flames contain more nitrogen. The location of the maximum value of the progress variable gradient depends also on the NO-PLIF signal variation with temperature. The location of the maximum gradient in the experimental graph is $c_{NO\text{-}PLIF}$=0.4 which corresponds to c_T=0.1 according to figure 2.20. This value is very small and it is doubtful that this corresponds to the maximum heat release.

- In the simulated graphs, the value of the maximum gradient increases with the equivalence ratio until the equivalence ratio reaches 0.7 and then stays roughly constant. The position of the maximum gradient decreases with an increasing equivalence ratio until the equivalence ratio reaches 1 and then stays roughly constant. These trends are illustrated in figures 5.21 and 5.22.

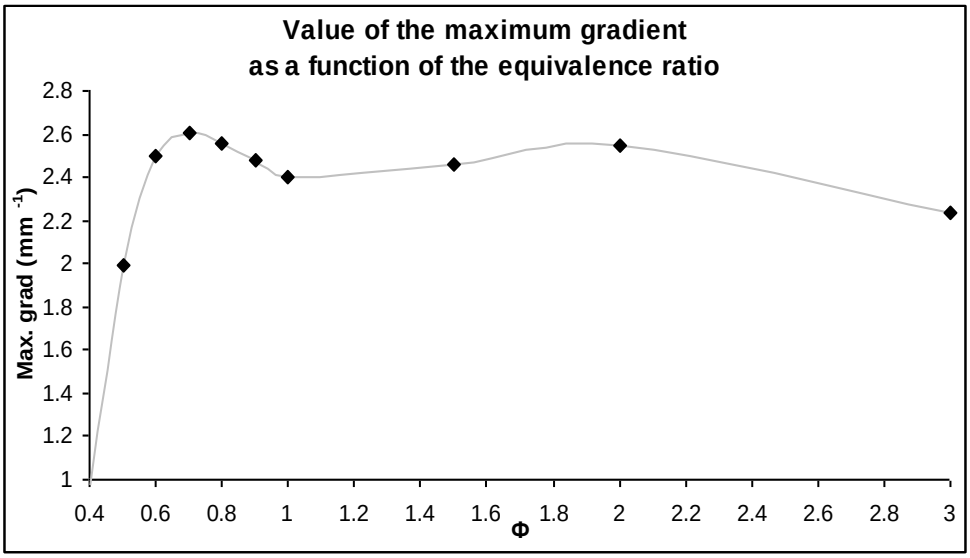

Figure 5.21: Value of the maximum gradient as a function of the equivalence ratio for hydrogen/air flames (dilution=0.21)

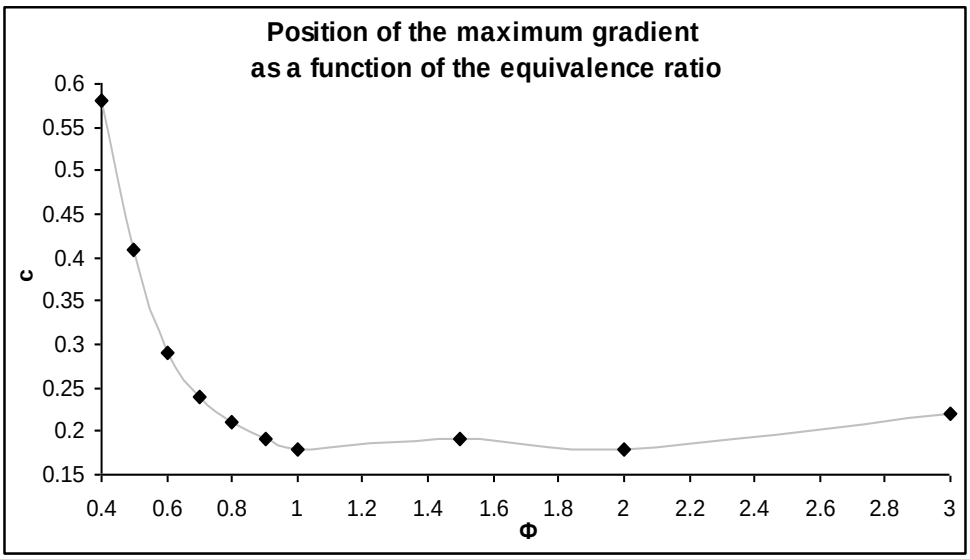

Figure 5.22: Position of the maximum gradient as a function of the equivalence ratio for hydrogen/air flames (dilution=0.21)

- In the simulated graphs, the value of the maximum gradient increases with dilution. The position of the maximum gradient increases with dilution between 0.14 and 0.16 and then decreases with increasing dilution between 0.16 and 0.20. These trends are illustrated in figures 5.23 and 5.24.

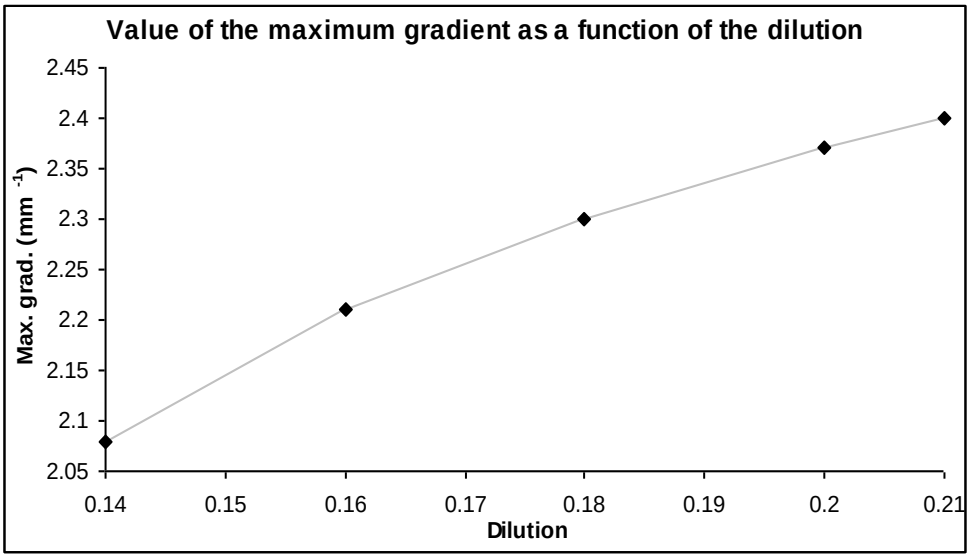

Figure 5.23: Value of the maximum gradient as a function of the dilution for stoichiometric nitrogen-diluted hydrogen/air flames

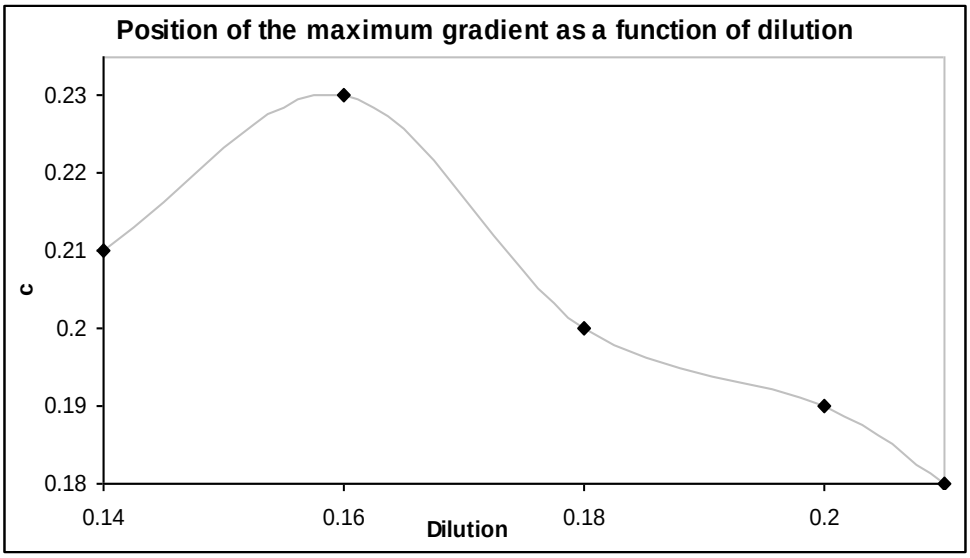

Figure 5.24: Position of the maximum gradient as a function of the dilution for stoichiometric nitrogen-diluted hydrogen/air flames

- The value of the maximum gradient varies widely with the equivalence ratio and slightly with the dilution which is consistent with the results obtained in chapter IV concerning the variation of the flame thickness with the dilution and equivalence ratio.

- The trends observed for the variation of the maximum gradient with the equivalence ratio and the dilution were to be expected. The value of the maximum gradient is a function of the local heat release and as a consequence

is a function of the flame temperature which varies similarly with the equivalence ratio and the dilution.

- The trend observed for the variation of the maximum gradient with the equivalence ratio was also observed in the experimental graphs (maximum gradient of respectively 18, 21 and 23 for the following equivalence ratio 0.38, 0.54 and 0.75).

- The trend observed concerning the variation of the maximum gradient with the dilution could not be investigated in this study because the experimental flames all have similar values of dilution (between 0.098 and 0.106).

- The location of the maximum gradient varies widely with the equivalence ratio and slightly with the dilution. This feature was not observed experimentally as the location of the maximum gradient is constant at $c_{NO\text{-}PLIF}$=0.4 for all flames studied.

- The maximum progress variable gradient cannot be associated with certainty with the maximum heat release because of the definition of the progress variable used here which makes it not a simple function of the temperature (section 2.2.3).

- As a consequence, various iso-c lines have been studied to verify whether the value of $c_{NO\text{-}PLIF}$ chosen to define the flame front had an impact on the results.

5.6 Presentation of a new method to calculate the 3D vectors normal to the isoscalar surfaces

Figure 5.25 shows the starting point of the explanation of the calculation of the 3rd component of the vectors normal to the iso-c line at c=0.4.

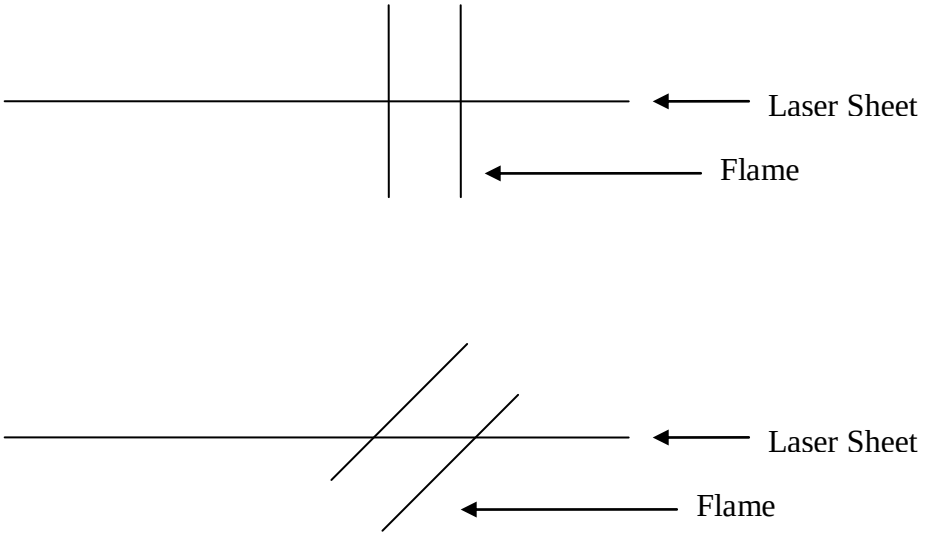

Figure 5.25: Sketch of the angle between the flame and the laser sheet

If the flame is perfectly orthogonal to the laser sheet, the vector normal to the flame front is two-dimensional i.e. its component in the z-direction is null. However if the flame is at an angle, the vector normal to the flame front is really three-dimensional i.e. its component in the z-direction is not null and cannot be assumed to be zero. As can be seen on the sketch, the flame thickness is at its minimum when the laser sheet and the flame are orthogonal. The flame thickness increases the more the angle between the laser sheet and the flame departs from 90°. Let's call θ the angle by which the flame departs from its ideal orthogonal position to the laser sheet. The flame thickness has an apparent increase in size of $\frac{1}{\cos(\theta)}$:

$$Apparentflamethickness = \frac{Realflamethickness}{\cos(\theta)} \tag{5.9}$$

The apparent flame thickness equals the real flame thickness when $\cos(\theta)=1$ i.e. when $\theta=0°$ i.e. when the angle between the flame and the laser sheet do not depart from 90°. The apparent flame thickness tends to infinity when $\cos(\theta)$ tends to zero i.e. when θ tends to 90° i.e. when the laser sheet coincides with the flame surface.

The spatial gradient of c as a function of c is at its maximum when θ=0° and decreases when θ increases:

$$ApparentGradient = RealGradient * \cos(\theta) \quad (5.10)$$

For each of the flames studied, the graphs showing the spatial gradient of c as a function of c were plotted. From the 400 graphs, it was possible to determine the maximum value of the spatial gradient of c at c=0.4. By dividing the value of the spatial gradient at c=0.4 by this maximum, it was possible to determine cos(θ).

Knowing cos(θ), it was possible to determine the real three-dimensional coordinate of the vector normal to the flame at c=0.4. There remained an uncertainty concerning the direction of the normal vectors. It is not possible to know their direction from the value of θ. It was assumed that the orientation of the vectors normal to the flame at c=0.4 would be the same as the direction of the three-dimensional PIV vectors.

The three-dimensional vectors normal to the flame at c=0.4 were hence calculated using the following methodology:

- for each two-dimensional vectors normal to the flame at c=0.4, calculation of the vectors normal to the two-dimensional vectors normal to the flame at c=0.4 around which the rotation of θ will be performed taking into account the orientation of the three-dimensional velocity vector,
- calculation of the corresponding cos*(θ)* and sin*(θ),*
- calculation of the new three-dimensional coordinates of the vector normal to the flame at c=0.4 by rotating the two-dimensional vector normal to the flame at c=0.4 of the angle θ around the vector normal to the two-dimensional vector normal to the flame at c=0.4.

This method of calculation of the 3rd component (in the z-direction) of the vectors normal to the flame at c=0.4 implicitly assumes that the thickening of the flame is only apparent and due to the flame not being at right angle to the laser sheet and does not take into account the fact that the flame might be locally thickened for

thermodynamical reasons. This could lead to an overestimation of the component in the z-direction.

In principle, this calculation could be performed for any value of c for the iso-c line. However, as the maximum value of the progress variable gradient is reached around c=0.4, the iso-c line c=0.4 is optimal for the calculation of the 3D vectors normal to the iso-c line at c=0.4.

The technique suggested here was applied to the flames studied in the present work. However, because it was not possible to evaluate the method during this work, no data are shown.

5.7 Critical evaluation of the NO-PLIF technique

The weaknesses and strengths of the NO-PLIF, which have been highlighted in this chapter and also in previous chapters (especially chapter II), may be summarised as follow:

- the resolution of the temperature by the one-line NO-PLIF technique decreases with temperature, as a consequence, it was not possible to study the iso-c line at c=0.9. Although, it may not be critical in this work. The excitation line used here may not be appropriate to work with when studying flames with higher adiabatic flame temperatures.
- Because of the difficulty encountered when calibrating the NO-PLIF signal as a function of temperature, it was not possible to determine with certainty the region of intense heat release as is possible with the OH-PLIF technique [14]. It also made it difficult to compare the experimental results with simulated/theoretical results.
- However, the NO-PLIF technique does allow the extraction of flame front properties at various values of c because a simple threshold technique can be used.
- Detection of extinction phenomena may be more difficult when using the NO-PLIF technique as employed here as evidenced in section 5.3. Chemiluminescent markers may be more appropriate in that they directly map the reaction in a flame instead of mapping the temperature.

CHAPTER VI

Processing and analysis of the SPIV data

This chapter describes the conversion of the SPIV data into velocity fields and strain rate fields. It also presents an analysis of the velocity fields and of the strain rate fields along chosen flame contours.

6.1 Calculation of the velocity vector fields

The velocity vector fields were computed using the DaVis 7.1 software package [60-61].

Four raw images (two images from camera 1 at t and t+dt and two images from camera 2 at t and t+dt) were taken to compute the two-dimensional velocity vector fields with three velocity components (so called 2D-3C velocity vector fields).

Each image is distorted because the cameras are not orthogonal to the object plane. So firstly, the images recorded are dewarped using the calibration data so as to match the true physical space.

The images from the two cameras are overlapped. The common area is determined and its corresponding blank vector image is created.

Each image is then divided into interrogation windows whose size can be chosen. Neighbouring interrogation windows can be overlapped. The higher the overlap, the tighter is the grid of computed velocity vectors. The overlap chosen for the interrogation windows in the present work is 50%. A 3D stereo cross-correlation technique with a standard FFT-based algorithm is used to calculate the velocity vector fields. The 3D stereo cross-correlation consists in calculating the vector fields using the four single-exposed images from two cameras. The standard FFT-based algorithm calculates a correlation of the interrogation window and can be related to the mathematical correlation [60]:

$$C(dx,dy) = \sum_{x=0,y=0}^{x<n,y<n} I_1(x,y) I_2(x+dx, y+dy), -\frac{n}{2} < dx, dy < -\frac{n}{2} \qquad (6.1)$$

where I_1 and I_2 are the image intensities of the interrogation windows in the first and second exposures images from camera 1 (or camera 2).

C is a measure of the correlation strength for all displacements (dx, dy) allowing to determine the displacement in the interrogation windows and as consequence the velocity.

A multi pass with decreasing interrogation window size strategy is employed: the vector fields are calculated after a certain number of iterations. This allows a smaller final size for the interrogation windows and as a consequence a better resolution. The initial interrogation window size was 64*64 pixels because it allowed a good correlation (enough paired particles between the first and second exposure images for both cameras) and the final interrogation window size was 32*32 pixels which is the best resolution that could be achieved. With this strategy, the displacement calculated after the first pass is used to shift the interrogation window so as to improve the correlation in the subsequent pass. After the last pass, the 2D-3C velocity vector field are calculated from the two planar displacement vector fields (from camera 1 and camera 2) as explained in section 2.3.4.

Figure 6.1 shows a schematic representation of the calculation of the 2D-3C velocity vector fields as is explained here.

Figure 6.2 shows an arbitrary vector field image for flame E. The flame contours corresponding to the iso-c line at c=0.4, 0.6, 0.8 and 0.9 are superimposed on the vector field image.

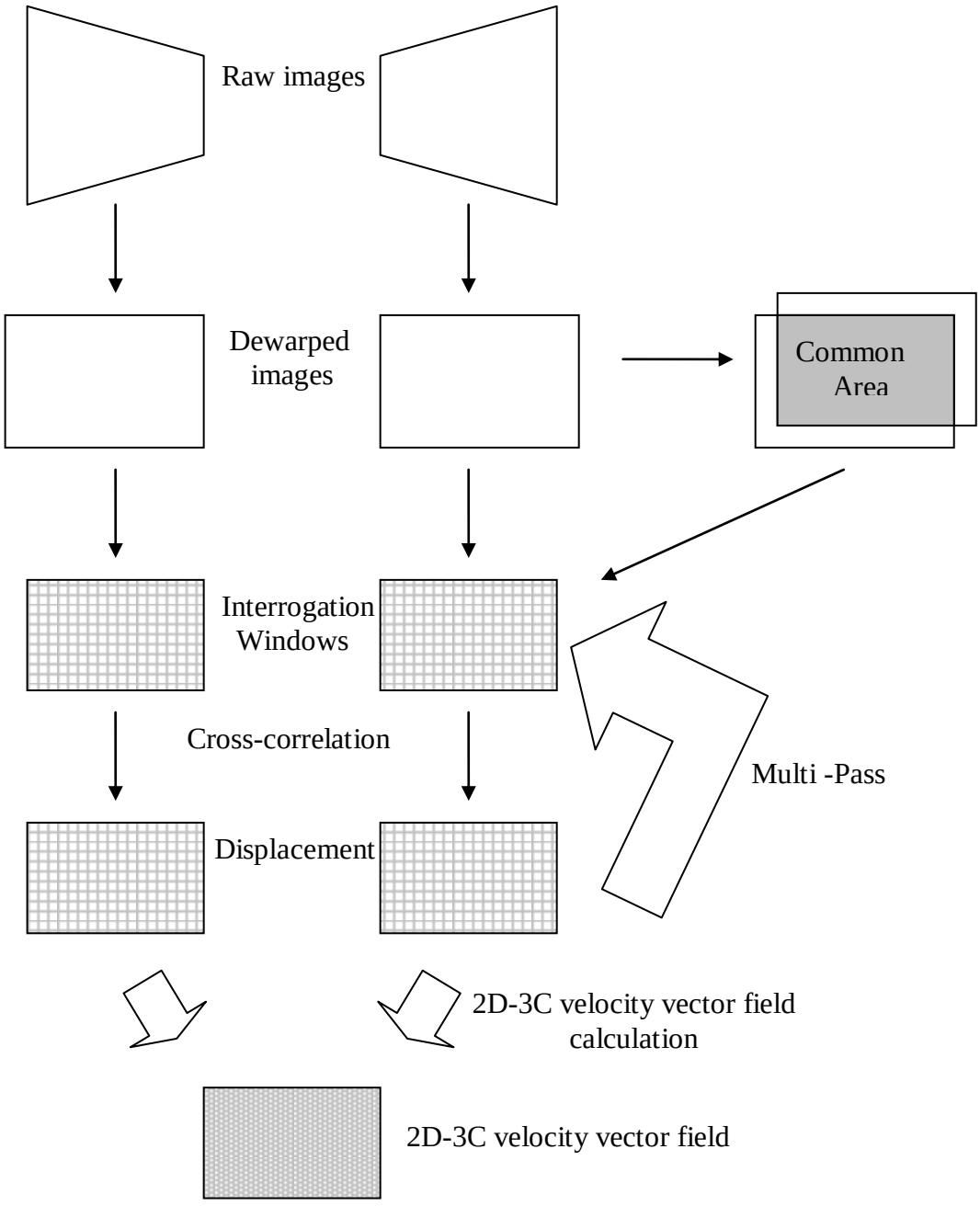

Figure 6.1: Schematic representation of the calculation of the velocity vector fields

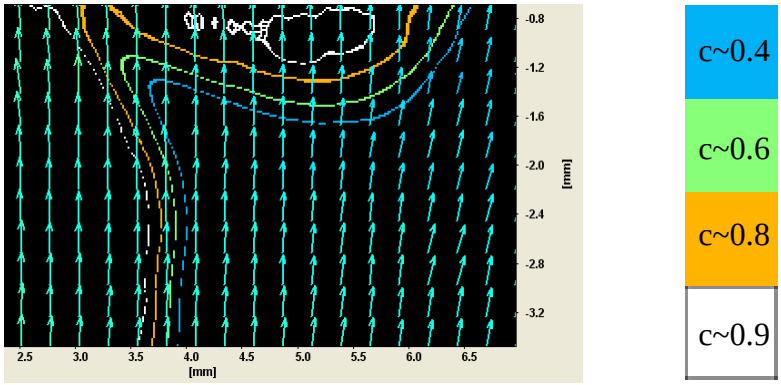

Figure 6.2: Vector field across different iso-c lines for flame E

6.2 Analysis of the velocity vector fields: acceleration across the flame front

As can be seen in figure 6.2, the velocity field does not seem affected by the presence of the flame, which is represented here by the iso-c lines at c=0.4, 0.6, 0.8 and 0.9. One would expect an acceleration to take place and/or a change in the direction of the velocity vectors. Clearly, this is not the case: both in the unburnt gases side and the burnt gases side and also through the reaction zone, the velocity vectors appeared of same magnitude and direction. This feature was a constant for all flames no matter the adiabatic flame temperature, the turbulence or the composition of the flame: superficially, the PIV data did not appear strongly influenced by the reaction zone.

In order to investigate the acceleration of the flow from the unburnt gases side to the burnt gases side due to the heat release, the velocity variation across the flame front along a normal vector was calculated for flame E which is the flame with the highest equivalence ratio (Φ=0.76) and one of the lowest nitrogen content and as a consequence, has the maximum adiabatic flame temperature (1396K). Flame E, being the flame with the greatest heat release for the conditions investigated, should experience the strongest acceleration. The velocity variation was defined as:

$$\Delta V = V_b^N - V_u^N \tag{6.2}$$

in which V_b^N is the velocity along the normal vector in the burnt gases side and V_u^N is the velocity in the unburnt gases side.

The velocity variation along the normal vector was calculated as follows:
- as for the calculation of the vectors normal to the flame front, the calculation of the velocity variation takes place in 16*16 pixel (262µm * 262µm) interrogation windows of the flame front image because the velocity vectors are only resolved in such boxes,
- when a 16*16 pixel interrogation window in the flame front image has two or more valid pixels (i.e. pixels with a value of 1 and not 0), the 2D components of the vectors normal to the flame front are interrogated and depending on their value, the velocity variation along the flame normal is calculated accordingly (see Figure 6.3).

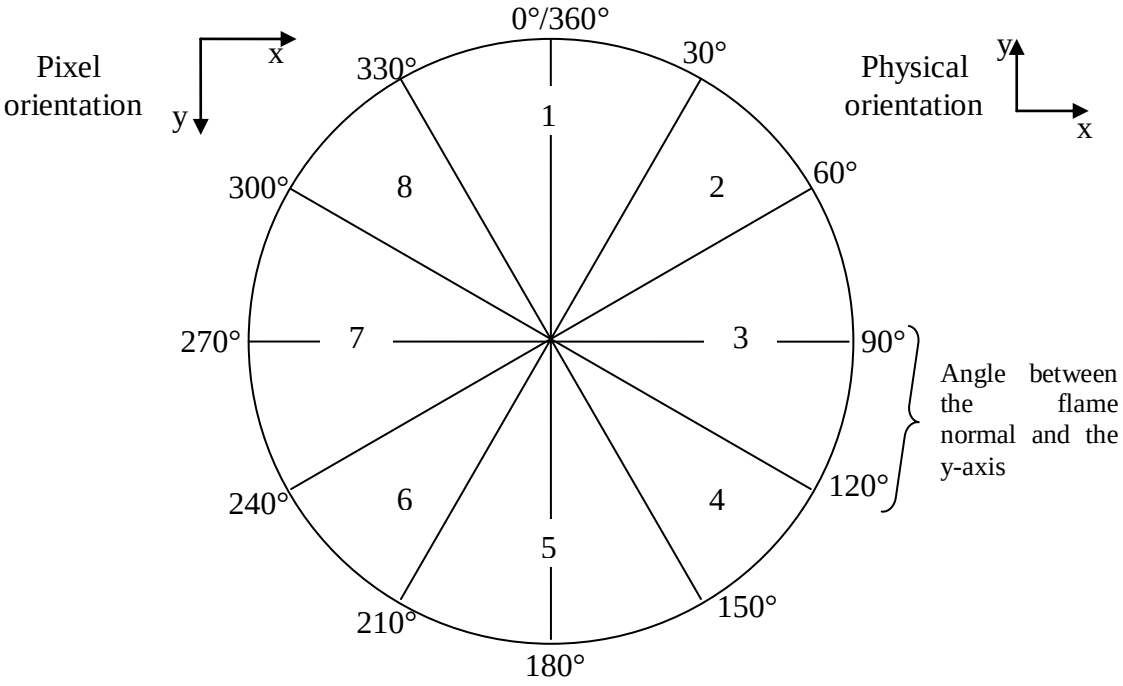

<u>Figure 6.3</u>: Sketch of the different zones of vector orientation corresponding to different expressions for the velocity variation

Table 6.1 shows the expressions used for the calculation of the velocity variation as a function of the value taken by the components of the vectors normal to the flame front.

The "velocity" mentioned in the table corresponds to the velocity along the normal vector i.e. the projection of the 2D velocity given by the PIV onto the normal vector direction. For example, the velocity "velocity(Pix(x, y+1)" is actually: $V_x(x, y+1)*N_x(x, y) + V_y*N_y(x, y)$ with Vx the component of the velocity in the x-direction, V_y the component of the velocity in the y-direction and N_x the component of the

normal vector in the x-direction and N_y the component of the normal vector in the y-direction, the normal vectors being unit vectors.

Zone	Angle between the flame normal and the y-axis	Range for the value of the component of the normal vector in the x-direction	Range for the value of the component of the normal vector in the y-direction	Expression for Δv
1	[330°, 360°] & [0°, 30°]	[-0.33, +0.33]	[+1, +0.67]	velocity(Pix(x, y-1)) - velocity(Pix(x, y+1))
2	[30°, 60°]	[+0.33, +0.67]	[+0.67, +0.33]	[velocity(Pix(x+1, y-1)) - velocity(Pix(x-1, y+1))] /√2
3	[60°, 120°]	[+0.67, +1]	[-0.33, +0.33]	velocity(Pix(x+1, y)) - velocity(Pix(x-1, y))
4	[120°, 150°]	[+0.33, +0.67]	[-0.67, -0.33]	[velocity(Pix(x+1, y+1)) - velocity(Pix(x-1, y-1))] /√2
5	[150°, 210°]	[-0.33, +0.33]	[-1, -0.67]	velocity(Pix(x, y+1)) - velocity(Pix(x, y-1))
6	[210°, 240°]	[-0.67, -0.33]	[-0.67, -0.33]	[velocity(Pix(x-1, y+1)) - velocity(Pix(x+1, y-1))] /√2
7	[240°, 300°]	[-1, -0.67]	[-0.33, +0.33]	velocity(Pix(x-1, y)) - velocity(Pix(x+1, y))
8	[300°, 330°]	[-0.67, -0.33]	[+0.67, +0.33]	[velocity(Pix(x-1, y-1)) - velocity(Pix(x+1, y+1))] /√2

Table 6.1: Table showing the expression for the velocity variation as a function of the value of the components of the normal vectors

Graph 6.4 shows the pdf of the velocity variation for flame E. The entire set of 400 images was analysed. As can be seen, the implied level of acceleration across the flame front is very weak. The curve peaks around 0.005m.s^{-1}. Most of the observed velocity is bulk motion (3.54m.s^{-1}) -see tables 4.1 and 4.2- as the laminar flame speed is expected to be only 0.21m.s^{-1} (see also figure 6.5). A quick analysis of a stationary laminar planar flame of same composition than flame E would suggest a value for ΔV of 0.72m.s^{-1} which is much higher than the value obtained experimentally. However, the flames studied in the present work are 3D turbulent flames. As a consequence, the heat release may have been compensated by further corrugation of the flame surface.

Since flame E has the highest adiabatic flame temperature of all the flames, this investigation was not extended to the complete data set.

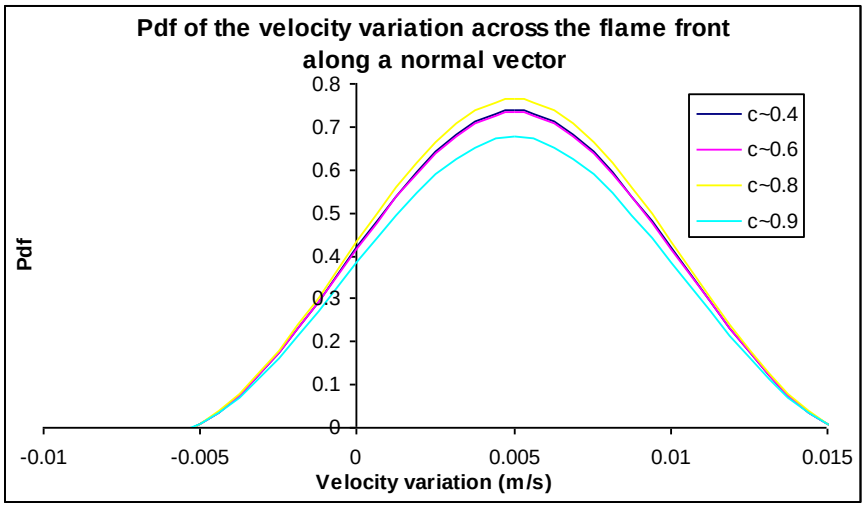

Figure 6.4: Pdf of the velocity variation across the flame front along a normal vector for flame E

Figure 6.5 shows the velocity vector field of a single shot image of flame E from which the average unburnt velocity has been subtracted. The iso-c lines at c=0.4, 0.6, 0.8 and 0.9 are also shown. Still no substantial acceleration across the flame zone is visible.

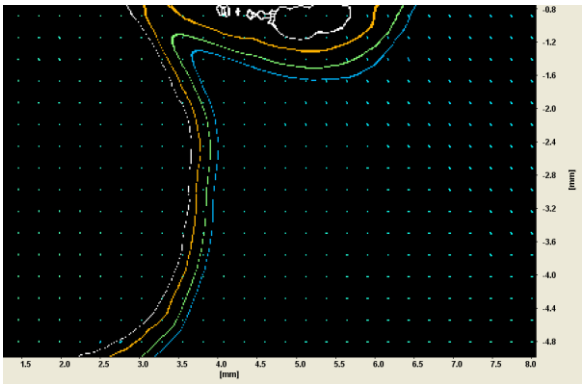

Figure 6.5: Velocity field minus average unburnt velocity across different iso-c lines for flame E

6.3 Calculation of the strain rate fields

The stereoscopic particle image velocimetry technique used here measures the component $V_x(x,y)$ of the velocity in the x-direction, the component $V_y(x,y)$ of the velocity in the y-direction, the component $V_z(x,y)$ of the velocity in the z-direction.

As a consequence, from the 2D-3C velocity vector fields, only 6 strains can be calculated: $E_{xx} = \frac{dV_x}{dx}$, $E_{xy} = \frac{dV_x}{dy}$, $E_{yx} = \frac{dV_y}{dx}$, $E_{yy} = \frac{dV_y}{dy}$, $E_{zx} = \frac{dV_z}{dx}$ and $E_{zy} = \frac{dV_z}{dy}$.

As explained in section 6.1, the velocity vectors are calculated on a discrete grid. As a consequence, the strain E_{xx}, E_{xy}, E_{yx}, E_{yy}, E_{zx} and E_{zy} are approximated as follow:

$$E_{ij} = \frac{\Delta V_i}{\Delta j} \tag{6.3}$$

For instance, for the calculation of the strain E_{xy}, at the position (n,m), the following formulas are used:

- if both neighbour velocity vectors in the y-direction exist:

$$E_{xy}(n,m) = \frac{(V_x(n,m+1) - V_x(n,m-1))}{2 * vectorgrid} \tag{6.4}$$

- if only the neighbour velocity vector above the position (n,m) in the y-direction exists:

$$E_{xy}(n,m) = \frac{(V_x(n,m) - V_x(n,m-1))}{vectorgrid} \tag{6.5}$$

- if only the neighbour velocity vector under the position (n,m) in the y-direction exists

$$E_{xy}(n,m) = \frac{(V_x(n,m+1) - V_x(n,m))}{vectorgrid} \tag{6.6}$$

where the vectorgrid is the physical distance between two neighbour velocity vector positions, in our case 262µm.

6.4 Analyses of the strain rate fields

6.4.1 Extinction strain rates: background

The critical strain rate to extinction (extinction strain rate) is a very important characteristic in turbulent combustion. It corresponds to the maximum velocity gradient a flame can sustain. It is a flow field property and its value depends on the composition of the mixture, its pressure and temperature.

Experimentally, extinction strain rates are mainly determined using counterflow flames. Few articles are available concerning extinction strain rates of premixed hydrogen-air flames: only two recent sources [109-110] investigating extinction in premixed hydrogen-air flames were found. However, these investigations are all the more interesting that they also include data for nitrogen-diluted hydrogen-air flames. Dong et al. [109] investigated experimentally and numerically ultra-lean H_2/air flames and lean and near-stoichiometric H_2/air flames with various amount of added nitrogen. The experimental values they obtained for the extinction strain rates are reported in figures 6.6 and 6.7. The numerical values reported in [109] depart significantly (up to 40%) from the experimental values. They attributed the discrepancies to failures in the models, either because of inaccuracies in the evaluation of kinetic rate constants or because of inaccuracies in the evaluation of molecular diffusion coefficients. As a consequence, the numerical values of extinction strain rates are not shown in the following figures. Bunkute [110] also investigated the effect of equivalence ratio and dilution on the extinction strain rates of premixed hydrogen-air flames. The results, which were obtained by numerical simulation, also depart from the experimental values reported in [109]. The experimental values reported in [109] were obtained using a counterflowing fuel/air jet against an air jet. The numerical values reported in [110] were obtained using the OPPDIF model in the commercial code Chemkin [15]. The discrepancies observed may be because the conditions specified in [110] differ from the one used in [109]: burner separation distance, nozzle diameter, inlet velocities…Some of these conditions may have an influence on the critical strain rates to extinction. In particular, it is acknowledged in

[109] that the burner separation distance can have an effect on the extinction strain rate.

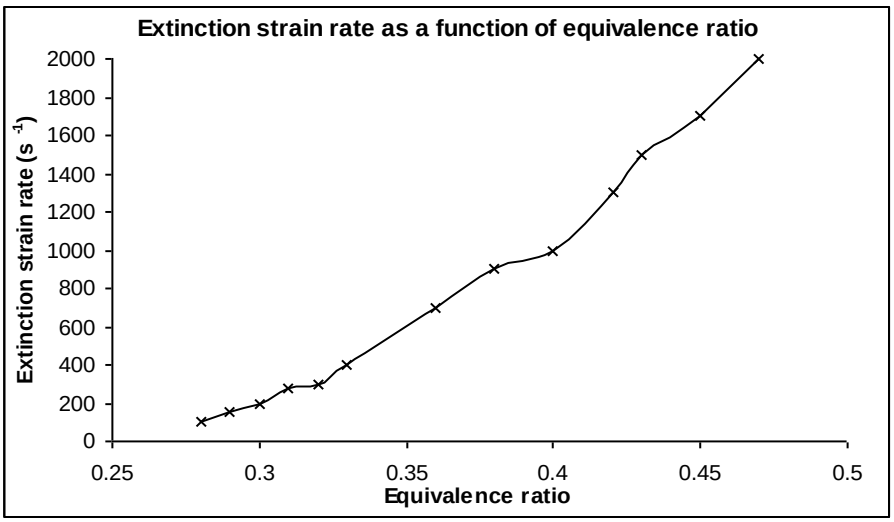

Figure 6.6: Extinction strain rates for hydrogen/air flames as a function of equivalence ratio [109]

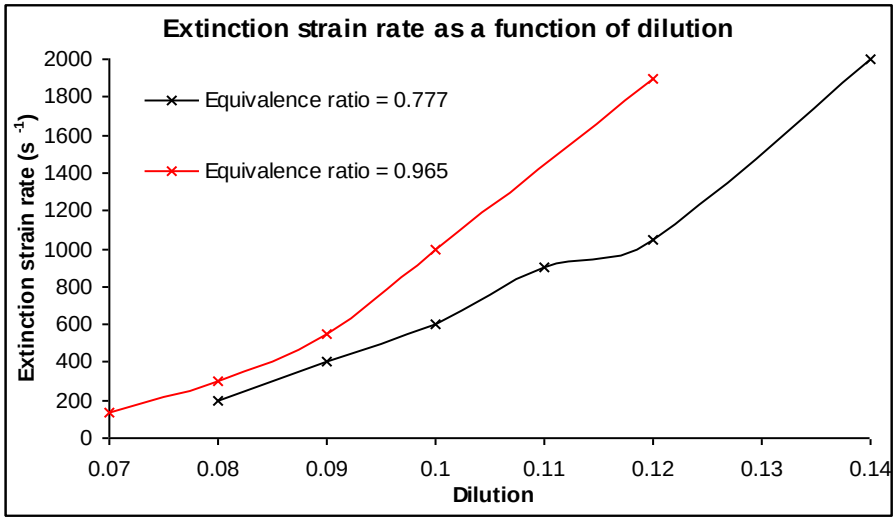

Figure 6.7: Extinction strain rates for hydrogen/air flames with added nitrogen as a function of dilution [109]*

$$^{*}\,Dilution = \frac{n_{O_2}}{n_{O_2} + n_{N_2}} \quad (4.1)$$

From [109], the extinction strain rates for flames C, E, F are expected to be of the order of $700s^{-1}$. The extinction strain rates for flames B, A and I are expected to be substantially lower.

6.4.2 Selected experimental results

6.4.2.1 Analyses of the strain rates along non-wrinkled iso-c contours

Figures 6.8, 6.9 and 6.10 show three instantaneous images taken from flame A, C and E. They have been selected because the flame front appears to be non-wrinkled. In each case, the strain rates E_{xx}, E_{xy}, E_{yx}, E_{yy} and E_{zx} and E_{zy} were plotted against the displacement along the non-wrinkled iso-c contours.

The goal was to study the strain rates variations along the apparently non-wrinkled iso-c contours.

It was expected that the strain rates would not vary significantly along the flame contours.
It was also expected that the strain rates E_{zx} and E_{zy} would have significantly lower value than the other strain rates because the value of the component of the velocity in the z-direction is much smaller than the value of the components of the velocity in the x- and y- direction.
Conversely, it was expected that the strain rate E_{yx} would be the strain rate assuming the highest values because the value of the component of the velocity in the y-direction is much higher than the value of the components of the velocity in the other directions and because of the orientation of the flame front.

Figures 6.8 to 6.10 show that the strain rates E_{xx}, E_{xy}, E_{yx}, E_{yy}, E_{zx} and E_{zy} vary substantially along those non-wrinkled iso-c contours no matter what value for c was taken for the contour.
It was also found that the strain rates E_{zx} and E_{zy} did not assume significantly lower values than the strain rates E_{xx}, E_{xy}, E_{yx} and E_{yy} and that the strain rate E_{yx} did not assume significantly higher values than the other strain rates.
The uncertainties on the velocity data was estimated to be similar to the uncertainties reported in [14]. As a consequence, the estimated uncertainties on the strain rates are expected to be of the order of $300s^{-1}$ which may partly explain the absence of pattern observed in figures 6.8 to 6.10 and 6.14 to 6.18.

Example 1: Flame A (Image 84)

(scale: 16μm/pixel)

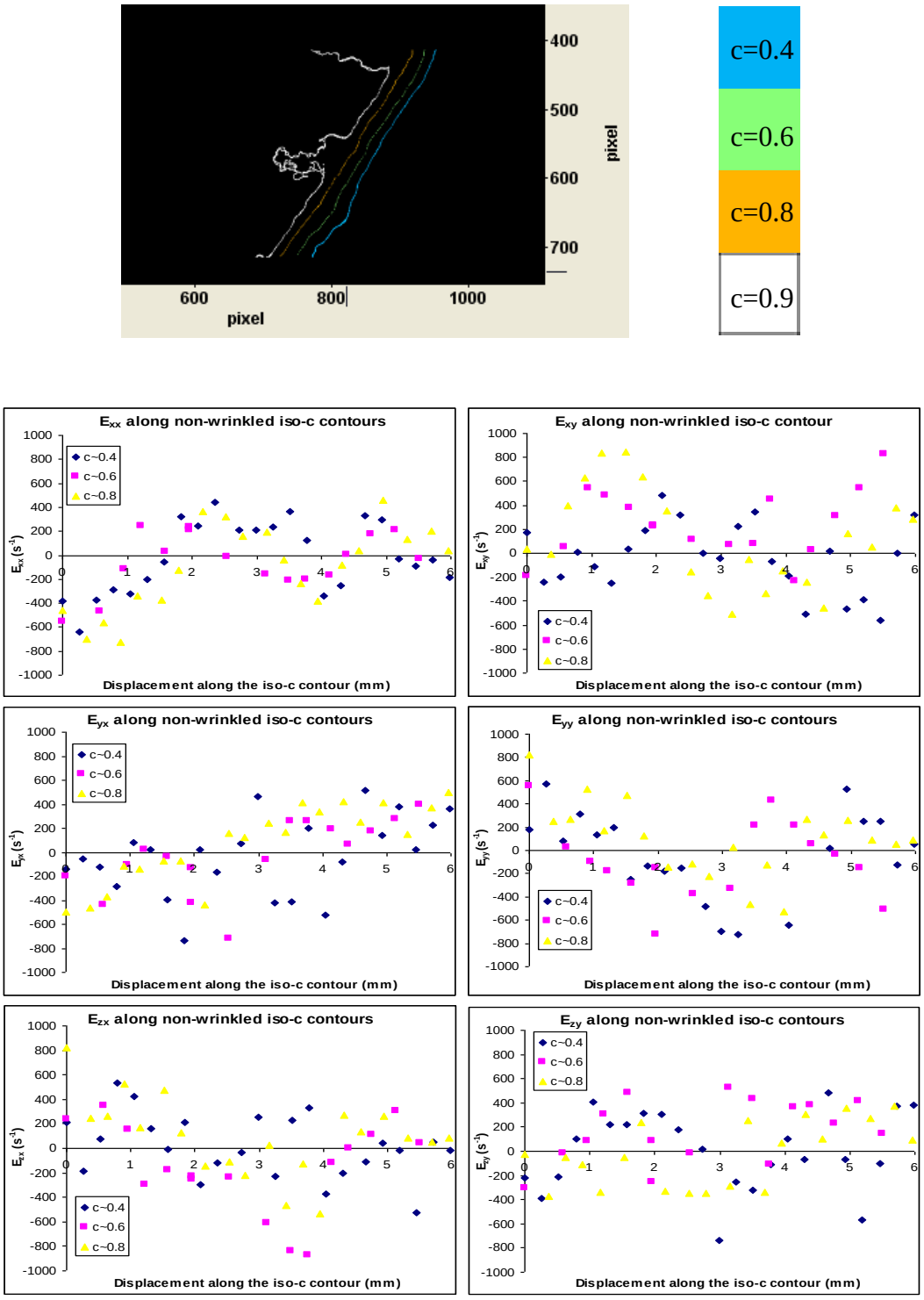

Figure 6.8: Strain rates along non-wrinkled iso-c contours in an instantaneous shot of flame A (from top left to bottom right: (a) Exx (b) Exy (c) Eyx (d) Eyy (e) Ezx and (f) Ezy)

Example 2: Flame C (Image 89)

(scale: 16μm/pixel)

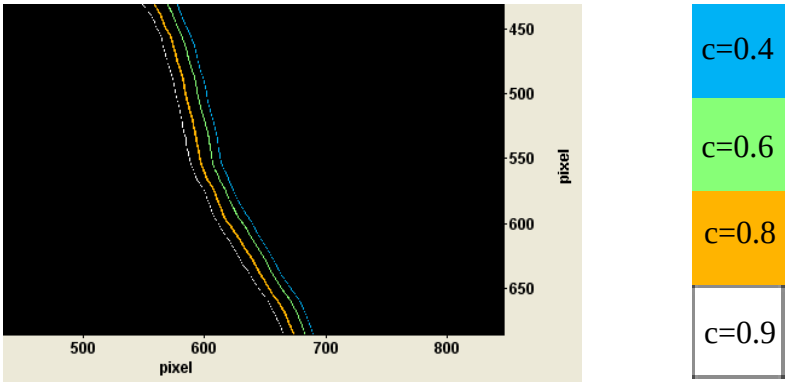

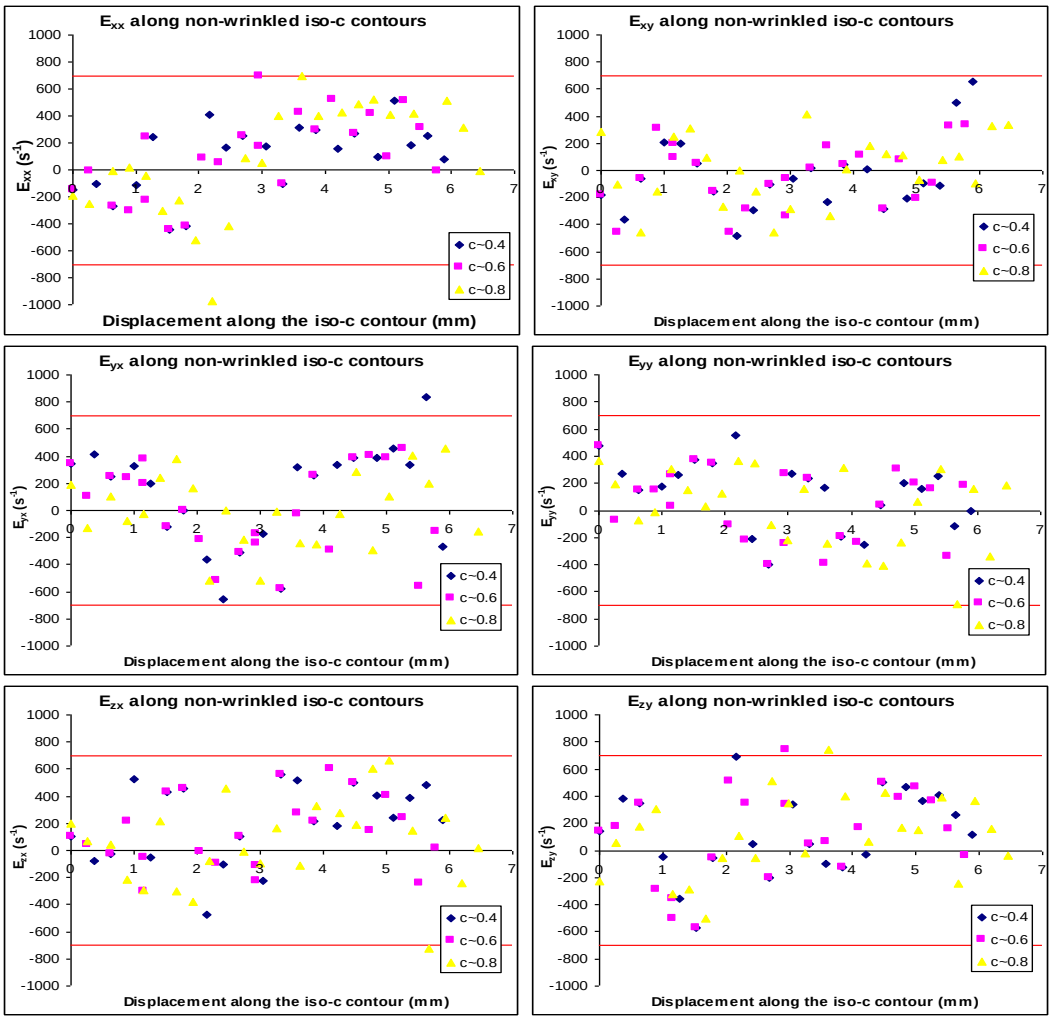

Figure 6.9: Strain rates along non-wrinkled iso-c contours in an instantaneous shot of flame C (from top left to bottom right: (a) Exx (b) Exy (c) Eyx (d) Eyy (e) Ezx and (f) Ezy)*

* red lines show critical value for the strain rate

Example 3: Flame E (Image 133)

(scale: 16μm/pixel)

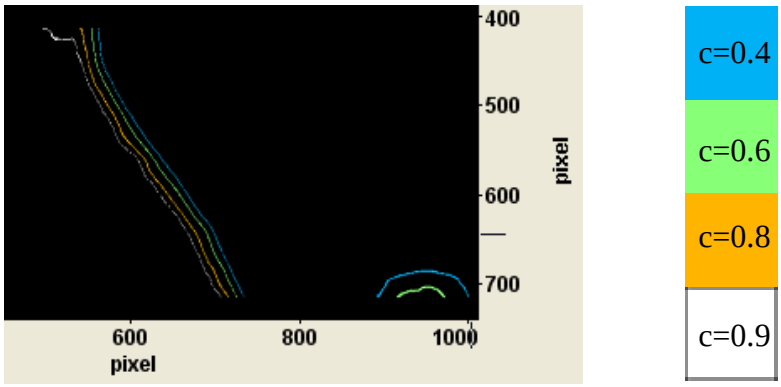

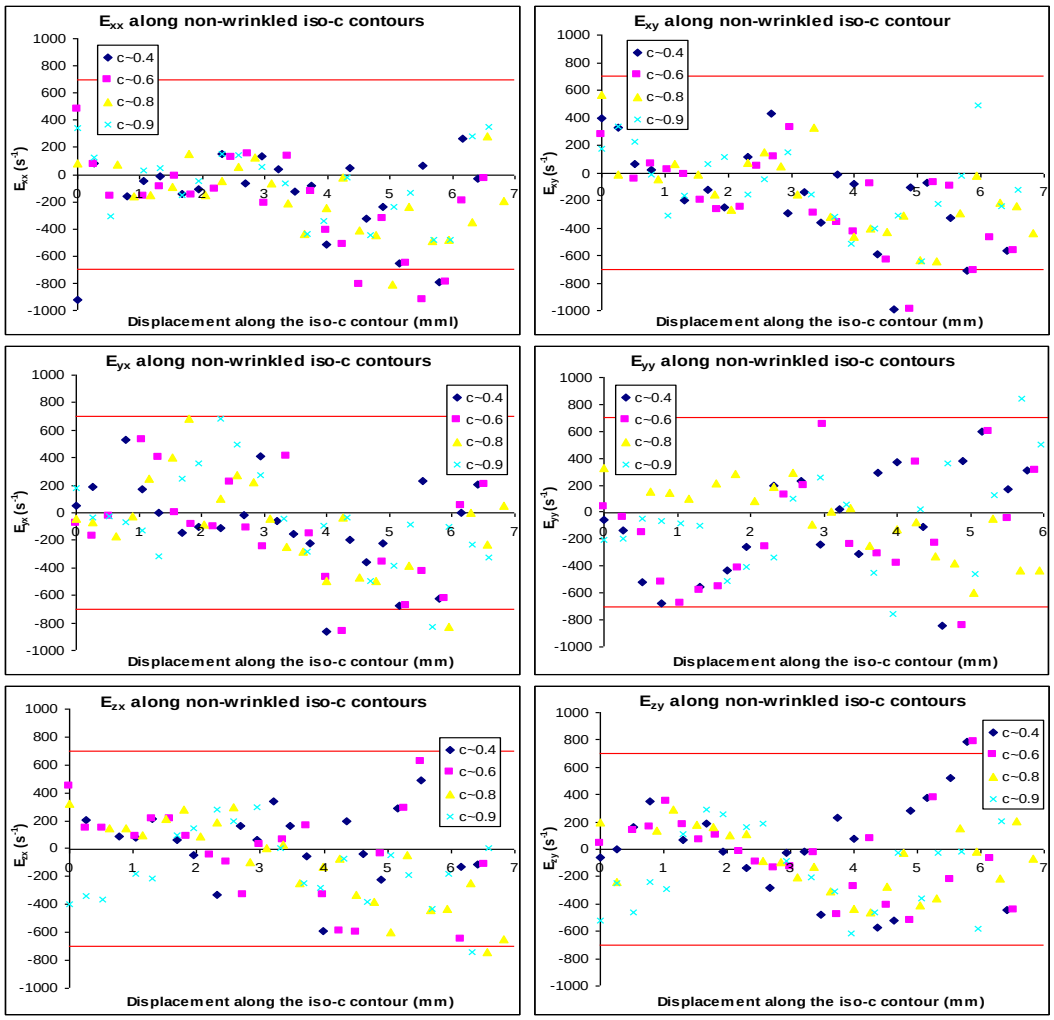

Figure 6.10: Strain rates along non-wrinkled iso-c contours in an instantaneous shot of flame E (from top left to bottom right: (a) Exx (b) Exy (c) Eyx (d) Eyy (e) Ezx and (f) Ezy)*

* red lines show critical value for the strain rate

The PLIF experiments only offer an image of the flame as a 2D object whereas it really is a 3D object. As a consequence, the flame fronts in figures 6.8 to 6.10 may be in reality wrinkled even though it does not appear so. As was explained in section 5.5, one possible solution to investigate the third dimensionality of the flame is to use the information contained in the gradient of the progress variable. The information contained in the gradient data can give us clue to the real 3D shape of the flames. Figures 6.11 to 6.13 show the spatial gradient of the progress variable plotted against the displacement along the iso-c contours for the cases corresponding to figures 6.8, 6.9 and 6.10.

If figures 6.8 to 6.10 had shown similar features than figures 6.11 to 6.13, it may have been possible to link the variation of the strain rates along the non-wrinkled iso-c contours with the real shape of the flame front in 3D. The results suggest that although the influence of curvature on the strain rates can not be eliminated, it is not possible to attribute the variation of the strain rates along the apparently non-wrinkled iso-c contours entirely to it.

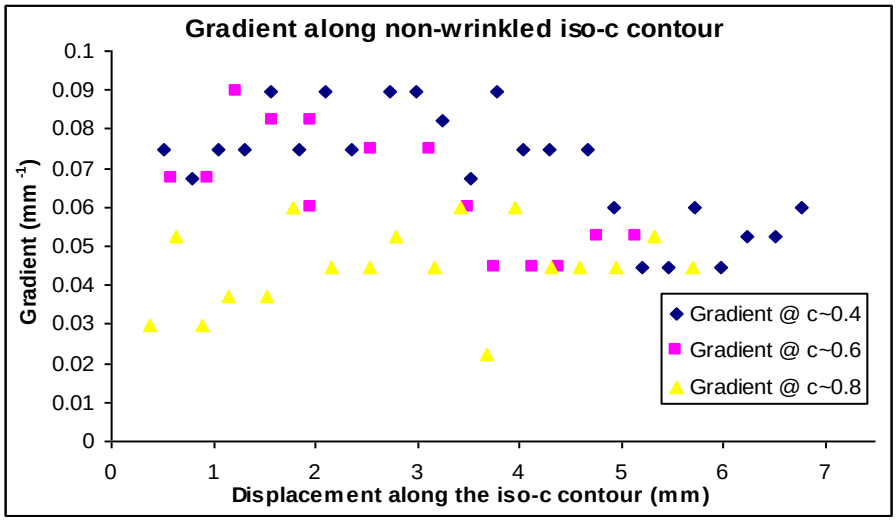

Figure 6.11: Gradient of the progress variable along non-wrinkled iso-c contours for flame A (image 84)

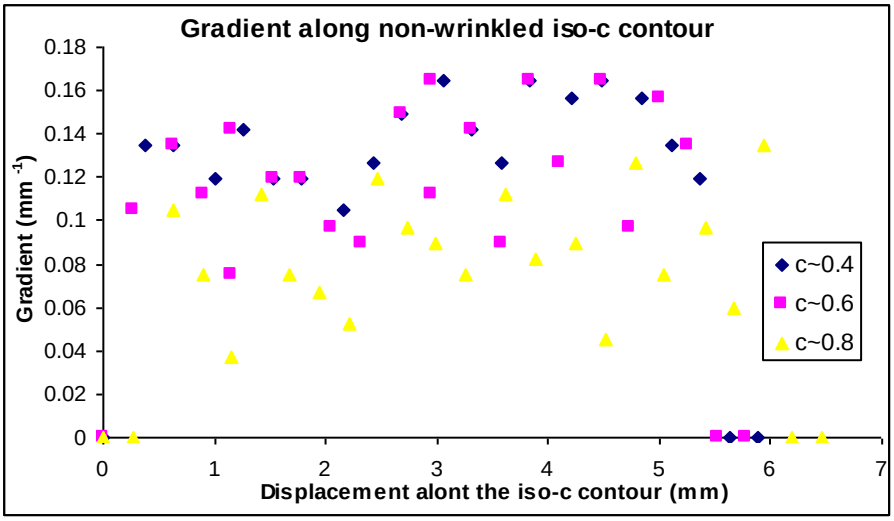

Figure 6.12: Gradient of the progress variable along non-wrinkled iso-c contours for flame C (image 89)

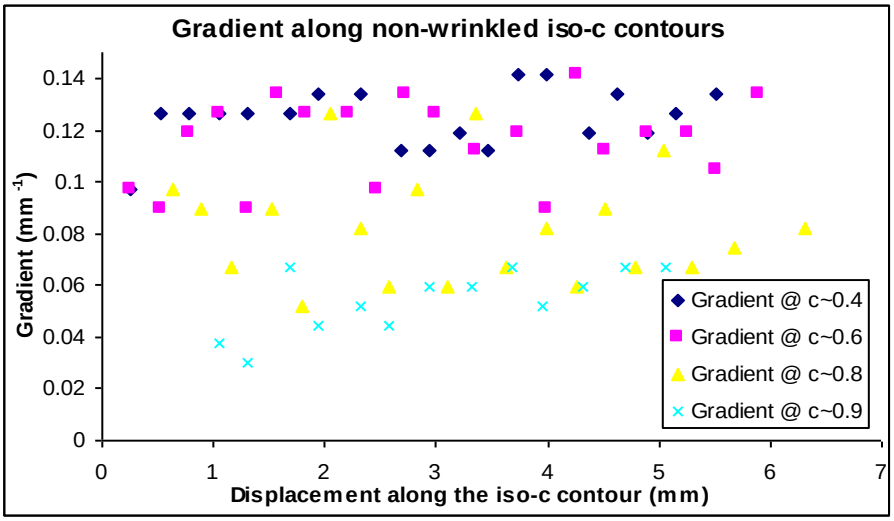

Figure 6.13: Gradient of the progress variable along non-wrinkled iso-c contours for flame E (image 133)

The fact that all components of strain rates take similar value is consistent with the previous result (in section 6.2) concerning the acceleration across the flame front. The (low) heat release may have been responsible for corrugating further the turbulent flame front instead of accelerating the gases through the flame zone.

Most values of strain rates in figures 6.9 and 6.10 fall below the value of the critical strain rate to extinction, suggesting that no extinction occurred in the images presented here.

6.4.2.2 Strain rates along wrinkled iso-c contours

Figures 6.14 to 6.18 illustrate various cases where the iso-c contours are clearly wrinkled. Again, the strain rates E_{xx}, E_{xy}, E_{yx}, E_{yy} and E_{zx} and E_{zy} were plotted against the displacement along the iso-c contours.

They all correspond to flame C so as to be able to compare them between themselves and with figure 6.8.

Figure 6.14 show a case where the iso-c contours are moderately wrinkled while figure 6.15 shows a case where the iso-c contours are strongly wrinkled.

Figure 6.16 and 6.17 show cases where the strain rates studied were around pockets of unburnt gases embedded in burnt gases while figure 6.18 shows a case where the strain rates studied were around a pocket of burnt gases embedded in unburnt gases.

Figures 6.14 to 6.18 are briefly commented on page 186.

Example 4: Flame C (161)

(scale: 16μm/pixel)

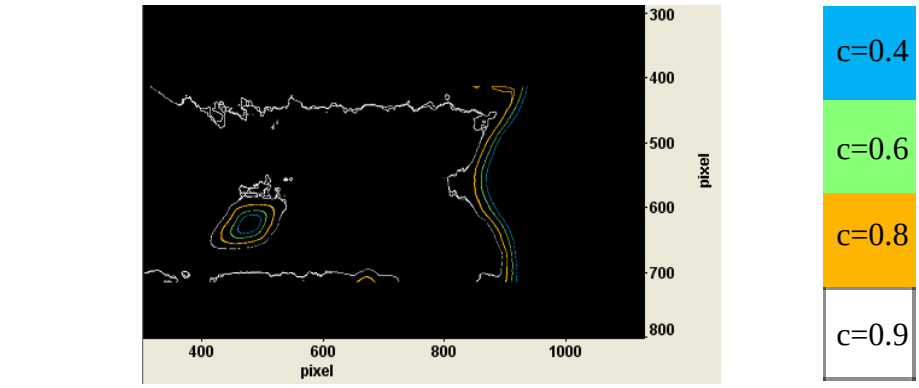

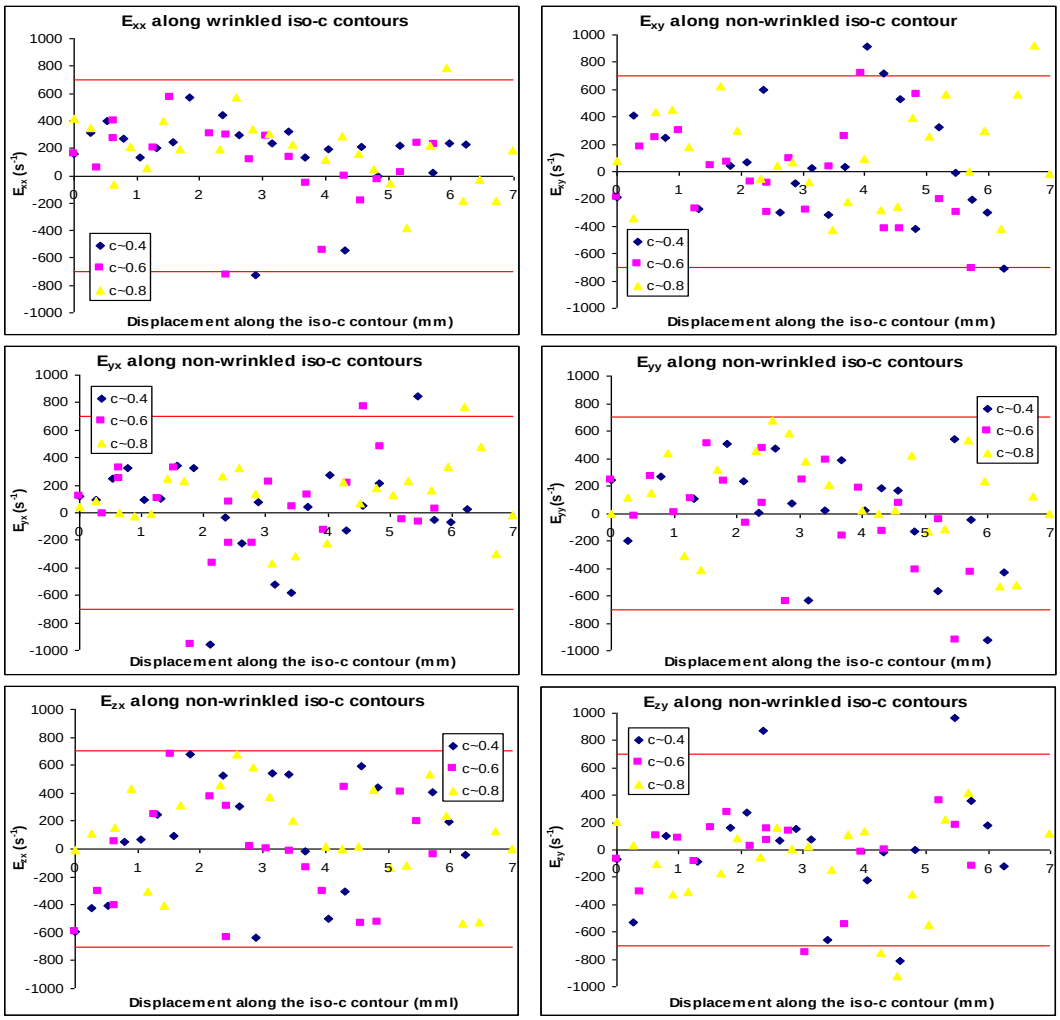

Figure 6.14: Strain rates along wrinkled iso-c contours in an instantaneous shot of flame C (from top left to bottom right: (a) Exx (b) Exy (c) Eyx (d) Eyy (e) Ezx and (f) Ezy)*

* red lines show critical value for the strain rate

Example 5: Flame C (124)

(scale: 16μm/pixel)

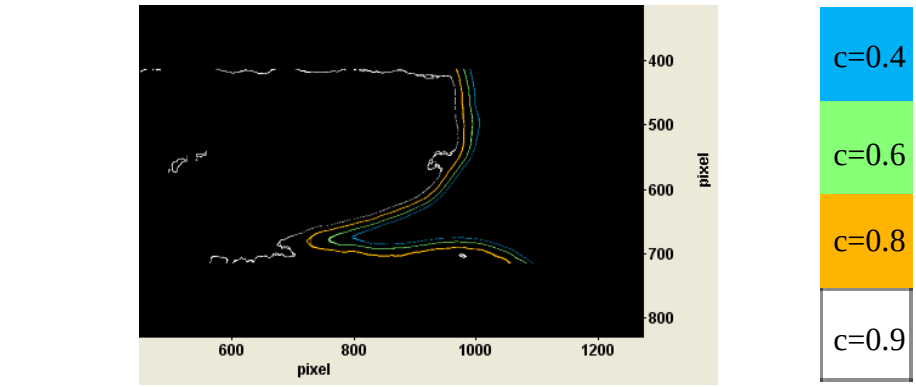

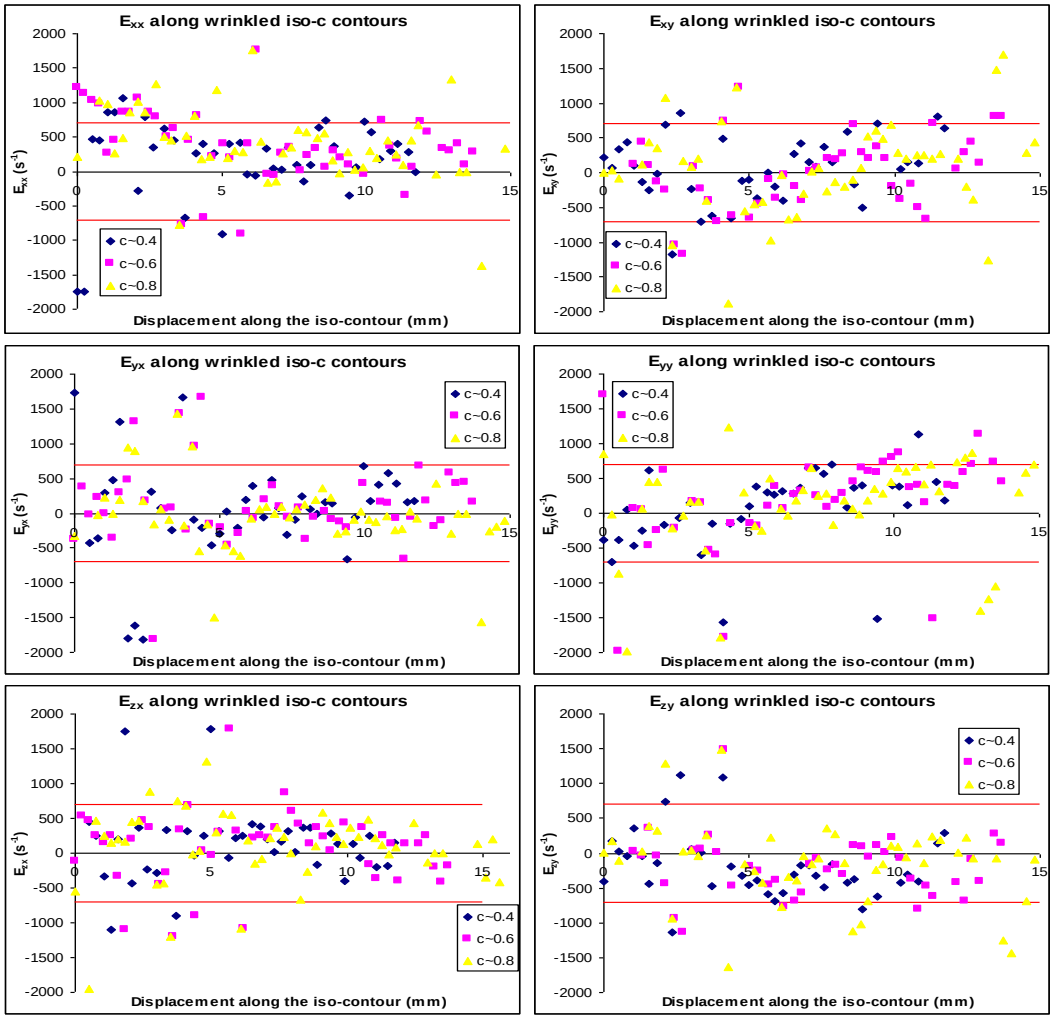

Figure 6.15: Strain rates along wrinkled iso-c contours in an instantaneous shot of flame C (from top left to bottom right: (a) Exx (b) Exy (c) Eyx (d) Eyy (e) Ezx and (f) Ezy)*

* red lines show critical value for the strain rate

Example 6: Flame C (161)

(scale: 16μm/pixel)

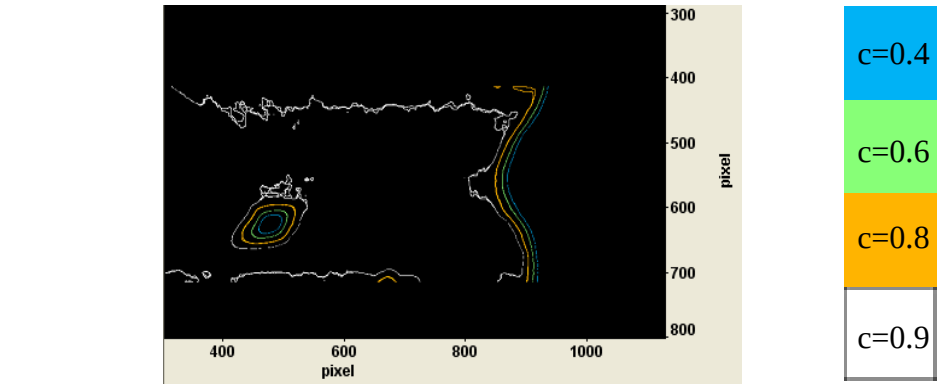

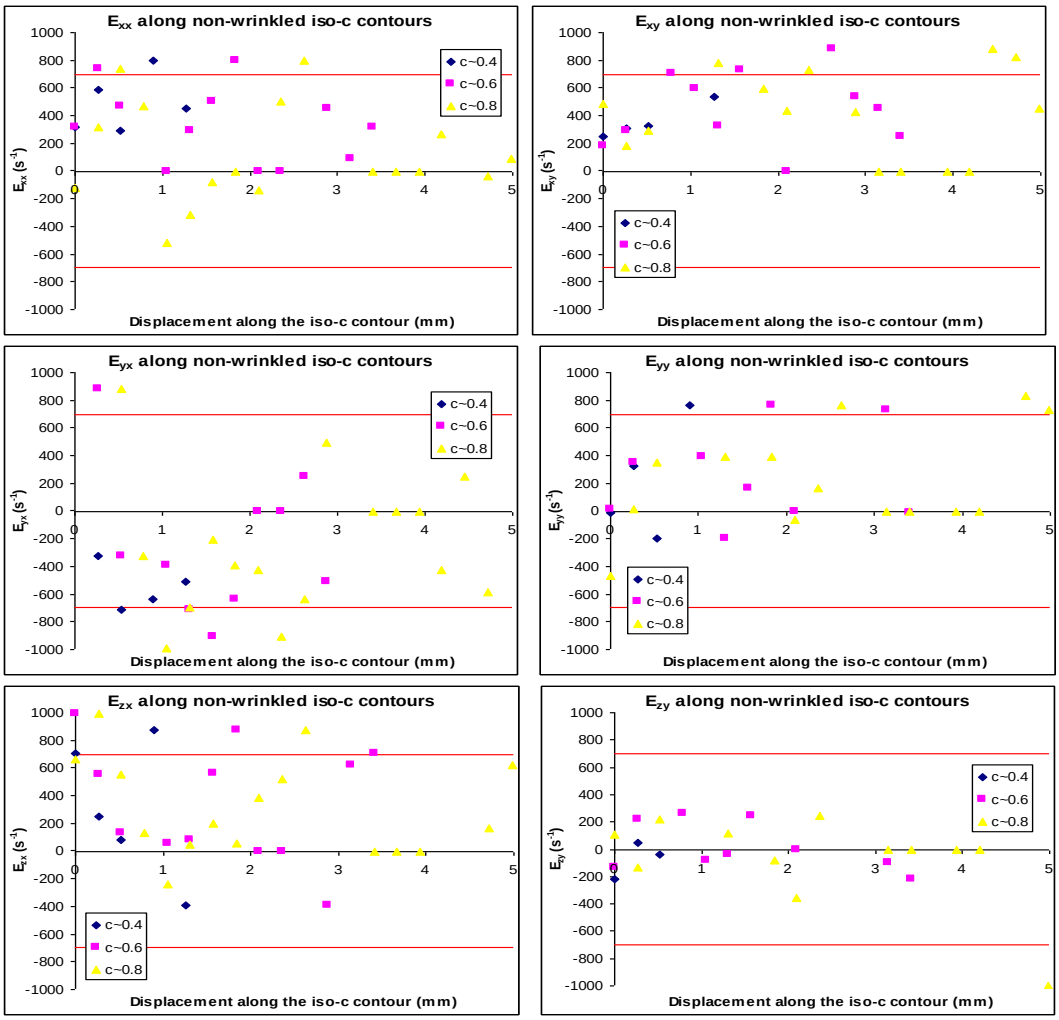

*Figure 6.16: Strain rates along the iso-c contours of a pocket of unburnt gases in burnt gases for flame C**
(from top left to bottom right: (a) Exx (b) Exy (c) Eyx (d) Eyy (e) Ezx and (f) Ezy)

* red lines show critical value for the strain rate

Example 7: Flame C (125)

(scale: 16µm/pixel)

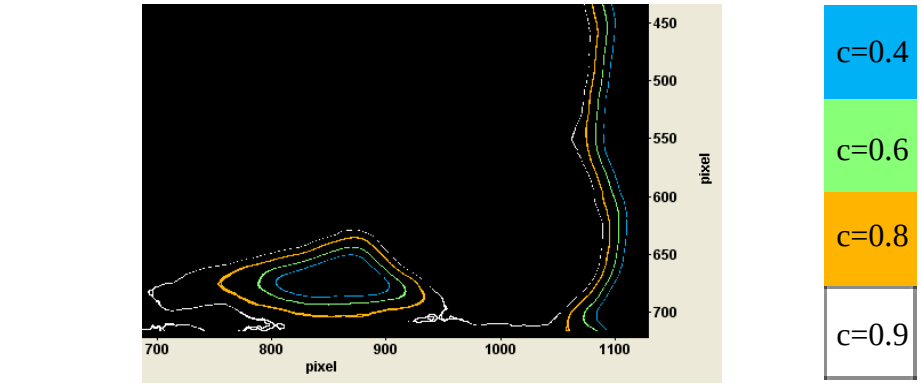

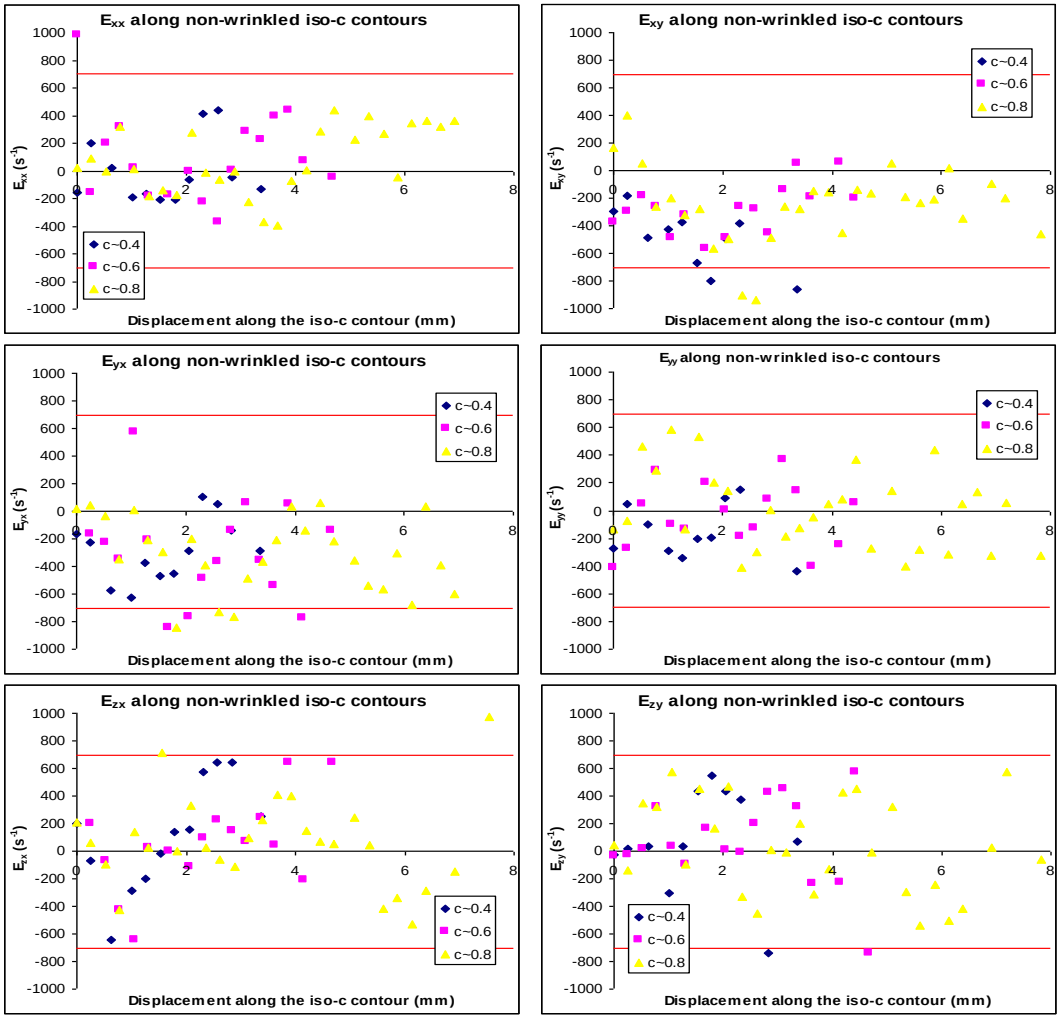

*Figure 6.17: Strain rates along the iso-c contours of a pocket of unburnt gases in burnt gases for flame C**
(from top left to bottom right: (a) Exx (b) Exy (c) Eyx (d) Eyy (e) Ezx and (f) Ezy)

* red lines show critical value for the strain rate

Example 8: Flame C (199)

(scale: 16µm/pixel)

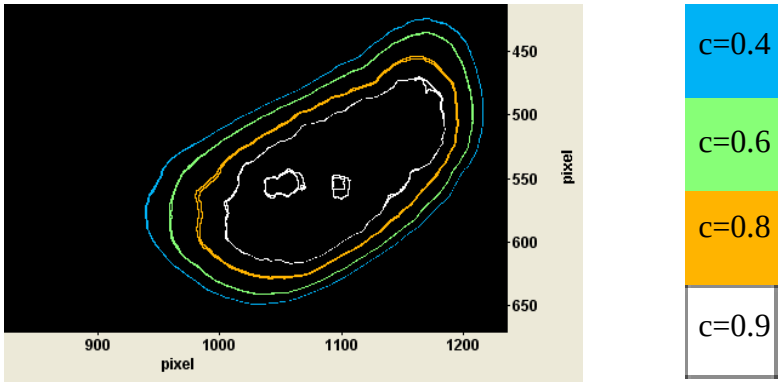

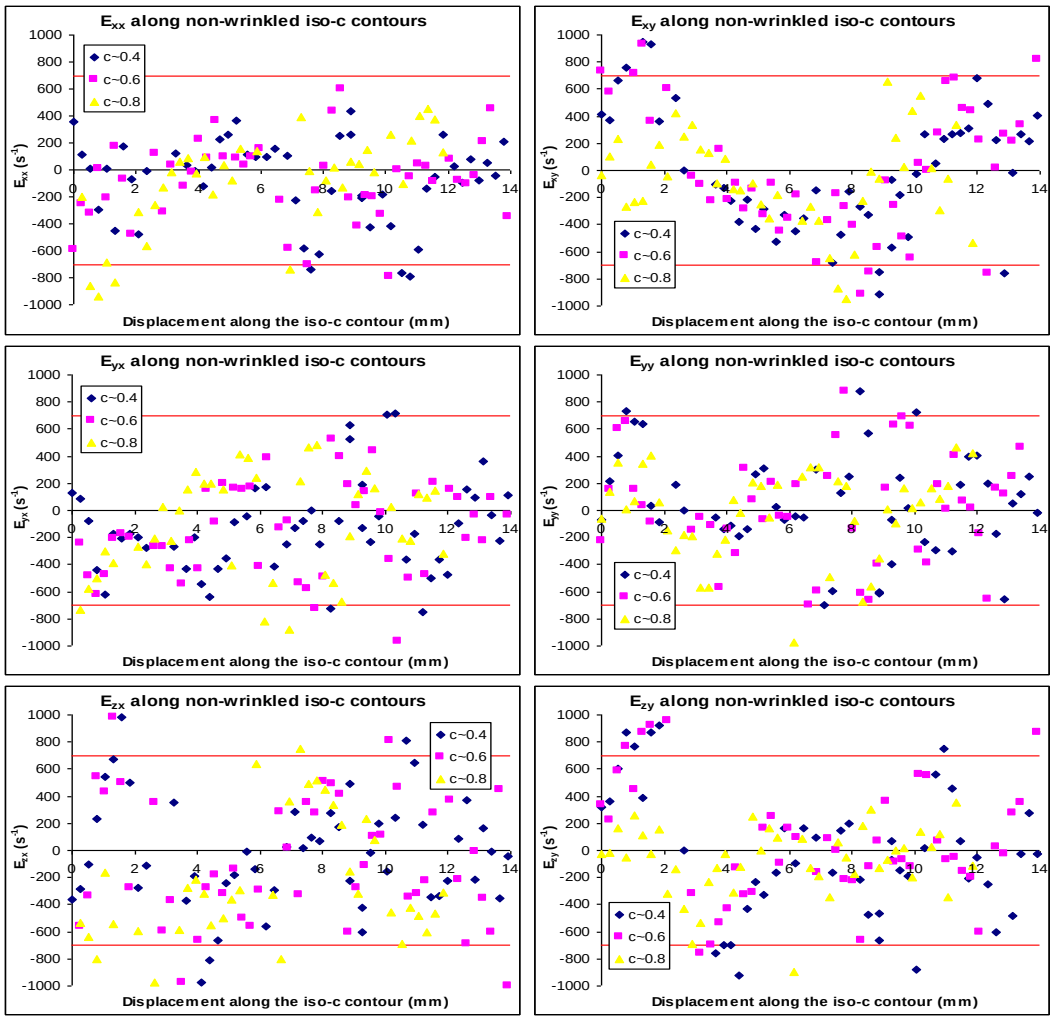

*Figure 6.18: Strain rates along the iso-c contours of a pocket of burnt gases in unburnt gases for flame C**
(from top left to bottom right (a) Exx (b) Exy (c) Eyx (d) Eyy (e) Ezx and (f) Ezy)

* red lines show critical value for the strain rate

The interpretation of the strain rate graphs along wrinkled iso-c contours is even more challenging due to the apparent 2D shape of the flame front. It would be of interest to be able to study the effect of curvature on the strain rates. However, this remains difficult when using such a technique as PLIF because this technique only enables the 2D imaging of the flame.

Figures 6.14 to 6.18 show again that most of the values of the strain rates along clearly wrinkled iso-c lines are comparable with the values of the strain rates observed in figure 6.9, suggesting again that no extinction occurred. Some of the values of strain rates, however, are higher than the expected critical strain rate to extinction. Nonetheless, it does not constitute sufficient proof that extinction occurred: the local conditions of the flame may have been different from the global condition.

6.5 Evaluation of the SPIV technique

As explained before, the SPIV technique is a technique which has been validated before and successfully used in numerous articles. (See chapter II).

The resolution for the velocity fields (and strain rate fields) was 262 μm in this work which is comparable to the resolution Hartung et al. [14] had in a similar study and which was 274 μm.

The main drawback of the SPIV technique as used here is its inability to measure the velocity gradients/strain rates in 3D. To remedy this, it is possible to use dual-plane SPIV. However, this technique requires substantially more equipment than ordinary SPIV.

CHAPTER VII

Flame normal alignment with the principal strain rates

This chapter describes how the principal strain rates were calculated from the SPIV data and compares them with the alignment of the flame normals inferred from the PLIF measurements. The results are discussed in the light of recent proposals regarding the modeling of turbulent premixed flames.

7.1 Calculation of the strain rate matrices, their eigenvalues and eigenvectors

As explained in Chapter VI, the Davis 7.1 software [60-61] permits the computation of the velocity gradients corresponding to $E_{xx}=\frac{\partial U}{\partial x}$, $E_{xy}=\frac{\partial U}{\partial y}$, $E_{yx}=\frac{\partial V}{\partial x}$, $E_{yy}=\frac{\partial V}{\partial y}$, $E_{zx}=\frac{\partial W}{\partial x}$, $E_{zy}=\frac{\partial W}{\partial y}$. As SPIV is a technique which allows only the determination of the 3D components of the velocity vectors on a planar domain, the following strains are not accessible: $E_{xz}=\frac{\partial U}{\partial z}$, $E_{yz}=\frac{\partial V}{\partial z}$ and $E_{zz}=\frac{\partial W}{\partial z}$.

Although we cannot calculate the full 3*3 strain rate matrices, it is possible to calculate the 2*2 strain rate matrices, having the following components:

- $E_{11}=E_{xx}$ (7.1),
- $E_{12}=\frac{1}{2}\left(E_{xy}+E_{yx}\right)$ (7.2),
- $E_{21}=\frac{1}{2}\left(E_{yx}+E_{xy}\right)=E_{12}$ (7.3),
- $E_{22}=E_{yy}$ (7.4).

A macro was written to calculate each of these components, from which the eigenvalues were then calculated:

- $E_1=\frac{1}{2}\left[\left(E_{11}+E_{22}\right)+\sqrt{\left(E_{11}+E_{22}\right)^2-4*\left(E_{11}*E_{22}-E_{12}*E_{21}\right)}\right]$ (7.5)
- $E_2=\frac{1}{2}\left[\left(E_{11}+E_{22}\right)-\sqrt{\left(E_{11}+E_{22}\right)^2-4*\left(E_{11}*E_{22}-E_{12}*E_{21}\right)}\right]$ (7.6)

where $E_1>E_2$.

Their corresponding eigenvectors were also calculated, having components in the x and y directions of:

- $V_{1x} = \dfrac{-E_{12} * E_{12} * E_{21}}{(E_{11} - E_1)^2 (E_{22} - E_1)}$ and $V_{1y} = \dfrac{E_{12} * E_{21}}{(E_{11} - E_1)(E_{22} - E_1)}$

(7.7) and (7.8),

- $V_{2x} = \dfrac{-E_{12} * E_{12} * E_{21}}{(E_{11} - E_2)^2 (E_{22} - E_2)}$ and $V_{2y} = \dfrac{E_{12} * E_{21}}{(E_{11} - E_2)(E_{22} - E_2)}$

(7.9) and (7.10).

which were then normalised.

These vectors (V_1 and V_2) correspond to the most extensive strain rate and the most compressive strain rate.

The angles between these strain rates and the 2D vectors normal to the flame front were then calculated for flame A, B, C, E, F and I. The pdf of these angles are shown in section 7.3 together with the curves showing the pdf of the strain rates E_1 and E_2.

7.2 Background to the role of strain rate in combustion modeling

A number of early studies describe the preferential alignment of the gradient vectors with the most compressive principal strain rate in scalar mixing investigations [91, 111-117]. These mainly referred to simulation of non-reacting flows, except for [91] & [116] which involved flows with isothermal chemical reactions and [117] which referred to turbulent diffusion flames.

Batchelor [111], in 1959, investigated theoretically the effect of turbulence on the small-scale structures of scalar fields. In particular, he analysed the form of the spectrum of a passive, conserved, scalar quantity, which he called θ, as a function of the wave-number. Emphasis is given to the validity range of the previously

established variation of the spectrum of θ for low wave-numbers for both the case when the scalar diffusivity is smaller than the kinematic viscosity of the fluid and when it is larger. He also put forward expressions for the θ-spectrum at high wave-number in the case when the scalar diffusivity is smaller than the kinematic viscosity of the fluid. Using the correlations between the velocity and θ, he was the first to forecast a tendency for the gradient vector to preferentially align with the most compressive strain rate.

Subsequently, in 1968, Gibson [112] also studied numerically the effect of turbulence on the small-scale structures of scalar fields. He stressed the importance of so-called "zero-gradient points" and "minimal gradient surfaces" and investigated the mechanisms by which they can be produced, destroyed or moved. He stressed the major role of local strain rates in the determination of the fine structure of the scalar fields in more general circumstances than had Batchelor.

In the 1980's and 1990's, a number of other studies [113-115] were dedicated to the subject which showed similar results.

The introduction of passive (isothermal) chemical reactions in the turbulent flows studied did not seem to alter the preferential alignment of the gradient vector with the most compressive strain rates as was shown in two numerical studies [91, 116].

As explained in chapter III (section 3.2.4), the scalar-turbulence interactions in premixed flames and, in particular, the production or destruction of scalar gradient by the turbulence have been investigated numerically [9-13]. These studies concluded that a preferential alignment of scalar gradient with the most extensive strain rates could be observed for turbulent flows in the presence of non-passive chemical reactions for large Da. For low Da, this alignment could still be observed but only in region of intense heat release.

Hartung & al. [14] investigated the alignment of the scalar gradients with the principal strain rates experimentally in five turbulent premixed ethylene-air flames (equivalence ratios: 0.55, 0.63 and 0.7 and Reynolds number between 14 000 and 21000) using SPIV and OH-PLIF. They only studied flames with Damköhler numbers greater than

one: 1.00 (*Ka*=13.76), 1.37 (*Ka*= 7.58), 1.69 (*Ka*= 5.93), 2.44 (*Ka*=4.13) and 4.01 (*Ka*=2.40). They observed a preferential alignment of the flame normal with the most extensive strain rates. They associated this observation with the tendency of dilatation to decrease the scalar gradient, produced by chemical reaction, when Da is large.

The goal, in the present study, was to establish whether this preferential alignment of the gradient vector with the most extensive strain rates persisted in flames with lower heat release and a much smaller Lewis number. The approach and analysis is broadly similar to that in [14].

7.3 Experimental results

The following graphs (figure 7.1 to figure 7.12) show the pdfs of the most extensive strain rates and the most compressive strain rates (figures 7.1, 7.3, 7.5, 7.7, 7.9 and 7.11) as well as the pdf of the flame normal alignment with the most compressive strain rates and the most extensive strain rates (figures 7.2, 7.4, 7.6, 7.8, 7.10 and 7.12) for flame A, B, C, E, F and I.

While the graphs showing the distributions of the principal strain rates are similar to those found in [14], the results for the flame normal alignment with the principal strain rates are quite different. While Hartung et al. [14] found a clear preferential alignment of the scalar gradients with the most extensive strain rates for the flames they studied, here, the measurements indicate no such preferential alignment.

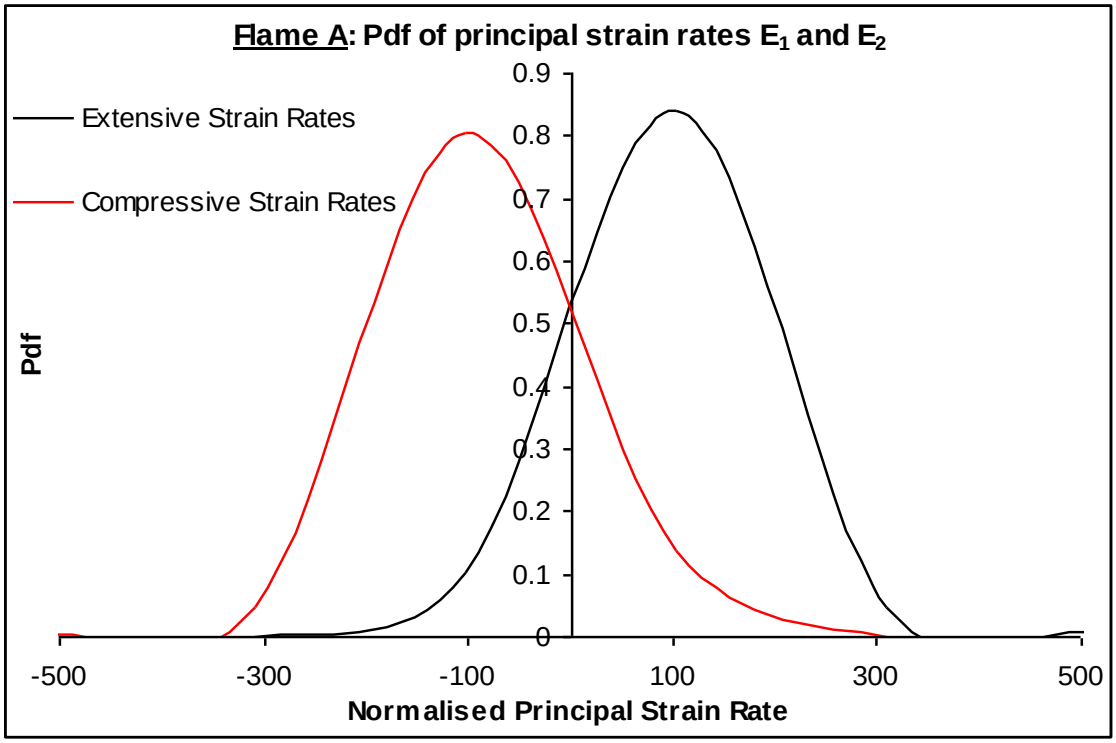

Figure 7.1: Pdf of principal strain rates in flame A (c=0.8)

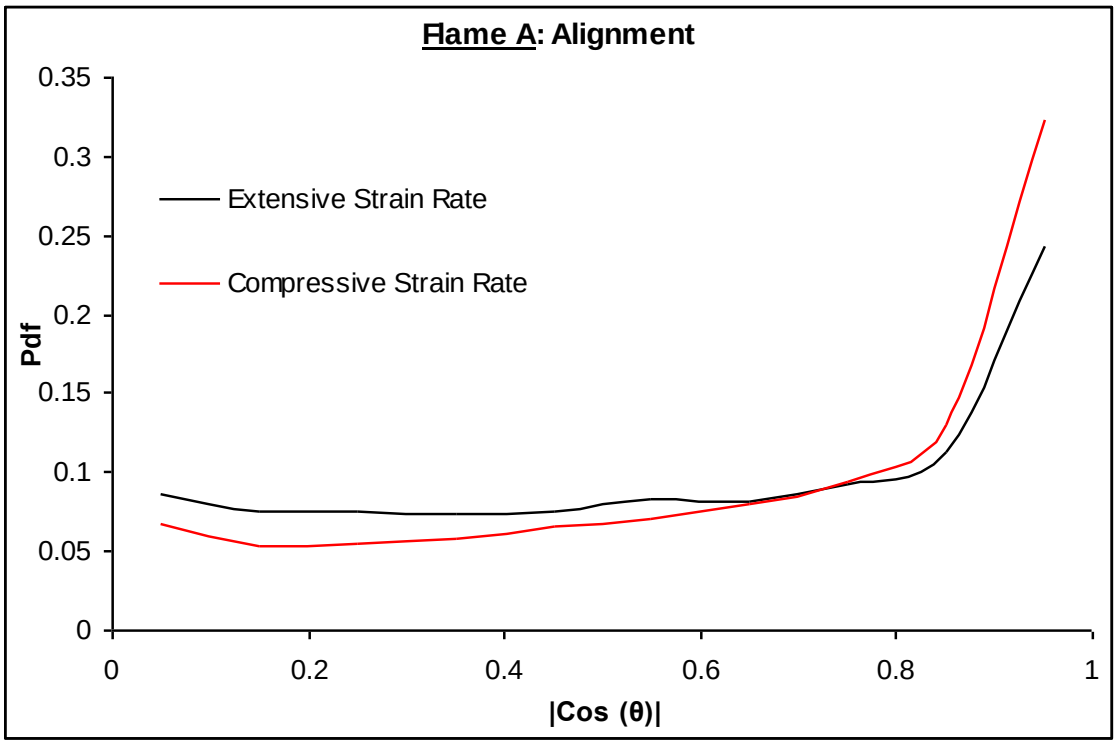

Figure 7.2: Pdf of flame normal alignment with the principal strain rates for flame A (c=0.8)

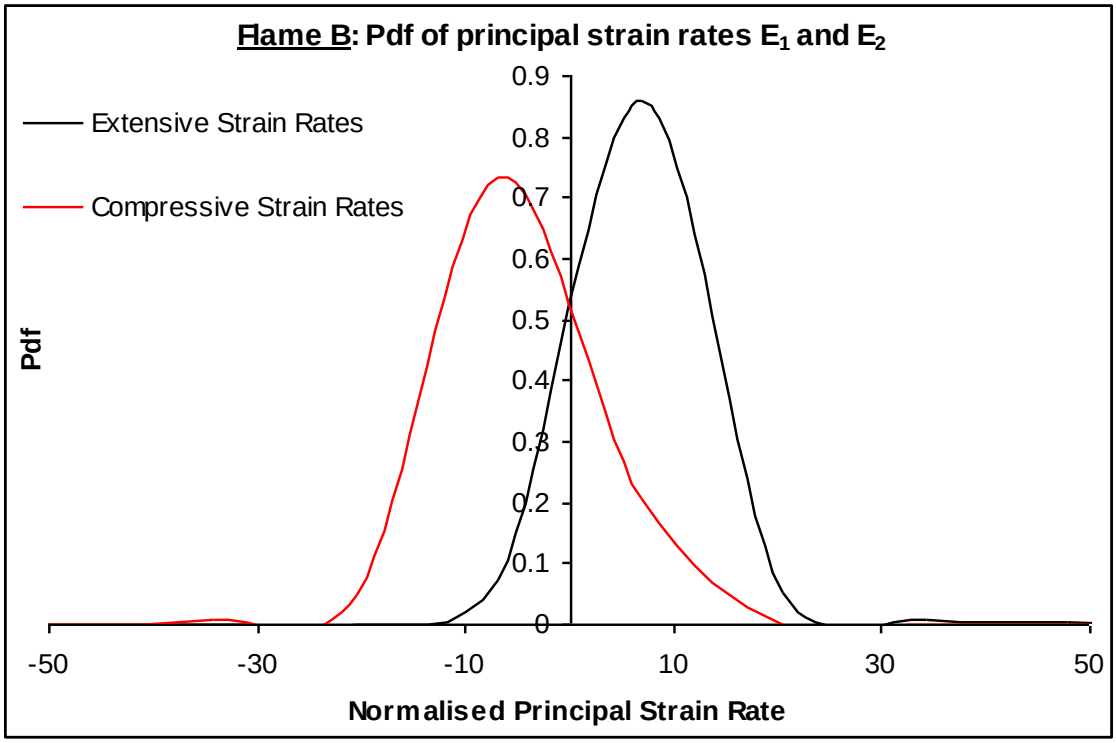

Figure 7.3: Pdf of principal strain rates in flame B (c=0.8)

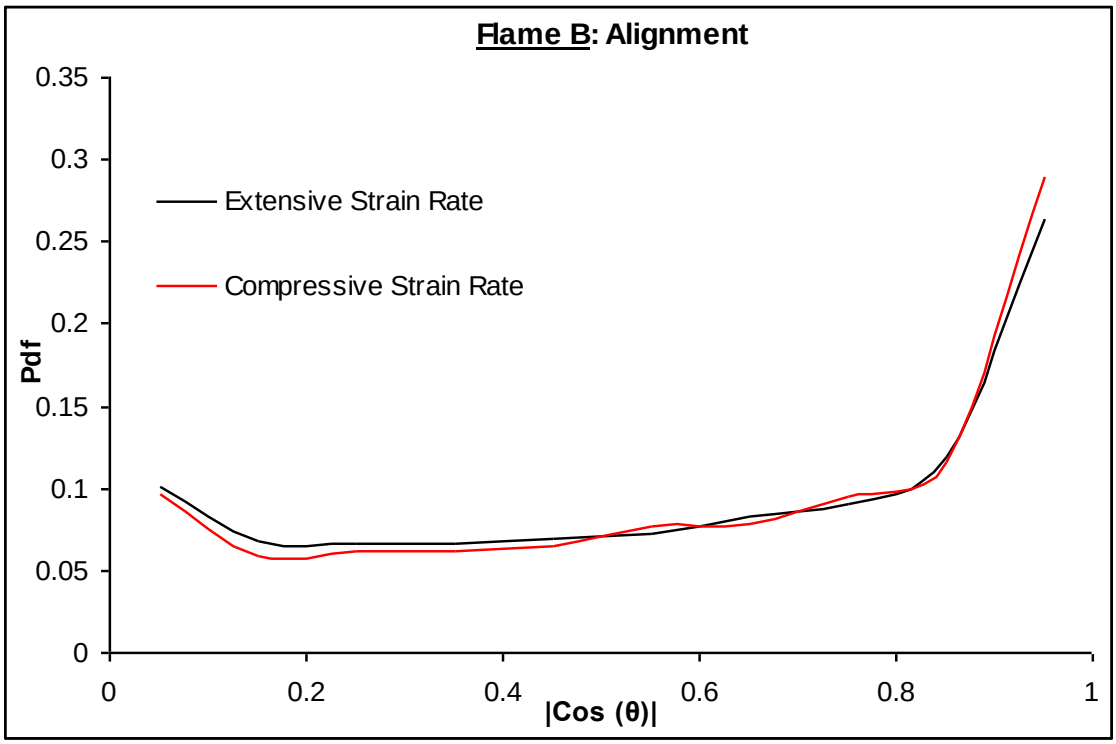

Figure 7.4: Pdf of flame normal alignment with the principal strain rates for flame B (c=0.8)

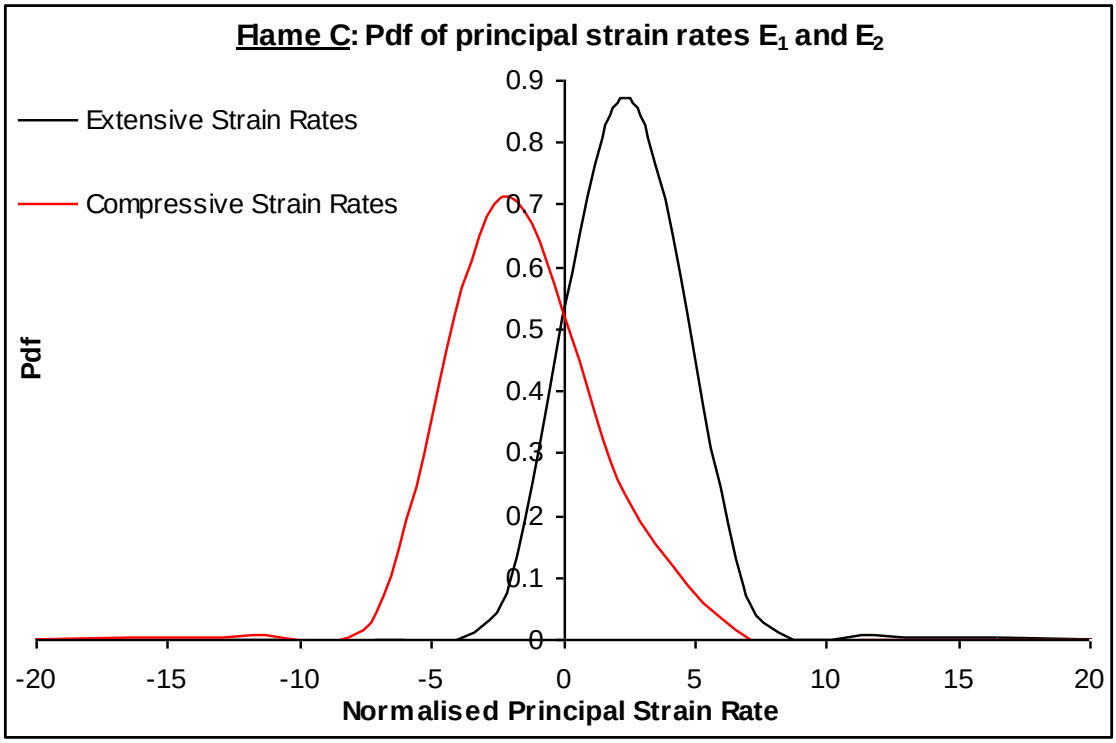

Figure 7.5: Pdf of principal strain rates in flame C (c=0.8)

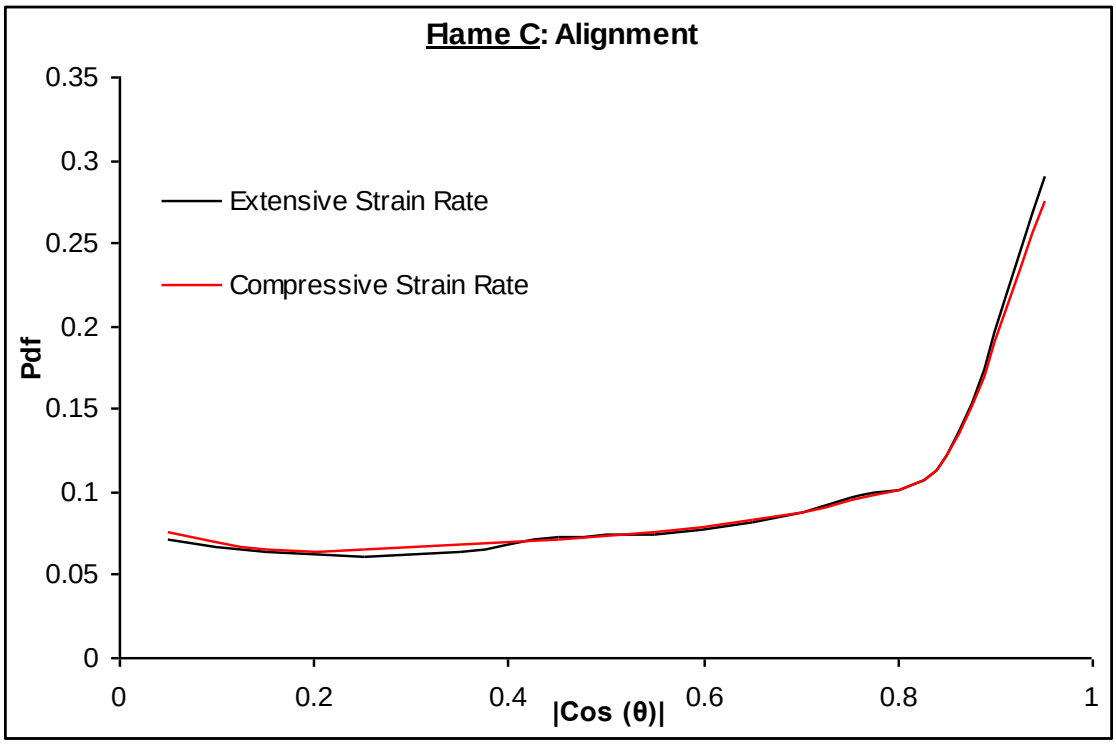

Figure 7.6: Pdf of flame normal alignment with the principal strain rates for flame C (c=0.8)

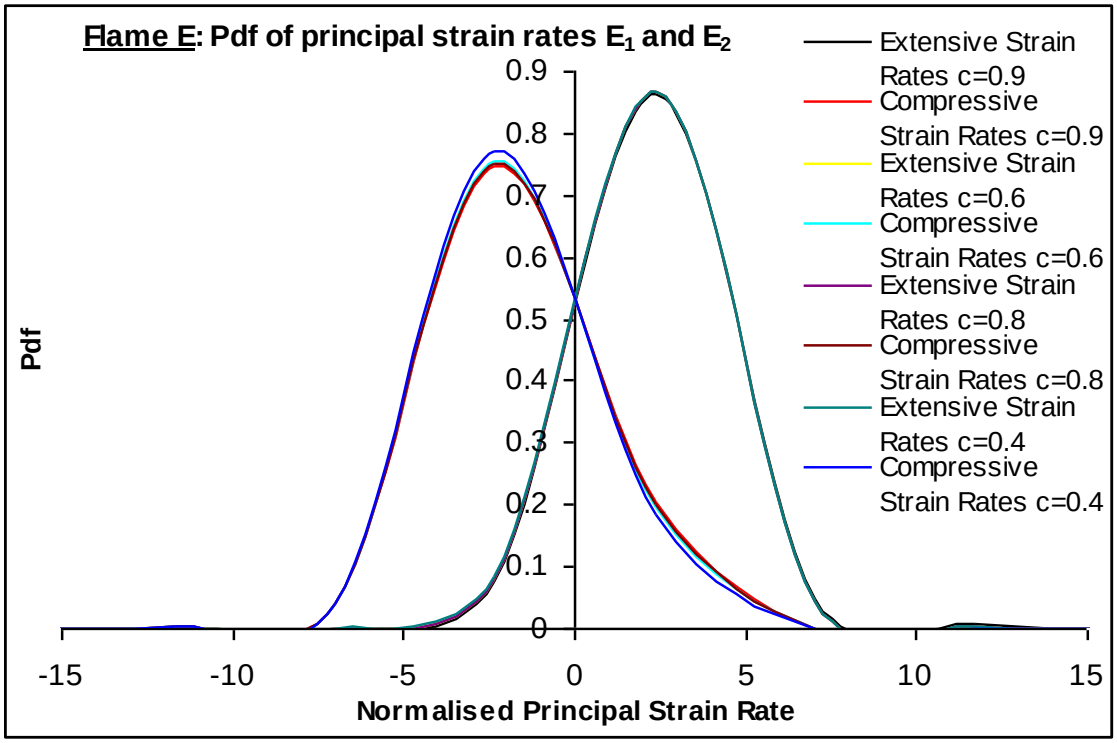

Figure 7.7: Pdf of principal strain rates in flame E

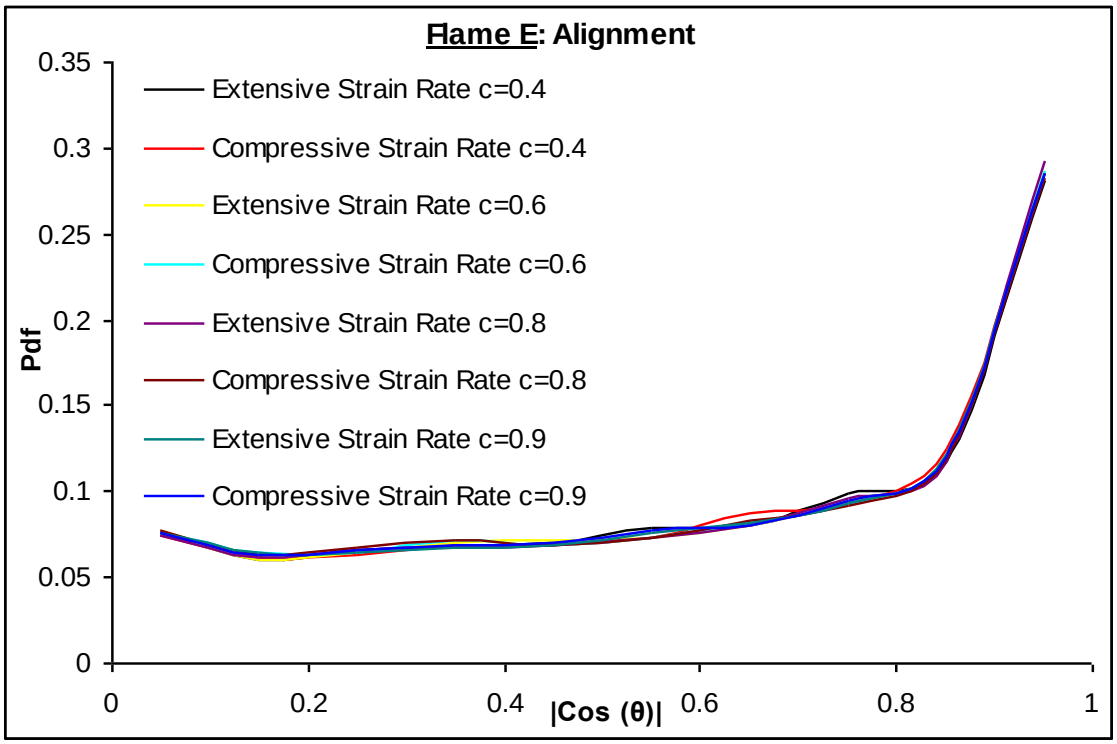

Figure 7.8: Pdf of flame normal alignment with the principal strain rates for flame E

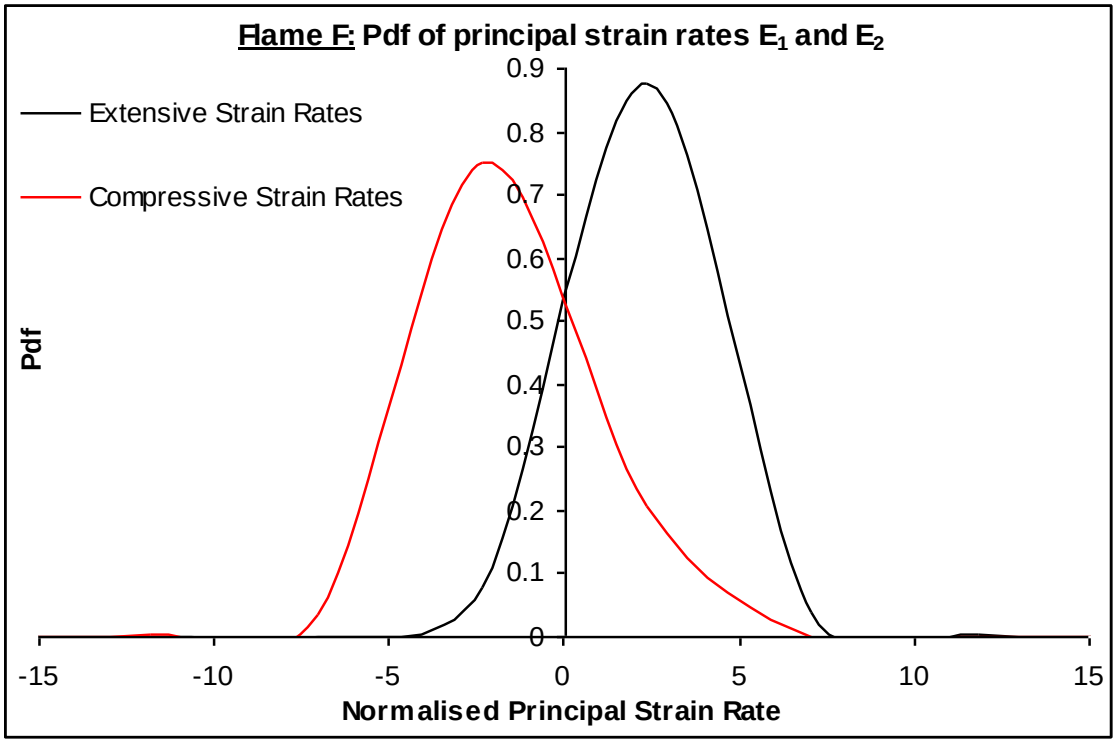

Figure 7.9: Pdf of principal strain rates in flame F (c=0.8)

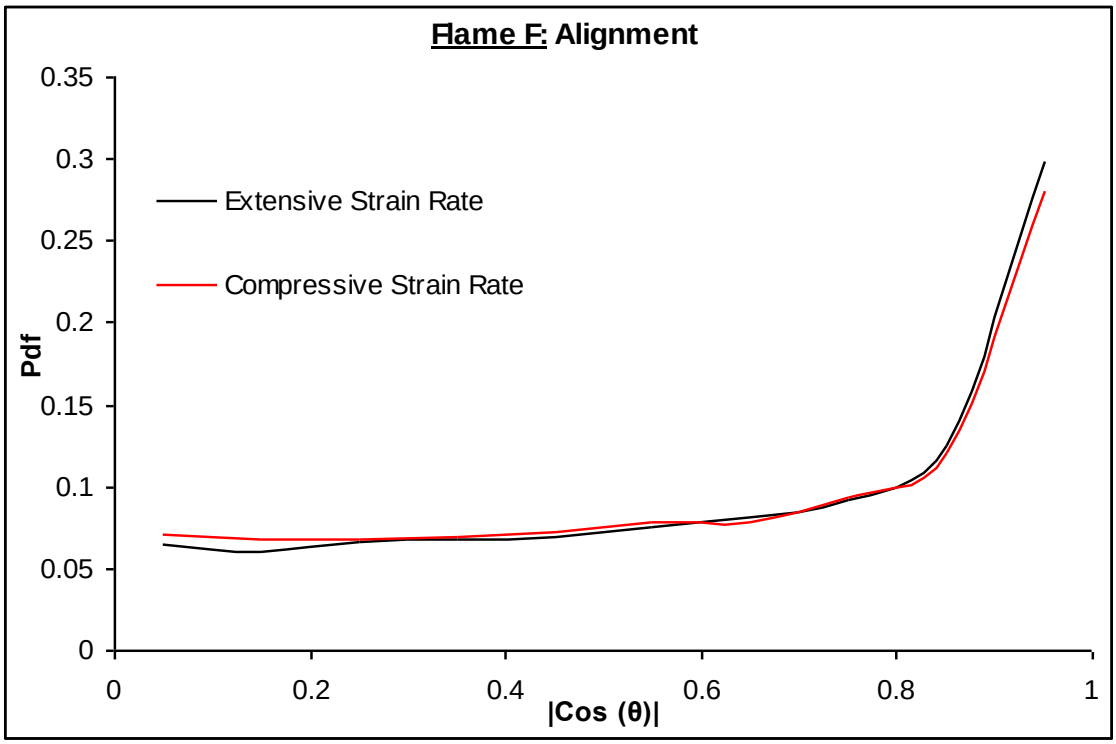

Figure 7.10: Pdf of flame normal alignment with the principal strain rates for flame F (c=0.8)

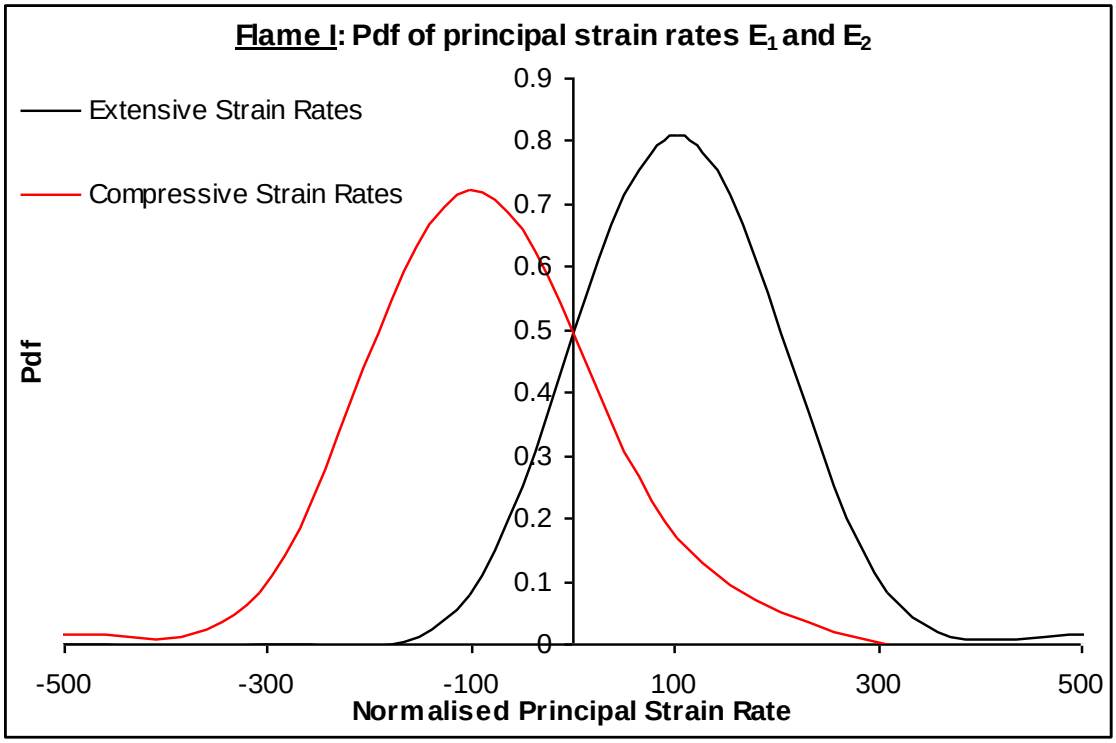

Figure 7.11: Pdf of principal strain rates in flame I (c=0.6)

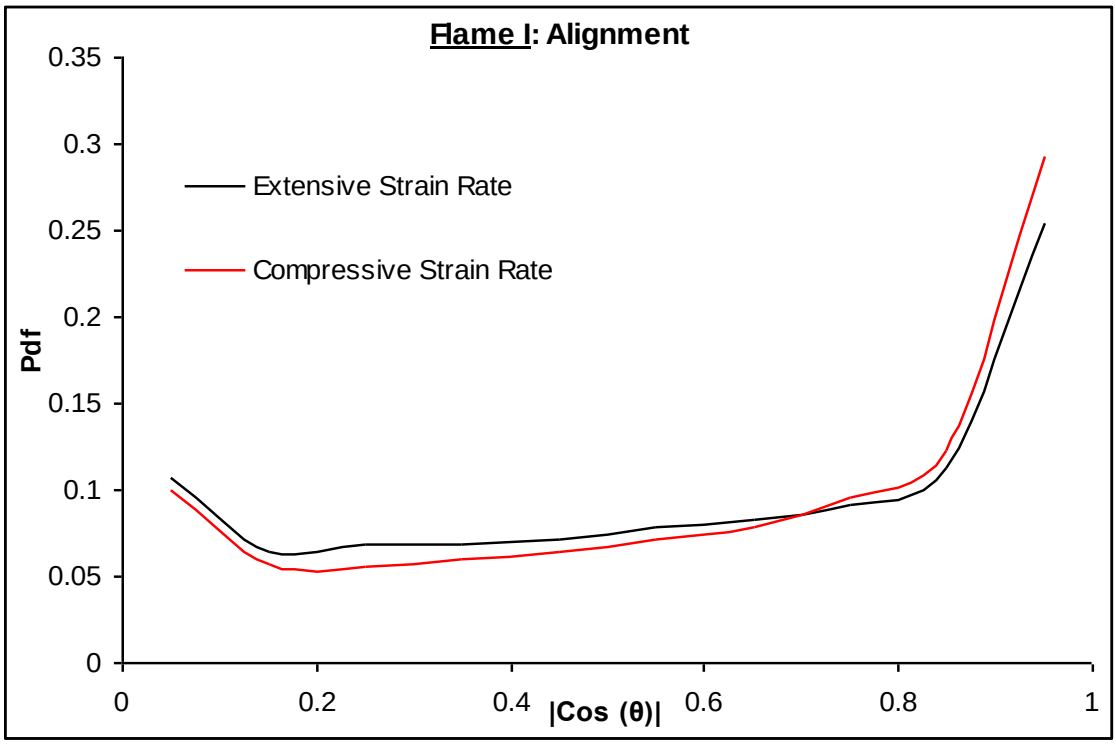

Figure 7.12: Pdf of flame normal alignment with the principal strain rates for flame I (c=0.6)

7.4 Analysis of the results: comparison with the ethylene flames results and explanation of the differences

In the present study, we were principally interested in the alignment of the scalar gradients with the principal strain rates. However, the graphs showing the pdfs of the strain rates were studied first.

7.4.1. Pdfs of the principal strain rates

Only two principal strain rates can be calculated because the component of the velocity gradients in the z-direction cannot be resolved when using SPIV. Although it would be interesting to gain access to all the components of the velocity gradients, for instance by using dual plane SPIV, it has been demonstrated in [14] that the pdfs of the principal strain rates and the alignment of the flame surfaces with the principal strain rates should not be qualitatively affected by the partial resolution of the velocity gradients.

The graphs showing the pdfs of the principal strain rates for flames A (Re~4800), B (Re~30), C (Re~200), E (Re~350), F (Re~600) and I (Re~15000) are shown respectively in figures 7.1, 7.3, 7.5, 7.7, 7.9 and 7.11. The strain rates were normalised using $\frac{\delta_L^0}{S_L^0}$ (table 4.2).

Figure 7.13 shows two of the graphs representing the distribution of the principal strain rates eigenvalues found in [14]. If we compare graphs 7.1 to 7.11 with these graphs, they are similar qualitatively i.e. they possess similar characteristics (slightly different most probable values for E_1 and E_2 and crossing of the pdfs around the zero value). However, the values for the most probable eigenvalues are quite different from the values obtained for the flames in the present work. The range of eigenvalues is also quite different. It is difficult to compare quantitatively both sets of data because the flames studied here vary considerably from the flames investigated in [14] (in terms of fuel, Lewis number, flame temperature, Reynolds number, Karlovitz number and Damköhler number).

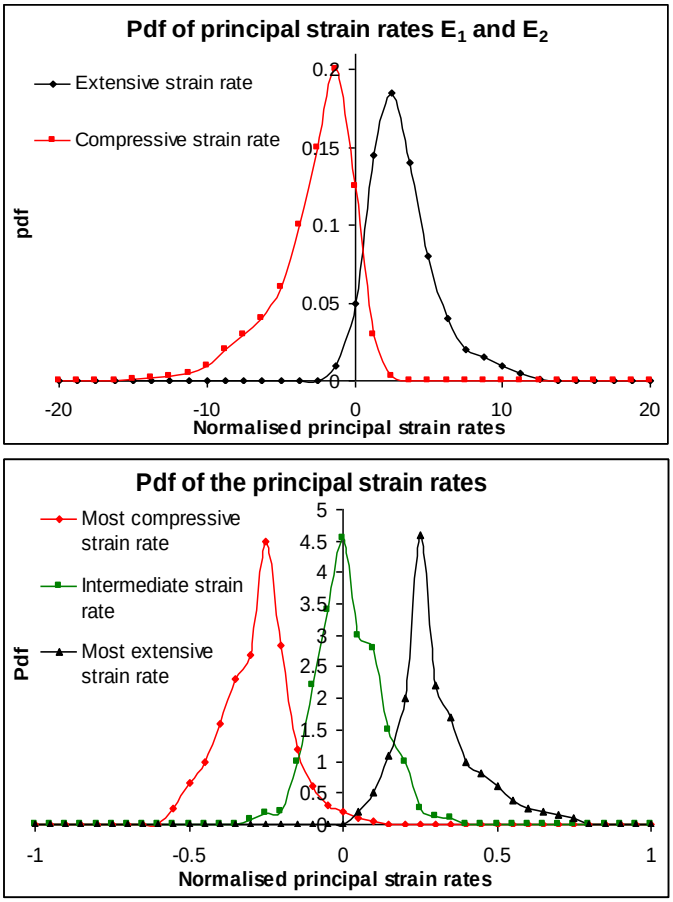

Figure 7.13: Graphs taken from [14]:
(a) experimental graph showing the pdfs of the principal strain rates for a premixed ethylene-air flame with Φ=0.55 (Da=1.37 and Ka=7.58)
(b) graph showing the pdfs of the principal strain rates of a DNS flame (Da=6.8, Ka=0.3)

In [14], it was found that the absolute value for the most probable eigenvalues increased with the Reynolds number, that the distribution for these eigenvalues was all the broader as the Reynolds number increased and that the average values for E_1 and E_2 increased with Re. These patterns were not recognised in graphs 7.1, 7.3, 7.5, 7.7, 7.9 and 7.11 although the effect of Reynolds number may not show in this study as clearly as in [14] because additional effects (effects of Da, Ka, or Φ) may take over. In the present work, the range of normalised principal strain rates decreases with increasing equivalence ratio (and flame temperature). This was also observed in [14] and was attributed to dilatational effects due to the increase in reactivity accompanying the increase in stoichiometry. Flames C, E and F have high Da and low Ka so dilatational effect may be more important for those flames than for the other flames studied and the influence of fluid mechanical processes on the flame front may

be reduced. The absolute values for E_1 and E_2 as well as their average values are also lower for flames C, E and F.

It would have been interesting to have access to DNS simulations of some of the present flames for purposes of comparison.

7.4.2 Flame normal alignment with the principal strain rates

Previous numerical studies [8-13] have predicted a preferential alignment of the flame normal vector with the most extensive strain rates for flames with a large Damköhler number and a preferential alignment of the flame normal vector with the most extensive strain rates in the region of intense heat release for flames with a smaller Damköhler number (<1), which demonstrates that the dynamics of the flame front can be influenced by dilatation and chemistry.

Figure 7.14 shows experimental results that have been reported in [14]. All graphs show preferential alignment of the flame normal with the most extensive strain rate for the flames studied. The results reported in the present work differ strongly from these results. As can be seen in figures 7.2 and 7.12, there seem to be a slight preferential alignment of the flame normal vectors with the most compressive rate for flame A and flame I. Flame A and flame I share similar characteristics: low equivalence ratio (Φ=0.38), and as a consequence low adiabatic flame temperature (T=906K), as well as low Da (<0.33), high Ka (>69) and the largest Re achieved in this study (>4800). The major factor that seems to influence the flame normal alignment is Da. For flame A and I, Da is much smaller than the cut-off value of one previously identified in [8-14], studies which also suggest that the alignment with the most extensive strain rate should still be observed in region of intense heat release. The experimental results obtained in the present work may not have been able to show this feature because the NO-PLIF may have been unable to locate the flame front in the most intense heat release region (section 5.4.1). However, this seems doubtful because, even for flames with higher Da, alignment with the most extensive strain rate has not been observed (figures 7.4, 7.6, 7.8 and 7.10). It is believed that the low adiabatic flame temperature may have contributed to the alignment observed in the

present study as the results resemble more results found for non-reacting cases. Figures 7.4, 7.6, 7.8 and 7.10 show no preferential alignment for the flames studied with higher Da (>4). A consequence of the high value of Da is that they should show unambiguous flame normal alignment with the most extensive strain rates at all location in the flame. This is not the case. This was again attributed to low adiabatic flame temperature. Figure 7.8 shows that the flame front location did not seem to influence the overall alignment for the flame studied and within the limit set by the NO-PLIF technique for the flame front location.

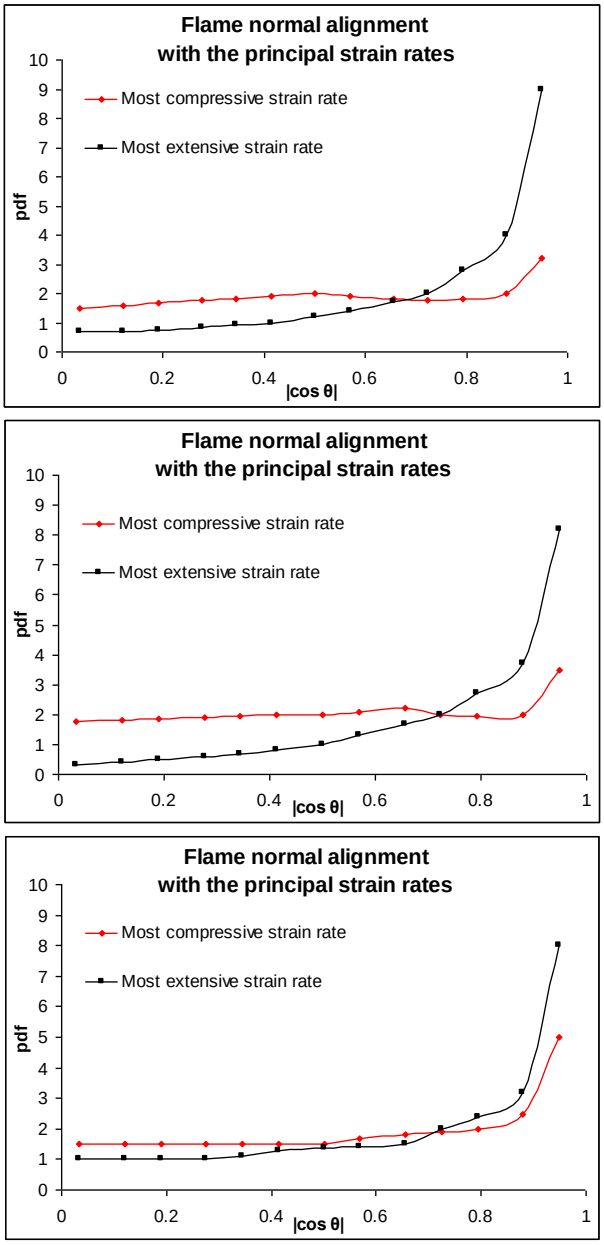

Figure 7.14: Flame normal alignment with the principal strain rates found in [14]: (a) Φ=0.55, Ka=7.58 and Da=1.37, (b) Φ=0.55, Ka=1.00 and Da=13.76 and (c) Φ=0.70, Ka=2.40 and Da=4.01

Some critical differences exist between our flames and the ethylene/air flames studied by Hartung [14]. One of them is the fuel; hydrogen is a much lighter molecule than the ethylene molecule. As a consequence, hydrogen diffuses much more rapidly than ethylene. In air, at 25°C, ethylene has a diffusivity of ~0.14 cm^2/s while hydrogen has a diffusivity of ~0.77 cm^2/s. This increased diffusivity is likely to cause some broadening of the local flame zone but may also generate flame curvature as evidenced in the cellular behaviour of some premixed flames.

Another difference between the flames studied here and the flames studied by Hartung et al. [14] is the presence of added nitrogen in our flames. A consequence of the addition of nitrogen is that our flames have a much lower adiabatic flame temperature (T between 900 and 1400K) than theirs (1700 to 2000K). In comparing cold flow data and flame data, Hartung et al. [14] stressed the influence of the heat release on the mean velocities and, as a consequence, on the characteristics of turbulent eddies in their flames. They also observed a strong acceleration across the flame. In the present study, no strong acceleration across the flame could be observed as indicated in the graph showing the pdf of velocity variation across the flame front along a normal vector in section 6.2 (figure 6.4).

This, and the fact that the alignment characteristics between the flame normal vectors and the principal strain rates resemble more non-reacting flows, seems to suggest that the heat released was insufficient to significantly perturb the flow and that, as a consequence, the effect of the heat release was overridden by the turbulence of the reactant flow.

Further experiments would be of great interest to decide generally of the alignment characteristics of the gradient vectors with the principal strain rates for turbulent premixed flames with low Lewis number, for example experiments in hydrogen/air flames with little or no added nitrogen. The effect of the heat release could be studied by performing experiments in hydrocarbon/air flames with varying nitrogen-dilution level. Also fully three-dimensional field measurements of velocities/velocity gradients, for instance using dual plane SPIV, would allow a more complete picture of the interaction between turbulence and scalar properties.

CHAPTER VIII

Conclusion

The goals of this work were principally:

- the development and evaluation of a new technique to resolve instantaneously and simultaneously velocity/strain rates fields and scalar/scalar gradient fields in turbulent premixed hydrogen-air flames,
- the collection and analysis of data concerning turbulent premixed hydrogen/air flames,
- the determination of the characteristics of the alignment of the flame normal vectors with the principal strain rates, the comparison of these results with earlier experimental and numerical results and the explanation of the differences between them.

Simultaneous and instantaneous imaging of velocity/strain rates fields and scalar fields are important in combustion because they provide information which could not be gained by any other means (see chapter III). They also provide a unique insight into the physical phenomena occurring in flames and allow the evaluation of theoretical models. In this work, the velocity/strain rates fields were investigated using Stereoscopic Particle Image Velocimetry (SPIV) while the scalar/scalar gradient fields were investigated using Planar Laser Induced Fluorescence of the radical NO (NO-PLIF) at 225.980 nm (excitation of the line $R_{11}+{}^{R}Q_{21}(9.5)$). The simultaneous and instantaneous combination of SPIV and NO-PLIF had never been attempted before. The major strengths and weaknesses of this technique have been highlighted in the present work.

Both techniques employed here are field techniques which is an asset compared to other techniques such as LDV (for the measurement of flow velocities) or CARS (for the measurement of scalars) which are generally only point-measurement techniques. The technique employed here also causes minimal disturbance to the flames studied unlike other methods, for example, using physical probes. However, both techniques require seeding: the SPIV technique required (ZrO_2-)particle seeding and the NO-PLIF required nitric oxide seeding. The main drawback of this is that the seeding may contribute to inexactitude in the measurement. Concerning the SPIV technique, for instance, one has to make sure that the inert particles seeded in the flow and whose velocity is actually measured represent the true motions of the fluid. Concerning the NO-PLIF technique, one has to make sure that the concentrations of NO stays

constant through the flames: it should not be consumed or be broken down nor should it be naturally be produced by the flame. More specifically both techniques have particular advantages and drawbacks. The SPIV technique is able to measure all components of the velocities. However, the main shortcoming of the SPIV technique is the fact that it does not allow the measurement of all components of the velocity gradients/strain rates which may again influence results especially results concerning turbulent fluxes or turbulent-scalar interactions, like the alignment of the scalar gradient with the principal strain rates that was studied here. Another shortcoming of the SPIV technique as it was employed here is that this technique is not continuous as a consequence the evolution of the flames cannot be studied. The NO-PLIF technique also has specific strengths and weaknesses. Its signal-to-noise ratios are reasonable compared to other techniques such as Raman. The NO-PLIF technique as employed here is not dependent on the concentration of the fluorescing species compared to the OH-PLIF technique, which makes it a technique potentially able to measure temperature fields. However, the measurement of temperature fields requires either a good experimental calibration of the NO-PLIF signal as a function of temperature or a good theoretical calibration of the signal. Neither of which could easily be achieved in this work: experimental calibration would have required to obtain uniform field of high temperature N_2-NO mixtures in a test cell and theoretical calibration may have been possible but only for more conventional flame compositions. The NO-PLIF technique, however, showed an interesting feature. Contrary to the OH-PLIF technique, for which a threshold technique for the determination of the flame contour is most imprecise, the flame contours can be determined with a simple threshold technique with the NO-PLIF technique. By varying the threshold, one could study the influence of the location of the flame front on measured properties of the flame i.e. one could study the influence of the heat release on this measured properties. The NO-PLIF technique was used in this work to locate the flame front and calculate the 2D vectors normal to the flame front. Although the NO-PLIF technique is, by essence, a 2D technique which prevents determining 3D vectors normal to the flame front, a new method was designed to infer from the scalar gradient the component of the normal vectors in the z direction. This method was presented in the present work but does still need further experimental validation.

Hydrogen is potentially a fuel with great prospects in particular because it is environmentally-friendlier than regular hydrocarbon fuels. However, because its properties differ strongly from more common hydrocarbon fuel, its combustion may show different characteristics. Fewer studies have been dedicated to hydrogen compared to, for instance, methane or propane. As a consequence, there is a need for data concerning hydrogen flames. In this work, the flames investigated were piloted turbulent premixed nitrogen-diluted hydrogen-air flames with seeded nitric oxide (500 ppm). The Damköhler number of the flames studied in this work ranged from 0.2 to 24 and their Karlovitz number ranged from 0.3 to 124. Their equivalence ratios ranged from 0.38 to 0.75. Their adiabatic flame temperature was comprised between 900K and 1400K.

The flames studied in this work were characterised by extrapolation of data obtained by hot wire anemometry and numerical simulation using the Chemkin 4.1 software [15]. More specifically, their laminar flame speed and thickness were estimated as well as their Damköhler and Karlovitz numbers. The flames studied belonged to a variety of combustion regimes [75]: three belonged to the corrugated flamelets regime, two to the thin reaction zones regime and one to the broken reaction zones regime.

The study of the progress variable images showed substantial wrinkling of the flame in particular for the flame belonging to the corrugated flamelets regime. The progress variable images also showed, for every flame, pockets of burnt gases in unburnt gases and pockets of unburnt gases in burnt gases, the latter of which may have been indicative of a past extinction. However, a survey of the occurrence of such pockets was undertaken and few differences were observed between the various flames suggesting that these pockets may not all be indicative of past extinction and be all genuine.

The NO-PLIF technique also allowed the study of the orientation of the flame front at various threshold value of c for the location of the flame front. It was found that, for the flames belonging to the corrugated flamelets regime, the range of values taken by the angle between the flame normal and the main axis of the burner was broader than for flames belonging to the broken reaction zones regime.

The curves showing the progress variable gradient as a function of the progress variable showed noticeable trend both numerically and experimentally. The value of the maximum gradient increases with the equivalence ratio and decreases with the addition of N_2 which makes sense since the adiabatic flame temperature and as a consequence the heat release also increases with the equivalence ratio and decreases with the addition of N_2.

The data obtained using the SPIV technique showed that, for the flames studied here, only a very weak acceleration across the flame front could be observed which was attributed to corrugation of the 3D flame front due to (low) heat release.

The strain rates E_{xx}, E_{xy}, E_{yx}, E_{yy}, E_{zx} and E_{zy} could not be solely linked to the curvature of the flame front, especially if the curvature is approximated using 2D progress variable image fields. Their values, for the most part, were either below or at the critical value for extinction found in the literature. In the regions where the strain rates were close to or at the expected critical value, no evidence of extinction could be observed. However, the detection of flame extinction may be ambiguous with the NO-PLIF technique as employed here.

The alignment of gradient vectors with the principal strain rates have been studied numerically and experimentally for some time now because it gives clues as to what the action of turbulence on scalar fields is. The vast majority of literature sources concerns flows with no chemical reactions or only passive chemical reactions, i.e. chemical reactions during which no heat is released. Only a few sources concern combusting flows. In flows with either no chemical reactions or only passive chemical reactions, it was found that the action of turbulence consisted principally in steepening scalar gradient. A similar result was also found for diffusion flames. Recent studies found that, in the case of premixed flames, the gradient vectors preferentially aligned with the most extensive rates everywhere for flames with a Damköhler number greater than one and in region of intense heat release for flames with a Damköhler number smaller than one which is contrary to what would be expected. Therefore, it seems that the action of turbulence in premixed flames consists in reducing scalar gradient.

This work mainly intended to study this alignment in hydrogen-air flames to study the effects of heat release and Lewis number on the alignment. The key outcome is that, for most flames, no preferential alignment could be found. For the flames with the lowest adiabatic flame temperature, a slight preferential alignment of the gradient vectors with the most compressive strain rate could be observed. This suggests that the alignment observed earlier in premixed flames may be not as general as first thought. However, it is still doubtful whether this is due to Lewis number effect or because of an insufficient heat release in the flames studied which all had low adiabatic flame temperatures. The fact that the alignment observed in this study resembles more non-reacting flows or iso-thermal flows leads to think that the low heat release is responsible for the differences in alignment observed between [14] and the present study. However, the high diffusivity of hydrogen, compared to ethylene [14], may have been responsible for the generation of curvature and influence the alignment observed in the present work, which is consistent with the fact that the velocity change across the flame front is much smaller than expected.

To confirm the results obtained here or in [14], it would be most interesting to perform further experiments such as the one undertaken in [14] and here, for instance, in turbulent premixed hydrogen/air flames with no added nitrogen or, for instance in hydrocarbon/air flames with and without added nitrogen. This would allow the determination of the influence of the Lewis number and the heat release separately. The excitation line used in this study may have to be changed for other cases to allow a wider range of flame front location.

A more precise numerical or experimental calibration of the NO-PLIF signal as a function of temperature would ideally be required so as to allow the precise determination of the iso-c line corresponding to the maximum heat release. This would allow for a same flame the determination of the influence of the heat release.

The use of dual plane SPIV would also improve the measurements. It would allow the determination of the full 3*3 strain rate matrices.

LIST OF REFERENCES

[1] James, S. R., “Hominid use of fire in the lower and middle pleistocene: a review of the evidence”, Current Anthropology, 30, 1, pp. 1-25, 1989

[2] Goren-Inbar, N., Alperson, N., Kislev, M. E., Simchoni, O., Melamed, Y., Ben-Nun, A., Werker, E., “Evidence of hominin control of fire at Gesher Benot Ya'aquov, Israel”, Science, 304, 5671, pp.725-727, 2004

[3] Karkanas, P., Shahack-Gross, R., Ayalon, A., Bar-Matthews, M., Barkai, R., Frumkin, A., Gopher, A., Stiner, M. C., “Evidence for habitual use of fire at the end of the lower paleolithic: site formation processes at Quesem cave, Israel”, Journal of Human Evolution, 53, pp. 197-212, 2007

[4] Goudsblom, J. “Fire, human use and consequences”, in International Encyclopedia of Social and Behavioral Sciences, edited by Smelser, N. J. and Baltes, P. B., pp.5672-5676, 2004

[5] Baird, C., Cann, M., “Environmental chemistry”, Freeman, W. H., New-York, 2004

[6] Kyoto protocol, full text available online: http://unfccc.int/resource/docs/convkp/kpeng.pdf, 1998

[7] Veynante, D., Vervish, L., “Turbulent combustion modeling”, Progress in Energy and Combustion Science, 28, pp.193-266, 2002

[8] Swaminathan, N., Bray, K. N. C., “Effect of dilatation on scalar dissipation in turbulent premixed flames”, Combustion and Flame, 143, pp. 549-565, 2005

[9] Swaminathan, N., Bilger, R. W., Cuenot, B., “Relationship between turbulent scalar flux and conditional dilatation in premixed flames with complex chemistry”, Combustion and Flame, 126, pp. 1764-1779, 2001

[10] Swaminathan, N., Grout, R. W., “Interaction of turbulence and scalar fields in premixed flames”, Physics of Fluids, 18, 045102, 2006

[11] Chakraborty, N., Swaminathan, N., “Influence of the Damköhler number on turbulence-scalar interaction in premixed flames. I. Physical insight”, Physics of Fluids, 19, 045103, 2007

[12] Chakraborty, N., Swaminathan, N., “Influence of the Damköhler number on turbulence-scalar interaction in premixed flames. II. Model development”, Physics of Fluids, 19, 045104, 2007

[13] Chakraborty, N., Rogerson, J. W., Swaminathan, N., “A priori assessment of closures for scalar dissipation rate transport in turbulent premixed flames using direct numerical simulation”, Physics of Fluids, 20, 045106, 2008

[14] Hartung, G., Hult, J., Kaminski, C. F., Rogerson, J. W., Swaminathan, N., "Effect of heat release on turbulence and scalar turbulence interaction in premixed combustion", Physics of Fluids, 20, 035110, 2008

[15] Kee, R. J., Rupley, F. M., Miller, J. A., Coltrin, M. E., Grcar, J. F., Meeks, E., Moffat, H. K., Lutz, A. E., Dixon-Lewis, G., Smooke, M. D., Warnatz, J., Evans, G. H., Larson, R. S., Mitchell, R. E., Petzold, L. R., Reynolds, W. C., Caracotsios, M., Stewart, W. E., Glarborg, P., Wang, C., McLellan, C. L., Adigun, O., Houf, W. G., Chou, C. P., Miller, S. F., Ho, P., Young, P. D., Young, D. J., Hodgson, D. W., Petrova, M. V., Puduppakkam, K. V., Chemkin Release 4.1, Reaction Design, San Diego, CA, 2006

[16] Eckbreth, A. C., "Laser diagnostics for combustion temperature and species", Abacus Press, Tunbridge Wells, 1988

[17] Hassel, E. P., Linow, S., "Laser diagnostics for studies of turbulent combustion", Measurement Science and Technology, 11, R37-R57, 2000

[18] Kohse-Höinghaus, K., Jeffries, J. B., "Applied combustion diagnostics", Taylor & Francis, New York, 2002

[19] Wolfrum, J., "Lasers in combustion: from basic theory to practical devices", 27th Symposium (International) on Combustion/The Combustion Institute, pp.1-41, 1998

[20] Atkins, P.; De Paula, J.; "Atkins' physical chemistry", 8th Edition, Oxford university press, Oxford, 2006

[21] López-Higuera, J. M.; "Handbook of optical fibre sensing technology", Wiley, New York, 2002

[22] Westerweel J., "Fundamental of digital particle image velocimetry", Measurement Science and Technology, 8, pp.1379-1392, 1997

[23] Schulz, C., Sick, V., "Tracer-LIF diagnostics: quantitative measurement of fuel concentration, temperature and fuel/air ratio in practical combustion systems", Progress in Energy and Combustion Science, 31, pp. 75-121, 2005

[24] Grieser, D. R., Barnes, R. H., "Nitric oxide measurements in a flame by laser fluorescence", Applied Optics, 19, 5, pp. 741-743, 1980

[25] Kychakoff, G., Knapp, K., Howe, R. D., Hanson, R. K., "Flow visualisation in combustion gases using nitric oxide fluorescence", AIAA journal, 22, pp. 153-154, 1984

[26] Westblom, U., Alden, M., "Simultaneous multiple species detection in a flame using laser-induced fluorescence", Applied Optics, 28, 13, pp. 2592-2599, 1989

[27] Westblom, U., Alden, M., "Simultaneous multiple species detection in a flame using laser-induced fluorescence: Errata", Applied Optics, 29, 33, pp. 4844-4851, 1990

[28] Heard, D. E., Jeffries, J. B., Smith, G. P., Crosley, D. R., "LIF measurements in methane/air flames of radicals important in prompt-NO formation", Combustion and Flame, 88, 2, 137-148, 1992

[29] Reisel, J. R., Carter, C. C., Laurendeau, N. M., "Laser-induced fluorescence measurements of nitric oxide in laminar C2H6/O2/N2 flames at high pressure", Combustion and Flame, 92, 4, 485-489, 1993

[30] Lee, M. P., McMillin, B. K., Hanson, R. K., "Temperature measurements in gases by use of planar laser-induced fluorescence imaging of NO", Applied Optics, 32, 27, 1993

[31] Tamura, M., Luque, J., Harrington, J. E., Berg, P. A., Smith, G. P., Jeffries, J. B., Crosley, D. R., "Laser-induced fluorescence of seeded nitric oxide as a flame thermometer", Applied Physics B, 66, pp. 503-510, 1998

[32] Scholz, J., "Untersuchungen der Fluoreszenzlöschung von heissen NO-Molekülen für die Anwendung der zwei-linien Thermometrie in Hochenthalpieströmungen", DLR, Froschungsbericht 2001-29, 2001

[33] Bessler, W. G., Schulz, C., Lee, T., Jeffries, J. B., Hanson, R. K., "Strategies for laser-induced fluorescence detection of nitric oxide in high pressure flames. I. A-X(0,0) excitation", Applied Optics, Vol. 41, No. 18, pp.3547-3557, 2002

[34] Bessler, W. G., Schulz, C., Lee, T., Jeffries, J. B., Hanson, R. K., "Strategies for laser-induced fluorescence detection of nitric oxide in high pressure flames. II. A-X(0,1) excitation", Applied Optics, 42, 12, pp.2031-2042, 2003

[35] Bessler, W. G., Schulz, C., Lee, T., Jeffries, J. B., Hanson, R. K., "Strategies for laser-induced fluorescence detection of nitric oxide in high pressure flames. III. Comparison of A-X excitation schemes", Applied Optics, 42, 24, pp.4922-4936, 2003

[36] Reisel, J. R., Carter, C. D., Laurendeau, N. M., "Einstein coefficient for rotational lines of the (0,0) band of the NO $A^2\Sigma^+$-$X^2\Pi$ system", Journal of Quantitative Spectroscopy and Radiative Transfer, 47, 1, pp.43-54, 1992

[37] Paul, P. H., "Calculation of transition frequencies and rotational line strengths in the γ-bands of nitric oxide", Journal of Quantitative Spectroscopy and Radiative Transfer, 57, 5, pp.581-589, 1997

[38] Chang, A. Y., DiRosa, M. D., Hanson, R. K., "Temperature dependence of collision broadening and shift in the NO A-X(0,0) band in the presence of argon and nitrogen", Journal of Quantitative Spectroscopy and Radiative Transfer, 47, 5, pp.375-390, 1992

[39] DiRosa, M. D., Hanson, R. K., "Collision broadening and shift of NO γ(0,0) absorption lines by O_2 and H_2O at high temperatures", Journal of Quantitative Spectroscopy and Radiative Transfer, 52, 5, pp.515-529, 1994

[40] Dodge, L. G., Dusek, J., Zabielski, M. F., "Line broadening and oscillator strength measurements for the nitric oxide γ(0,0) band", Journal of Quantitative Spectroscopy and Radiative Transfer, 24, pp.237-249, 1980

[41] Paul, P. H., Gray, J. A., Durant, J. L., Thoman, J. W., "Collisional quenching corrections for laser-induced fluorescence measurements of NO $A^2\Sigma^{+"}$, AIAA Journal, 32, 8, pp.1670-1675, 1994

[42] DiRosa, M. D., Klavuhn, K. G., Hanson, R. K., "LIF spectroscopy of NO and O_2 in high-pressure flames", 34th Aerospace Science Meeting and Exhibit, AIAA 96-0844, 1996

[43] Partridge, W. P., Laurendeau, N. M., "Formulation of a dimensionless overlap fraction to account for spectrally distributed interactions in fluorescence studies", Applied Optics, 34, 15, pp.2645-2647, 1995

[44] Herzberg, G., "Molecular spectra and molecular structure: spectra of diatomic molecules", D. Van Nostrand company, Princeton, 1950

[45] Aquilanti, V., Cavalli, S., Grossi, G., "Hund's cases for rotating diatomic molecules and for atomic collisions: angular momentum coupling schemes and orbital alignment", Zeitschrift für Physik D, 36, 3-4, pp.215-219, 1996

[46] Bessler, W. G., Schulz, C., Sick, V., Daily, J. W., "A versatile modeling tool for nitric oxide LIF spectra", Proceedings of the Third Joint Meeting of the U.S. Sections of the Combustion Institute, Chicago, March 16-19, 2003 (www.lifsim.com)

[47] Berg, J.O., Shackleford, W. L., "Rotational redistribution effect on saturated laser-induced fluorescence", Applied Optics, 18, 13, pp. 2093-2094, 1979

[48] Bell, J. B., Day, M. S., Grcar, J. F., Bessler, W. G., Schulz, C., Glarborg, P., Jensen, A. D., "Detailed modeling and laser induced fluorescence of nitric oxide in a NH_3-seeded non-premixed methane/air flame", 1998 (report)

[49] Ciucci, F., Kang, D-M., Ratner, A., Culick, E. C., **"**Detection of NO in a methane-air, steady, flat flame with CO_2/N_2 seeding using degenerate four-wave mixing and laser-induced fluorescence", AIAA-2003-4492 (2003)

[50] Lucht, R. P., Peterson, R. C., Laurendeau, N. M., "Fundamentals of absorption spectroscopy for selected diatomic flame radicals", Report PURDU-CL-78-06, School of mechanical engineering, Purdue University, West Lafayette, IN, 1978

[51] Luque, J.; Crosley, R. D.; "LIFBASE: database and spectral simulation for OH A-X, OD A-X, NO A-X, NO D-X and CH A-X, B-X, C-X", SRI Report MP 96-001, 1996

[52] Stanislas, M., Monnier J. C., "Practical aspects of image recording in particle image velocimetry", Measurement Science and Technology, 8, pp.1417-1426, 1997

[53] Melling, A., “Tracer particles and seeding for particle image velocimetry”, Measurement Science and Technology, 8, pp.1406-1416, 1997

[54] Hinsch, K. D., “Three-dimensional particle velocimetry”, Measurement Science and Technology, 6, pp.742-753, 1995

[55] Soloff, S. M., Adrian, R. J. and Liu, Z-C., “Distortion compensation for generalized stereoscopic particle image velocimetry”, Measurement Science and Technology, 8, pp.1441-1454, 1997

[56] Prasad, A. K., “Stereoscopic particle image velocimetry”, Experiments in Fluids 29, pp.103-116, 2000

[57] Willert, C., “Stereoscopic digital particle image velocimetry for application in wind tunnel flows”, Measurement Science and Technology, 8, pp.1465-1479, 1997

[58] Lawson, N. J. and Wu, J., “Three-dimensional particle image velocimetry: experimental error analysis of a digital angular stereoscopic system”, Measurement Science and Technology, 8, pp.1455-1464, 1997

[59] Lawson, N. J. and Wu, J., “Three-dimensional particle image velocimetry: error analysis of stereoscopic techniques”, Measurement Science and Technology, 8, pp.894-900, 1997

[60] LaVision, DaVis flowmaster software manual for DaVis 7.0, LaVision GmbH, 2004

[61] LaVision, Command language manual for DaVis 7.0, LaVision GmbH, 2004

[62] Zang, W., Prasad, A. K., “Performance evaluation of a Scheimpflug stereocamera for particle image velocimetry”, Applied Optics, 36, 33, pp. 8738-8744, 1997

[63] Frank, J. H., Lyons, K. M., Long, M. B., “Simultaneous scalar/velocity field measurements in turbulent gas-phase flows”, Combustion and Flame, 107, pp. 1-12, 1996

[64] Hasselbrink, E. F., Mungal, M. G., Hanson, R. K., “Planar velocity measurements and OH imaging in a transverse jet”, AIAA 97-0118, 1997

[65] Carter, C. D., Donbar, J. M., Driscoll, J. F., “Simultaneous CH planar laser-induced fluorescence and particle image velocimetry in turbulent nonpremixed flames”, Applied Physics B, 66, pp. 129-132, 1998

[66] Frank, J. H., Kalt, P. A. M., Bilger, R. W., “Measurements of conditional velocities in turbulent premixed flames by simultaneous OH PLIF and PIV”, Combustion and Flame, 116, pp. 220-232, 1999

[67] Welle, E. J., Roberts, W. L., Carter, C. D., Donbar, J. M., "Evaluation of the transient response of a counter-flow diffusion flame usind two-line OH-PLIF thermometry and PIV", AIAA 2001-0785, 2001

[68] Filatyev, S. A., Driscoll, J. F., Carter, C. D., Donbar, J. M., "Measured properties of turbulent premixed flames for model assessment, including burning velocities, stretch rates, and surface densities", Combustion and Flame, 141, pp. 1-21, 2005

[69] Griffiths, J.F., Barnard, J. A., "Flame and Combustion", Blackie Academic & Professional, London, 1995

[70] Peters, N., "Turbulent Combustion", Cambridge University Press, Cambridge, 2004

[71] Kolmogorov, A. N., "The local structure of turbulence in incompressible viscous fluid for very large Reynolds numbers", Proceedings of the Royal Society London, A 434, 1890, pp. 9-13, 1991 (Reprint)

[72] Kolmogorov, A. N., "Dissipation of energy in locally isotropic turbulence", Proceedings of the Royal Society London, A 434, 1890, pp. 15-17, 1991 (Reprint)

[73] Kolmogorov, A. N., "A refinement of previous hypotheses concerning the local structure of turbulence in a viscous incompressible fluid at high Reynolds number", Journal of Fluid Mechanics, 13, pp. 82-85, 1962

[74] Borghi, R. W., "On the structure and morphology of turbulent premixed flames", Recent Advances in the Aerospace Science, Ed. C. Casci, pp. 117-138, 1985

[75] Peters, N., "Laminar flamelet concepts in turbulent combustion", Twenty-first Symposium (International) on Combustion, pp. 1231-1250, 1986

[76] Goix, P. J., Shepherd, I. G., Trinité, M., "A fractal study of a premixed V-shaped H_2/Air flame", Combustion Science and Technology, 63, pp. 275-286, 1989

[77] Goix, P. J., Shepherd, I. G., "Lewis number effects on turbulent premixed flame structure", Combustion Science and Technology, 91, pp. 191-206, 1993

[78] Goix, P. J., Paranthoen, P., Trinité, M., "A tomographic study of measurements in a V-shaped H_2-air flame and a lagrangian interpretation of the turbulent flame brush evolution", Combustion and Flame, 81, pp. 229-241, 1990

[79] Kwon, S., Wu, M.-S., Driscoll, J. F., Faeth, G. M., "Flame surface properties of premixed flames in isotropic turbulence: measurements and numerical simulations", Combustion and Flame, 88, pp. 221-238, 1992

[80] Aung, K. T., Hassan, M. I., Kwon, S., Tseng, L.-K., Kwon, O.-C., Faeth, G. M., "Flame/stretch interactions in laminar and turbulent premixed flames", Combustion Science and Technology, 174, pp. 61-99, 2002

[81] Wu, M.-S., Kwon, S., Driscoll, J. F., Faeth, G. M., "Turbulent premixed hydrogen/air flames at high Reynolds numbers", Combustion Science and Technology, 73, pp. 327-350, 1990

[82] Wu, M.-S., Kwon, S., Driscoll, J. F., Faeth, G. M., "Preferential diffusion effects on the surface structure of turbulent premixed hydrogen/air flames", Combustion Science and Technology, 78, pp.69-96, 1991

[83] Kwon, S., Tseng, L.-K., Faeth, G. M., "Laminar burning velocities and transition to unstable flames in $H_2/O_2/N_2$ and $C_3H_8/O_2/N_2$ mixtures", Combustion and Flame, 90, pp. 230-246, 1992

[84] Lee, J. G., Lee, T.-W., Nye, D. A., Santavicca, D. A., "Lewis number effects on premixed flames interacting with turbulent Kármán vortex streets", Combustion and Flame, 100, pp. 161-168, 1995

[85] Renou, B., Boukhalfa, A., Puechberty, D., Trinité, M., "Local scalar flame properties of freely propagating premixed turbulent flames at various Lewis number", Combustion and Flame, 123, pp. 507-521, 2000

[86] Renou, B., Boukhalfa, A., "An experimental study of freely propagating premixed flames at various Lewis numbers", Combustion Science and Technology, 162, pp. 347-370, 2001

[87] Renou, B., Mura, A., Samson, E., Boukhalfa, A., "Characterization of the local flame structure and the flame surface density for freely propagating premixed flames at various Lewis numbers", Combustion Science and Technology, 174, pp. 143-179, 2002

[88] Chen, Y.-C., Bilger, R. W., "Experimental investigation of three-dimensional flame front structure in premixed turbulent combustion. II. Lean hydrogen/air Bunsen flames", Combustion and Flame, 138, pp. 155-174, 2004

[89] Chakraborty, N., Hawkes, E. R., Chen, J. H., Cant, R. S., "The effects of strain rate and curvature on surface density function transport in turbulent premixed methane-air and hydrogen-air flames: a comparative study", Combustion and Flame, 154, pp. 259-280, 2008

[90] Haworth, D. C., Poinsot, T., J., "Numerical simulations of Lewis number effects in turbulent premixed flames", Journal of Fluid Mechanics, 244, pp. 405-436, 1992

[91] Rutland, C. J., Trouvé, A., "Direct numerical simulations of premixed turbulent flames with nonunity Lewis numbers", Combustion and Flame, 94, pp. 41-57, 1993

[92] Trouvé, A., Poinsot, T., "The evolution equation for the flame surface density in turbulent premixed combustion", Journal of Fluid Mechanics, 278, pp.1-31, 1994

[93] Dandekar, A., Collins, L. R., "Effect of nonunity Lewis number on premixed flame propagation through isotropic turbulence", Combustion and Flame, 101, pp. 428-440, 1995

[94] Bonaldo, A., Ph. D. thesis, "Experimental characterization of swirl stabilized annular stratified flames", University of Cranfield, Cranfield, 2007

[95] Morley, C., "Gaseq", www.arcl02.dsl.pipex.com, 2005

[96] Ó Conaire, M., Curran, H. J., Simmie, J. M., Pitz, W. J., Westbrook, C. K., "A comprehensive modeling study of hydrogen oxidation", International Journal of Chemical Kinetics, 36, 11, pp. 603-622, 2004

[97] Baukal, C. E., Schwartz, R. E., "The John Zink combustion handbook", CRC Press, Tulsa, Oklahoma, 2001

[98] Liu, D. D. S., MacFarlane, R., "Laminar burning velocities of hydrogen-air-steam flames", Combustion and Flame, 49, pp. 59-71, 1983

[99] Qin, X., Kobayashi, H., Niioka, T., "laminar burning velocity of hydrogen-air premixed flames at elevated pressures", Experimental Thermal and Fluid Science, 21, pp. 58-63, 2000

[100] Tse, S. D., Zhu, D. L., Law, C. K., "Morphology and burning rates of expanding spherical flames in H2/O2/inert mixtures up to 60 atmospheres", Proceedings of the Combustion Institute, 28, pp. 1793-1800, 2000

[101] Kwon, O. C., Faeth, G..M., "Flame stretch interactions of premixed hydrogen-fueled flames: measurements and predictions", Combustion and Flame, 124, pp. 590-610, 2001

[102] Saxena, P., Williams, F.A., "Testing small detailed chemical-kinetic mechanism for the combustion of hydrogen and carbon monoxide", Combustion and Flame, 145, pp. 316-323, 2006

[103] Bradley, D.; Lawes, M., Kexin Liu; Verhelst, S., Woolley, R.; "Laminar burning velocities of lean hydrogen-air mixtures at pressures up to 1.0 MPa", Combustion and Flame, 149, pp. 162-172, 2007

[104] Kitagawa, T., Nakahara, T., Maruyama, K., Kado, K., Hayakawa, A., Kobayashi, S., "Turbulent burning velocity of hydrogen-air premixed propagating flames at elevated pressures", International Journal of Hydrogen Energy, 33, pp. 5842-5849, 2008

[105] Fernández-Galisteo, D., Sánchez, A. L., Liñán, A., Williams, F. A., "One step reduced kinetics for lean hydrogen-air deflagration", Combustion and Flame, 156, 5, pp.985-996, 2009

[106] Jørgensen, F. E., "How to measure turbulence with hot-wire anemometers: a basic guide", Dantec Dynamics A/S, 2004

[107] Exciton, "Laser wavelength chart", available online, www.exciton.com/wavelength_chart.html, 2006

[108] Li, Z. S., Kiefer, J., Zetterberg, J., Linvin. M., Leipertz, A., Bai, X. S., Aldén, M., "Development of improved PLIF CH detection using an Alexandrite laser for single-shot investigation of turbulent and lean flames", Proceedings of the Combustion Institute, 31, pp. 727-735, 2007

[109] Dong, Y., Holley, A. T., Andac, M. G., Egolfopoulos, F. N., Davis, S. G., Middha, P., Wang, H., "Extinction of premixed H_2/air flames: chemical kinetics and molecular diffusion effects", Combustion and Flame, 142, pp. 374-387, 2005

[110] Bunkute, B., Ph.D. thesis, "Burning velocities of coal-derived syngas mixtures", University of Cranfield, Cranfield, 2008

[111] Batchelor, G. K., "Small-scale variation of convected quantities like temperature in turbulent fluid", Journal of Fluid Mechanics, 5, pp. 113-133, 1959

[112] Gibson, C. H., "Fine structure of scalar fields mixed by turbulence. I. Zero-gradient points and minimal gradient surfaces", Physics of Fluids, 11, 11, pp. 2305-2315, 1968

[113] Kerr, R. M., "Higher-order derivative correlations and the alignment of small-scale structures in isotropic numerical turbulence", Journal of Fluid Mechanics, 153, pp. 31-58, 1985

[114] Ashurst, W. T., Kerstein, A. R., Kerr, R. M., Gibson, C. H., "Alignment of vorticity and scalar gradient with strain rate in simulated Navier-Stokes turbulence", Physics of Fluids, 30, 8, pp. 2343-2353, 1987

[115] Ruetsch, G. R., Maxey, M. R., "Small-scale features of vorticity and passive scalar fields in homogeneous isotropic turbulence", Physics of Fluids A, 3, pp. 1587-1597, 1991

[116] Ashurst, W. T., Peters, N., Smooke, M. D., "Numerical simulation of turbulent flame structure with non-unity Lewis number", Combustion Science and Technology, 53, pp. 339-375, 1987

[117] Nomura, K. K., Elghobashi, S. E., "Mixing characteristics of an inhomogeneous scalar in isotropic and homogeneous sheared turbulence", Physics of Fluids A, 4, pp. 606-625, 1992

APPENDIX CHAPTER II

J	e 1/2 v=0	f 1/2 v=0	e 3/2 v=0	f 3/2 v=0
0.5	-59.8824	-59.8706	59.8702	59.8702
1.5	-54.8724	-54.8487	65.0308	65.0308
2.5	-46.5184	-46.4829	73.6313	73.6314
3.5	-34.8205	-34.7733	85.6711	85.6714
4.5	-19.7786	-19.7198	101.1494	101.1500
5.5	-1.3928	-1.3226	120.0648	120.0659
6.5	20.3369	20.4183	142.4162	142.4178
7.5	45.4102	45.5028	168.2018	168.2043
8.5	73.8272	73.9306	197.4199	197.4234
9.5	105.5876	105.7016	230.0683	230.0731
10.5	140.6911	140.8155	266.1450	266.1513
11.5	179.1375	179.2719	305.6473	305.6554
12.5	220.9263	221.0705	348.5727	348.5829
13.5	266.0571	266.2108	394.9184	394.9310
14.5	314.5293	314.6921	444.6814	444.6967
15.5	366.3422	366.5138	497.8586	497.8770
16.5	421.4949	421.6751	554.4467	554.4685
17.5	479.9867	480.1750	614.4423	614.4678
18.5	541.8164	542.0126	677.8419	677.8714
19.5	606.9830	607.1866	744.6416	744.6755
20.5	675.4849	675.6957	814.8379	814.8765
21.5	747.3209	747.5384	888.4266	888.4704
22.5	822.4892	822.7132	965.4038	965.4530
23.5	900.9882	901.2183	1,045.7654	1,045.8204
24.5	982.8160	983.0518	1,129.5070	1,129.5681
25.5	1,067.9703	1,068.2115	1,216.6243	1,216.6919
26.5	1,156.4491	1,156.6953	1,307.1129	1,307.1873
27.5	1,248.2498	1,248.5008	1,400.9682	1,401.0498
28.5	1,343.3701	1,343.6254	1,498.1855	1,498.2745
29.5	1,441.8070	1,442.0664	1,598.7600	1,598.8569
30.5	1,543.5578	1,543.8209	1,702.6870	1,702.7920
31.5	1,648.6193	1,648.8859	1,809.9614	1,810.0748
32.5	1,756.9884	1,757.2581	1,920.5781	1,920.7003
33.5	1,868.6617	1,868.9342	2,034.5321	2,034.6634
34.5	1,983.6356	1,983.9106	2,151.8181	2,151.9588
35.5	2,101.9064	2,102.1836	2,272.4307	2,272.5811
36.5	2,223.4703	2,223.7493	2,396.3645	2,396.5249
37.5	2,348.3231	2,348.6038	2,523.6139	2,523.7846
38.5	2,476.4608	2,476.7427	2,654.1733	2,654.3546
39.5	2,607.8789	2,608.1619	2,788.0370	2,788.2290

Figure A2.1: Energies for the radical NO in the lambda doubled spin-split ground electronic state in the vibrational level v=0 for rotational level J=0.5-39.5*

* calculated with the equations found in [37]

J	-1/2	1/2
0.5	44198.9430	44202.9182
1.5	44202.9142	44210.8644
2.5	44210.8577	44222.7827
3.5	44222.7733	44238.6726
4.5	44238.6606	44258.5337
5.5	44258.5190	44282.3653
6.5	44282.3479	44310.1666
7.5	44310.1464	44341.9365
8.5	44341.9137	44377.6740
9.5	44377.6486	44417.3780
10.5	44417.3499	44461.0470
11.5	44461.0162	44508.6796
12.5	44508.6461	44560.2741
13.5	44560.2379	44615.8287
14.5	44615.7899	44675.3417
15.5	44675.3001	44738.8108
16.5	44738.7666	44806.2341
17.5	44806.1872	44877.6091
18.5	44877.5596	44952.9335
19.5	44952.8813	45032.2047
20.5	45032.1497	45115.4199
21.5	45115.3622	45202.5763
22.5	45202.5160	45293.6709
23.5	45293.6079	45388.7007
24.5	45388.6350	45487.6623
25.5	45487.5939	45590.5524
26.5	45590.4814	45697.3675
27.5	45697.2937	45808.1038
28.5	45808.0274	45922.7577
29.5	45922.6786	46041.3252
30.5	46041.2434	46163.8021
31.5	46163.7177	46290.1844
32.5	46290.0973	46420.4677
33.5	46420.3779	46554.6475
34.5	46554.5551	46692.7193
35.5	46692.6241	46834.6782
36.5	46834.5803	46980.5194
37.5	46980.4188	47130.2378
38.5	47130.1347	47283.8285
39.5	47283.7226	47441.2859

Figure A2.2: Energies for the radical NO in the spin-split first excited electronic state in the vibrational level v=0 for rotational level J=0.5-39.5*

* calculated with the equations found in [37]

J''	P_{11}	$^{Q}P_{21}$	Q_{11}	$^{R}Q_{21}$	R_{11}	$^{S}R_{21}$
1.5	6.3250E+16	5.3350E+16	1.9420E+17	1.7840E+17	1.0770E+17	1.0180E+17
2.5	7.7900E+16	6.2090E+16	1.9320E+17	1.6610E+17	1.0540E+17	9.4040E+16
3.5	8.5590E+16	6.4470E+16	1.9620E+17	1.5860E+17	1.0510E+17	8.8660E+16
4.5	9.0940E+16	6.4740E+16	2.0020E+17	1.5260E+17	1.0580E+17	8.4340E+16
5.5	9.5210E+16	6.4070E+16	2.0460E+17	1.4710E+17	1.0700E+17	8.0630E+16
6.5	9.8870E+16	6.2920E+16	2.0900E+17	1.4190E+17	1.0840E+17	7.7280E+16
7.5	1.0220E+17	6.1490E+16	2.1350E+17	1.3700E+17	1.1010E+17	7.4190E+16
8.5	1.0520E+17	5.9900E+16	2.1800E+17	1.3220E+17	1.1180E+17	7.1290E+16
9.5	1.0800E+17	5.8220E+16	2.2240E+17	1.2760E+17	1.1350E+17	6.8550E+16
10.5	1.1070E+17	5.6480E+16	2.2670E+17	1.2310E+17	1.1530E+17	6.5930E+16
11.5	1.1320E+17	5.4720E+16	2.3090E+17	1.1870E+17	1.1710E+17	6.3430E+17
12.5	1.1560E+17	5.2960E+16	2.3500E+17	1.1450E+17	1.1890E+17	6.1030E+17
13.5	1.1790E+17	5.1220E+16	2.3900E+17	1.1030E+17	1.2070E+17	5.8720E+17
14.5	1.2010E+17	4.9490E+16	2.4290E+17	1.0630E+17	1.2240E+17	5.6500E+17
15.5	1.2220E+17	4.7790E+16	2.4670E+17	1.0250E+17	1.2410E+17	5.4360E+17
16.5	1.2430E+17	4.6130E+16	2.5030E+17	9.8690E+16	1.2580E+17	5.2310E+17
17.5	1.2620E+17	4.4510E+16	2.5380E+17	9.5060E+16	1.2740E+17	5.0330E+17
18.5	1.2810E+17	4.2930E+16	2.5720E+17	9.1550E+16	1.2900E+17	4.8430E+20
19.5	1.2990E+17	4.1400E+16	2.6050E+17	8.8170E+16	1.3050E+17	4.6600E+16
20.5	1.3160E+17	3.9910E+16	2.6370E+17	8.4900E+16	1.3200E+17	4.4840E+16
21.5	1.3320E+17	3.8470E+16	2.6670E+17	8.1760E+16	1.3340E+17	4.3150E+16
22.5	1.3480E+17	3.7080E+16	2.6960E+17	7.8730E+16	1.3470E+17	4.1530E+16
23.5	1.3630E+17	3.5730E+17	2.7240E+17	7.5810E+16	1.3600E+17	3.9970E+20
24.5	1.3770E+17	3.4440E+16	2.7510E+17	7.3010E+16	1.3730E+17	3.8470E+16
25.5	1.3910E+17	3.3190E+16	2.7770E+17	7.0320E+16	1.3850E+17	3.7040E+16
26.5	1.4040E+17	3.1990E+16	2.8020E+17	6.7730E+16	1.3970E+17	3.5660E+16
27.5	1.4170E+17	3.0830E+16	2.8250E+17	6.5250E+16	1.4080E+17	3.4300E+16
28.5	1.4290E+17	2.9720E+16	2.8480E+17	6.2870E+16	1.4190E+17	3.0800E+16
29.5	1.4400E+17	2.8650E+16	2.8690E+17	6.0580E+16	1.4290E+17	1.8700E+16
30.5	1.4510E+17	2.7630E+16	2.8900E+17	5.8390E+16	1.4380E+17	3.0700E+16
31.5	1.4610E+17	2.6640E+16	2.9100E+17	5.6280E+16	1.4480E+17	2.9590E+16
32.5	1.4710E+17	2.5690E+16	2.9280E+17	5.4260E+16	1.4570E+17	2.8520E+16
33.5	1.4810E+17	2.4790E+16	2.9460E+17	5.2330E+16	1.4650E+17	2.7500E+16
34.5	1.4900E+17	2.3910E+16	2.9630E+17	5.0480E+16	1.4730E+17	2.6520E+16
35.5	1.4980E+17	2.3080E+16	2.9790E+17	4.8700E+16	1.4810E+17	2.5580E+16
36.5	1.5060E+17	2.2270E+16	2.9950E+17	4.6990E+16	1.4880E+17	2.4680E+16
37.5	1.5140E+17	2.1500E+16	3.0100E+17	4.5360E+16	1.4950E+17	2.3820E+16
38.5	1.5210E+17	2.0770E+16	3.0240E+17	4.3790E+16	1.5020E+17	2.3000E+16
39.5	1.5280E+17	2.0060E+16	3.0370E+17	4.2290E+16	1.5080E+17	2.2210E+16

Figure A2.3: Einstein $B_{i,k}$ coefficients for absorption for the γ(0,0) band of NO originating from $\Pi_{1/2}$ [36]

J''	$^{O}P_{12}$	P_{22}	$^{P}Q_{12}$	Q_{22}	$^{Q}R_{12}$	R_{22}
1.5	1.7020E+17	1.8010E+17	1.3220E+17	1.4810E+17	3.2090E+16	3.8030E+16
2.5	1.3210E+17	1.4790E+17	1.4660E+17	1.7370E+17	4.4460E+16	5.5750E+16
3.5	1.1440E+17	1.3560E+17	1.4810E+17	1.8560E+17	5.0260E+16	6.6680E+16
4.5	1.0350E+17	1.2970E+17	1.4600E+17	1.9370E+17	5.3090E+16	7.4510E+16
5.5	9.5710E+16	1.2680E+17	1.4280E+17	2.0020E+17	5.4340E+16	8.0650E+16
6.5	8.9600E+16	1.2550E+17	1.3890E+17	2.0590E+17	5.4660E+16	8.5750E+16
7.5	8.4520E+16	1.2510E+17	1.3480E+17	2.1130E+17	5.4390E+16	9.0180E+16
8.5	8.0130E+16	1.2530E+17	1.3070E+17	2.1630E+17	5.3730E+16	9.4120E+16
9.5	7.6220E+16	1.2590E+17	1.2650E+17	2.2100E+17	5.2810E+16	9.7690E+16
10.5	7.2680E+16	1.2680E+17	1.2230E+17	2.2560E+17	5.1710E+16	1.0100E+17
11.5	6.9430E+16	1.2780E+17	1.1820E+17	2.3000E+17	5.0490E+16	1.0400E+17
12.5	6.6410E+16	1.2890E+17	1.1410E+17	2.3430E+17	4.9200E+16	1.0690E+17
13.5	6.3590E+16	1.3010E+17	1.1020E+17	2.3840E+17	4.7850E+16	1.0960E+17
14.5	6.0940E+16	1.3130E+17	1.0630E+17	2.4230E+17	4.6840E+16	1.1210E+17
15.5	5.8440E+16	1.3260E+17	1.0250E+17	2.4620E+17	4.5090E+16	1.1450E+17
16.5	5.6070E+16	1.3390E+17	9.8910E+16	2.4980E+17	4.3710E+16	1.1680E+17
17.5	5.3820E+16	1.3510E+17	9.5380E+20	2.5340E+17	4.2330E+16	1.1900E+17
18.5	5.1680E+16	1.3640E+17	9.1980E+16	2.5680E+17	4.0980E+16	1.2110E+17
19.5	4.9650E+16	1.3760E+17	8.8690E+16	2.6000E+17	3.9650E+16	1.2300E+17
20.5	4.7720E+16	1.3880E+17	8.5510E+16	2.6320E+17	3.8350E+16	1.2490E+17
21.5	4.5880E+16	1.4000E+17	8.2460E+16	2.6620E+17	3.7080E+16	1.2670E+17
22.5	4.4120E+16	1.4110E+17	7.9510E+16	2.6900E+17	3.5850E+16	1.2840E+17
23.5	4.2450E+16	1.4230E+17	7.6680E+16	2.7180E+17	3.4650E+16	1.3000E+17
24.5	4.0850E+16	1.4330E+17	7.3960E+16	2.7440E+17	3.3490E+16	1.3150E+17
25.5	3.9330E+16	1.4440E+17	7.1350E+16	2.7700E+17	3.2370E+16	1.3300E+17
26.5	3.7880E+16	1.4530E+17	6.8840E+16	2.7940E+17	3.1280E+16	1.3430E+17
27.5	3.6490E+16	1.4630E+17	6.6430E+16	2.8170E+17	3.0240E+16	1.3570E+17
28.5	3.5170E+16	1.4720E+17	6.4120E+16	2.8390E+17	2.9230E+16	1.3690E+17
29.5	3.3900E+16	1.4810E+17	6.1900E+16	2.8590E+17	2.8260E+16	1.3810E+17
30.5	3.2700E+16	1.4890E+17	5.9780E+16	2.8790E+17	2.7320E+16	1.3930E+17
31.5	3.1550E+16	1.4970E+17	5.7750E+16	2.8980E+17	2.6430E+16	1.4030E+17
32.5	3.0450E+16	1.5050E+17	5.5800E+16	2.9170E+17	2.5560E+16	1.4140E+17
33.5	2.9400E+16	1.5120E+17	5.3930E+16	2.9340E+17	2.4730E+16	1.4230E+17
34.5	2.8390E+16	1.5190E+17	5.2140E+16	2.9500E+17	2.3930E+16	1.4330E+17
35.5	2.7430E+16	1.5260E+17	5.0430E+16	2.9660E+17	2.3170E+16	1.4410E+17
36.5	2.6520E+16	1.5320E+17	4.8790E+16	2.9810E+17	2.2430E+16	1.4500E+17
37.5	2.5640E+16	1.5390E+17	4.7210E+16	2.9950E+17	2.1720E+16	1.4580E+17
38.5	2.4800E+16	1.5440E+17	4.5710E+16	3.0080E+17	2.1050E+16	1.4650E+17
39.5	2.4000E+16	1.5500E+17	4.4260E+16	3.0210E+17	2.0400E+16	1.4720E+17

Figure A2.4: Einstein $B_{i,k}$ coefficients for absorption for the γ(0,0) band of NO originating from $\Pi_{3/2}$ [36]

J''	P_{11}	$^{Q}P_{21}$	Q_{11}	$^{R}Q_{21}$	R_{11}	$^{S}R_{21}$
1.5	1.8180E+05	1.5340E+05	2.7930E+05	2.5660E+05	1.0330E+05	9.7670E+04
2.5	1.6790E+05	1.3390E+05	2.7780E+05	2.3900E+05	1.1370E+05	1.1060E+05
3.5	1.6400E+05	1.2360E+05	2.8210E+05	2.2830E+05	1.2100E+05	1.0220E+05
4.5	1.6330E+05	1.1640E+05	2.8790E+05	2.1970E+05	1.2690E+05	1.0140E+05
5.5	1.6410E+05	1.1060E+05	2.9420E+05	2.1190E+05	1.3210E+05	9.9730E+04
6.5	1.6560E+05	1.0560E+05	3.0060E+05	2.0450E+05	1.3670E+05	9.7650E+04
7.5	1.6760E+05	1.0110E+05	3.0720E+05	1.9750E+05	1.4100E+05	9.5300E+04
8.5	1.6990E+05	9.6960E+04	3.1360E+05	1.9070E+05	1.4510E+05	9.2790E+04
9.5	1.7230E+05	9.3100E+04	3.2000E+05	1.8410E+05	1.4900E+05	9.0200E+04
10.5	1.7480E+05	8.9450E+04	3.2630E+05	1.7770E+05	1.5270E+05	8.7550E+04
11.5	1.7730E+05	8.5980E+04	3.3250E+05	1.7150E+05	1.5620E+05	8.4890E+04
12.5	1.7990E+05	8.2660E+04	3.3860E+05	1.6550E+05	1.5970E+05	8.2240E+04
13.5	1.8240E+05	7.9500E+04	3.4450E+05	1.5960E+05	1.6300E+05	7.9610E+04
14.5	1.8490E+05	7.6460E+04	3.5030E+05	1.5400E+05	1.6620E+05	7.7020E+04
15.5	1.8740E+05	7.3550E+04	3.5590E+05	1.4850E+05	1.6930E+05	7.4480E+04
16.5	1.8980E+05	7.0750E+04	3.6130E+05	1.4310E+05	1.7230E+05	7.1990E+04
17.5	1.9220E+05	6.8070E+04	3.6670E+05	1.3800E+05	1.7520E+05	6.9560E+04
18.5	1.9450E+05	6.5500E+04	3.7180E+05	1.3300E+05	1.7800E+05	6.7200E+04
19.5	1.9670E+05	6.3020E+04	3.7680E+05	1.2820E+05	1.8070E+05	6.4900E+04
20.5	1.9890E+05	6.0650E+04	3.8170E+05	1.2360E+05	1.8330E+05	6.2670E+04
21.5	2.0100E+05	5.8380E+04	3.8640E+05	1.1910E+05	1.8590E+05	6.0510E+04
22.5	2.0310E+05	5.6200E+04	3.9090E+05	1.1480E+05	1.8830E+05	5.8430E+04
23.5	2.0510E+05	5.4100E+04	3.9530E+05	1.1070E+05	1.9070E+05	5.6410E+04
24.5	2.0700E+05	5.2100E+04	3.9960E+05	1.0680E+05	1.9300E+05	5.4460E+04
25.5	2.0890E+05	5.0180E+04	4.0370E+05	1.0290E+05	1.9520E+05	5.2590E+04
26.5	2.1070E+05	4.8340E+04	4.0770E+05	9.9270E+04	1.9740E+05	5.0780E+04
27.5	2.1240E+05	4.6570E+04	4.1150E+05	9.5750E+04	1.9950E+05	4.9040E+04
28.5	2.1410E+05	4.4880E+04	4.1520E+05	9.2380E+04	2.0150E+05	4.7360E+04
29.5	2.1580E+05	4.3270E+04	4.1880E+05	8.9140E+04	2.0340E+05	4.5750E+04
30.5	2.1740E+05	4.1720E+04	4.2230E+05	8.6030E+04	2.0530E+05	4.4200E+04
31.5	2.1890E+05	4.0230E+04	4.2570E+05	8.3050E+04	2.0720E+05	4.2710E+04
32.5	2.2040E+05	3.8810E+04	4.2890E+05	8.0190E+04	2.0890E+05	4.1280E+04
33.5	2.2180E+05	3.7450E+04	4.3210E+05	7.7450E+04	2.1060E+05	3.9910E+04
34.5	2.2320E+05	3.6150E+04	4.3520E+05	7.4820E+04	2.1230E+05	3.8590E+04
35.5	2.2450E+05	3.4910E+04	4.3810E+05	7.2300E+04	2.1390E+05	3.7320E+04
36.5	2.2580E+05	3.3710E+04	4.4100E+05	6.9880E+04	2.1550E+05	3.6100E+04
37.5	2.2710E+05	3.2570E+04	4.4380E+05	6.7570E+04	2.1700E+05	3.4930E+04
38.5	2.2830E+05	3.1470E+04	4.4650E+05	6.5340E+04	2.1850E+05	3.3810E+04
39.5	2.2950E+05	3.0430E+04	4.4910E+05	6.3210E+05	2.1990E+05	3.2730E+04

Table A2.5: Einstein $A_{k,j}$ coefficients for spontaneous emission [36]

J''	$^{O}P_{12}$	P_{22}	$^{P}Q_{12}$	Q_{22}	$^{Q}R_{12}$	R_{22}
1.5	4.8520E+05	5.1360E+05	1.8860E+05	2.1130E+05	3.0530E+04	3.6210E+04
2.5	2.8250E+05	3.1650E+05	2.0910E+05	2.4790E+05	4.7590E+04	5.9740E+04
3.5	2.1740E+05	2.5770E+05	2.1110E+05	2.6500E+05	5.7400E+04	7.6260E+04
4.5	1.8430E+05	2.3120E+05	2.0830E+05	2.7650E+05	6.3180E+04	8.8810E+04
5.5	1.6360E+05	2.1710E+05	2.0360E+05	2.8600E+05	6.6540E+04	9.8930E+04
6.5	1.4890E+05	2.0890E+05	1.9810E+05	2.9430E+05	6.8340E+04	1.0750E+05
7.5	1.3750E+05	2.0400E+05	1.9240E+05	3.0200E+05	6.9110E+04	1.1490E+05
8.5	1.2830E+05	2.0120E+05	1.8640E+05	3.0930E+05	6.9160E+04	1.2150E+05
9.5	1.2060E+05	1.9970E+05	1.8050E+05	3.1630E+05	6.8690E+04	1.2750E+05
10.5	1.1380E+05	1.9900E+05	1.7450E+05	3.2300E+05	3.7860E+04	1.3300E+05
11.5	1.0780E+05	1.9900E+05	1.6870E+05	3.2950E+05	6.6770E+04	1.3810E+05
12.5	1.0240E+05	1.9940E+05	1.6300E+05	3.3580E+05	6.5480E+04	1.4280E+05
13.5	9.7510E+04	2.0020E+05	1.5740E+05	3.4190E+05	6.4050E+04	1.4730E+05
14.5	9.2970E+04	2.0110E+05	1.5190E+05	3.4780E+05	6.2530E+04	1.5150E+05
15.5	8.8770E+04	2.0220E+05	1.4660E+05	3.5350E+05	6.0950E+04	1.5550E+05
16.5	8.4860E+04	2.0350E+05	1.4150E+05	3.5910E+05	5.9320E+04	1.5940E+05
17.5	8.1190E+04	2.0480E+05	1.3650E+05	3.6440E+05	5.7680E+04	1.6300E+05
18.5	7.7750E+04	2.0620E+05	1.3170E+05	3.6960E+05	5.6040E+04	1.6640E+05
19.5	7.4510E+04	2.0760E+05	1.2710E+05	3.7460E+05	5.4400E+04	1.6980E+05
20.5	7.1450E+04	2.0900E+05	1.2260E+05	3.7950E+05	5.2780E+04	1.7290E+05
21.5	6.8570E+04	2.1040E+05	1.1830E+05	3.8410E+05	5.1190E+04	1.7590E+05
22.5	6.5840E+04	2.1190E+05	1.1420E+05	3.8870E+05	4.9630E+04	1.7890E+05
23.5	6.3250E+04	2.1330E+05	1.1020E+05	3.9300E+05	4.8100E+04	1.8160E+05
24.5	6.0790E+04	2.1470E+05	1.0630E+05	3.9730E+05	4.6610E+04	1.8430E+05
25.5	5.8470E+04	2.1600E+05	1.0270E+05	4.0130E+05	4.5170E+04	1.8690E+05
26.5	5.6250E+04	2.1740E+05	9.9140E+04	4.0530E+05	4.3760E+04	1.8930E+05
27.5	5.4150E+04	2.1870E+05	9.5760E+04	4.0910E+05	4.2400E+04	1.9170E+05
28.5	5.2160E+04	2.2000E+05	9.2510E+04	4.1280E+05	4.1090E+04	1.9400E+05
29.5	5.0260E+04	2.2130E+05	8.9400E+04	4.1630E+05	3.9810E+04	1.9620E+05
30.5	4.8450E+04	2.2250E+05	8.6420E+04	4.1970E+05	3.8580E+04	1.9830E+05
31.5	4.6730E+04	2.2370E+05	8.3570E+04	4.2300E+05	3.7400E+04	2.0040E+05
32.5	4.5100E+04	2.2490E+05	8.0830E+04	4.2620E+05	3.6260E+04	2.0230E+05
33.5	4.3540E+04	2.2600E+05	7.8210E+04	4.2930E+05	3.5160E+04	2.0420E+05
34.5	4.2050E+04	2.2710E+05	7.5700E+04	4.3240E+05	3.4100E+04	2.0610E+05
35.5	4.0640E+04	2.2820E+05	7.3300E+04	4.3530E+05	3.3080E+04	2.0790E+05
36.5	3.9290E+04	2.2920E+05	7.1000E+04	4.3810E+05	3.2100E+04	2.0960E+05
37.5	3.8000E+04	2.3030E+05	6.8800E+04	4.4080E+05	3.1160E+04	2.1120E+05
38.5	3.6770E+04	2.3130E+05	6.6690E+04	4.4350E+05	3.0250E+04	2.1280E+05
39.5	3.5600E+04	2.3220E+05	6.4660E+04	4.4600E+05	2.9380E+04	2.1440E+05

Table A2.6: Einstein $A_{k,j}$ coefficients for spontaneous emission [36]

APPENDIX CHAPTER V

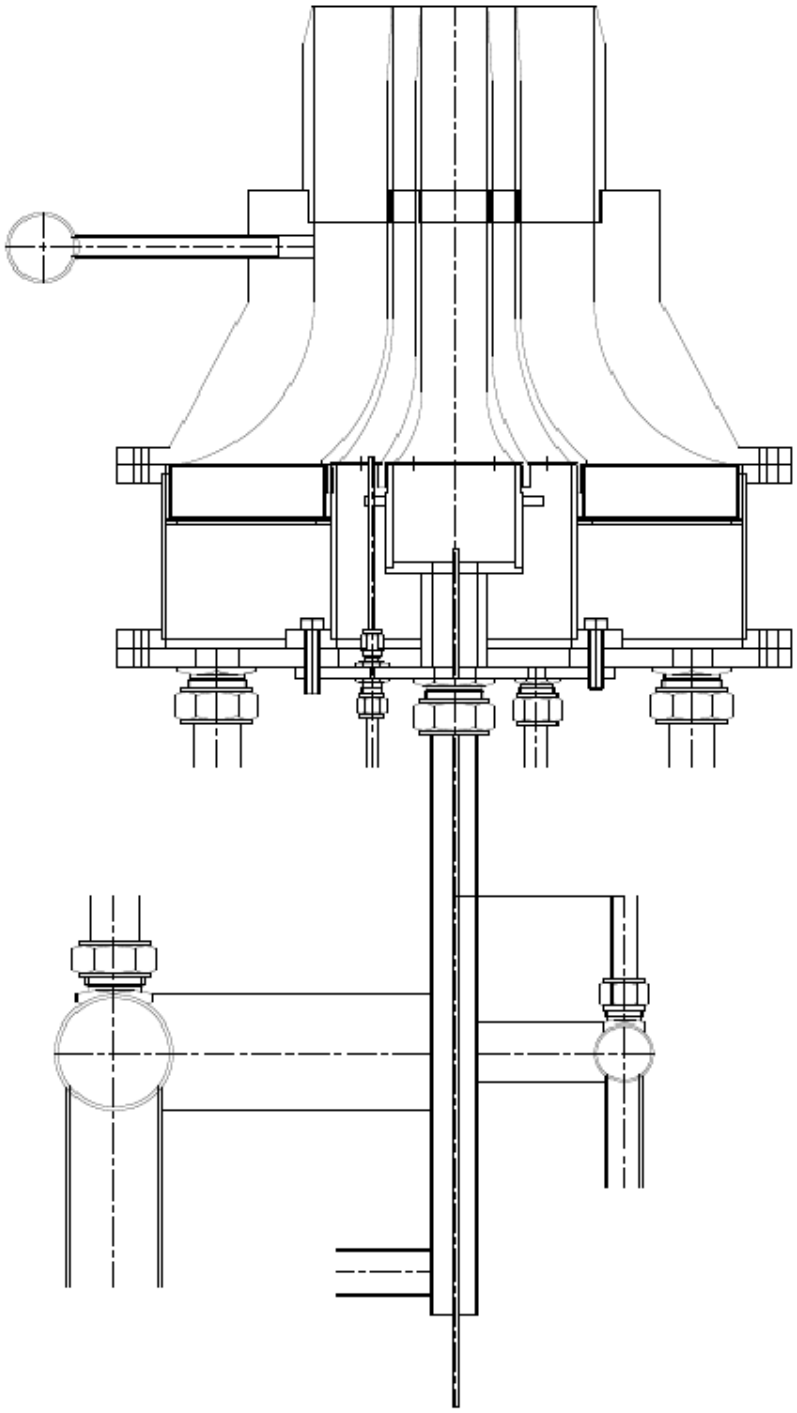

DRAWING No.	
ME/A3/38027	
ISSUE	MODIFICATION
A	———

ALL DIMENSIONS IN MILLIMETRES UNLESS OTHERWISE STATED

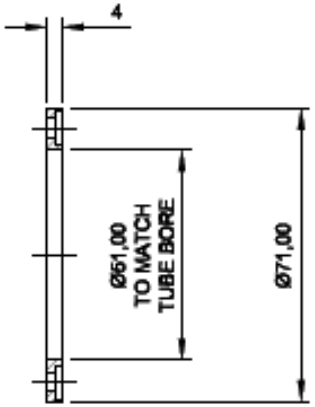

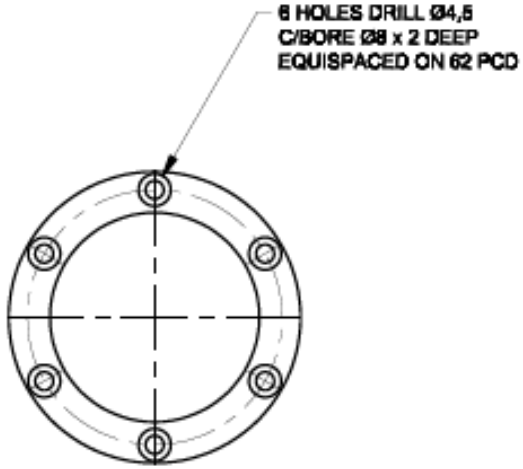

NOTES

1. MACHINE ALL OVER
2. REMOVE ALL SHARP EDGES

PRINT No	
ISSUED TO	WORKSHOP
ISSUED FOR	MANUFACTURE
	QUOTATION
	INFORMATION
DATE	
JOB No	

THIRD ANGLE PROJECTION

SHEET SIZE	ITEM	PART No.	DESCRIPTION	No. OFF	MATL.	SPEC.	REMARKS
A3	1	A3/38027	CLAMP RING	1	SS	316L	??

GENERAL TOLERANCE ON DIMENSIONS	COST CODE	No. OF SETS REQ.
MACHINED ±0,2		
UNMACHINED	R44006	1
OTHER DIMENSIONS AS STATED		
WELD WHERE SHOWN THUS		
MACHINE WHERE SHOWN THUS	USED ON DRG. ME/A2/38000	

SCALE	DRAWN	CHKD.	APPVD.	STRESS APPVD.
FULL	A HUTCHINGS	A H		
SIZE	19/01/07	19/01/07		

TITLE: MAIN RIG TITLE
CLAMP RING

FINISH: SELF

SCHOOL OF ENGINEERING
CRANFIELD UNIVERSITY

DRAWING No. ME/A3/38027

SHT. 1 OF 1 SHEETS

DRAWING No.	
ME/A3/38025	
ISSUE	MODIFICATION
A	

ALL DIMENSIONS IN MILLIMETRES UNLESS OTHERWISE STATED

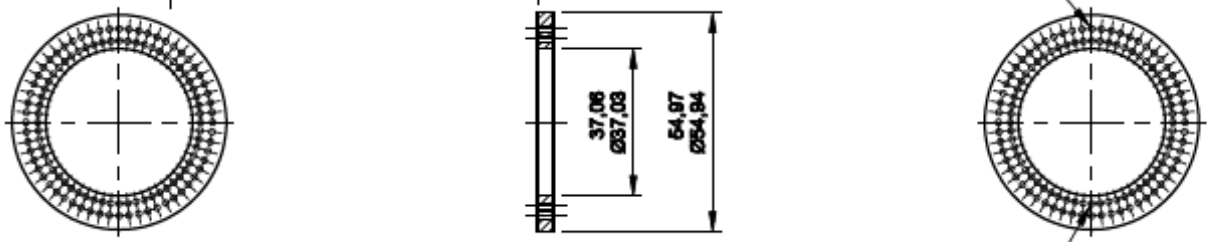

NOTES

1. MACHINE ALL OVER
2. REMOVE ALL SHARP EDGES

PRINT No	
ISSUED TO	WORKSHOP
ISSUED FOR	MANUFACTURE
	QUOTATION
	INFORMATION
DATE	
JOB No	

THIRD ANGLE PROJECTION

SHEET SIZE	ITEM	PART No.	DESCRIPTION	No. OFF	MATL.	SPEC.	REMARKS
A3	1	A3/38025	DISTRIBUTION PLATE	1	SS	316L	77

GENERAL TOLERANCE ON DIMENSIONS	COST CODE	No. OF SETS REQ.
MACHINED ±0,2 UNMACHINED OTHER DIMENSIONS AS STATED	R44006	1
WELD WHERE SHOWN THUS		
MACHINE WHERE SHOWN THUS	USED ON DRG. ME/A2/38030	

SCALE	DRAWN	CHKD.	APPVD.	STRESS APPVD.
FULL SIZE	A HUTCHINGS	A H		
	19/01/07	19/01/07		

TITLE: MAIN RIG TITLE
DISTRIBUTION PLATE

FINISH: SELF

SCHOOL OF ENGINEERING
CRANFIELD UNIVERSITY

DRAWING No. ME/A3/38025

SHT. 1 OF 1 SHEETS

DRAWING No.	
ME/A3/38029	
ISSUE	MODIFICATION
A	———

ALL DIMENSIONS IN MILLIMETRES UNLESS OTHERWISE STATED

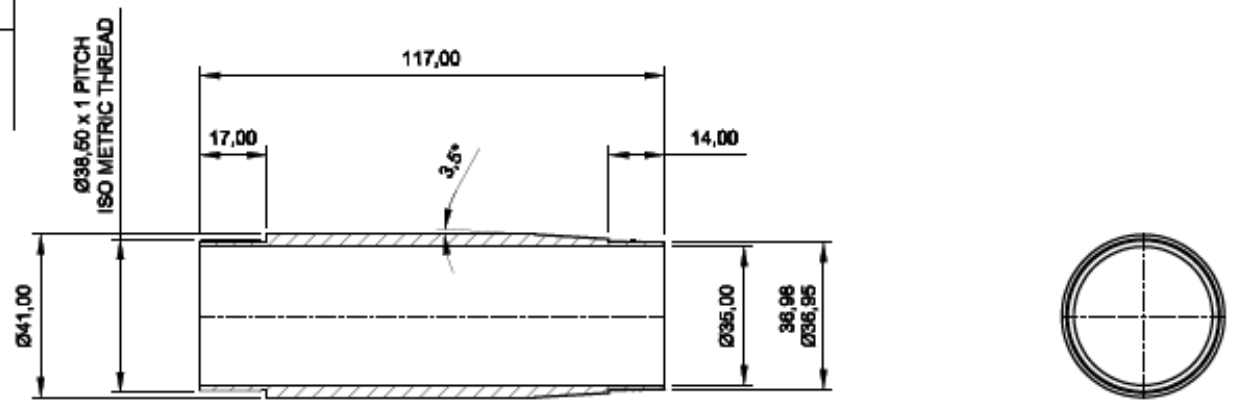

NOTES

1. MACHINE ALL OVER
2. THREAD TO MATCH THREAD IN ME/A0/31803
3. REMOVE ALL SHARP EDGES

PRINT No	
ISSUED TO	WORKSHOP
ISSUED FOR	MANUFACTURE
	QUOTATION
	INFORMATION
DATE	
JOB No	

THIRD ANGLE PROJECTION

SHEET SIZE	ITEM	PART No.	DESCRIPTION	No. OFF	MATL.	SPEC.	REMARKS
A3	1	A3/38029	INNER FLOW TUBE	1	SS	316L	??

GENERAL TOLERANCE ON DIMENSIONS
MACHINED ±0,2
UNMACHINED
ANGLES ±1°
OTHER DIMENSIONS AS STATED

COST CODE	No. OF SETS REQ.
R44006	1

WELD WHERE SHOWN THUS ⌐

USED ON DRG. ME/A2/38030

SCALE: FULL SIZE

	DRAWN	CHKD.	APPVD.	STRESS APPVD.
	A HUTCHINGS	A H		
	27/03/07	27/03/07		

FINISH: SELF

TITLE: MAIN RIG TITLE
INNER FLOW TUBE

SCHOOL OF ENGINEERING
CRANFIELD UNIVERSITY

DRAWING No. ME/A3/38029

SHT. 1 OF 1 SHEETS

DRAWING No. ME/A2/38030	
ISSUE	MODIFICATION
A	———

ALL DIMENSIONS IN MILLIMETRES UNLESS OTHERWISE STATED

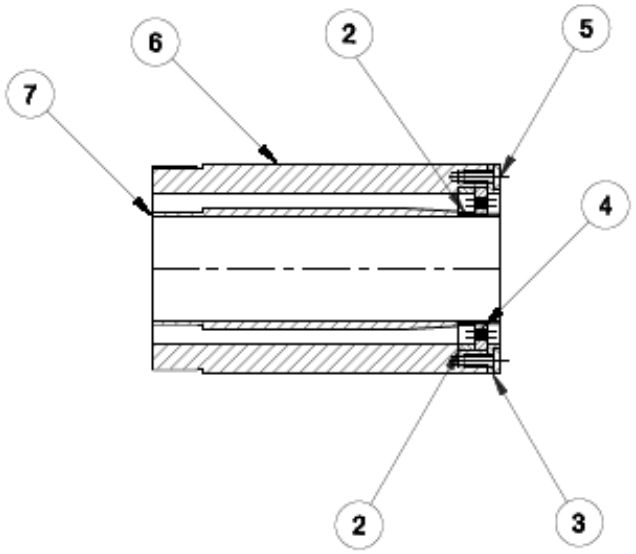

PRINT No							
ISSUED TO	WORKSHOP						
ISSUED FOR	MANUFACTURE						
	QUOTATION						
	INFORMATION						
DATE							
JOB No							

ITEM	PART No.	DESCRIPTION		No. OFF	MATL.	SPEC.	REMARKS
7	A3/38029	INNER TUBE		1			
6	A3/38028	TUBE		1			
5		BUTTON HEAD CAP SCREW		6	88	304	M4 x 10 LONG
4	A3/38025	DISTRIBUTION PLATE		1			
3	A3/38027	CLAMP RING		1			
2	A3/38026	SPACER TUBE		2			
1	A3/38030	ASSEMBLY OF MODS	1				

THIRD ANGLE PROJECTION

SHEET SIZE A2

SCALE FULL SIZE

FINISH SELF

DRAWN	CHKD.	APPVD.	STRESS APPVD.
A HUTCHINGS	A.H.		
25/03/07	26/03/07		

TITLE MAIN RIG TITLE
ASSEMBLY OF MODIFICATIONS

GENERAL TOLERANCE ON DIMENSIONS
MACHINED ±0.2
UNMACHINED
ANGLES ±1°
OTHER DIMENSIONS AS STATED

WELD WHERE SHOWN THUS

COST CODE	No. OF SETS REQ.
R44D38	1
USED ON DRG. A1/?????	

SCHOOL OF ENGINEERING
CRANFIELD UNIVERSITY

DRAWING No. ME/A2/38030

SHT. 1 OF 1 SHEETS

DRAWING No.	
ME/A3/38028	
ISSUE	MODIFICATION
A	———

ALL DIMENSIONS IN MILLIMETRES UNLESS OTHERWISE STATED

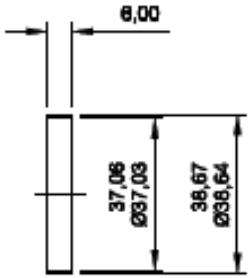

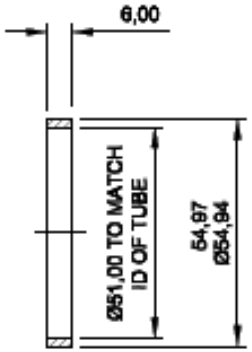

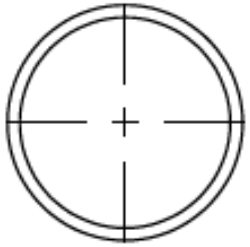

NOTES

1. MACHINE ALL OVER

2. REMOVE ALL SHARPEDGES

PRINT No	
ISSUED TO	WORKSHOP
ISSUED FOR	MANUFACTURE
	QUOTATION
	INFORMATION
DATE	
JOB No	

THIRD ANGLE PROJECTION	SHEET SIZE	ITEM	PART No.	DESCRIPTION	No. OFF	MATL.	SPEC.	REMARKS
	A3	1	A3/38028	SPACER TUBE	1 EACH	SS	316L	77

GENERAL TOLERANCE ON DIMENSIONS MACHINED ±0,2 UNMACHINED ANGLES ±1° OTHER DIMENSIONS AS STATED	COST CODE	No. OF SETS REQ.	SCALE	DRAWN	CHKD.	APPVD.	STRESS APPVD.	TITLE	MAIN RIG TITLE SPACER TUBE
	R44006	1	FULL SIZE	A HUTCHINGS 28/03/07	A H 28/03/07				
			FINISH	SCHOOL OF ENGINEERING CRANFIELD UNIVERSITY				DRAWING No.	ME/A3/38028
WELD WHERE SHOWN THUS ⌞	USED ON DRG. ME/A2/38030		SELF					SHT. 1 OF 1 SHEETS	

DRAWING No.	
ME/A3/38026	
ISSUE	MODIFICATION
A	———

ALL DIMENSIONS IN MILLIMETRES UNLESS OTHERWISE STATED

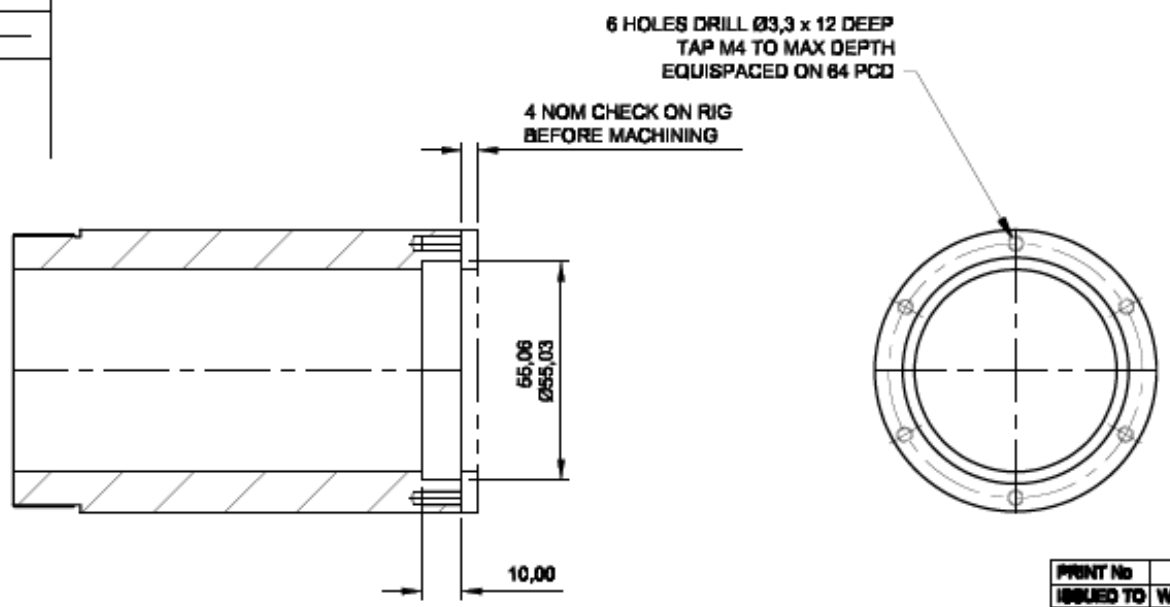

NOTE

1. MODIFY EXISTING PART
2. REMOVE ALL SHARP EDGES

PRINT No	
ISSUED TO	WORKSHOP
ISSUED FOR	MANUFACTURE
	QUOTATION
	INFORMATION
DATE	
JOB No	

THIRD ANGLE PROJECTION			SHEET SIZE	ITEM	PART No.	DESCRIPTION	No. OFF	MATL.	SPEC.	REMARKS
			A3	1	A3/38026	TUBE MODS	1	??	??	??

GENERAL TOLERANCE ON DIMENSIONS MACHINED ±0,2 UNMACHINED OTHER DIMENSIONS AS STATED	COST CODE	No. OF SETS REQ.	SCALE	DRAWN	CHKD.	APPVD.	STRESS APPVD	TITLE
	R44006	1	FULL SIZE	A HUTCHINGS 19/01/07	A H 19/01/07			MAIN RIG TITLE TUBE MODIFICATIONS
WELD WHERE SHOWN THUS			FINISH	SCHOOL OF ENGINEERING CRANFIELD UNIVERSITY				DRAWING No. ME/A3/38026
MACHINE WHERE SHOWN THUS	USED ON DRG. ME/A2/38030		SELF					SHT. 1 OF 1 SHEETS